Detection and quantification of the emissions of nitrogen oxides using satellite data across the eastern Mediterranean and Middle East region

Anthony Rey-Pommier

To cite this version:

Anthony Rey-Pommier. Detection and quantification of the emissions of nitrogen oxides using satellite data across the eastern Mediterranean and Middle East region. Ocean, Atmosphere. Université Paris-Saclay; The Cyprus Institute, 2023. English. NNT : 2023UPASJ034 . tel-04522729

HAL Id: tel-04522729
https://theses.hal.science/tel-04522729
Submitted on 27 Mar 2024

Détection et quantification des émissions d'oxydes d'azote à l'aide de données satellitaires dans la région de la Méditerranée orientale et du Moyen-Orient

Detection and quantification of the emissions of nitrogen oxides using satellite data across the eastern Mediterranean and Middle East region

Thèse de doctorat de l'Université Paris-Saclay et de The Cyprus Institute

École doctorale n° 129, Sciences de l'Environnement d'Île de France (SEIF)
Spécialité de doctorat: Géosciences
Graduate School : Géosciences, climat, environnement et planètes.
Référent : Université de Versailles-Saint-Quentin-en-Yvelines

Thèse préparée dans l'unité de recherche **Laboratoire des Sciences du Climat et de l'Environnement** (CEA/CNRS/UVSQ), sous la direction de **Frédéric CHEVALLIER**, Directeur de recherche, la co-direction de **Theodoros CHRISTOUDIAS**, Directeur de recherche, le co-encadrement de **Philippe CIAIS**, Professeur, **Jonilda KUSHTA**, Chercheuse, et **Jean SCIARE**, Professeur

Thèse soutenue à Paris-Saclay, le 8 Décembre 2023, par

Anthony REY-POMMIER

Composition du jury

Membres du jury avec voix délibérative

Charbel AFIF Professeur, The Cyprus Institute	Président
Trissevgeni STAVRAKOU Directrice de recherche, BIRA-IASB	Rapporteur & Examinatrice
Pepijn VEEFKIND Directeur de recherche, KNMI	Rapporteur & Examinateur
Claire GRANIER Professeur, Laboratoire d'Aérologie	Examinatrice
Isabelle PISON Maitresse de conférence, LSCE/UVSQ	Examinatrice

THESE DE DOCTORAT

NNT : 2023UPASJ034

DETECTION AND QUANTIFICATION OF THE EMISSIONS OF NITROGEN OXIDES USING SATELLITE DATA ACROSS THE EASTERN MEDITERRANEAN AND MIDDLE EAST REGION

by

ANTHONY REY-POMMIER

DOCTOR OF PHILOSOPHY

A THESIS SUBMITTED TO THE CYPRUS INSTITUTE
TOWARDS THE FULFILLMENT OF THE REQUIREMENTS
FOR THE DUAL DEGREE OF DOCTOR OF PHILOSOPHY

IN ACADEMIC PARTNERSHIP WITH UNIVERSITÉ PARIS-SACLAY

PARIS-SACLAY AND NICOSIA, DECEMBER 2023

universite
PARIS-SACLAY

ÉCOLE DOCTORALE
Sciences de
l'Environnement
d'Île-de-France (SEIF)

Titre : Détection et quantification des émissions d'oxydes d'azote à l'aide de données satellitaires dans la région de la Méditerranée orientale et du Moyen-Orient

Mots clés : oxydes d'azote, Méditerranée, Moyen-Orient, satellite, émissions, pollution

Résumé : Les zones urbaines et les installations industrielles concentrent la majorité des émissions de polluants atmosphériques et de gaz à effet de serre. Dans la région de la Méditerranée orientale et du Moyen-Orient, ces émissions ont des effets néfastes sur la qualité de l'air et de graves répercussions sur le climat mondial. Pour de nombreux pays de cette région, les inventaires d'émissions sont incertains ou obsolètes, ce qui empêche une mise en œuvre optimale des stratégies d'atténuation du changement climatique et de surveillance de la qualité de l'air. Pour résoudre ces problèmes, l'utilisation de systèmes d'observation indépendants devient de plus en plus courante. Les mesures satellitaires à résolution spectrale du rayonnement solaire rétrodiffusé permettent de quantifier les concentrations de polluants atmosphériques, qui peuvent être utilisés pour identifier et calculer les émissions. En particulier, les mesures de l'instrument TROPOMI à bord du satellite Sentinel-5 Precursor récupèrent des densités de colonne de dioxyde d'azote à haute résolution spatiale qui peuvent être utilisées pour cartographier les émissions d'oxydes d'azote à partir de différentes méthodes. Parmi ces méthodes, le schéma flux-divergence fournit une cartographie simple et efficace des émissions des villes et des installations industrielles isolées de l'ensemble de la région. Bien que cette méthode présente des limites, elle démontre l'importance de la contribution des systèmes d'observation indépendants pour surmonter les faiblesses des inventaires d'émissions pour la qualité de l'air, avec la possibilité d'étendre son champ d'application aux inventaires de gaz à effet de serre à travers l'utilisation de facteurs d'émission sectoriels entre les oxydes d'azote et le dioxyde de carbone.

Title: Detection and quantification of the emissions of nitrogen oxides using satellite data across the eastern Mediterranean and Middle East region

Keywords: nitrogen oxides, Middle East, Mediterranean, satellite, emissions, pollution

Abstract: Urban areas and industrial facilities concentrate the majority of air pollutant and greenhouse gas emissions. In the Eastern Mediterranean and Middle East region, these emissions result in adverse impacts on air quality and serious implications for global climate. In many countries of this region, emission inventories are uncertain or outdated, which hinders an optimal implementation of climate change mitigation and air quality monitoring strategies. To overcome such issues, the use of independent observation systems is becoming increasingly prevalent. Spectrally resolved satellite measurements of solar backscattered radiation enable the quantification of atmospheric pollutant concentrations, which can be used to identify and calculate emissions. In particular, measurements from the TROPOMI instrument on board the Sentinel-5 Precursor satellite retrieve nitrogen dioxide column densities at high spatial resolution which can be used to map emissions of nitrogen oxides from different methods. Among these methods, the flux-divergence scheme provides a simple and efficient mapping of emissions from cities and isolated industrial facilities of the entire region. Although limitations exist for this method, it demonstrates the importance of the contribution of independent observation systems to overcome the weaknesses of emission inventories for air quality, with potential to expand its scope to greenhouse gas inventories through the use of sectoral emission factors between nitrogen oxides and carbon dioxide.

VALIDATION PAGE

Doctoral Candidate: Anthony Rey-Pommier

Title of the thesis: Detection and quantification of the emissions of nitrogen oxides using satellite data across the eastern Mediterranean and Middle East region

This thesis was submitted towards the fulfillment of the requirements for the dual degree of Doctor of Philosophy at the Graduate School of The Cyprus Institute and the Université Paris-Saclay and was validated on November 10th 2023 by the Academic Committee of The Cyprus Institute.

Doctoral Examination Committee:

Pr. Charbel Afif, The Cyprus Institute & Université Saint-Joseph de Beyrouth (Chair of the Committee)
Dr. Trissevgeni Stavrakou, Institut royal d'aéronomie spatiale de Belgique
Dr. Pepijn Veefkind, Koninklijk Nederlands Meteorologisch Instituut & Delft University of Technology
Pr. Claire Granier, Laboratoire d'Aérologie, Université Toulouse III - Paul Sabatier
Dr. Isabelle Pison, Laboratoire des Sciences du Climat et de l'Environnement

Charbel Afif

DECLARATION

This thesis was submitted towards the fulfillment of the requirements for the award of a Doctor of Philosophy from The Cyprus Institute. It is the product of my own original work unless otherwise mentioned through references, notes or other statements.

Anthony Rey-Pommier

Acknowledgements

Je tiens premièrement à remercier l'ensemble du jury d'évaluation de cette thèse, et tout particulièrement les rapporteurs pour l'examen de ce mémoire. Un tel exercice est chronophage et votre engagement m'honore. Je tiens également à remercier Cathy Clerbaux et Alexandre d'Aspremont pour leur implication dans mon comité de suivi de thèse.

If I had to use one word to best describe these 36 months of doctoral studies, I would choose the word "exchange". Firstly, because they led me to take an interest in distant and different countries, where collaborations with local researchers have been fruitful. Secondly, and above all, because the joint supervision that structured these studies took me to Nicosia for a year. This was an opportunity to discover a new country, with a culture and history very different from those of hexagonal France, which is itself quite different from the Guadeloupe I left seven years ago. I firmly believe that languages are the greatest testimony to these differences. Learning the basics of Greek, in its Cypriot variant, seemed to me to be a moral obligation. Putting in the effort to engage a dialogue in someone else's language, even for a few sentences, is a way of expressing recognition for their richness. In that respect, since the acknowledgement section is an increasingly personal exercise, I would like the following words to be an ode to the need for multilingualism. I have no doubt that the reader will have the tools to switch between the French, the English and the Greek that coexist in these lines.

Mon intérêt pour les sciences du climat a commencé lors d'un stage à l'Université de Cambridge sous la supervision de Peter Haynes. Il me paraît donc normal formuler mes remerciements en commençant par ce dernier. Par la suite, je veux exprimer ma reconnaissance envers le système éducatif français et l'écosystème académique européen, dont je mesure l'importance après 24 ans de scolarité et d'études supérieures à des frais personnels minimes. De telles structures ne sont pas sans effets sur leurs bénéficiaires, et de toute évidence, mon cheminement professionnel aurait été différent dans une autre région du monde.

Ce travail de thèse n'aurait pas pu voir le jour sans la bienveillance de mes superviseurs. Au LSCE, j'ai eu l'immense chance d'être encadré par de brillants scientifiques que je cherche à remercier chaleureusement. Frédéric, merci pour tes précieux conseils scientifiques et pour l'exigence professionnelle dont tu as fait preuve à mon égard. Merci également pour la précision de ton langage dans laquelle je me suis souvent reconnu. Philippe, merci d'avoir été aussi présent malgré tes nombreuses responsabilités. Les discussions que nous avons eu, tant sur le plan humain que scientifique, ont enrichi ma vision du monde. Merci aussi à Grégoire qui m'a aidé a plusieurs reprises; ta méticulosité est toujours la bienvenue.

J'ai évidemment une pensée pour ma collègue de bureau Jinghui avec qui j'ai partagé tant de commérages, de rires, de tickets en tout genre et beaucoup de nourriture. Je pense également également aux doctorants, post-doctorants, stagiaires et permanents du LSCE avec lesquels j'ai pu partager repas, pauses, soirées festives et divers débats de société. Merci tout particulièrement à Robin, Adrien, Zoé, Alexandre, Léa, Nicole, Hannah, Alvin, Audrey, Aurélie, Élise, Marielle, Isabelle, Pramod, Juliette, Rimal et Varunika qui ont autant apprécié que subi mon humour et mon excentricité. Merci enfin à Alexandre que j'ai eu le plaisir d'encadrer pendant quelques mois. Je crois pouvoir dire que l'enrichissement a été mutuel lors de cette expérience.

Στην άλλη πλευρά της Μεσογείου, στο Ινστιτούτο Κύπρου, κατάφερα να βρω τεχνογνωσία που αποδείχτηκε καϑοριστική για την πρόοδο της διατριβής μου και που ϑα ήϑελα να αναγνωρίσω εδώ. Θεόδωρε Χ., σε ευχαριστώ για τις μεϑοδικές και πάντα συνετές συμβουλές σου, που με βοήϑησαν στο ερευνητικό μου έργο εις βάϑος. Θα ήϑελα επίσης να σε ευχαριστήσω για την αξιοσημείωτη επιστημονική σου ακεραιότητα. Ιόνη, σε ευχαριστώ που μεταδίδεις το πάθος σου σε άλλους. Εκτίμησα την καθοδήγησή σου που με ενθάρρυνε να μοιραστώ τις γνώσεις μου και να συνεργαστώ με συναδέλφους, όταν ήμουν πραγματικά προδιατεθειμένος να δουλέψω μόνος μου. Jean, σε ευχαριστώ για την καθοδήγησή σου, η οποία αν και από απόσταση, ήταν θεμελιώδης για την αποτελεσματική πορεία της έρευνας και των ευκαιριών μου για δικτύωση.

Θα ήθελα επίσης να ευχαριστήσω όλη την ομάδα στο κτήριο Αννεξ, που κατάφερνε πάντα να δημιουργεί μια υπέροχη ενέργεια στο γραφείο, από τη Μαρίνα, την οποία άκουγα συχνά να γελάει πίσω από την πόρτα του γραφείου της, μέχρι τα ζωηρά γεύματα στην τραπεζαρία με την Άννα, τον Θεόδωρο Εκ., το Γεώργιο, τη Γεωργία, την Κατιάνα, το Γιώργο, την Ελεονώρα, τη Νίκη, τον Παντελή, τον Πάνο, ακόμη και τον Jos σε κάποιες περιπτώσεις. Θα ήθελα επίσης να στείλω τους χαιρετισμούς μου στη Φλορανς, τον Άγγελο και την Corey από την ομάδα καταγραφής εκπομπών.

I have a special thought for the international students and researchers who shared my expatriation experience in Cyprus, and with whom I shared genuine and happy moments: Naveen, Thanos, Konstantina, Rawan, Pranay, Luis, Giulia, Theo, Vincent, Elie, Thaleia and Pierre-Yves. I regret I got to know some of you so late, and hope our paths will cross again.

Enfin, si le doctorat est une aventure scientifique qui comporte ses excitations et ses victoires, il comporte aussi son lot de stress, de longueurs, de galères administratives et d’échecs collaboratifs. Je tiens à remercier tous ceux qui ont célébré les meilleures étapes de cette aventure, et m’ont encouragé dans les pires. Merci à mes amis qui, de la prépa’ de Baimbridge à l’équipe du Maine en passant par les camarades de Cachan et les amis de lycée, sont à mes côtés depuis si longtemps. Merci enfin à ma famille pour son soutien pendant ces trois années. Merci d’avoir toujours cru en moi. Merci d’avoir veillé à rendre mes aspirations possibles. Merci d’avoir pavé ma route. Je suis reconnaissant et fier d’avoir ma place au sein de votre univers.

Contents

1 General introduction 11
  1.1 Emissions of greenhouse gases and air pollutants in the EMME region 11
    1.1.1 On the conceptual nature of the EMME region 11
    1.1.2 Historical greenhouse gas emissions in the EMME region 12
    1.1.3 The climate of the EMME region 14
    1.1.4 Emissions reporting and the United Nations Framework Convention on Climate Change 15
    1.1.5 Bottom-up and top-down estimations 16
    1.1.6 Observation of carbon dioxide and co-emitted species from space 17
    1.1.7 Main NO_x emitters in the EMME region 18
  1.2 Chemistry of nitrogen oxides 23
    1.2.1 Nitrogen-containing species, nitrogen oxides, and NO_x 23
    1.2.2 Leighton relationship 25
    1.2.3 Reactive nitrogen and NO_x sinks 26
    1.2.4 Daily and annual cycles in the EMME region 30
    1.2.5 NO_x abatement methods 30
  1.3 Remote sensing instruments and methods 31
    1.3.1 Differential optical absorption spectroscopy 31
    1.3.2 The Sentinel-5 Precursor satellite 33
    1.3.3 The TROPOMI instrument 34
    1.3.4 Previous instruments 36
    1.3.5 TROPOMI tropospheric and stratospheric column densities 37
    1.3.6 TROPOMI air mass factor and averaging kernels 37
    1.3.7 TROPOMI quality flag insurance 40
    1.3.8 TROPOMI product and version differences 40

2 Inversion methods - from NO_2 observations to NO_x emissions 43
  2.1 The flux-divergence model 43
    2.1.1 Mass balance 43
    2.1.2 Modelling of the sink term 45
    2.1.3 The flux-divergence equation for NO_x emissions 46
    2.1.4 Background removal 47
    2.1.5 Diffuse sources and point sources 48
    2.1.6 Vertical structure and topographic correction 53
    2.1.7 OH feedback and model resolution 53
  2.2 Alternative methods to derive emissions from column densities 55
    2.2.1 Comparison with an exponentially-modified Gaussian function 55
    2.2.2 Other alternative methods 57
  2.3 Estimation of parameters 59
    2.3.1 ERA5 59
    2.3.2 CAMS 59

3 Results - NO_x emissions in the EMME region 61
3.1 Estimation of NO_x emissions in Egypt with the flux-divergence method . . . 61
3.1.1 Presentation of the article . . . 61
3.1.2 Abstract . . . 62
3.1.3 Introduction . . . 62
3.1.4 Instrumentation and data . . . 63
3.1.5 Method . . . 67
3.1.6 Results and discussion . . . 73
3.1.7 Conclusions . . . 83
3.2 Estimation of NO_x emissions in Qatar and comparison with electricity data . . . 85
3.2.1 Presentation of the article . . . 85
3.2.2 Abstract . . . 85
3.2.3 Introduction . . . 86
3.2.4 General features of Qatar and overview of reported NO_x emissions in 2007 . . . 86
3.2.5 Instruments and data . . . 88
3.2.6 Method . . . 90
3.2.7 Results . . . 92
3.2.8 Comparison with air pollution inventories and electricity generation data . . . 99
3.2.9 Uncertainties and assessment of results . . . 103
3.2.10 Conclusion . . . 105
3.3 NO_x emission factors differences in Cypriot power plants . . . 107
3.3.1 Presentation of the article . . . 107
3.3.2 Abstract . . . 107
3.3.3 Introduction . . . 108
3.3.4 General features of NO_x emitters in Cyprus . . . 109
3.3.5 Instrumentation and data . . . 110
3.3.6 Method . . . 112
3.3.7 Results . . . 116
3.3.8 Comparison with regional and global inventories for power plants . . . 120
3.3.9 Conclusion . . . 123
3.4 Limitations of the method . . . 125
3.4.1 Limits in the TROPOMI a priori profiles and quality flags . . . 125
3.4.2 Limits in the estimation of the sink term . . . 125
3.4.3 Limits in the estimation of the transport term . . . 127
3.4.4 Vertical transport effects . . . 129
3.4.5 Overlapping of emissions . . . 130
3.4.6 Scaling of NO_2 production to NO_x emissions . . . 130
3.5 Extension of the method . . . 131
3.5.1 Estimation of traffic and shipping emissions . . . 131
3.5.2 Combination with estimated activity from satellite RGB images . . . 133

4 Conclusion and perspectives 135
4.1 Conclusion . . . 135
4.2 Perspectives . . . 137

List of figures and tables 139

Bibliography 146

Annexes 167
Notations . . . 167
Acronyms . . . 170
Supplementary Materials . . . 171
Demonstations . . . 184

Chapter 1

General introduction

The aim of this chapter is to understand the value of observing greenhouse gas emissions and co-emitted species by using satellite observations in the Eastern Mediterranean and Middle East region, and to justify subsequently the focus on the observation of nitrogen oxides. This will require, firstly, a precise definition of the terms of the subject, but also a comparative analysis of the advantages and weaknesses of the satellite detection methods for each species. Secondly, the chemistry of nitrogen oxides is presented in order to identify the major limitations to account for in the process of quantifying emissions based on observations. A general description of the TROPOMI NO_2 product, which is the main resource used in the course of this thesis, is then carried out to better understand the construction of satellite observations, regardless of the method used to derive emissions.

1.1 Emissions of greenhouse gases and air pollutants in the EMME region

1.1.1 On the conceptual nature of the EMME region

A given geographical area can be characterised, and therefore named, with respect to one or several main features. To define these features, a distinction is usually made between physical geography, which is the spatial study of the natural environment such as the atmosphere, the hydrosphere, the biosphere or the geosphere, and human geography, which is the spatial study of human activities at the surface of the globe. Physical geography can define areas according to their topographical (i.e. the Alpes), geological (i.e. the Permian Basin) or hydrographic (i.e. the Caspian Sea) features, while human geography defines areas according to their linguistic (i.e. the Basque Country), political (i.e. the European Union), socio-economic (i.e. the Blue Banana) or geopolitical (i.e. the Indo-Pacific region) features.

The term "Eastern Mediterranean" originally stems from the definitive partition of the Roman Empire in two different entities on the death of the emperor Theodosius I in 395 CE. This historical definition has gradually been replaced by a geographical definition referring to the eastern half (or third) of the Mediterranean. It typically includes all the coastal zones of this area, i.e. the southern half of Anatolia, the island of Cyprus, the Greek islands, as well as the countries of Egypt, Israel, Jordan, Palestine, Syria and Lebanon. Its broadest uses can also embrace Eastern Libya, continental Greece and European Türkiye (East Thrace). Conversely, the term "Middle East" is a forged expression referring to British interests on the route to India, although the term did not appear until the beginning of the 20th century (Mahan, 1902). Defined as opposed to the Near East and the Far East within the Asian continent, its geopolitical definition fluctuates, but generally includes the entire Arabian Peninsula, Mesopotamia and Iran. The two regions of the Eastern Mediterranean and the Middle East can be grouped together into a larger region, simply called the Eastern Mediterranean - Middle East region, and often referred to by the acronym "EMME". This definition is political, as it covers a group of

20 countries*: Bahrain, Cyprus, Egypt, Greece, Iran, Iraq, Israel, Jordan, Kuwait, Lebanon, Northern Cyprus, Oman, Palestine, Qatar, Saudi Arabia, Syria, Türkiye, the United Arab Emirates and Yemen. They represent a combined population of over 450 million inhabitants.

The EMME region can be examined from a historical perspective: it is the birthplace of agriculture, which fueled the arrival of several major civilisations. Several areas of the region have been put under the control of larger entities throughout history (Achaemenid, Roman, Abassid, Ottoman and British Empires), but the entire region has never been entirely politically unified. From a linguistic perspective, Arabic is the most widely spoken language in the region, followed by Persian, Turkish, Kurdish, Greek and Hebrew. Multiple minor languages and dialects are also present. Economically, there are major disparities: Yemen ranks 181th in the world in terms of gross domestic product per capita based on purchasing power parity, while Qatar ranks 4th (International Monetary Fund, 2023). Income inequalities can be relatively low in countries such as Iraq or the United Arab Emirates, or significantly high in countries such as Iran or Türkiye (World Bank, 2022). Finally, some countries in the region are mostly flat, such as Egypt or Qatar, while others, such as Iran or Lebanon, are mountainous. Such historical, linguistic, economic and topographic differences can therefore be perceived as sufficiently important to question the relevance of the EMME region as a concept.

There is, however, one feature common to the countries of the EMME region: the region is particularly vulnerable to climate change. Indeed, under a "business as usual" scenario (i.e. a scenario which assumes no significant change in attitudes and priorities, and no major changes in technology, economics and policies for future patterns of activity), the major part of the region faces a 5°C-increase in the mean annual temperature by the end of the century (Zittis et al., 2022), which would bring catastrophic consequences in terms of hyperthermia risk, water scarcity or biodiversity loss. The Eastern Mediterranean and Middle East Climate Change Initiative, launched by the presidents of Cyprus and Egypt at the COP27 on November 8th 2022, gathered Heads of State of the EMME countries to coordinate a concerted regional response to address the climate crisis, in line with the goals of the Paris Agreement, the 2030 Agenda for Sustainable Development, the Convention on Biological Diversity, the UN Convention to Combat Desertification and the Barcelona Convention (EMME-CCI, 2022). This initiative expressed their willingness to take coordinated action by implementing policies and measures outlined on a Regional Action Plan, promoting regional cooperation and environmental policies, but without creating legal obligations or financial implications. Ultimately, the relevance of the EMME region concept can thus be understood in the light of global warming: that of a cooperation between diverse states that share the same vulnerability to the effects of climate change (Carlucci et al., 2021).

1.1.2 Historical greenhouse gas emissions in the EMME region

A greenhouse gas (GHG) is a gas that has the capacity to trap infra-red radiation that would otherwise escape back into space. Different greenhouse gases are naturally present in the atmosphere in quantities determined by geophysical equilibria (Berner, 2003). However, anthropogenic greenhouse gas emissions have significantly increase the amount of many GHGs in the atmosphere. In particular, carbon dioxide (CO_2), methane (CH_4) and nitrous oxide (N_2O) concentrations have increased in the troposphere (i.e. the lowest layer of the atmosphere) since the Industrial Revolution, resulting in a disruption of the energy balance of the Earth leading to long-term effects on the global climate and commonly referred to as climate change (Masson-Delmotte et al., 2021). In particular, anthropogenic greenhouse gas emissions in the EMME region have seen a significant increase over the last seventy years. From

---

*The New Eastern Mediterranean and Middle East Climate Initiative, from which this list is derived, was launched during COP27, an international conference organised by the United Nations. Within this organisation, the State of Palestine has a status of a non-member observer state. Conversely, the United Nations does not recognise the Turkish Republic of Northern Cyprus. For scientific purposes, we will consider the territories of the Turkish Republic of Northern Cyprus, as well the British Sovereign Base Areas of Dhekelia and Akrotiri, as part of the EMME region. This choice is not intended to influence the reader, and should not be interpreted as a position statement from the author, supervisors or reviewers of this thesis. A position of neutrality is also adopted with regard to jurisdictional claims in published maps.

the PRIMAP-hist dataset (Gütschow et al., 2016) regarding greenhouse gas emissions, Zittis et al. (2022) produced a quantitative and sectoral analysis of GHG emissions (which are generally measured as tons of carbon dioxide equivalents "t_{CO2eq}" in order to account for the global warming potential differences between greenhouse gases) in the EMME region over the last decades in comparison with other regions of the world. In the 1960s, emissions were at 0.6 $Gt_{CO2eq}.yr^{-1}$, but by the 2010s, they rose to 3.6 $Gt_{CO2eq}.yr^{-1}$. This growth rate outpaced the global increase in greenhouse gas emissions. Consequently, the share of the EMME region in global GHG emissions more than doubled, rising from 3% in the 1960s to 7.7% in the 2010s. During this last decade, the emissions of the region surpassed those of India and closely approached those of the European Union. Moreover, these emissions are expected to keep rising, potentially exceeding those of the European Union in the near future. Figure 1.1, extracted from Zittis et al. (2022) SI, shows historical total emissions in the EMME region by gas and the corresponding share in global emissions.

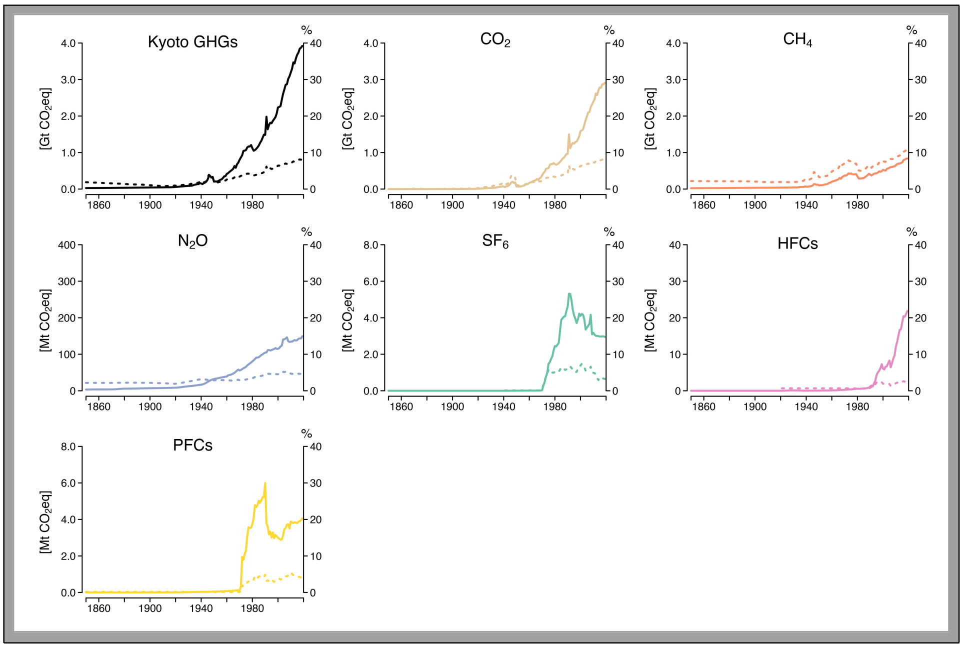

Figure 1.1: Historical total emissions in the EMME region by greenhouse gas (solid lines, left ordinate) and share of total world emissions (dashed lines, right ordinate). Data sources: country reported emissions from the PRIMAP-hist dataset version 2.3.1 (Gütschow et al., 2016). Figure extracted from Zittis et al. (2022) SI.

The emission trends in the EMME region have been fluctuating over the past five decades. Greenhouse gas emissions were negligible before the 1950s compared to industrialised regions such as western Europe or the United States. Between the early 1960s and late 1970s, emissions started to grow by 0.04 $Gt_{CO2eq}.yr^{-1}$, before declining by about 10% during the years 1980–1983 due to the second oil crisis. Afterward, emissions picked up again, increasing at a rate of 0.076 $Gt_{CO2eq}.yr^{-1}$. The study of emissions by gases and sectors reveals that methane, followed by nitrous oxide, were historically the dominant contributors to total GHG emissions in the EMME region, mainly due to the agricultural sector until the late 1910s and early 1920s. However, with global economic growth and increasing global energy demand driving fossil fuel extraction, a shift occurred in the sectoral composition of greenhouse gas emissions, and the energy sector became the first source of emissions, particularly for CO_2 and CH_4. Emissions of these two species within the energy sector accounted together for 91%–96% of the total anthropogenic emissions over the past five decades. They were also responsible for 96% of the emission increases between the 1960s and the 2010s, with CO_2 becoming the dominant contributor from the 1980s. Concurrently, methane emissions decreased overall, peaking between the 1950s and the 1970s, mainly due to fugitive sources. The increase in methane emissions since the 1960s can be attributed to expanded gas extraction. Within the EMME region, the major emitting countries are Iran, Saudi

Arabia, Türkyie, Egypt, and Iraq, collectively responsible for 73% of the total CO_2 emissions during the 2010s and 74% of the increase in emissions over the past five decades (Gütschow et al., 2016).

The majority of these emissions being directly or indirectly associated with the energy sector, the region is heavily reliant on the extraction and combustion of fossil fuels. Several of its countries are reliant on their exploitation since they are oil and gas-producing states. For instance, between 2014 and 2018, Saudi Arabia had the 2nd largest production of crude oil while Iran and Qatar had the 3rd and 4th largest productions of natural gas (OPEC, 2020). Overall, these significant contributors to the global greenhouse gas emissions, which are the primary drivers of climate change, are such that the EMME countries have a considerable responsibility in the current global warming.

1.1.3 The climate of the EMME region

The interest in greenhouse gas emissions in the EMME region is all the more necessary given that this part of the world is a climate change hotspot. Indeed, it is directly influenced by different atmospheric circulation patterns and meteorological processes coming from Europe, Asia and Africa (Lelieveld et al., 2002; Carmona, Alpert, 2009). Important feedbacks, mainly due to the complex topography and the effects of the different seas within the region (i.e. the Mediterranean, Red, Arabian, Black and Caspian Seas), influence the regional particularities of the environmental conditions (Lelieveld et al., 2012; Belda et al., 2014). The region has therefore always included a diversity of climatic zones. Although the climates of these different zones have varied over the centuries (Lelieveld et al., 2012; Luterbacher, Xoplaki, 2017; Finné et al., 2019; Sinha et al., 2019; Jones et al., 2019; Luterbacher et al., 2021), most of them show a clear drying trend for the last two centuries. Today, most of the EMME region encompasses large, arid and hot deserts with sparse vegetation and near zero precipitation (Hamidi et al., 2013; Francis et al., 2021; Fonseca et al., 2022). Average summer temperatures regularly exceed 40°C, and can even surpass 50°C in some locations during heatwaves. Moreover, the Arabian Desert, which is the major desert of the region, frequently experiences major dust storms (Prakash et al., 2014), which are boosted by the lack of precipitation. These extreme events significantly affect ecosystems and human activity. The northern part of the EMME region is the only one characterised by a mostly temperate climate (Lionello et al., 2006), with high precipitation over the Taurus, Caucasus and Alborz mountains. The observed changes over the past century in the region are marked by a significant warming that is consistent with the global trend. This increase has accelerated over the last four decades to reach about 1.4°C–1.5°C compared to the beginning of the 20th century. Similar trends have been identified for most individual EMME countries (Freiwan, Kadioğlu, 2008; Shohami et al., 2011; Tanarhte et al., 2012; Ramadan et al., 2013; Almazroui et al., 2014; Donat et al., 2014; Mariotti et al., 2015; Xoplaki et al., 2016; Mohammed, Fallah, 2019; Mostafa et al., 2019; Almazroui, 2020; Fonseca et al., 2022). At the scale of the region, Zittis et al. (2022) reveal a warming trend of 0.45°C/decade for 1981–2019, which is nearly twice the global trend for the same period (0.27°C/decade). Concerning the changes in the hydrological cycle, the observed trend is a decrease in total precipitation and an increase of drought intensity (Hoerling et al., 2012; Nastos et al., 2013; Caloiero et al., 2018; Spinoni et al., 2019), despite an increase in the amplitude of extreme rainfall or in the number of heavy precipitation events for some Mediterranean regions (Alpert et al., 2002; Founda et al., 2013). Between 1951 and 2016, about 10% of the most extreme macro-regional drought events globally occurred in the EMME region and neighbouring countries (Spinoni et al., 2019), such as the 1989–1991 drought in the southern Balkans, the 2000–2002 drought in Cyprus and Greece, the 2007–2008 drought in Türkiye and Cyprus, and recent drought events in the Middle East that affected many countries in the region including Syria, Iraq, and Iran (Spinoni et al., 2019). Reduced precipitation may result in diminished vegetation, expanding exposed surfaces that are more vulnerable to wind erosion, leading to amplified and more frequent dust storms (Middleton, 2019; Gholami et al., 2020; Rashki et al., 2021).

Such considerable changes in environmental and climate conditions could suggest substantial repercussions for diverse sectors and socio-economic activities. These may encompass water resource and agriculture management, impacts on human health, fluctuations in energy demand and production, changes in transportation patterns, influences on ecosystems, biodiversity considerations, and an increased risk of forest fires (Cramer et al., 2018; Waha et al., 2017). These impacts will likely be exacerbated by additional factors, such as rapid regional population growth and urbanisation, which will inevitably increase the demand and competition for natural resources. The EMME region thus faces a complex and interdependent relationship between its significant contribution to global greenhouse gas emissions and its vulnerability to the impacts of climate change. Balancing economic growth and sustainability is an important challenge for the region, requiring a transition towards renewable energy sources, energy efficiency, and sustainable development practices to mitigate further climate impacts while ensuring energy security and economic stability.

1.1.4 Emissions reporting and the United Nations Framework Convention on Climate Change

An effective reduction of greenhouse gas emissions strategy requires an accurate knowledge of the GHG-emitting sectors and sources, as well as the amount of their respective emissions. Reporting mechanisms thus provide essential information for assessing contributions to climate change and developing strategies to mitigate impact. Accurate and transparent reporting allows policymakers to make informed decisions, implement effective policies, and monitor progress towards emission reduction targets. It also facilitates multilateral cooperation, and drives innovation by identifying opportunities for developing energy efficiency measures and low-carbon technologies. As such, reliable emission inventories form the basis for developing and implementing climate policies.

The United Nations Framework Convention on Climate Change (UNFCCC) established an international environmental treaty negotiated at the United Nations Conference on Environment and Development held in June 1992. The ultimate objective of the treaty is to stabilise greenhouse gas concentrations "at a level that would prevent dangerous anthropogenic interference with the climate system". It states that "such a level should be achieved within a time-frame sufficient to allow ecosystems to adapt naturally to climate change, to ensure that food production is not threatened, and to enable economic development to proceed in a sustainable manner" (United Nations, 1992). The treaty provides a framework for negotiating specific international treaties (called "protocols") that may set binding limits on greenhouse gases and entered into force on March 21st 1994. 43 Parties to the UNFCCC are classified as industrialised (developed) countries and "economies in transition" and listed in Annex I of the convention. Among those parties, 24 are also listed in Annex II of the convention, and are required to provide financial and technical support to other countries to assist them in reducing their climate change mitigation and adaptation strategies. Parties to the UNFCCC not listed in Annex I of the convention are considered as mostly low-income developing countries and may volunteer to become Annex I countries when they are sufficiently developed.

The Paris Agreement establishes an Enhanced Transparency Framework designed to build trust and confidence that all countries are contributing their share to the global effort in reducing global greenhouse gases emissions. The framework established by the Paris Agreement complements and extends the existing reporting and verification mechanisms set by the UNFCCC (United Nations, 2015). The quality of GHG inventories relies on the integrity of the methodologies used, the completeness of reporting, and the procedures for compilation of data. Standardised requirements for reporting national inventories have been developed to this end: by April 15th each year, Annex I Parties must provide their annual GHG inventories covering emissions and removals of direct greenhouse gases from five sectors (energy, industrial processes and product use, agriculture, land use, land-use change and forestry and waste), and for all years from the base year (or period) to two years before the inventory is due. Under the UNFCCC reporting guidelines on annual inventories for Annex I Parties, inventory submissions are given as a series of standardised data tables containing mainly quantitative information, as well as a report containing transparent and detailed information on the inventory.

Within the EMME region, only Cyprus, Greece and Türkiye are Annex I Parties, with Greece being the only Annex I and II Party[†]. Other EMME nations are listed as non-Annex I parties, although many of them can be considered as developed countries. As a result, they have no obligation to follow the UNFCCC reporting guidelines and report GHG emissions annually, in accordance with the principle of common but differentiated responsibilities and respective capabilities promoted by the Framework. As a result, reported emissions in these countries can be outdated by several years. For instance, the last national report on GHG emissions from Iraq dates back to 2017 but concerns emissions in 1997, with a benchmarking constructed with information from 1990, which is the nearest year for which information was available. Figure 1.2 shows, for each EMME country, the year of the last submission of GHG emission inventory, as well as the last year reported in the submission. National reports for non-Annex I countries can be found at `https://unfccc.int/non-annex-I-NCs`.

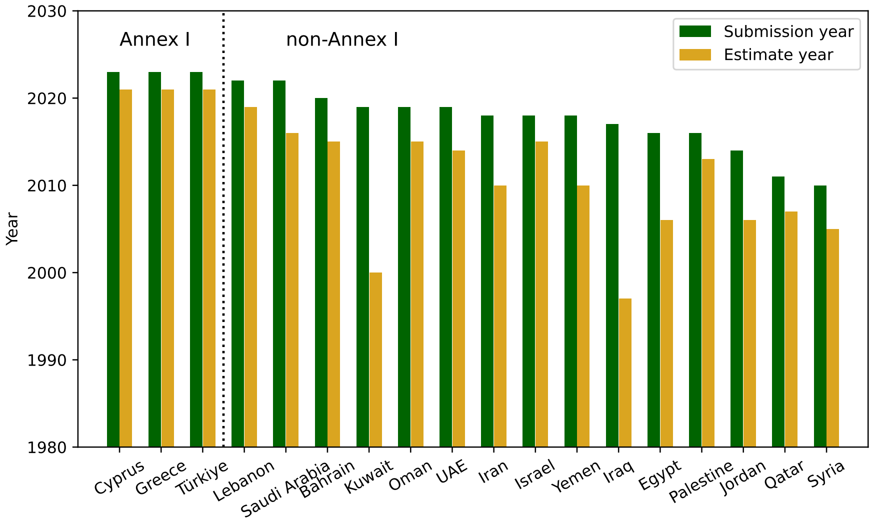

Figure 1.2: Year of last submission of GHG inventories in EMME countries (green). The last year for which emissions are estimated is also shown (yellow). This graph has been produced on July 21st 2023 based on available data at that time on the UNFCCC website.

In many developing countries, the problem of updating self-reported emissions comes with difficulties in estimating their emissions of greenhouse gases, due to the lack of local infrastructure to obtain detailed information on technical factors such as energy consumption, fuel type and technology (Kouyakhi, 2022; Jafar et al., 2023), but also due to potential misallocations of emissions or missing sources. In particular, the lack of information on the processes involved contributes greatly to the uncertainty of emission inventories (Silva, Arellano, 2017). In order to address such biases in the self-reporting mechanism, the contribution of independent observation systems is being increasingly sought (IPCC, 2019). Most independent system can take the form of local, national or regional inventories built on bottom-up or top-down estimations.

1.1.5 Bottom-up and top-down estimations

Estimating emissions of a given species involves quantifying the sources and sinks involved in its cycle. Such a cycle can be complex, because the reactivity of a given molecule depends not only on its physical and chemical features, but also on the environment in which it is found. Sinks are generally chemical in nature, but other removal sources such as deposition or radioactivity can also have an effect on its dynamics at the global scale. The bottom-up approach and the top-down approach are the two general methods for estimating emissions:

[†] Türkiye was deleted from Annex II by an amendment that entered into force June 28th 2002, pursuant to decision 26/CP.7 adopted at COP7.

- The bottom-up approach integrates various methods that independently estimate emissions from different categories. It seeks to describe critical parts of the emission process and then aggregates it to a larger scale. A standard modus operandi is to combine data on demographics, socio-economic features, technology knowledge and emission factors related to a country or region to infer the corresponding emissions (Höglund-Isaksson, 2012; Tubiello et al., 2013; Janssens-Maenhout et al., 2019; Hoesly et al., 2018). This method is widely used, for example, to create CO_2 emission inventories for industry, transport and energy. Another method involves examining the processes that contribute to the formation of pollutants, allowing for their modelling and the deduction of emissions. This requires profound knowledge of physical processes involved in the cycle of the species, and its implementation can be achieved, for instance, through the use of numerical models designed to describe the exchanges between the biosphere and the first layers of the atmosphere (usually the troposphere and the following layer called stratosphere). This is one of the methods used to estimate methane emissions from wetlands (Poulter et al., 2017) or biomass combustion (Van Der Werf et al., 2017). These methods can be improved by integrating data from satellites or ground measurements (Oda et al., 2018), in order to constrain the models and improve their estimates. A third method involves extrapolating observations obtained by direct measurement of flows (Rosentreter et al., 2021). This method is particularly used for natural methane emissions, such as from freshwater or geological sources.

- The top-down approach relies on understanding the atmospheric transport and dispersion of gases to attribute emissions to their respective origins, such as cities, industrial facilities or natural sources. This understanding is based on atmospheric inversion models. Most often, statistical methods are used to minimise the differences between simulations and observations (e.g. atmospheric concentrations of pollutants measured by air sampling stations or satellite retrievals) by adjusting the input variables of a chemistry-transport model (e.g. emissions). Optimal values of the input variables, which are best able to explain the observations, are thus estimated (Kadygrov et al., 2015; Berchet et al., 2015; Lian et al., 2023). Alternatively, atmospheric observations can be used directly to estimate the associated emissions without prior optimisation, which usually requires less computing time and modelling complexity.

1.1.6 Observation of carbon dioxide and co-emitted species from space

Direct satellite observations of CO_2 are increasingly used as a base for top-down estimates of CO_2 emissions from various sources. The NASA second Orbiting Carbon Observatory (OCO-2) polar satellite is one of the best existing instruments for the retrieval of column-averaged dry-air mole fraction of CO_2. It observes the Earth with a 1.29×2.25 km^2 resolution and a $\sim$10 km-wide swath for each orbit, which makes it particularly suitable for informing on natural CO_2 budget at the continental scales (Eldering et al., 2017). It has already acquired more than nine years of data since its launch in July 2014, which allowed estimating many CO_2 emissions at different scales in many regions of the world (Hakkarainen et al., 2016; Ye et al., 2020; Zheng et al., 2020; Lei et al., 2021; Chevallier et al., 2022). While numerous methods have been suggested for estimating local CO_2 emissions based on single satellite overpasses (Varon et al., 2018), the direct observation of CO_2 emissions from space confronts its own set of challenges. One such challenge is posed by the limited swath width of OCO-2, which confines the coverage area in a singular overpass. This restriction results in extended revisit times, decreased observation frequencies, and complications in capturing rapidly changing atmospheric conditions or localized CO_2 emissions. In the design of observation instruments, the selection of swath width often results from arbitrage between spatial coverage and other factors like instrument design and data volume. Strategies such as operating in constellations or using additional instruments like OCO-3 on the International Space Station aim to increase coverage and revisit frequency to compensate for the narrow swath. Moreover, the presence of clouds or methane sources, which emit their own thermal radiation, interfere with CO_2 measurements.

Such limitations fueled the exploration of alternative approaches. Observation of species that are co-emitted with fossil CO_2 during combustion has the potential to provide information to fill the carbon cycle knowledge gaps. Estimating the emissions of co-emitted species is also important for understanding global climate, since they can affect the lifetime of greenhouse gases (Stevenson et al., 2022). These proxy species, such as $NO_x = NO + NO_2$, share many sources that are co-located in time and space with those of CO_2, and thus can be used to help constrain fossil CO_2 emissions and monitor temporal changes in emissions (Berezin et al., 2013; Goldberg et al., 2019a). Through observations of air pollutants such as NO_2, plumes of CO_2 can be detected (Kuhlmann et al., 2019; Reuter et al., 2019; Hakkarainen et al., 2021, 2022). By monitoring NO_x emissions and their correlation with CO_2 emissions, it thus becomes possible to estimate CO_2 emissions indirectly. Carbon monoxide (CO) observations, which is also co-emitted with CO_2 in certain circumstances, are sometimes added as well (Konovalov et al., 2016; Silva, Arellano, 2017; Park et al., 2021). NO_x and CO emissions can also be used together to characterise burning efficiencies (Lama et al., 2020). Such co-emitted species can even be used as a proxy to indirectly measure CO_2 emissions, because emission ratios between these species and CO_2 are characteristic of each emission sector and fuel type, making them valuable indicators for estimating CO_2 emissions indirectly. For instance, Zhang et al. (2023) quantified urban CO_2 emissions from NO_2 observations in China using a CO_2:NO_x emission ratio of 591 $g_{CO2}.{g_{NOx}}^{-1}$ derived from an air quality inventory (Zhao et al., 2013; Zheng et al., 2019). Similarly, Kuhlmann et al. (2021) derived CO_2:NO_x emission ratios for power plants in Czechia, Germany and Poland ranging from $\sim$ 600 to $\sim$ 4200 $g_{CO2}.{g_{NOx}}^{-1}$ using different measures from observations of a constellation of Copernicus CO_2 monitoring satellites, but with high uncertainties. Those estimations were close to calculated emission ratios from inventories ranging from 665 to 1257 $g_{CO2}.{g_{NOx}}^{-1}$. Finally, Hakkarainen et al. (2021) derived CO_2:NO_x emission ratios ranging between $\sim$ 50 and $\sim$ 700 $g_{CO2}.{g_{NOx}}^{-1}$ for a power plant in South Africa using satellite data and assuming different NO_2 lifetimes.

The approach of using NO_2 observations to constrain or infer CO_2 emissions are particularly interesting because NO_2 has a short lifetime. In comparison to CO_2, the lifetime of NO_2 is very short (only a few hours), which leads to anthropogenic activity patterns that can be observed from space with a high signal-to-noise ratio. For these reasons, nitrogen oxide emissions areas can be easily identified by averaging satellite NO_2 concentrations over a sufficiently long period of time. Additionally, NO_2 retrievals are less affected by clouds, allowing for a larger acquisition of observations. However, this short-lifetime advantage is compensated by necessary assumptions of NO_2 lifetime when inferring NO_x emissions from NO_2 observations that are not needed for CO_2. Besides, NO_x:CO_2 ratios change with distance from the source, and are different under different weather conditions. Such complicating factors need to be accounted for when trying to estimate CO_2 emissions from NO_2 observations.

Finally, given that species co-emitted with CO_2 are mostly harmful air pollutant, the observation and quantification of such species from space has a dual benefit. Through the calculation of the emission factor between CO_2 and NO_x, the observation of NO_2 provides independent methods to combat climate change, but also to monitor air quality and to support policies aimed at protecting public health and the environment. This benefit is all the more necessary since NO_2 emission inventories usually suffer from the same defects as CO_2 inventories: they can be outdated or highly uncertain, especially in developing countries. As a consequence, the EMME region is appropriate to perform a detection and a quantification of NO_x emissions to provide a better monitoring of global anthropogenic emissions of greenhouse gases and air pollutants, therefore helping various stakeholders in their strategies and obligations to tackle air pollution issues and climate change.

1.1.7 Main NO_x emitters in the EMME region

In most places of the world, the growing industrialisation has been accompanied by an increase in NO_x emissions. When counted as NO_2[‡], total anthropogenic emissions of NO_x were 123 Mt in 2000,

---

[‡] NO_x are usually counted in mass terms as NO_2. An alternative approach is to count the mass of nitrogen atoms.

with the majority attributed to fossil fuel combustion and industrial processes (93 Mt). Agriculture contributed to 12 Mt, while biomass and biofuel burning accounted for 18 Mt. In contrast, natural sources of emissions were 37 Mt in 2000, with soils contributing to 24 Mt and lightning contributing to 13 Mt (Stocker, 2014). Since then, global emissions have been growing in spite of the successful reduction of emissions in developed regions of the world (Crippa et al., 2016; Miyazaki et al., 2017), and later, China (de Foy et al., 2016), partly driven by continuous efforts to strengthen the emissions standards for road vehicles in the corresponding countries. In other regions, an increase in vehicle fleet as well as non-compliance with emission standards (Anenberg et al., 2017), growing aviation and demand for fossil energy, and consequently large number of new fossil fuel power plants, have been overcompensating these reductions. Since about 2011, global NO_x emissions appear to have stabilised or slightly declined.

In the EMME region, natural NO_x sources are minor and the emissions are dominated by fossil fuel combustion. In recent years, satellite observations have been used to derive long-term trends in tropospheric NO_2 at the scale of cities (Abdelsattar et al., 2021), countries (Oner, Kaynak, 2016; Rabiei-Dastjerdi et al., 2022) and regions (Rajab et al., 2020; Stavrakou et al., 2020), or short-term effects due to abrupt changes in anthropogenic activities (Abou El-Magd, Zanaty, 2020; Koukouli et al., 2021). Overall, strong upward NO_2 trends have been reported for the Middle East, including the Arabian Gulf and Eastern Mediterranean (Lelieveld et al., 2015). Those satellite observations can be completed with ground measurements of NO_2 levels (Butenhoff et al., 2015; El Kenawy et al., 2019). The AQABA (Air Quality and Climate Change in the Arabian Basin) campaign in 2017 also provided in-situ characterisation of the photochemical and aerosol processes in the EMME region (Friedrich et al., 2021), including the identification of NO_2 sources. NO_x emissions have also been linked to economic and industrial activities (Vrekoussis et al., 2013). It was also shown that NO_2 trends were often related to a combination of economic development and emission controls aimed at improving air quality (Castellanos, Boersma, 2012).

At high levels, NO_x pollution is characterised by a reddish-brown color. This coloration is attributed to the formation of nitrogen dioxide (NO_2), a prominent component of NO_x emissions. Nitrogen dioxide contributes to the formation of photochemical smog, reducing visibility and impacting air quality. Figure 1.3 shows the aspect of NO_x pollution in four megacities of the EMME region.

Figure 1.3: Examples of NO_x pollution in four megacities of the EMME region, with clockwise from the top-left corner: Athens (extracted from Athanasios et al. (2015)), Istanbul (photographer: Dmitry Papkovich), Tehran (unknown source) and Dubai (unknown source). NO_2 is responsible for the reddish-brown color of the lower layers of the atmosphere.

In the EMME region, several factors contribute to the presence of NO_x pollution. The region experiences rapid industrialization, population growth, and a significant reliance on fossil fuel combustion for fuel extraction and transformation, energy generation and transportation. Industrial activities, as well as the burning of fossil fuels in vehicles and power plants, are the primary sources of NO_x emissions. The resulting levels of pollution can vary throughout the year. However, it is often more pronounced during periods of increased industrial and transportation activities, such as peak energy demand seasons or when weather conditions trap pollutants near the ground. Urban areas with high traffic congestion and industrial centres experience higher NO_x emissions, leading to elevated pollution levels in these regions.

During combustion processes, nitrogen and oxygen molecules react at high temperatures to form NO_x. In combustion processes, four primary sources are usually distinguished, and referred to as thermal, fuel, prompt and feed NO_x (Cox, 1999; Baukal, 2005):

- Fuel NO_x is estimated to contribute to a significant portion of anthropogenic NO_x emissions, particularly from transportation fuels. Nitrogen-bearing fuels like certain coals and oils release nitrogen during combustion. The released nitrogen can ultimately form free N_2 or NO. In the case of oil combustion, it can contribute to most of the emissions, while coal combustion, especially in combustors designed to minimise thermal NO_x, can contribute up to 80% due to their elevated content of organically bound nitrogen.

- Prompt NO_x is generated during the manufacturing of nitrogen fertilizers. Although nitrous oxide is emitted during fertilizer application, it reacts in the atmosphere to form nitrogen oxides. It should be noted that the abundance of prompt NO_x is unclear, as it is depends on fuel composition and many other factors.

- Feed NO_x is associated with the combustion of nitrogen present in the feed material of cement rotary kilns, typically occurring at temperatures between 300°C and 800°C. It is generally considered as minor contributor in other industrial processes.

- Thermal NO_x formation is highly temperature-dependent and is recognised as the most relevant source when combusting natural gas. Fuel NO_x also tends to dominate during the combustion of fuels with significant nitrogen content such as coal. For such fuels, combustion at temperatures below around 1,300°C usually forms less thermal NO_x.

Important NO_x sources are therefore coal and oil power plants (fuel NO_x), cement plants (feed NO_x) and gas power plants (thermal NO_x). Upstream oil and gas extraction activities, which usually burn natural gas (flaring), are also localised sources of thermal NO_x. Other sectors are notable sources of NO_x: for instance, iron and steel production involves industrial processes that tend to use fossil fuels such as natural gas and coke. The corresponding NO_x generation tends to be thermal NO_x. Emissions from sintering and fugitive emissions from coke ovens may also be sources of fuel emissions. Aluminum smelters are also sources of thermal NO_x pollution, since natural gas is combusted there to melt the solid aluminum and heat the liquid metal. Finally, large and dense cities, which experience a significant traffic, are also important hotspots of NO_x pollution through fuel NO_x from traffic. Within the EMME region, we can therefore identify the main hotspots of NO_x pollution by listing such facilities: coal, oil and gas power plants, flaring sites, cement factories, iron and steel mills, aluminium smelters and large cities). The identified sites are shown on Figure 1.4. Here the location and population of cities of more than 100,000 inhabitants have been taken from a global dataset constructed using NGIA, US Geological Survey, US Census Bureau and NASA inventories (`https://simplemaps.com/data/world-cities`). The location of industrial facilities have been retrieved from the Global Energy Observatory (`https://globalenergyobservatory.org/`) for oil- and gas-fired power plants, from the work of Elvidge et al. (2016) for flaring sites, and from the work of Steven J. Davis (University of California, Irvine) and Dan Tong (Tsinghua University) for cement plants. The locations of other industrial facilities, such as aluminium and iron smelters, were obtained from various sources. Data concerning sintering sites are difficult to obtain, and this source of NO_x has been discarded as a consequence.

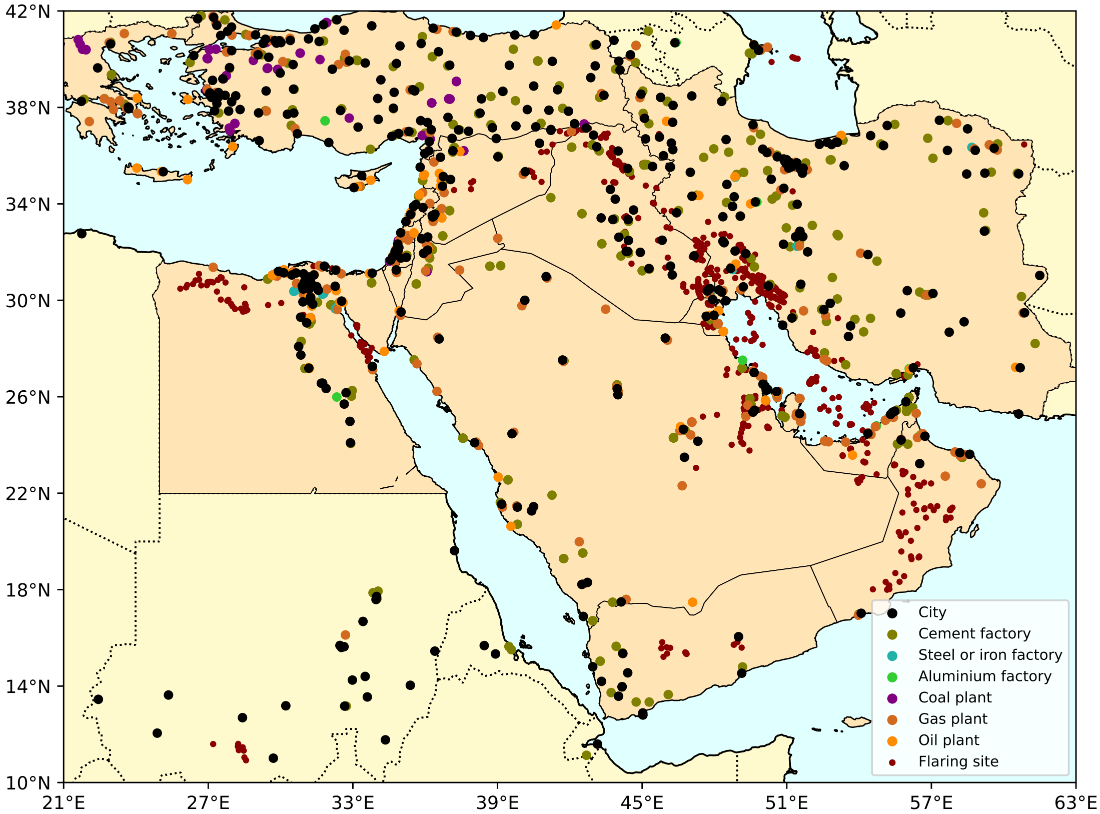

Figure 1.4: Location of the main industrial facilities that produce nitrogen oxides (flaring sites, fossil fuel-fired power plants, aluminium smelters, steel mills and cement kilns) in the EMME region, along with the urban areas having more than 100,000 inhabitants. EMME countries are displayed in light orange.

The main emitting sites shown in Figure 1.4 are consistent with existing global air quality inventories. Many national and regional inventories exist for NO_x, but there is no air-quality gridded inventory that only focuses on the EMME region. Global inventories, such as the Emissions Database for Global Atmospheric Research (EDGAR) or the CAMS global anthropogenic emissions (CAMS-GLOB-ANT), can be used as a consistent database for gridded emissions covering the whole region. They both constitute the latest steps of successive developments of global emission inventories, which started in the 1990s with the Global Emissions Inventory Activity (GEIA) project (Benkovitz et al., 1996), with the aim of bringing together various researchers and organisations to improve the quality and consistency of analyses. EDGAR emissions are based on activity data (population, energy production, fossil fuel extraction, industrial processes, agricultural statistics, etc.) derived from the International Energy Agency (IEA) and the Food and Agriculture Organization (FAO), corresponding emission factors, national and regional information on technology mix data, and end-of-pipe measurements. Version 6.1 of the inventory covers the years 1970–2018 and differs from the previous version 5.0 (up to 2015) and also from the version 4.3.2, which does not use splitting factors derived from the Energy Information Administration (EIA) data on fuel consumption of coal, oil and natural gas for specific countries (Crippa et al., 2020). Conversely, the version 5.3 of CAMS-GLOB-ANT has emissions based on various existing sectors in EDGARv5.0 up to 2015, which are extrapolated to 2021 using sectorial trends from the Community Emissions Data System (CEDS) inventory (Granier et al., 2019). In the two inventories, gridded emissions are thus derived from the type of technologies used, the dependence of emission factors on fuel type, combustion conditions, and activity data and low-resolution emission factors. Figure 1.5 shows the average NO_x emissions in the EMME region for EDGARv6.1 and CAMS-GLOB-ANT_v5.3.

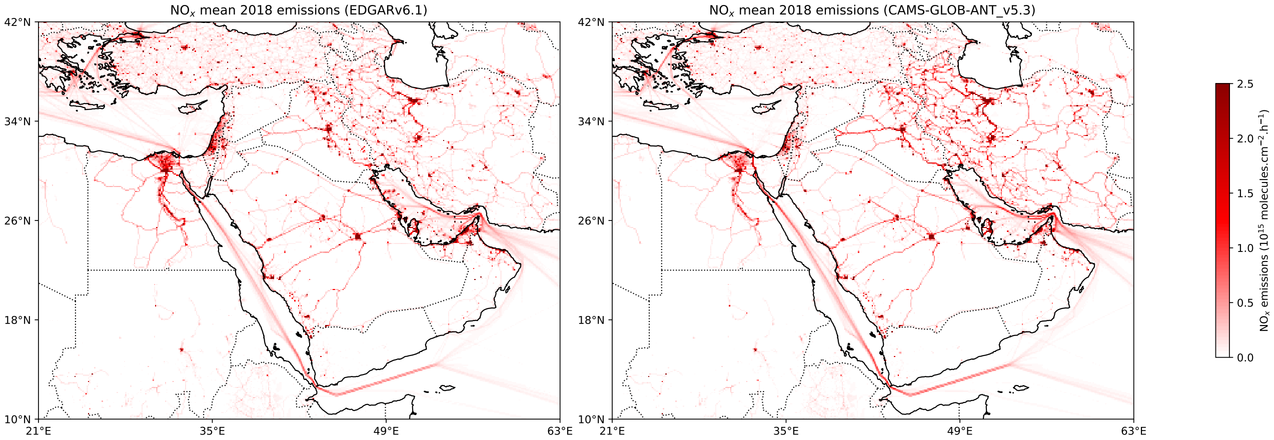

Figure 1.5: Mean NO_x emissions in the EMME region for year 2018 estimated by bottom-up inventories EDGARv6.1 (left) and CAMS-GLOB-ANT_v5.3 (right).

Highways and shipping lanes are evident features that appear; they act as line sources with low emissions per unit area compared to industrial areas and cities. There are notable differences between the two inventories: for instance, traffic emissions in Iran and Iraq seem higher in CAMS-GLOB-ANT than in EDGAR, while they seem lower in Egypt and Türkiye. Megacities and industrial areas appear with emissions having similar orders of magnitude for the two inventories.

Both emissions inventories categorize emissions by sector, allowing the proportion of each sector to be determined for every pixel. In Figure 1.6, the comparison of the two inventories is depicted at the pixel level, along with the identification of the dominant sector. A sector is considered dominant if it constitutes more than 40% of the total emissions budget (this value is chosen arbitrarily). As already highlighted as the main contributors to anthropogenic NO_x, the sectors that are considered are power (electricity generation), transportation (traffic, shipping and aviation), industry (oil refineries and transformation industry, combustion for manufacturing and chemical processes).

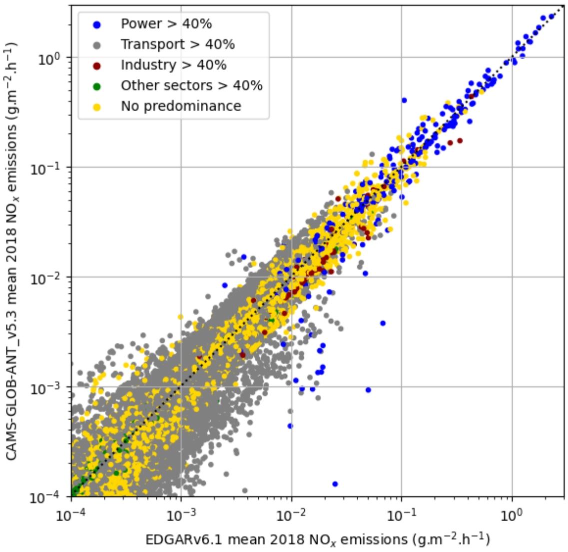

Figure 1.6: Comparison of mean anthropogenic NO_x emissions from the EDGARv6.1 and CAMS-GLOB-ANT_v5.3 inventories in 2018. Each point represents a pixel of the gridded inventories in the EMME region. The colors indicates the sector with the highest emissions proportion among power generation, transportation, industry, and other sources (blue, grey, dark red and green respectively). When no sector accounts for more than 40% of the NO_x budget, the point is represented in yellow. The 1:1 ratio is represented with a dashed line (note the logarithmic scale). The corresponding domain lies between parallels 10°N and 42°N and meridians 21°E and 63°E.

With respect to the orders of magnitude of the emissions, three groups of pixels stand out in Figure 1.6. The first group is made of pixels with low emissions per unit area (less than 5 $mg.m^{-2}.h^{-1}$), with a predominance of transport in most cases. The majority of these pixels represent roads or shipping lanes. The large number of these points compensates for their low emissions per unit area. It is for these points that EDGAR and CAMS-GLOB-ANT inventories differ the most, sometimes by more than an order of magnitude. The second group are pixels with intermediate emissions per unit area (between 5 and 50 $mg.m^{-2}.h^{-1}$). These are mainly industrial areas and cities, the latter being often characterised by a superposition of emissions from different sectors. The relative differences between EDGAR and CAMS-GLOB-ANT are smaller than for the first group. Finally, the third group, with high emissions per unit area (more than 50 $mg.m^{-2}.h^{-1}$), comprises mainly power plants, but also many megacities such as Athens, Baghdad, Doha, Kuwait City, Istanbul or Tehran. This is the group with the lowest number of points (around 250). For these points, the relative difference between EDGAR and CAMS-GLOB-ANT emissions is the lowest, but the absolute difference is the highest.

Overall, the dominant sector for 2018 NO_x emissions in the EMME region is transport, which accounts for 45% of emissions in EDGAR and 46% in CAMS-GLOB-ANT, followed by power (around 34% in both inventories). Industrial emissions account for 14% of the total in EDGAR and 13% in CAMS-GLOB-ANT. Other sectors account for only 7% of emissions. These similar annual averages nevertheless conceal greater differences between the inventories on a monthly or sub-regional basis. The localisation of emitters for each sector, the associated orders of magnitude, as well as the uncertainties in the estimation of their emissions, manifested in the discrepancies between the inventories, must be accounted for to facilitate a more accurate comparison with the emissions that can be estimated by satellite detection.

1.2 Chemistry of nitrogen oxides

1.2.1 Nitrogen-containing species, nitrogen oxides, and NO_x

The nitrogen cycle has been extensively studied during the last century (Galloway et al., 2008; Fowler et al., 2013). In the atmosphere, the N_2 molecule is the most abundant species, but its strong triple bond makes it practically inert. As a result, it is extremely stable chemically and is not involved in the chemistry of the troposphere or stratosphere. The other dominant nitrogen-containing species in the atmosphere are trace gases such as nitrous oxide N_2O, nitric oxide NO, nitrogen dioxide NO_2, nitric acid HNO_3 and ammonia NH_3. Many other chemical trace species containing nitrogen exist in the atmosphere. Among those species, nitrogen oxides represents a group of six chemical compounds: nitrous oxide, nitric oxide, nitrogen dioxide, but also nitrate radical NO_3, dinitrogen trioxide N_2O_3 and dinitrogen pentoxide N_2O_5. Generally speaking, term "nitrogen oxides" refer to a binary compound of oxygen and nitrogen, or a mixture of such compounds. The dimers of all those species can be therefore included in the list. Finally, the term "NO_x" only refers to NO and NO_2, because they are the most abundant nitrogen oxides in the atmosphere during daytime. The features of the six main species of nitrogen oxides are the following:

- Nitrous oxide N_2O is emitted predominantly by biological sources in soils and water, but also other anthropogenic sources such as biomass burning, degassing of irrigation water, agricultural activities, and industrial processes. Although by comparison to CO_2 and H_2O, it has a far lower concentration in the atmosphere, it has a much higher Global Warming Potential, due to its high half-life estimated at from 100 to 150 years (Masson-Delmotte et al., 2021) and its relatively large energy absorption capacity per molecule. Nitrous oxide is relatively inert in the troposphere. However, it is the primary source of NO in the stratosphere (Portmann et al., 2012), yielding to both molecular oxygen and NO.

- Nitric oxide NO is the primarily form of NO_x from combustion: it is generated to the limit of available oxygen in air at high temperatures. Combustion NO is generated as a function of air-to-fuel ratio and is more pronounced when the mixture is on the fuel-lean side of the stoichiometric ratio. The formation of NO is given by the Zeldovich equations (Zeldovich, 1946):

$$N_2 + O \rightarrow NO + N \tag{1.1}$$

$$N + O_2 \rightarrow NO + O \tag{1.2}$$

At fuel-rich conditions, due to the lack of oxygen, Reaction 1.2 becomes minor, and a third reaction involving the hydroxyl radical (OH) is included in the mechanism:

$$N + OH \rightarrow NO + H \tag{1.3}$$

NO is largely anthropogenic: biogenic sources, which are soils, lightning and natural fires, account for less than 10% of total NO emissions (Cox, 1999). NO can be detrimental to human health as it hinders the absorption of oxygen into the blood. However, due to its limited solubility in water, it is not a significant threat except to children and sensitive individuals. NO, or its dimer N_2O_2, is transformed into NO_2, following reactions highlighted in Section 1.2.2.

- Nitrogen dioxide NO_2 typically arises via the oxidation of NO by oxygen in air. It can be decomposed back to NO by absorption of light. With a higher lifetime (a few hours), its presence in the atmosphere is higher than NO. It produces nitric acid (HNO_3) when oxidized by hydroxyl radical. Along with those reactions, NO_2 is involved in various atmospheric reactions and contributes to the complex chemistry of the troposphere. NO_2 is the most "visible" part of NO_x, due to its color, its high concentration in the troposphere and its role in the formation of acid rain and adverse health effects. Note that NO_2 is in equilibrium with its colourless dimer dinitrogen tetroxide N_2O_4, but the latter only predominates at low temperatures (Clugston, Flemming, 2000).

- Nitrate radical NO_3 is a highly reactive and thus unstable species, which can be formed when nitrogen dioxide reacts with ozone. During daytime, is rapidly photodissociated. During nighttime however, when sunlight is absent, NO_3 radicals can accumulate in the atmosphere and participate in a different set of chemical reactions.

- Dinitrogen trioxide N_2O_3 is involved in atmospheric reactions and contributes to the formation of nitric acid and other nitrogen compounds. It is a transient species in the atmosphere and participates in complex chemical processes. N_2O_3 exists in very small concentrations in flue gas, but in quantities so low that it is often ignored.

- Dinitrogen pentoxide N_2O_5 is the most highly ionized form of nitrogen oxide. It is generated in air at very small concentrations, unless emitted from a specific process (such as a nitric acid production facilities). N_2O_5 is highly reactive, and can be an intermediate in the formation of nitrate aerosols.

When any of these forms of nitrogen oxides dissolve into water and decompose, they form acids, the most prevalent being nitric acid (HNO_3). Thus, nitrogen oxides and their derivatives exist and react either as gases in the air, as acids in droplets of water, or as salts. These gases contribute to pollution effects, as well as acid rain (Singh, Agrawal, 2007; Burns et al., 2016). Most environmental regulatory and/or oversight agencies regulate only nitrogen dioxide as a surrogate for this family of compounds. This is due to the fact that NO_2 is easier to measure than other nitrogen oxides, but also because it is involved in the formation of secondary pollutants such as tropospheric ozone. As a consequence, these regulations take the form of standards for NO_2 and tropospheric ozone, i.e. levels of air quality that are necessary, with a reasonable margin of safety, to protect public health and welfare from any known or anticipated adverse effects of pollution. For instance, the World Health Organisation air quality guidelines are limits of 40 $\mu g.m^{-3}$ (annual mean) and 200 $\mu g.m^{-3}$ (1-hour mean) for NO_2 and 100 $\mu g.m^{-3}$ (8-hour mean) for ozone (WHO, 2021).

1.2.2 Leighton relationship

Nitrogen dioxide is a precursor for the formation of secondary pollutants, including ozone. Generally speaking, the concentration of tropospheric ozone in the presence of nitrogen oxides can be determined by an equation called the Leighton relationship (Leighton, 1961). It is based on the fact that ozone in the troposphere is primarily produced through the photolysis of nitrogen dioxide at wavelengths lower than 420 nm, which are able to reach the lowest levels of the atmosphere. The following mechanism highlights the main conversion paths between the major components of NO_x, i.e. NO_2 and NO:

$$\mathrm{NO_2} + h\nu \rightarrow \mathrm{NO} + \mathrm{O} \tag{1.4}$$

$$\mathrm{O(^3P)} + \mathrm{O_2} + \mathrm{M} \rightarrow \mathrm{O_3} + \mathrm{M} \tag{1.5}$$

$$\mathrm{NO} + \mathrm{O_3} \rightarrow \mathrm{NO_2} + \mathrm{O_2} \tag{1.6}$$

The symbol M represents a "third body", i.e. an unspecified molecular species that must interact with the reactants in order to carry away energy from the exothermic reaction (usually air). This series of reactions creates a null cycle, in which there is no net production or loss of any species involved. When only these three reactions are considered, they reach a point where NO_2 is destroyed and reformed so fast that a steady state cycle is maintained, due to the reactivity of $O(^3P)$[§] and the abundance of O_2. From this assumption, called photostationary hypothesis, the relation between NO_2, NO and O_3 can be derived:

$$[\mathrm{O_3}] = \frac{J[\mathrm{NO_2}]}{k_L[\mathrm{NO}]} \tag{1.7}$$

J is the photolysis frequency of NO_2, which has been parameterised by Dickerson et al. (1982), and k_L is the kinetic constant for the reaction between NO and O_3 (Atkinson et al., 2013). This equation, called Leighton relationship, shows how production of ozone is directly related to the solar intensity, and hence to the zenith angle, due to the reliance on photolysis of NO_2. The yield of ozone is therefore greater during the day, especially at noon and during the summer season. This relationship also demonstrates how high concentrations of both ozone and nitric oxide are unfeasible, as shown by measurement in different places throughout the world (Kalabokas, Bartzis, 1998; Khoder, 2009; Butenhoff et al., 2015; Kasparoglu et al., 2018; Vrekoussis et al., 2022). In the latter mechanism, reaction 1.4 is the step determining the rate of the forward reaction. The temporal variation of ozone concentration is given by $\frac{\partial[\mathrm{O_3}]}{\partial t} = J[\mathrm{NO_2}] - k_L[\mathrm{NO}][\mathrm{O_3}]$, highlighting a characteristic relaxation time τ_L to the steady state:

$$\tau_L = \frac{1}{k_L[\mathrm{NO}]} \tag{1.8}$$

In low-pollution areas (typically with [NO] lower than 10 ppb), this stabilisation time never exceeds 30 minutes. However, as diurnal NO concentrations in urban areas are generally above 20 ppb, it is lowered to less than 5 minutes (Graedel et al., 1976; Seinfeld, 1989).

Neglecting components in NO_x others than NO and NO_2, the ratio $\mathcal{L}$ between NO_x and NO_2 is derived from the Leighton relationship as:

$$\mathcal{L} = \frac{[\mathrm{NO_x}]}{[\mathrm{NO_2}]} = \frac{[\mathrm{NO_2}] + [\mathrm{NO}]}{[\mathrm{NO_2}]} = 1 + \frac{J}{k_L[\mathrm{O_3}]} \tag{1.9}$$

With typical conditions at 298 K around noontime, $k_L = 1.9\times10^{-14}$ cm^3 and $J = 0.015$ s^{-1}. With $[O_3] = 100$ ppb, the previous equation leads to $\mathcal{L} \simeq 1.32$. Because J is at its maximum at noon, it is close to this moment of the day that NO has the largest possible fraction within NO_x. As a

---

[§] The designation "^{3}P" is used to describe an excited state of atomic oxygen in which the outermost electron is in a P orbital with a principal quantum number of 3.

consequence, this value of 1.32 is usually kept to scale up NO_2 to NO_x when the precise calculation of $\mathcal{L}$ is not possible. For a daytime average, the NO fraction is lower, and the mean $\mathcal{L}$ value is about 1.1.

It might be noted that the photostationary state is a hypothesis which might not be verified at the scale of a source of NO_x, such as a power plant stack. Li et al. (2023b) found that the value of $\mathcal{L}$ could be much higher than 1 at the scale of industrial facilities in northern China, with a correlation with the combustion temperature and energy efficiency of large energy consuming sources, showing that the scaling up NO_2 to NO_x can be the source of high uncertainties. Moreover, the assumption of photostationary equilibrium between NO_2 and NO may not hold true for urban environments with high pollution levels due to the presence of other species like volatile organic compounds (VOCs) that can affect the balance between the two compounds (Seinfeld, Pandis, 2006). In particular, the hydroxyl radical OH, which can react with both VOCs and NO_x, can lead to the production of oxygenated VOCs, but also to the conversion of NO to NO_2 and the subsequent formation of ozone. This is a key step in the formation of ground-level ozone, which is a major component of smog and a harmful air pollutant. This competition between VOCs and NO_x for the hydroxyl radical is in favor of VOCs at high ratios of VOC to NO_x concentrations; at a low ratios, the reaction with NO_x can predominate. The two reactions reach equal rates at a given ratio between VOCs and NO_x, which depends on the type of VOC present, as the OH rate constant differ from each VOC species. At a given level of VOC, there exists a NO_x concentration at which a maximum amount of ozone is produced. For ratios less than this optimum ratio, a NO_x increase lead to an ozone decrease. Conversely, for ratios larger than this optimum ratio, a NO_x increase lead to an ozone increase.

1.2.3 Reactive nitrogen and NO_x sinks

Reactive nitrogen, often denoted as NO_y, is defined as the sum of NO_x and all the compounds that are products of their oxidation in the atmosphere. These include nitric acid HNO_3, nitrous acid (HONO), the nitrate radical (NO_3), dinitrogen pentoxide (N_2O_5), peroxynitric acid (HNO_4), peroxyacetyl nitrate ($CH_3C(O)OONO_2$, generally refered to as PAN) and its homologs, alkyl nitrates ($RONO_2$, where R represents any alkyl group), and peroxyalkyl nitrates (RO_2NO_2). Nitrous oxide and ammonia are not considered in this context as reactive nitrogen compounds. NO_y is closer to a conserved quantity than any of its constituent species (Roberts, 1995). Measurement of total NO_y concentration in the atmosphere thus provides an important measure of the total oxidized nitrogen content, while concentrations of individual NO_y species relative to the total indicate the extent of interconversion among species. In addition to the interconversion relationships between NO and NO_2 highlighted in the previous section, the study of NO_x removal processes must account for other species present in NO_y. These processes are multiple and complex, and a first line of distinction, in the context of using satellite retrievals by backscattered sunlight measurements, is to distinguish the dynamics of NO_x during daytime from its nighttime behaviour. Finally, because transport of species from the troposphere into the stratosphere is much slower than mixing within the troposphere itself, and because anthropogenic emissions of NO_x take place in the troposphere, reactions involving NO_x in the stratosphere are not discussed. In this section, all reactions will not be explicitly written.

1.2.3-A Daytime behaviour

During daytime, the reactions involving NO_x are not limited to the ozone production mechanism highlighted in Section 1.2.2. Before sunrise, nitrogen is mostly contained in the nitrate radical NO_3 produced during the night. NO_3 is thus photolysed at dawn via two paths forming NO_x:

$$NO_3 + h\nu \rightarrow NO + O_2 \text{ (wavelengths lower than 700 nm)} \tag{1.10}$$

$$NO_3 + h\nu \rightarrow NO_2 + O \text{ (wavelengths lower than 580 nm)} \tag{1.11}$$

NO_3 also reacts with NO according to the following equation:

$$NO_3 + NO \rightarrow 2\ NO_2 \tag{1.12}$$

These reactions occur very rapidly, and NO and NO_3 cannot coexist at mixing ratios of a few parts per trillion or higher. As photon activity increases and the hydroxyl radical is formed in the atmosphere, daytime NO_x losses are increasingly dominated by the three-body reaction involving NO_2 and OH (Seinfeld, 1989). Two channels have been identified for this reaction (Chakraborty et al., 1998), leading to the production of nitric acid HNO_3 and pernitrous acid HOONO:

$$NO_2 + OH + M \rightarrow HNO_3 + M \tag{1.13}$$

$$NO_2 + OH + M \rightarrow HOONO + M \tag{1.14}$$

The second path is minor, and HOONO can be rapidly decomposed back to NO_2 and OH in the lower troposphere. The daytime lifetime of NO_x is mostly explained by this reaction and is about of few hours. Section 2.1.2 details the calculation of NO_x lifetime. HNO_3 can undergo effective photolysis to form NO, NO_2 or HONO, the latter being subsequently subject to another photolysis to form OH and NO (Ye et al., 2016). In low-NO_x forested area, this can be another source of NO_x in the atmosphere.

Although the oxidation of NO_2 by OH to form HNO_3 is the dominant mechanism for NO_x loss, other sinks exist during daytime. As a dominant oxidant in the lower troposphere, the hydroxyl radical also initiates reactions with volatile organic compounds (VOCs), leading to the formation of hydroperoxy radicals (HO_2) and organic peroxy radicals (RO_2) that subsequently react with NO_x species. In particular, the reaction between NO and HO_2 plays a key role in recycling OH, contributing to ozone production in the troposphere (Howard, Evenson, 1977). This reaction proceeds through two distinct channels: the primary pathway involves the formation of an excited HOONO intermediate complex, which rapidly decomposes into OH and NO_2. The secondary channel is a three-body reaction leading to the production of nitric acid:

$$HO_2 + NO \rightarrow HOONO \rightarrow OH + NO_2 \tag{1.15}$$

$$HO_2 + NO + M \rightarrow HNO_3 + M \tag{1.16}$$

While previous studies have predominantly focused on the primary channel, the second is significant in the upper troposphere (Butkovskaya et al., 2005). Note that the yield of the first pathway is strongly enhanced in presence of water vapour, in which case it cannot be neglected (Butkovskaya et al., 2009).

While HNO_3 is a short-lived trace gas, NO_x can be transformed to longer-lived reservoir species that can be transported over long distances and act as a source of NO_x. In the troposphere, VOCs are oxidised by OH to form organic peroxy radicals (RO_2). These compounds can oxidise a significant amount of NO_x (Day et al., 2003), leading to the formation of peroxy nitrates (RO_2NO_2) and organic nitrates ($RONO_2$):

$$RO_2 + NO_2 + M \rightarrow RO_2NO_2 + M \tag{1.17}$$

$$RO_2 + NO + M \rightarrow RONO_2 + M \tag{1.18}$$

Note that alkyl peroxynitrates rapidly thermally decompose back to reactants in a few seconds at ambient temperatures (Atkinson, 2000), which means Equation 1.17 can be neglected. However, alkyl nitrates have longer lifetimes. They undergo photolysis and reaction with the OH radical in the troposphere to form NO_2. Organic peroxy radicals also react with NO, yielding to the conversion of NO into NO_2:

$$RO_2 + NO \rightarrow RO + NO_2 \tag{1.19}$$

The characterisation of the yields of Equation 1.18 and Equation 1.19 remains an important source of uncertainty in chemistry models (Butkovskaya et al., 2010; Khan et al., 2015). While reaction 1.19 has no net impact on NO_x, reaction 1.18 can recycle, temporarily sequester or permanently remove NO_x

from the atmosphere, depending on the lifetime and fate of the species produced (Fisher et al., 2016). These three reactions between peroxy radicals and NO_x becomes more significant as the concentration of volatile organic compounds increases and can be especially relevant in forested areas (Romer Present et al., 2020) and, generally speaking, in low-NO_x environments (i.e. with NO fractions much lower than 0.1 ppb). The formation of organic nitrates can also recycle NO_x downwind plumes, where NO_x emitted by cities and industrial facilities encounter VOCs in forests (Browne, Cohen, 2012; Fisher et al., 2016). Conversely, in situations characterised by elevated NO_2 concentrations relative to VOC concentrations, the contribution of Equation 1.17 and Equation 1.18 to the overall NO_x loss becomes less prominent compared to the reaction between NO_2 and OH.

Finally, PAN ($CH_3C(O)OONO_2$) is another major reservoir species for NO_x (Moxim et al., 1996). It is formed by the reaction of the peroxyacetyl radical (generally formed by reaction between acetaldehyde and OH) with NO_2:

$$CH_3C(O)O_2 + NO_2 + M \rightarrow CH_3C(O)OONO_2 + M \tag{1.20}$$

PAN is one of the most abundant reactive nitrogen-containing species in the troposphere (Roberts, 1995). Because of this, its atmospheric lifetime is important, especially at low temperatures. Potential atmospheric removal processes for PAN include thermal decomposition (which is the reverse of Equation 1.20) and UV photolysis. PAN is not highly water-soluble; it is more soluble than NO or NO_2 but considerably less soluble than HNO_3. Thus, wet deposition is not an important removal process. PAN production peaks in the late afternoon and early evening (Seinfeld, 1989).

1.2.3-B Nighttime behaviour

Photolysis cannot occur at night, and as a result, the nighttime NO_x chemistry is different than during daytime. Any NO present at night reacts rapidly with ozone according to reaction 1.6. This complete conversion of NO_2 to NO_x is followed by a reaction of NO_2 with ozone to produce the nitrate radical (Ehhalt, Drummond, 1982):

$$NO_2 + O_3 \rightarrow NO_3 + O_2 \tag{1.21}$$

This reaction is the only direct source of NO_3 in the atmosphere, yielding concentrations that can be higher than 100 ppt, i.e. than two orders of magnitude higher than during daytime. NO_3 can then reacts with another NO_2 molecule to produce N_2O_5:

$$NO_2 + NO_3 + M \rightarrow N_2O_5 + M \tag{1.22}$$

N_2O_5 itself can thermally decompose back to NO_2 and NO_3 following the reverse reaction. There is thus a nighttime equilibrium between NO_2, NO_3 and N_2O_5, which is reached in a few minutes. The thermodynamic constant of this equilibrium decreases rapidly with temperature (Seinfeld, Pandis, 2006), shifting the equilibrium towards the formation of N_2O_5 at midnight and at high altitudes. Finally, N_2O_5 can be hydrolysed (Harker, Strauss, 1981):

$$N_2O_5 + H_2O(s) \rightarrow 2\ HNO_3 \tag{1.23}$$

This hydrolysis takes place is heterogeneous (particle-phase), and mostly occur in the stratosphere. It is one of the major paths for NO_x removal in the atmosphere.

Finally, NO_3 can also react with alkenes (noted with their characteristic double bond R=R'), producing organic nitrates ($RONO_2$):

$$NO_3 + R{=}R' \rightarrow R(ONO_2)R' \tag{1.24}$$

The fate of NO_x at night is therefore controlled by the balance of the NO_3 reaction pathways. NO_x can be lost via NO_3 reaction with alkenes, or via the reaction with NO_2 to form N_2O_5 in thermal equilibrium, followed by aerosol uptake and heterogeneous hydrolysis to produce HNO_3. In certain environments, NO_3 may also react with species such as dimethylsulfide, aldehydes, and peroxy radicals. The competition between these reaction pathways is controlled by both the relative availability of alkenes and by the fate of N_2O_5. The production of organic nitrates during the night increases in areas characterised by elevated biogenic alkene emissions, including isoprene and monoterpenes, as well as in regions with high anthropogenic alkene emissions, such as ethene and propene. This trend is particularly notable when either of these emission sources persists overnight (Kenagy et al., 2020).

1.2.3-C Other heterogeneous processes

Along with these gas-phase reactions that occur during both daytime and nighttime, heterogeneous processes involving NO_x can also be mentioned, such as the deposition of NO_2 through the leaf stomata of vegetation. In this process, NO_2 enters through the stomatal cavity and dissolves into the apoplastic fluid, forming nitrate, which is then reduced to ammonium by the enzyme nitrate reductase (Park, Lee, 1988; Tischner, 2000). This reaction can be significant in forested areas, and the overall deposition rate of NO_2, whether it is done during daytime or nighttime, varies by tree species (Delaria et al., 2020). Additionally, wet deposition plays a crucial role in removing NO_x from the atmosphere: NO_2 can undergo dissolution in rainwater, forming nitric acid in aqueous phase. This process is the heterogeneous formation of acid rain which completes the homogeneous formation through the formation of nitric acid in gas phase (Xie, Zhang, 2013). The acid rainwater can then be deposited onto the Earth surface, contributing to the removal of NO_x from the atmosphere. The overall impact of wet deposition, whether it leads to permanent removal or potential release back into the atmosphere, depends on various factors such as temperature, humidity, and the presence of other gases. Finally, the adsorption of NO_2 by black carbon particles can also be mentioned among the heterogeneous processes, as it temporarily removes NO_2 from the surrounding atmosphere (Longfellow et al., 1999). However, whether or not NO_2 is permanently removed or can be released back into the atmosphere depends on various factors, including temperature, humidity, and the presence of other gases.

1.2.3-D Overview of NO_x chemistry

Figure 1.7 sums up all the reactions involving NO_x compounds that have been previously mentioned, allowing a schematic overview of both daytime and nighttime NO_x chemistry:

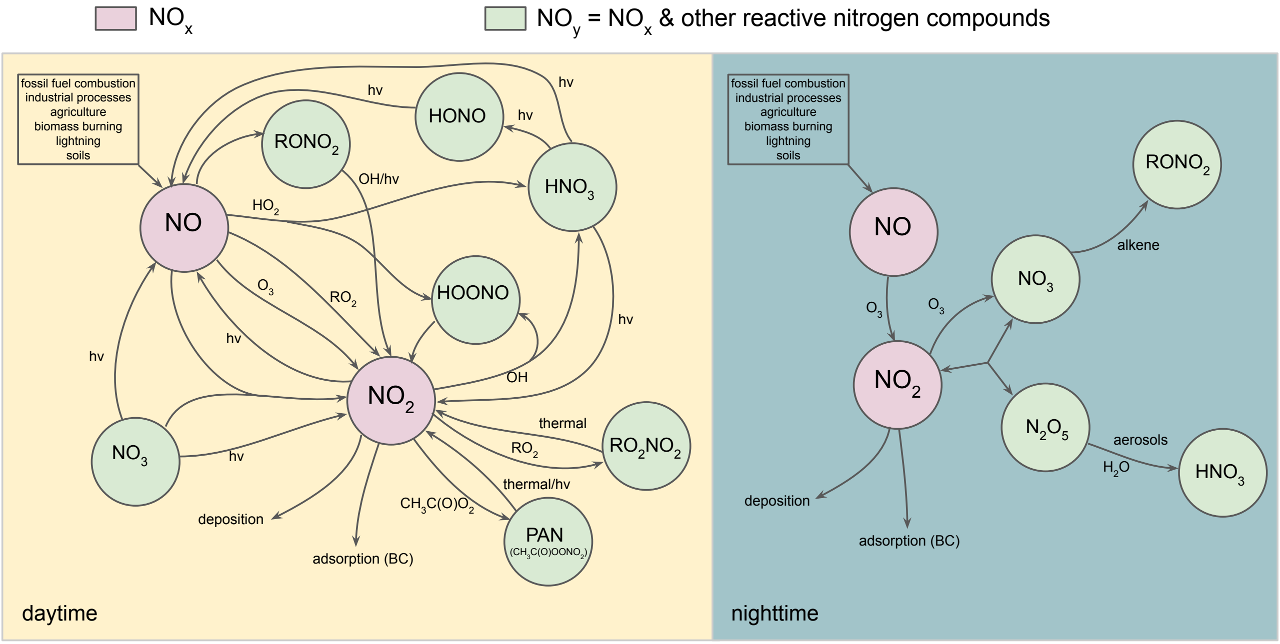

Figure 1.7: Sketch of the NO_x chemistry in the troposphere during daytime (left) and nighttime (right).

1.2.4 Daily and annual cycles in the EMME region

The daily cycle of nitrogen oxides in the EMME region has been widely characterised by many in situ observations in various areas over the last decades. Observed levels are influenced by various factors, including urbanisation, local pollution sources, and meteorological conditions. In urban areas, the cycle begins with a morning peak during rush hour, typically between 6:00 and 9:00 local time (LT), driven by increased traffic and industrial activities, but also a low planetary boundary layer (PBL) which reduces the mixing of air pollutants. This peak is followed by a rapid decrease in NO_x levels during the late morning and early afternoon, with a local minimum around 13:00-14:00 LT. This drop can be attributed to reduced traffic and industrial activity, as well as increased dispersion of pollutants due maximum solar radiation increasing the yield of the OH sink. The boundary layer height also peaks in the afternoon in response to solar insolation and increases the mixing volume, diluting pollutant concentrations. After the midday drop, NO_x levels rise again in the late afternoon and early evening, often between 17:00 and 20:00 LT, associated with the evening rush hour and industrial resurgence. At night, NO_x levels slowly decrease due to the transformation into NO_3 (Kalabokas, Bartzis, 1998; Khoder, 2009; Alghamdi et al., 2014; Butenhoff et al., 2015; Kasparoglu et al., 2018; Vrekoussis et al., 2022). Urban areas tend to exhibit more pronounced daily cycles with higher peak concentrations compared to rural areas, which may have a milder cycle influenced by natural sources and experience lower NO_x levels (Butenhoff et al., 2015; Kasparoglu et al., 2018; Vrekoussis et al., 2022). Ozone concentrations generally follow a diurnal pattern inversely related to NO_x levels. Ozone levels tend to be lower in the morning and increase through the day, peaking in the late afternoon or early evening. In addition to this daily NO_x cycle, annual variations are observed, with summer months having lower mean levels, while the reduced photochemical activity during late fall and winter leads to high mean values (Khoder, 2009; Alghamdi et al., 2014). This makes the mornings of winter months more prone to exceed air quality guidelines.

It must be noted that the trends presented here represent the general case in the EMME region. For some areas in the region, the trend can be different, due to specific climate features, but also additional drivers of NO_x pollution. In particular, high-level income countries experiencing extreme temperatures during summer rely heavily on air conditioning, which makes the power generation higher at noon. This can potentially lead to flatter daily profiles near power plants (Butenhoff et al., 2015).

1.2.5 NO_x abatement methods

Because of their adverse effects on air quality, which translate into effects on health, industries are required to deploy NO_x reduction plans, in cooperation with local authorities and in accordance with regional or international standards. Depending on the sector, NO_x abatement can be a complex issue. The effectiveness of pollution prevention measures in reducing NO and NO_2 generation is generally expressed in terms of amount of NO_x generation that is reduced by using a prevention technology compared to NO_x generation when not using that technology. Six methods are commonly used to reduce NO_x. They are extensively described by Cox (1999) and summarised as follows:

1. Reducing temperature – Reducing combustion temperature means avoiding the ideal stoichiometric ratio which produces higher temperatures, leading to higher concentrations of thermal NO_x. This technique dilutes calories with an excess of fuel, air, flue gas, or steam. Combustion controls use different forms of this technique and are different for fuels with high and low nitrogen content. Low-NO_x burners are based partially on this principle.

2. Reducing residence time – Reducing residence time at high combustion temperatures can be done by ignition or injection timing with internal combustion engines. It can also be done in boilers by restricting the flame to a short region in which the combustion air becomes flue gas. This is immediately followed by injection of fuel, steam, more combustion air, or recirculating flue gas. This short residence time at peak temperature keeps the vast majority of nitrogen from becoming ionized. This bears no relationship to total residence time of a flue gas in a boiler.

3. Chemical reduction of NO_x – This technique provides a chemically reducing substance to remove oxygen from nitrogen oxides. technologies using such methods attempt to chemically reduce the valence level of nitrogen to zero after the valence has become higher.

4. Oxidation of NO_x – This technique is based on the greater solubility of NO_x at higher valence: it intentionally raises the valence of the nitrogen atom to allow water to absorb it. This is accomplished either by using a catalyst, injecting hydrogen peroxide, creating ozone within the air flow, or injecting ozone into the air flow.

5. Removal of nitrogen from combustion – This is accomplished by removing nitrogen as a reactant either by using oxygen instead of air in the combustion process or using ultra-low nitrogen content fuel to form less fuel NO_x. Eliminating nitrogen by using oxygen tends to produce a rather intense flame that must be subsequently and suitably diluted.

6. Adsorption and absorption – This is done by the injection of sorbents (such as carbon, ammonia, powdered limestone or aluminum oxide) in the flue gas can remove NO_x.

1.3 Remote sensing instruments and methods

1.3.1 Differential optical absorption spectroscopy

Atoms and molecules interact with light via energy absorption (Einstein, 1917). They reach discrete energy states that are determined by their electronic composition, according to quantum mechanical principles. In presence of incident light, such as solar radiation, a molecule in a lower energy state becomes excited. An incoming photon with the right energy, i.e. frequency, can be absorbed, moving the receiving molecule to a higher energy state. The molecule can thus be characterised by an ensemble of discrete frequency absorption lines in the light spectrum which correspond to the discrete energy states. To be able to observe light absorption of a given molecule, it is therefore necessary to measure light intensity over a large spectral range and with a spectral resolution sufficiently high to identify its absorption spectral lines. Passive satellite instruments whose purpose is to detect trace gases are therefore spectrometers looking downward (nadir point of view), i.e. they measure the ascending radiance corresponding to the backscattered sunlight at the top of the atmosphere. The photons detected by the instrument are converted into electrons (Einstein, 1905), and the detected signal is analysed and decomposed into a series of energy intensity as a function of received frequency (Duncan et al., 2014). The study of the obtained radiance spectrum provides all the information on the chemical composition of the atmosphere. Absorption spectroscopy allows to focus on the spectral regions of interest for tropospheric trace gas analysis. For instance, the reddish-brown color of NO_2 is the result of its transition in the visible spectral domain, while it absorbs the light in the blue band (about 405-470 nm). The Beer-Lambert law (or Bouguer-Lambert law) is therefore at the basis of studies focusing on the absorption properties of trace gases in the ultraviolet and visible spectral ranges. It describes the attenuation of light along its path as a function of gas concentration (Bouguer, 1729; Lambert, 1760; Beer, 1852):

$$I(\nu,\theta,\zeta) = I_0(\nu,\theta,\zeta)\exp\left(-\int_{\mathrm{path}} \Sigma(\nu)C(s)\mathrm{d}s\right) \tag{1.25}$$

In this equation, $I_0(\nu,\theta,\zeta)$ is the initial light intensity, $I(\nu,\theta,\zeta)$ is the measured radiation intensity (or radiance) for light frequency ν and at viewing zenith and azimuth angles θ and ζ, C is the trace gas concentration that varies along the curvilinear coordinate s describing the light path, and Σ is the absorption cross-section of the gas, which represents the effective area with which the molecule is capable of removing the energy of incoming photons (the variations of this quantity with respect to light frequency are usually tabulated for most chemical species).

In Equation 1.25, the absorption cross-section is independent from the curvilinear coordinate. The integrated content along the light path $\int_{\text{path}} C(s)\mathrm{d}s = \hat{\Omega}_s$, which corresponds to a slant column density (SCD), can therefore be obtained from the knowledge of the absorption cross-section and the measured reflectance, i.e. the ratio between the measured and the initial lights:

$$\hat{\Omega}_s(\nu, \theta, \zeta) = -\frac{1}{\Sigma(\nu)} \ln\left(\frac{I(\nu, \theta, \zeta)}{I_0(\nu, \theta, \zeta)}\right) \tag{1.26}$$

The Differential Optical Absorption Spectroscopy (DOAS) method is a specific retrieval approach that exploits this relation. It is mostly employed for visible and ultraviolet absorbing trace gases, and its origin goes back to the first measurements of the ozone layer (Fabry, Buisson, 1921). This method relies on a synchronous fit of several trace gas slant column densities (commonly NO_2, but also ozone, formaldehyde HCHO and sulfur dioxide SO_2) from their fine spectral features (Platt et al., 2008). Since the calculated slant column density is not in direct contact with the measuring instrument, the measurement technique is referred to as remote sensing. To take into account the simultaneous presence of M different species (denoted by indexes $j = 1, 2, ..., M$) together with Rayleigh and Mie scattering, Equation 1.25 is commonly re-written as:

$$I(\nu, \theta, \zeta) = I_0(\nu, \theta, \zeta) \exp\left(-\Sigma_R \hat{\Omega}_R - \Sigma_M \hat{\Omega}_M - \sum_{j=1}^{M} \Sigma_j(\nu) \hat{\Omega}_{s,j}\right) \tag{1.27}$$

Here Σ_M and Σ_R are Mie and Rayleigh scattering cross-sections and $\hat{\Omega}_M$ and $\hat{\Omega}_R$ are the corresponding column densities. The Rayleigh scattering is a phenomenon that plays a key role in the blue hue of the sky, as the efficiency of scattering inversely varies with the fourth power of the wavelength (Strutt, 1871). Rayleigh scattering is not species-selective, and its amplitude is directly proportional to the gas density for a single-component gas with a known scattering cross-section. Mie scattering, on the other hand, refers to the elastic scattering of light by particles that are similar in size or larger than the wavelength of the incident light (Mie, 1908). It produces a stronger signal compared to Rayleigh scattering, posing a potential interference for the latter. The intensity of Mie scattering exhibits a significant angular dependency, particularly for smaller particles. In the DOAS method, the argument of the exponential appearing in Equation 1.27 is usually divided into two parts. The first part, modeled by a polynomial $\mathcal{P}$, captures spectrally smooth elements such as Rayleigh and Mie scattering, surface reflection, and the low frequency of absorption cross-sections. The second part is spectrally differential and serves as the source for extracting trace gas information. Due to the presence of the polynomial term, the fit of the total slant column density is influenced only by the highly structured features of differential absorption. The logarithm of $I(\nu, \theta, \zeta)/I_0(\nu, \theta, \zeta)$ is therefore fitted over a spectral window with the following function:

$$\ln\left(\frac{I(\nu, \theta, \zeta)}{I_0(\nu, \theta, \zeta)}\right) = -\sum_{j=1}^{M} \Sigma_j(\nu) \hat{\Omega}_{s,j} + \mathcal{P} \tag{1.28}$$

Figure 1.8 summarises the principle of the DOAS method with the simplified situation of a plane parallel atomsphere. Note that Equation 1.28 represents only one of the many possible implementations of the DOAS methods: other variations, which are used to optimise retrieval quality for a given spectral window or altitude, involve different equations or a polynomial with different coefficients (Chanda et al., 1997; Hönninger et al., 2004).

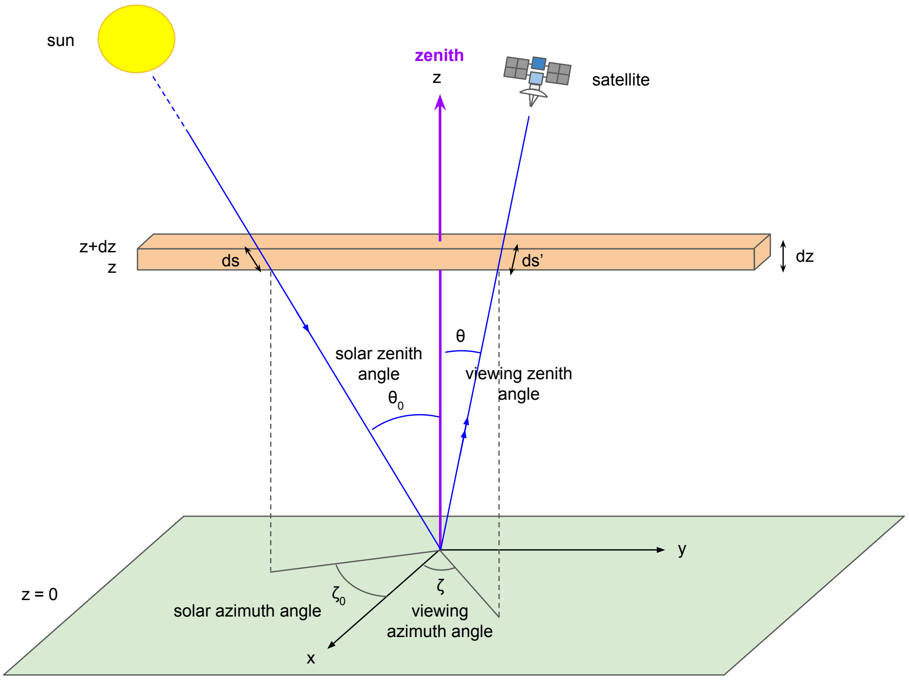

Figure 1.8: Sketch of satellite reflectance measurement in a plane parallel atmosphere. The DOAS algorithm consists in measuring the light absorption along the optical path relevant to the slant column density (blue line) in order to derive the integrated content of absorbers in the corresponding vertical column from the ground ($z = 0$) to the top of the troposphere and the total atmosphere (purple line).

The DOAS algorithm enables to measure the atmospheric slant column density of a given trace gas. It should be noted that the DOAS method is only suitable for optically thin absorbers, such as NO_2 (typical slant optical thickness of 0.005 at 440 nm (Boersma et al., 2004)), because molecules with high absorption optical thickness highly affect the average light path by themselves.

1.3.2 The Sentinel-5 Precursor satellite

Sentinel-5 Precursor, also known as Sentinel-5P (S-5P), is an Earth Observation satellite, developed by the European Space Agency (ESA) as the 6th operational Sentinel satellite of the Copernicus program (`https://sentinels.copernicus.eu/web/sentinel/missions/sentinel-5p`). The project involved several major stakeholders. ESA played a key role in the design, development and launch of the satellite, while Airbus Defence and Space took charge of the construction. ESA collaborated with the European Organisation for the Exploitation of Meteorological Satellites (EUMETSAT) for in-orbit operations management. Sentinel-5P was launched on October 13th 2017 and deployed into orbit using a Russian Rokot launcher from the Plesetsk Cosmodrome. The primary objective of the satellite is to provide comprehensive and up-to-date data for environmental monitoring and control. The satellite orbits the Earth at an altitude of 824 kilometers with a 97.74° tilt. It became operational a few weeks after launch, following equipment verification and instrument calibration. Its cycle consists of 227 orbits. Each orbit is a near-polar, sun-synchronous orbit with an equatorial crossing at 13:30 mean local solar time (ascending node). The data provided by Sentinel-5P is freely available to the scientific community and the general public, and is essential for policymakers to develop effective environmental policies regarding the reduction of greenhouse gas emissions and the monitoring of forest fires, volcanic eruptions, and industrial pollution. Acting as a bridge between the ENVISAT and Aura missions (Bovensmann et al., 1999; Levelt et al., 2006), Sentinel-5P ensures continuity in atmospheric measurements until the launch of the Sentinel-5 instrument, which will be carried onboard the MetOp-SG meteorological satellites circulating in sun-synchronous orbit, whose first launch is planned for 2025.

1.3.3 The TROPOMI instrument

The TROPOspheric Monitoring Instrument (TROPOMI) is the instrument onboard Sentinel-5P. It uses a push-broom scanner[¶] and covers a spectral range from ultraviolet and visible (UV-Vis, 270–500 nm) to near-infrared (NIR, 675–775 nm) to short-wave infrared (SWIR, 2305–2385 nm). It scans with a swath width of 2,600 km at high resolution (originally 3.5×7 km^2 at nadir, improved to 3.5×5.5 km^2 since August 6th 2019), which allows to observe the fine-scale structure of the atmosphere for species absorbing in these spectral ranges. TROPOMI provides measurements of various atmospheric components such as ozone, methane, formaldehyde, aerosols, carbon monoxide, sulfur dioxide and nitrogen dioxide. For the latter, the UV–Vis spectral band at 405–465 nm is used. The TROPOMI NO_2 product is publicly available on the corresponding Open hub (`http://www.tropomi.eu/data-products/data-access`) and on other platforms, generally sorted by Sentinel-5P orbits. The Algorithm Theoretical Basis Document for the NO_2 official product can be found at `https://sentinel.esa.int/documents/247904/2476257/sentinel-5p-tropomi-atbd-no2-data-products`. TROPOMI NO_2 products constitute an improvement over previous NO_2 datasets (Van Geffen et al., 2022), particularly in their unprecedented spatial resolution. The calulation of the TROPOMI NO_2 retrieval consists of the following three-step procedure:

1. The total NO_2 slant column density is calculated from the radiance and irradiance spectra measured by the TROPOMI instrument using the DOAS method.

2. The total NO_2 slant column density is separated into a stratospheric part and a tropospheric part, using various information coming from a data assimilation system. This step is detailed in Section 1.3.5.

3. The tropospheric slant column density is converted into a tropospheric vertical column density by applying an appropriate tropospheric air mass factor which depends on the satellite geometry, topography, cloud fraction and height, surface albedo, and daily information on the vertical distribution of NO_2 from an internal chemistry-transport model. This step is detailed in Section 1.3.6.

Differences in these three steps result in a different product of version of the NO_2 data, whose differences are explained in Section 1.3.8. Figure 1.9 shows an example of one type of TROPOMI NO_2 product (L2 product, OFFL stream, processor version 2.3.1) on a Sentinel-5P orbit passing above the western part of the EMME region, Eastern Europe and Eastern Africa. NO_2 columns are measured over Johannesburg (South Africa), the Bab-el-Mandeb strait (Djibouti/Yemen), Istanbul (Türkiye), Kaliningrad (Russia) and central Svalbard (Norway) at 11:06, 11:17, 11:25, 11:30 and 11:36 Universal Coordinated Time (UTC) respectively, which correspond to local times of 12:58, 14:01, 13:17, 12:46 and 12:48 due to longitude differences.

[¶] A push-broom scanner is designed so that the field of view of the instrument is divided into multiple adjacent strips, with each strips corresponding to a specific portion of the surface. The scanner collects data by continuously scanning across the swaths as the satellite or aircraft moves along its path. As such, a push-broom scanner thus differs from a whisk-broom scanner, which uses a scanning mirror to point the instrument at different portions of the surface and collect data intermittently.

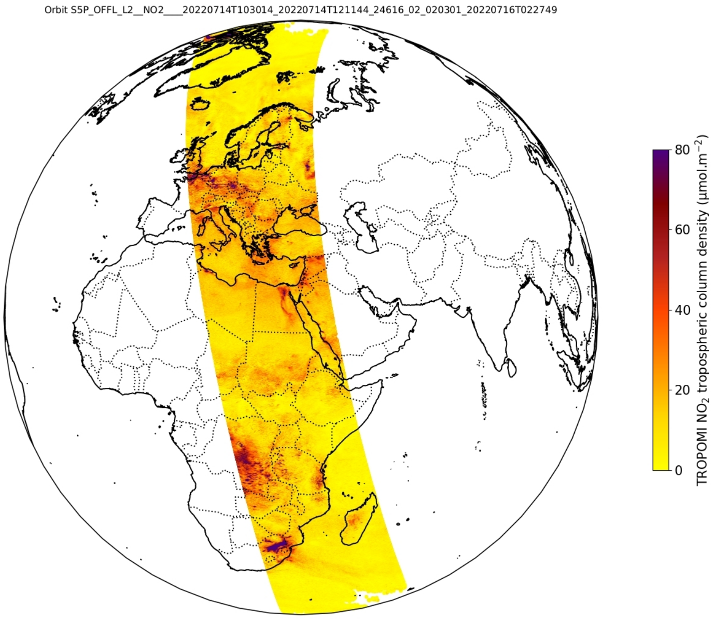

Figure 1.9: NO_2 tropospheric vertical column density on a Sentinel-5P orbit covering part of the EMME region on July 14th 2022 (L2 product, OFFL stream, processor version 2.3.1). White pixels correspond to areas with low-quality data or no data (with a quality assurance limit at 0.70, see Section 1.3.7).

Because Sentinel-5P completes a full scan of the Earth surface in 24 hours with an overpass time at about 13:30 local time near the equator, it is possible to construct composite asynchronous maps of NO_2 columns, i.e. maps that represent the NO_2 columns at different moments that correspond to the approximate same local time for each of its pixels. Some areas are covered two times on the same day but with a different viewing angle; in this case, the corresponding columns are averaged. The construction of such composite maps must therefore be performed along preferred axis, such as the north-south and east-west axes using a Cartesian coordinate system which is more convenient for combination with other parameters. Such a map is shown in Figure 1.10 for the EMME region on a 0.0625°×0.0625° grid. Note that the validity of the composite and asynchronous nature of such maps is less verified for high-latitude regions, for which the overpass time becomes significantly different from 13:30 LT due to the different local times of the pixels scanned in a single scanline.

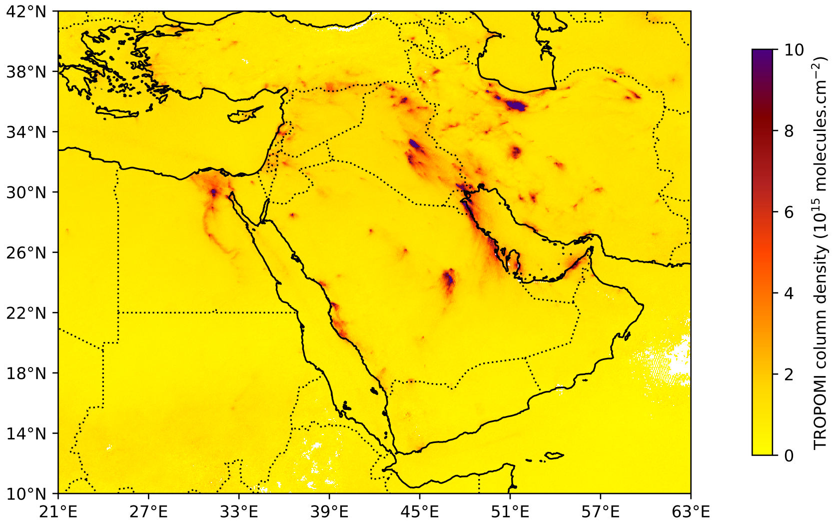

Figure 1.10: Composite asynchronous map representing gridded mean TROPOMI nitrogen dioxide tropospheric vertical column density above the EMME region for July 1st 2022 to July 14th 2022 (L2 product, OFFL stream, processor version 2.3.1). White pixels correspond to areas with low-quality data or no data during the period (with a quality assurance limit at 0.75, see Section 1.3.7).

1.3.4 Previous instruments

The Sentinel-5P mission continues a series of missions involving spectrometers measuring atmospheric composition since 1995. Among those that have a spectrometer retrieving NO_2, we can mention the following instruments:

- The Global Ozone Monitoring Experiment (GOME) onboard the European Remote Sensing Satellite (ERS-2), was launched in April 1995. It measured the sunlight scattered from the Earth atmosphere and/or reflected by the surface in nadir viewing mode in the 240–790 nm spectral region, at a spectral resolution of between 0.2 and 0.4 nm. Using a 960-km swath width, its spatial resolution was 40×320 km^2, and global coverage was achieved in three days after 43 orbits. Using the DOAS approach, operational data products were derived in two levels (absolute radiometrically calibrated earthshine radiance spectrum and solar irradiance spectra for level 1 and total column amounts of ozone and nitrogen dioxide for level 2). The ERS-2 satellite was taken out of service on September 5th 2011, due to low levels of remaining fuel.

- The SCanning Imaging Absorption SpectroMeter for Atmospheric CHartographY (SCIAMACHY) was one of ten instruments onboard the ESA ENVIronmental SATellite (ENVISAT) launched from Kourou, French Guiana, in March 2002. It was designed to measure sunlight, transmitted, reflected and scattered by the Earth atmosphere or surface in the ultraviolet, visible and near infrared wavelength region (240-2380 nm) at moderate spectral resolution (0.2-1.5 nm) during 10 years. Its mission ended in May 2012.

- The Global Ozone Monitoring Experiment-2 (GOME-2) is a scanning spectrometer onboard the satellite onboard the Metop-A satellite, which was launched on October 19th 2006, from the Baikonur Cosmodrome. GOME-2 was designed by DLR and developed by SELEX Galileo as the successor of GOME. It measures the distribution of surface ultraviolet radiation and subsequently calculate ozone and nitrogen dioxide column densities, as well as sun-induced chlorophyll fluorescence which is used as a proxy for gross primary production. A second GOME-2 instrument is operating since 2012 on MetOp-B.

- The Ozone Monitoring Instrument (OMI) is a nadir-viewing visual and ultraviolet spectrometer onboard the NASA Aura satellite. Aura orbits the Earth in a polar Sun-synchronous pattern. It was launched on July 15th 2004, and OMI has been collecting data since August 9th 2004. The OMI project is a cooperation between the Netherlands Agency for Aerospace Programmes, the Finnish Meteorological Institute and the NASA. OMI can distinguish between aerosol types, such as smoke, dust, and sulfates, and measures cloud pressure and coverage, which provide data to derive tropospheric ozone and nitrogen dioxide. OMI measurements cover a spectral region of 264–504 nm and measures atmospheric composition with a ground resolution of 13×24 km^2 at nadir. The Aura satellite orbits at an altitude of 705 km in a sun-synchronous polar orbit with an exact 16-day repeat cycle and with a local equator crossing time of 13:45 LT on the ascending node. The orbital inclination is 98.1°, providing latitudinal coverage from 82°N to 82°S with a daily global coverage due to its swath of 2400 km.

The main characteristics (corresponding satellites, measurement type, spectral range, resolution, swath, cycle, revisit and overpass times and years of operation) of these different instruments are summarised in Table 1.1 and compared to those of the TROPOMI instrument. This list is to be completed in the upcoming years due to future launches of sun-synchronous (Irizar et al., 2019) and geostationary satellites over North America, Europe and Eastern Asia (Gulde et al., 2017; Zoogman et al., 2017; Kim et al., 2020b).

Instrument	**GOME**	**SCIAMACHY**	**GOME-2**	**OMI**	**TROPOMI**
Satellite	ESR-2	ENVISAT	MetOp-A&B	Aura	Sentinel-5P
Technical concept	Whisk-broom	Whisk-broom	Whisk-broom	Push-broom	Push-broom
Spectral range	240-790 nm	240-2400 nm	250-790 nm	270-500 nm	270-2385 nm
Resolution	320×40 km^2	30×215 km^2	80×40 km^2	13×24 km^2	3.5×7 km^2
Swath	960 km	1000 km	1920 km	2600 km	2600 km
Orbit cycle	29 days	35 days	29 days	16 days	16 days
Revisit time	3 days	3 days	1.5 days	1 day	1 day
Overpass time	10:30 LT	10:00 LT	9:30 LT	13:45 LT	13:30 LT
Operational years	1995-2011	2002-2012	2006-present	2004-present	2017-present
Reference	Burrows et al. (1999)	Bovensmann et al. (1999)	Munro et al. (2016)	Levelt et al. (2006)	Veefkind et al. (2012)

Table 1.1: Different technical features of different instruments measuring nitrogen dioxide column densities onboard satellites launched in the last 30 years.

1.3.5 TROPOMI tropospheric and stratospheric column densities

The TROPOMI NO_2 algorithm uses data assimilation in the Tracer Model 5 (TM5-MP) chemistry transport model (CTM) as the baseline method to separate the stratospheric and tropospheric contributions to the total slant columns (Williams et al., 2017). This model operates at a horizontal resolution of 1°×1° with different vertical pressure levels up to 0.1 hPa, using forecast and meteorological fields from the European Centre for Medium-range Weather Forecasts (ECMWF) operational model with a temporal resolution of 3 hours (Dee et al., 2011). NO_2 and nitrogen reservoirs are derived from 20 different reactions. This approach, extensively employed by the Royal Dutch Meteorological Institute (Dirksen et al., 2011), accounts for chemistry and dynamics in the stratosphere. The assimilation updates the CTM simulation of the three-dimensional troposphere-stratosphere NO_2 distribution using available measurement data, ensuring the best match between the simulated stratospheric NO_2 columns and the TROPOMI slant columns in regions which are known to have minimal tropospheric NO_2. The assimilation relies thus heavily on slant columns that are measured over areas dominated by stratospheric NO_2 such as remote oceans. For regions with significant tropospheric contributions, the slant column is a poor proxy for stratospheric NO_2, resulting in minimal analysis adjustment, but the total reactive nitrogen NO_y (introduced in Section 1.2.4) is conserved. Using this quantity, the information obtained from observations can be stored in the model over extended periods (the wind in the stratosphere transports the stratospheric analysis results from low tropospheric NO_2 regions to polluted areas). The assimilation scheme employs a Kalman filter technique (Labbe, 2014) with a prescribed parameterisation of horizontal correlations between forecast errors. The analysis is performed at 30-minute intervals, simultaneously analysing a full orbit of TROPOMI observations to avoid discontinuities. The analysed profile field includes modelled NO_2 in both the troposphere and stratosphere, calculated based on the forecast and satellite observations. These are constructed by averaging the observations and averaging kernels (see Section 1.3.6) over each model grid cell (Boersma et al., 2016). A simplified observation error model is employed, with a small error for the stratospheric slant column and a large error for the tropospheric contribution, optimised to minimise the impact of major source regions on the analysis and ensure strong forcing over clean regions. Once the assimilation scheme is performed, the tropospheric slant column Ω_s is calculated from its total slant column $\hat{\Omega}_s$. Ths stratospheric component is given by $\hat{\Omega}_s - \Omega_s$.

1.3.6 TROPOMI air mass factor and averaging kernels

The column retrieved from the DOAS method, as well as its tropospheric part, are inclined with respect to the local vertical, with an inclination that depends on the viewing geometry and also the light path between the instrument and the ground, the latter depending on the vertical distribution of absorbers. To estimate vertical columns from DOAS retrievals, this inclination must be accounted for. Usually, the effect of light path is expressed with the air mass factor (AMF), a unitless quantity describing the ratio between slant and vertical columns. For overhead sun and a nadir viewing instrument, a total air mass factor of 2 is obtained when all photons come from the sun, pass through the absorber, be reflected on the ground and travel back to the instrument through the absorber. Generally speaking, the geometrical part in the AMF is given as a function of solar zenith angle θ_0 and viewing angle θ by $1/\cos(\theta_0) + 1/\cos(\theta)$. In the real atmosphere, many photons are scattered, and depending on surface albedo, solar zenith angle and wavelength, the sensitivity of the measurement and thus the air mass factor can deviate significantly from the geometrical approximation. In TROPOMI products, altitude-dependent air mass factors are as default pre-calculated air-mass factor look-up tables over all the atmospheric layers from the surface to top-of-atmosphere. They represent the ratio between portions of the retrieved slant column and the corresponding portions of vertical columns. A total AMF $\hat{m}$ is then calculated by using these altitude-dependent air mass factors. This quantity therefore represents the ratio between the retrieved slant column and the atmospheric vertical column: $\hat{m} = \hat{\Omega}_s/\hat{\Omega}$. A tropospheric air mass factor m is computed the same way by considering only the layers from the surface up to the stratosphere: $m = \Omega_s/\Omega$. It focuses only on the column of NO_2 within the troposphere, which is where most of the anthropogenic activity occur.

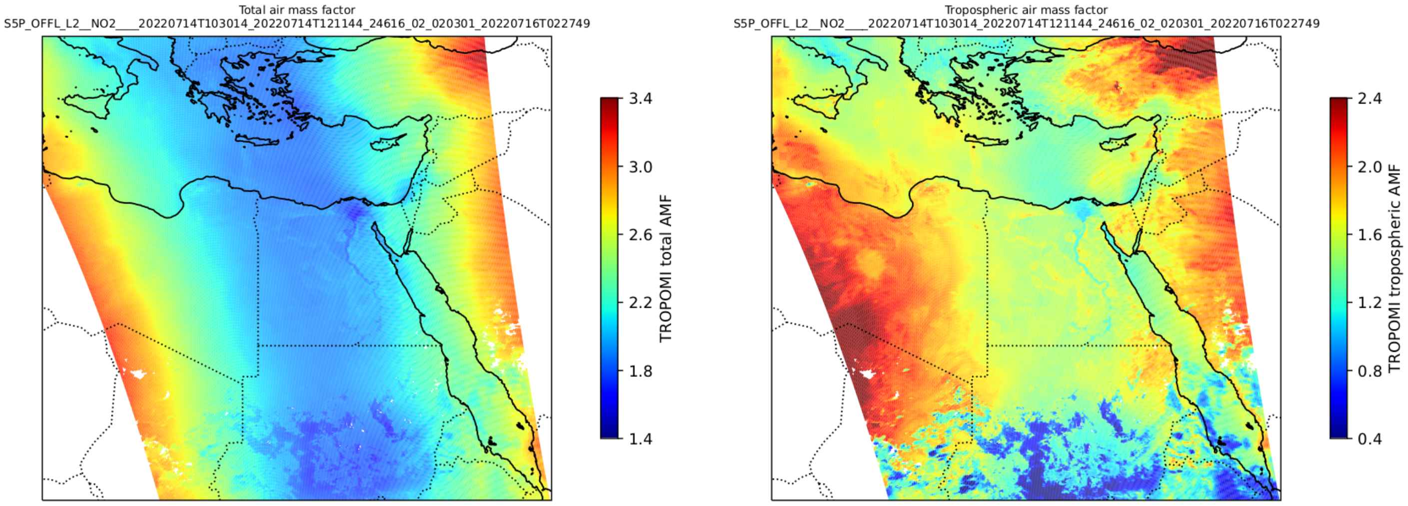

Figure 1.11: Total air mass factor (left) and tropospheric air mass factor (right) for a Sentinel-5P orbit over part of the EMME region on July 14th 2022 (L2 product, OFFL stream). Note that the colorbar bounds are different.

The difference between total AMF $\hat{m}$ and tropospheric AMF m lies in the distribution of NO_2 in the atmosphere. NO_2 has both natural and anthropogenic sources, and its concentration is not uniform vertically. It typically decreases with altitude, with the highest levels found near the surface. The detected signal includes cumulative contributions from both tropospheric and stratospheric NO_2, but the contribution to NO_2 in the stratosphere is generally much lower than in the troposphere because the stratospheric concentrations are significantly lower. Such differences are illustrated on Figure 1.11, where relative differences in total AMF are mainly due to its tropospheric component. Overall, the geometry effect is characterised by higher AMF values for pixels corresponding to highest viewing angles on the edges of the swath. Focusing on the tropospheric only, regions with higher albedos appear with higher AMFs. It is for instance the case in Egypt, where the Nile Valley, which is mostly composed of croplands, have lower AMFs than the rest of the country composed of high-albedo deserts. Cloudy scenes correspond to low AMF values, due to increased light path lengths and a higher optical thicknesses in such media.

Through the calculation of the AMF, which is calculated with a radiative transfer model based on an a priori profile (de Haan et al., 1987), the retrieved NO_2 column always represent a weighted average over all parts of the atmosphere that contribute to the signal observed by the satellite instrument. It is a source of structural uncertainty in NO_2 measurements due to differences in the vertical sensitivity and a priori vertical profiles in the measurement method (Wang et al., 2017; Compernolle et al., 2020), which becomes non-negligible in polluted environments (Verhoelst et al., 2021). This representation is not anecdotic, because in practice the sensitivity of the instrument to the tracer density varies with altitude, especially in the troposphere. The resulting profile dependence may introduce large systematic errors in the retrieved columns that are difficult to quantify without proper additional information (Boersma et al., 2004). The averaging kernel (AK) quantifies the contribution of the different atmospheric layers to the observations. This quantity, which is proportional to the vertical sensitivity profile, is derived by quantifying factors such as clouds, surface albedo, viewing angles, and solar zenith angle. It provides a nuanced interpretation of the air-mass factor, establishing a relationship with the vertical sensitivity of satellite observations to variations in tracer concentration. This sensitivity can then be used for combining model outputs with in situ observations, thus emphasizing the central role that the averaging kernel has in remote sensing methods (Eskes, Boersma, 2003).

The averaging kernel is an important concept in remote sensing studies. Examples of applications include extracting atmospheric profiles, such as temperature and trace gases from satellite measurements. Retrieval groups now frequently incorporate kernel information into the profile data products that are distributed to users. This is the case for TROPOMI products. Figure 1.12 shows examples of AKs computed for different NO_2 retrievals in different locations of the Eastern Mediterranean. The actual shape of the kernel changes from one pixel to another, depending in particular on the presence of clouds, aerosols and on the surface albedo of the scene. For all chosen locations, the profile peaks in the middle/upper stratosphere, where the air-mass factor approaches its simple geometrical approximation. Generally, there is a large difference between the sensitivities of the retrieval in the stratosphere as compared to the lower troposphere. For instance, over low-albedo surfaces (green and red curves), the profile shows sensitivities with a factor 2 difference between the planetary boundary layer, where most of the NO_2 is located, and the stratosphere. Since the retrieved vertical column is directly proportional to the air-mass factor, this profile variability implies a large profile dependence of the vertical column retrieved. In Figure 1.12, optically thick clouds (purple curve) have a profile which is consistent with assumptions that are often used in cloud retrieval algorithms (Koelemeijer et al., 2001): these algorithms will retrieve an effective approximate cloud top (here between $0.7p_0$ and $0.95p_0$), which can be expected to be lower than the actual cloud top (Koelemeijer et al., 2001).

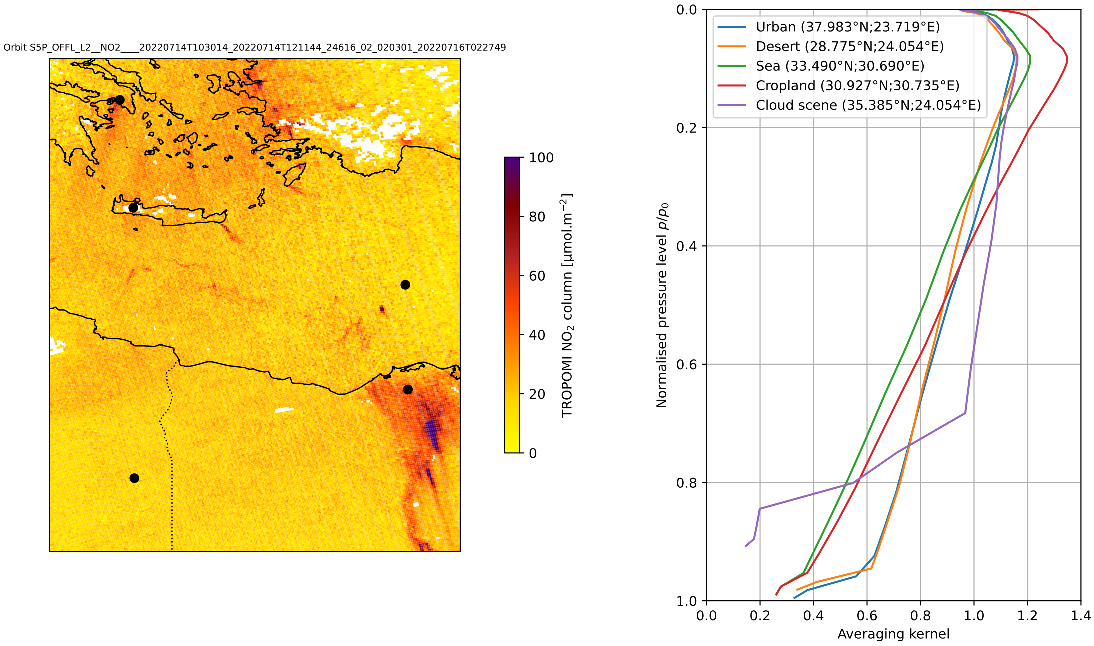

Figure 1.12: Example of TROPOMI averaging kernels for five pixels within the EMME region on July 14th 2022: pixels with low surface albedos (Nile Valley croplands and Mediterranean Sea), pixels with high surface albedos (Sahara Desert and Athens urban area) and pixel with an optically thick cloud characterised by $q_a < 0.75$ (over Crete). The pressure is normalised as a fraction of the standard pressure $p_0 = 1013.25$ hPa. Corresponding locations and vertical columns are shown on the left.

The a priori profiles in the TROPOMI retrievals can be replaced by any other model NO_2 profile information, resulting in a new retrieved tropospheric NO_2 column. A direct comparison of the NO_2 tropospheric column as provided in the TROPOMI product and a model-generated column would introduce extra uncertainties and biases, as the TROPOMI tropospheric columns depend on the retrieval a priori and therefore on the quality of the TM5-MP profiles used. Because Sentinel-5P validation activities indicate that TROPOMI tropospheric NO_2 columns are systematically biased low by about 30%-50% over cities (Verhoelst et al., 2021), and because this under-estimation is likely related to the a priori profiles used within the operational retrieval that do not reflect well the NO_2 peak close to ground, such comparisons provides possible improvements for future CTMs that could be implemented in future products. For instance, Lorente et al. (2017) addressed the issue of AMF structural uncertainty via a comparison of AMF calculation methods that are structurally different between different retrieval groups for OMI NO_2 retrievals, and estimated an average AMF uncertainty of 42% over polluted regions and 31% over unpolluted regions, mostly driven by differences in the a priori trace gas profiles, as well as surface albedo and cloud parameters. Besides, Beirle et al. (2023) corrected the TROPOMI AMF from the AK based on a delta-peak profile at plume height to account for the NO_2 excess added by a NO_x emitter, with a mean AMF correction of 1.61 for the considered point sources. Nevertheless, it must be noted that the EMME region, the impact of the a priori profile is less critical, as surface albedo is generally high and cloud fractions are generally low.

1.3.7 TROPOMI quality flag insurance

TROPOMI data outputs include automated quality assurance parameters, which can take the form of limits on zenith angle, albedo threshold, pressure, cloud radiance fraction, quality of the DOAS fit, etc. Those parameters can be derived from the TM5-MP model or other algorithms (Wang, Stammes, 2007). These processing quality flags are made uniform across all products. Besides these quality flags detailing condition on specific quanties, the NO_2 data products include a combined quality assurance value q_a for each retrieval, enabling end users to easily filter data for their own purpose. The successive versions of TROPOMI products, which included progressive improvements in the estimation of quality assurance parameters as well as the resolution used in the underlying model, therefore include more realistic estimates of q_a values. The evolution of q_a with respect to the product version will be investigated in Section 1.3.8. The Product User Manual (Eskes et al., 2019a) recommends a threshold of $q_{a,\mathrm{lim}} = 0.75$ for most users in order to perform a pixel filtering. This removes cloud-covered scenes (cloud radiance fraction higher than 0.5), part of the scenes covered by snow/ice, errors and problematic retrievals. For stratospheric applications, where clouds are more occasional, a more relaxed threshold of $q_{a,\mathrm{lim}} = 0.50$ adds the good quality retrievals over clouds and over scenes covered by snow or ice. Errors and problematic retrievals are still filtered out.

1.3.8 TROPOMI product and version differences

As precised in Section 1.3.3, the retrieval of NO_2 columns within the TROPOMI product is a 3-step process including a slant column density from the DOAS method, a separation between stratospheric and tropospheric component within the slant column, and the conversion of tropospheric/stratospheric slant columns into tropospheric/stratospheric vertical columns using AMFs. The last two steps involve the use of the TM5-MP CTM. This model can be run either in forecast mode, using 1-day forecast meteorological data from ECMWF, or in a more delayed processing mode, using 0-12 hour forecast meteorological data. The former is used for near-real-time (NRTI) processing of the TROPOMI measurements, the latter for the offline (OFFL) production, leading to two different TROPOMI products.

The main difference between the NRTI and OFFL data processors lies in the use of either forecast or analysis ECMWF meteorological data as input, and consequently the use of either forecast or analysis TM5-MP vertical NO_2 profiles. The mutual consistency between the NRTI and OFFL data products is monitored routinely using data and tools provided by the Level-2 Quality Control Portal (`https://mpc-l2.tropomi.eu`). A reprocessed version (RPRO) is also made available after the release of the OFFL version. Finally, a new NO_2 dataset, reprocessed with the Sentinel-5P Product Algorithm Laboratory (PAL), is available to the users to allow consistent long-term data analysis (e.g. trends in air pollution based on COVID-19 impact). It covers the period from May 1st 2018 to November 14th 2021 and is available at `https://data-portal.s5p-pal.com` (Eskes et al., 2021). It is planned to replace this data set during 2023 by an upgraded product reprocessed with the Payload Data Ground Segment (operated from DLR). The main improvement of the PAL version is the change in the cloud product due to an update in the cloud algorithm (replacement of the algorithm FRESCO-S by FRESCO-wide, (Wang, Stammes, 2007)), generally leading to higher cloud altitudes and thus lower AMFs and higher vertical column densities, mainly in wintertime and mainly over polluted northern mid-latitude regions. It offers a consistent dataset for the period 2018-2021 based on one processor version.

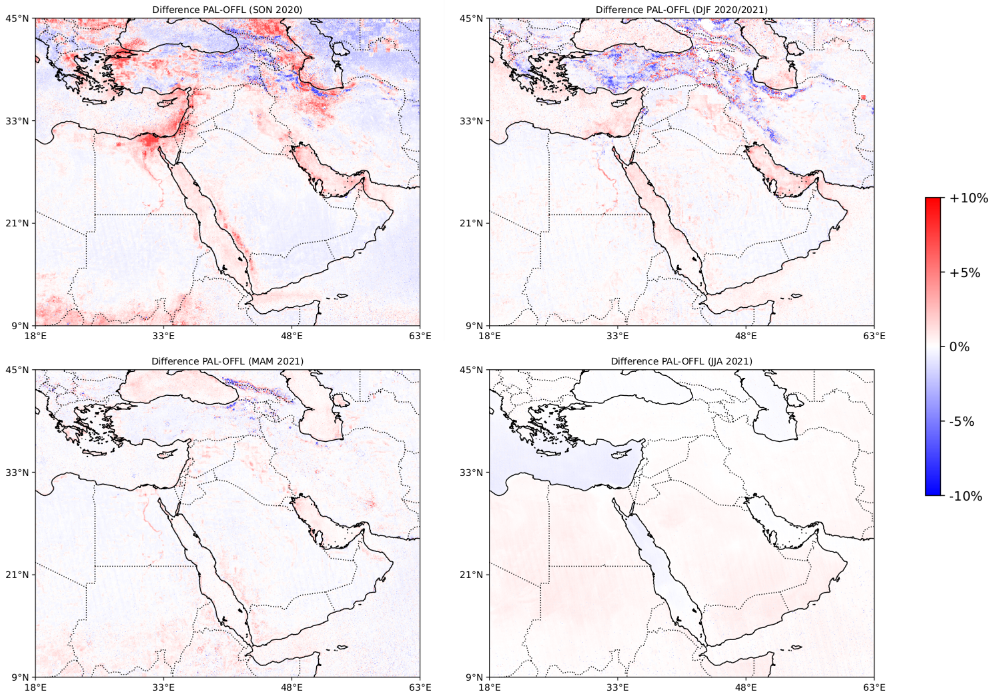

Figure 1.13: Mean seasonal differences in tropospheric vertical column densities between PAL and OFFL versions of TROPOMI data (PAL/OFFL-1) above the EMME region between September 2020 and August 2021.

Figure 1.13 shows that, looking at global means of the NO_2 total column, most differences between PAL and OFFL streams concern the mountainous areas of the EMME regions. They are higher during autumn and winter months. The PAL stream also provides slightly higher NO_2 columns above urban areas than the OFFL versions.

In addition to the different streams in TROPOMI products, each product has undergone a series of successive modifications. The TROPOMI data has undergone a succession of processor and algorithm versions since Sentinel-5P was launched into orbit in 2017. The track of changes is available in the TROPOMI Algorithm Theoretical Basis Document (ATBD, `https://sentinel.esa.int/documents/247904/2476257/sentinel-5p-tropomi-atbd-no2-data-products`) of the total and tropospheric NO_2 data products and the current processor version (on July 6th 2023) is 2.4.0. Processor version changes can have a significant impact on the retrieved columns or the quality attached to them. For instance, between versions 2.3.1 and 2.4.0, the surface albedo climatology (SAC) used in the NO_2 fitting window and derived from OMI and GOME-2 was replaced by a SAC derived from TROPOMI observations (Eskes et al., 2022). This new TROPOMI SAC is consistently applied in the cloud fraction, the cloud pressure retrievals, and in the air-mass factor calculation. As a consequence, it affects the calculation of the different quality assurance parameters introduced in Section 1.3.7. Figure

1.14 shows the difference in observation densities, defined as the frequency of observations above a given quality insurance threshold value, above the Persian Gulf in December 2020 (processor version 2.3.1) and December 2022 (processor version 2.4.0) using the OFFL stream, with two different quality assurance thresholds.

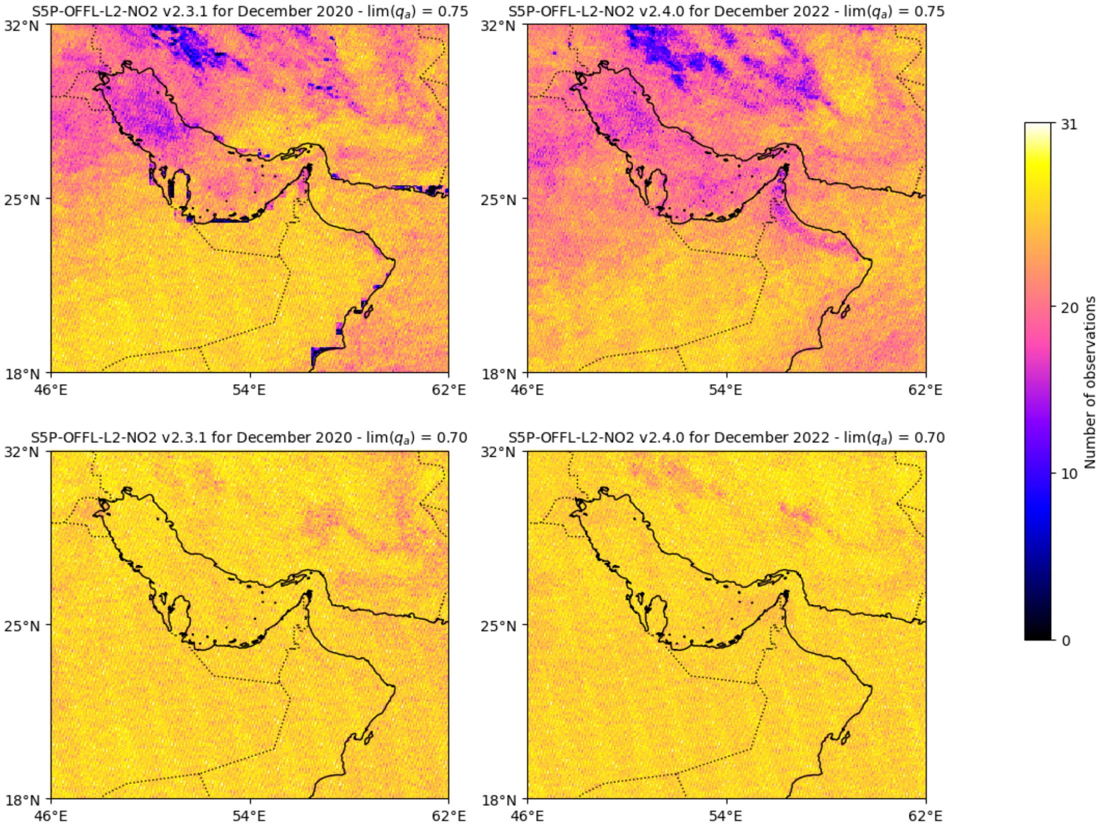

Figure 1.14: Number of TROPOMI observations of NO_2 tropospheric columns above quality assurance value thresholds $q_{a,\mathrm{lim}} = 0.75$ and $q_{a,\mathrm{lim}} = 0.70$ for the Persian Gulf region in December 2020 (data product version 2.3.1) and December 2022 (OFFL product version 2.4.0).

This figure shows that with a quality flag threshold of $q_{a,\mathrm{lim}} = 0.75$, some parts of the region, especially on the coasts, are not visible most of the time for version 2.3.1. Observation density with this threshold is lower than 5 days out of 31 for the western coast of the United Arab Emirates, and the west coast of Qatar. The pixels that are concerned describe a shape which denotes the use of a coarse resolution in the mapping of q_a. However, the effect does not appear for version 2.4.0, suggesting an improvement in the resolution of the different constitutive flags (despite a loss of high-quality observations on the coasts of Oman, but this loss might be due to meteorological differences between December 2020 and December 2022 in this region). Because the bottom panels show that the entire region is covered most of the time with a quality flag threshold of $q_{a,\mathrm{lim}} = 0.70$, it can be assumed that is effect results from few flags in the final calculation of q_a. This case illustrates the possible upgradings of the TROPOMI versions with time, regardless of the streams. In the case of Qatar, the comparison between versions 2.3.1 and 2.4.0 is conducted more precisely in Section 3.2.

The EMME region has been characterised by its geographical but also economic and industrial features. Notably, its reliance on fossil fuel makes it a region with a high density of emitters. Many of these emitters can be observed from space, particularly through their NO_x emissions. The TROPOMI NO_2 observations have been described through many aspects in this chapter. They constitute a potential tool to complete air quality inventories, provided that they are combined with a modelling system that allows NO_x emissions to be inferred from column densities. The next chapter aims to describe several methods to perform this transformation.

Chapter 2

Inversion methods - from NO_2 observations to NO_x emissions

The purpose of this chapter is to present how satellite retrievals of NO_2 can be used to infer NO_x emissions. Different methods will be presented, along with their advantages and drawbacks, but the flux-divergence method, which is widely used during the outcome of this thesis, is described in detail. In particular, the calculation assumptions will be clearly explained, and the practical limitations regarding the parameters used in the calculation of emissions will be discussed. The differences of our version of the flux-divergence method and other implementations will be highlighted. Illustrations will be provided with theoretical and practical examples.

2.1 The flux-divergence model

2.1.1 Mass balance

In fluid mechanics, the flow of a medium such as air can be described with an Eulerian approach to account for the deformations inherent to the system at every fixed point in space (commonly using Cartesian coordinates x, y and z) as a function of time t. The flow is described by a velocity field $\vec{w}$ in each point of the fluid. Physical quantities, such as pressure, temperature or particle density of a given pollutant are defined at the scale of a fluid parcel, i.e. an elementary volume of fluid which is small enough for the quantity being studied to be considered as a point, and large enough to be able to consider the medium as continuous. Governing equations, derived from fundamental principles of mechanics and thermodynamics, describe the spatial and temporal evolution of the main quantities that characterise the fluid. Among them, mass balance serves as a powerful tool for deriving the spatial and temporal evolution of particle density. It expresses the application of the fundamental principle of conservation of mass, and invariably revolves around the core principle that the total mass entering a control volume must equal the total mass exiting it.

In our case, the NO_2 columns observed by the TROPOMI instrument can serve as control volumes: their horizontal boundaries correspond to the footprint of the observations and their vertical boundaries can be assumed to correspond to the ground level and the top of the planetary boundary layer (PBL). For more convenience, TROPOMI retrievals can be re-gridded on north-south and east-west axes, as described in Figure 1.10. To perform a mass balance and derive a conservation equation, we can consider a tropospheric vertical column density Ω whose base is $\mathrm{d}x \times \mathrm{d}y$ and its height is h. We note d^2N the number of NO_2 molecules in the column, i.e. $\mathrm{d}^2N = \Omega \mathrm{d}x\mathrm{d}y$. Assuming that the NO_2 concentrations, noted C, vary little vertically within the PBL, and assuming that horizontal variations in the PBL occur on scales larger than the size of a pixel, h can be considered as a constant for the mass balance. Under these two hypotheses, which are questioned in Section 3.4.2, the average particle density within this column is $\bar{C} = \frac{1}{h}\int_{z_0}^{z_0+h} C\,\mathrm{d}z = \Omega/h$ where z_0 is the ground altitude. Within a given column, the variations of the column density can be established from a mass balance. During a time interval $\mathrm{d}t$, column density varies under the effect of particle fluxes on each of the faces of the column, but also due to formation and loss of molecules within the column. Figure 2.1 summarises the calculations involved in the mass balance.

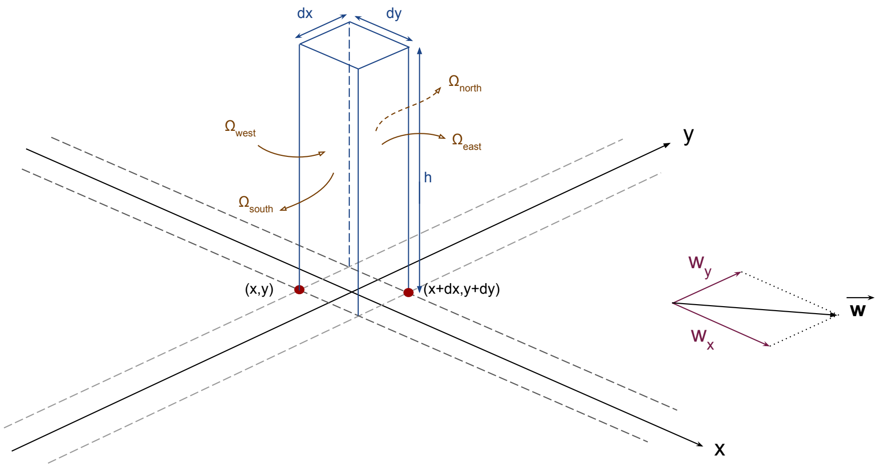

Figure 2.1: Mass balance within a tropospheric column.

The temporal derivative of N can be defined, at the first order with respect to $\mathrm{d}t$, as follows:

$$N(x, y, t + \mathrm{d}t) = N(x, y, t) + \frac{\partial N}{\partial t}(x, y, t)\mathrm{d}t \tag{2.1}$$

This relation can be linked to the algebraic variations of particles on the four lateral faces $\mathrm{d}^2N_{\text{north}}$, $\mathrm{d}^2N_{\text{south}}$, $\mathrm{d}^2N_{\text{east}}$, $\mathrm{d}^2N_{\text{west}}$, as well as the gains and losses of particles within the control volume during this time interval $\mathrm{d}^3N_{\text{created}}$ and $\mathrm{d}^3N_{\text{dissipated}}$:

$$N(x, y, t + \mathrm{d}t) = N(x, y, t) + \mathrm{d}^2N_{\text{north}} + \mathrm{d}^2N_{\text{south}} + \mathrm{d}^2N_{\text{est}} + \mathrm{d}^2N_{\text{west}} + \mathrm{d}^3N_{\text{created}} + \mathrm{d}^3N_{\text{dissipated}} \tag{2.2}$$

The algebric variation $\mathrm{d}^2N_{\text{face}}$ of particles resulting from the arrival/leaving of particles to/from a face whose orientation, conventionally described with a orthogonal and unitary vector going into the system $\vec{u}_{\text{face}}$, is given by $\mathrm{d}^2N_{\text{face}} = \bar{C}(x_{\text{face}}, y_{\text{face}}, t)\mathrm{d}S_{\text{face}}\vec{u}_{\text{face}} \cdot \vec{w}(x_{\text{face}}, y_{\text{face}}, t)\mathrm{d}t$, with $\mathrm{d}S_{\text{face}}$ being the surface of the face and $(x_{\text{face}}, y_{\text{face}})$ the coordinates of the face. Using this relation, the algebraic particle variations from all directions are given by:

$$\mathrm{d}^2N_{\text{north}} = \bar{C}(x, y + \mathrm{d}y/2, t)\ h(x, y + \mathrm{d}y/2, t)\ \mathrm{d}x\ \vec{w}(x, y + \mathrm{d}y/2, t) \cdot (-\vec{u_y})\ \mathrm{d}t \tag{2.3}$$

$$\mathrm{d}^2N_{\text{south}} = \bar{C}(x, y - \mathrm{d}y/2, t)\ h(x, y - \mathrm{d}y/2, t)\ \mathrm{d}x\ \vec{w}(x, y - \mathrm{d}y/2, t) \cdot \vec{u_y}\ \mathrm{d}t \tag{2.4}$$

$$\mathrm{d}^2N_{\text{east}} = \bar{C}(x + \mathrm{d}x/2, y, t)\ h(x + \mathrm{d}x/2, y, t)\ \mathrm{d}y\ \vec{w}(x + \mathrm{d}x/2, y, t) \cdot (-\vec{u_x})\ \mathrm{d}t \tag{2.5}$$

$$\mathrm{d}^2N_{\text{west}} = \bar{C}(x - \mathrm{d}x/2, y, t)\ h(x - \mathrm{d}x/2, y, t)\ \mathrm{d}y\ \vec{w}(x - \mathrm{d}x/2, y, t) \cdot \vec{u_x}\ \mathrm{d}t \tag{2.6}$$

By noting E and S the creation (emissions) and dissipation of pollutant per time and surface unit, we obtain $\mathrm{d}^3N_{\text{created}}(x, y, t) = E(x, y, t)\ \mathrm{d}x\ \mathrm{d}y\ \mathrm{d}t$ and $\mathrm{d}^2N_{\text{dissipated}}(x, y, t) = -S(x, y, t)\ \mathrm{d}x\ \mathrm{d}y\ \mathrm{d}t$. Equation 2.2 becomes:

$$\Omega(x, y, t + \mathrm{d}t) = \Omega(x, y, t) + (-\frac{\partial \Omega w_x}{\partial x}(x, y, t) - \frac{\partial \Omega w_y}{\partial y}(x, y, t) + E(x, y, t) - S(x, y, t))\mathrm{d}t \tag{2.7}$$

Similarly, Equation 2.1 becomes:

$$\Omega(x, y, t + \mathrm{d}t) = \Omega(x, y, t) + \frac{\partial \Omega}{\partial t}(x, y, t)\mathrm{d}t \tag{2.8}$$

These two developments constitute the basis of the mass balance in fluid mechanics. By combining Equation 2.7 and Equation 2.8 and using the relationships $\mathrm{d}^2N = \Omega \mathrm{d}x\mathrm{d}y$ and $\bar{C} = \Omega/h$, the behaviour of Ω can be obtained:

$$\frac{\partial \Omega}{\partial t} + \frac{\partial \Omega w_x}{\partial x} + \frac{\partial \Omega w_y}{\partial y} = E - S \tag{2.9}$$

This equation is the local conservation of mass equation, which highlights that any local change of the NO_2 content within a column (given by $\frac{\partial \Omega}{\partial t}$) can only be due to wind transport* (given by $\frac{\partial \Omega w_x}{\partial x} + \frac{\partial \Omega w_y}{\partial y}$) or net creation of NO_2 molecules (given by $E - S$). Here, we disregard density variations along the vertical. The local conservation of mass reflects the fact that the density of a pollutant in a fluid particle of a given fluid (in this case, air) varies according to the flow of the fluid and the processes of creation and dissipation. These processes can have several origins: chemical reactions, radioactivity, etc. Under steady-state conditions, the time derivative disappears and emissions can be expressed as the sum of sinks and horizontal variations:

$$E = \mathrm{div}(\Omega \vec{w}) + S \tag{2.10}$$

Here div is the horizontal divergence operator. The term S is called the sink term and the term $D = \mathrm{div}(\Omega \vec{w})$ is called the transport term. Like all continuity equations, this equation can be expressed integrally (Batchelor, 1967).

2.1.2 Modelling of the sink term

The sink term involves all the processes that consume NO_2. These processes are essentially non-conservative, since the density of the tracer is reduced by reorganisation of the matter. Here, we only consider the chemical reactions that involve NO_2. These were highlighted in Section 1.2.4. Noting $(\mathrm{R}_r)_{1 \leq r \leq N_P}$ the ensemble of species reacting with NO_2, the reactions can be written as:

$$\mathrm{NO_2} + \mathrm{R}_r \rightarrow \mathrm{P}_r \text{ for } r = 1, ..., N_P \tag{2.11}$$

Such chemical equations, with identical stoichiometric numbers for each reactants, correspond to a first-order kinetics with respective rate constants $(k_r)_{1 \leq r \leq N_P}$, which means the local chemical loss of NO_2 due to those reactions can be written as:

$$\left(\frac{\partial C}{\partial t}\right)_{\text{chemistry}} = \sum_{r=1}^{N_p} \left(\frac{\partial C}{\partial t}\right)_r = -\sum_{r=1}^{N_p} k_r \; [\mathrm{R}_r] \; C = -C \sum_{r=1}^{N_p} k_r \; [\mathrm{R}_r] \tag{2.12}$$

The quantity $\sum_{r=1}^{N_p} k_r \; [\mathrm{R}_r]$ is homogeneous to the inverse of a time. It represents the exponential decay of NO_2 due to chemistry which is characteristic of first-order reactions. We thus define the lifetime $\tau = \left(\sum_{r=1}^{N_p} k_r \; [\mathrm{R}_r]\right)^{-1}$ and, assuming that all concentrations do not vary much with time and altitude within the PBL (compared to horizontal variations), we can replace C by Ω in Equation 2.12 and infer the sink term S as:

$$S = \frac{\Omega}{\tau} \tag{2.13}$$

Such a relationship is interesting for two reasons. Firstly, the expression of the lifetime can be written as a sum of terms individually representing lifetimes that would appear in the presence of a single reaction with NO_2. Secondly, it shows that under the assumption of first-order reactions, the sink term is proportional to the NO_2 concentration. This property will be used in Section 3.4.2 to estimate the average underestimation of the sink term and thus deduce which reactions involving NO_2 can be neglected or not.

The development of the sink term is interesting from a theoretical point of view, since it expresses a simple decrease through the expression of the lifetime τ. In practical terms, however, the multiplicity

---

[*] The terms "convection" and "advection" are also used.

of reactions involved in the sink term makes it very difficult to calculate the effective lifetime precisely. Numerous studies using the flux-divergence method use a constant and uniform value of the lifetime (Beirle et al., 2019; de Foy, Schauer, 2022; Liu et al., 2023). The horizontal and temporal variabilities of the lifetime are thus neglected, and compensating for such a neglect requires heavy averaging over time. Each species reacting with NO_2 has its own dynamics involving other molecules, and therefore its own cycle which differs from one region to another. Taking this multiplicity of reactant cycles into account requires a heavy parameterisation that is only involved in transport chemistry models, which have their own assumptions, uncertainties and inconsistencies at different spatial scales. Avoiding the use of a Chemistry-Transport Model (CTM), and therefore the need for heavy modelling, inevitably involves simplifying the cycles of the various molecules involved in NO_2 dynamics. When the lifetime is not assumed to be constant, certain reactions are neglected because they are minor in a certain region or at a certain time of day (Lama et al., 2020). Since the local overpass time of TROPOMI occurs is in the middle of the day, NO_2 losses are largely dominated by the three-body reaction involving NO_2 and OH (Seinfeld, 1989), leading to the production of nitric acid HNO_3 and pernitrous acid HOONO. We re-write here Equation 1.13 and Equation 1.14:

$$\mathrm{NO_2 + OH + M \rightarrow HNO_3 + M} \tag{2.14}$$

$$\mathrm{NO_2 + OH + M \rightarrow HOONO + M} \tag{2.15}$$

Both reactions above follow first order kinetics, and the NO_2 lifetime can therefore be calculated as follows:

$$\tau = \frac{1}{k_{\mathrm{mean}}(T, [\mathrm{M}])[\mathrm{OH}]} \tag{2.16}$$

τ appears here as the characteristic mixed lifetime of NO_2 in the atmosphere. The reaction rate k_{mean} characterises the reactions between NO_2 and OH and depends on atmospheric conditions. Burkholder et al. (2020) provide a general expression of this rate as a function of both temperature T and total air concentration [M]. Note that HOONO can be rapidly decomposed back to NO_2 and OH in the lower troposphere. We assume here that this decomposition is slow and does not affect the NO_2 horizontal gradients. Both pathways are therefore taken into account, and the value of k_{mean} represent the total loss of NO_2 due to OH, with a contribution of the HOONO forming reaction between 5 to 15% under atmospheric conditions (Sander et al., 2011; Nault et al., 2016).

The formation of HNO_3 accounts for most of the total NO_x loss at the global scale (Stavrakou et al., 2013), and the lifetime in Equation 2.16 can be used as a first estimate to calculate the sink term. The effects of not accounting for the removal of NO_x from the other sinks, which have been presented in Section 1.2.4, will be detailed in Chapter 3.

2.1.3 The flux-divergence equation for NO_x emissions

The ratio $\mathcal{L}$ between NO_2 and NO_x concentrations, introduced in Section 1.2.2, is often used to convert directly NO_2 production to NO_x emissions. The reactions involved in the transformations between NO and NO_2 do not appear in the lifetime. NO_x emissions can be inferred from NO_2 column densities using the transport term $D = \mathrm{div}(\Omega\vec{w})$, the sink term $S = k_{\mathrm{mean}}(T, [\mathrm{M}])[\mathrm{OH}]\Omega$ and the NO_x:NO_2 ratio $\mathcal{L} = [\mathrm{NO_x}]/[\mathrm{NO_2}]$ as:

$$E = \mathcal{L}(D + S) \tag{2.17}$$

The use of the NO_x:NO_2 ratio implies the hypothesis of a steady state. As discussed in Section 1.2.2, the characteristic duration of the transient regime that precedes the photostationary state is of a few minutes in polluted environments, when only the ozone-forming mechanism is considered in the inter-conversion between NO and NO_2. In remote sensing studies, considering the resolution of instruments such as TROPOMI used and usual wind modules near the ground, this order of magnitude is lower than the inter-pixel transport time (from 15 min to 1 h), and we can reasonably neglect the effect of the stabilization time of the conversion factor on the total composition of the emissions and treat each pixel from its direct environment. The latter equation is the basis of the flux-divergence method applied for NO_2 columns to infer NO_x emissions.

2.1.4 Background removal

In satellite observations such as TROPOMI retrievals, the NO_2 signal from a sparsely populated area or a small industrial facility may be covered by noise or by the signal generated by natural NO_x emissions. As a consequence, detecting traces of non-natural emissions in TROPOMI NO_2 images is not a straightforward process. In the absence of anthropogenic sources, the NO_2 columns that are observed constitute a tropospheric background. At the global scale, this background is mostly due to soil emissions in the lower troposphere (Yienger, Levy, 1995; Hoelzemann et al., 2004). In the upper troposphere, NO_2 sources include lightning, convective injection and downwelling from the stratosphere (Ehhalt et al., 1992), but the factors controlling the resulting concentrations are poorly understood. According to state-of-art estimates, anthropogenic NO_x accounts for most of the emissions, whereas natural emissions from fires, soils and lightning are smaller (Jaeglé et al., 2005; Müller, Stavrakou, 2005; Lin, 2012). In most of the EMME region, the desert climate features limit lightning and fire, and the share of the corresponding emissions within the background is thus expected to be low.

Figure 2.2 shows the daily NO_2 background in six different areas of the EMME region: the Eastern Mediterranean Sea, the North-East Africa (corresponding to Southern Egypt and Northern Sudan), the Arabian Desert, Mesopotamia and Iran moutains (which corresponds to parts of Elbourz and Zagros mountain chains) and the North-West Indian Ocean. For a given sub-region, this background is estimated as the average of pixels whose associated column is below the first quartile (25th percentile) in the distribution of the corresponding TROPOMI retrievals (it should be noted that in the case studies that followed (Section 3.2 and Section 3.3), as the areas considered were much smaller, the choice of percentile to estimate this background is modified downwards). The six domains chosen correspond to locations with different climatic regimes. Their size is sufficiently large (several tens of thousands of TROPOMI pixels each) to prevent any statistical over-estimation of the background; the pixels above anthropogenic activities are too few in number to have any influence on the result.

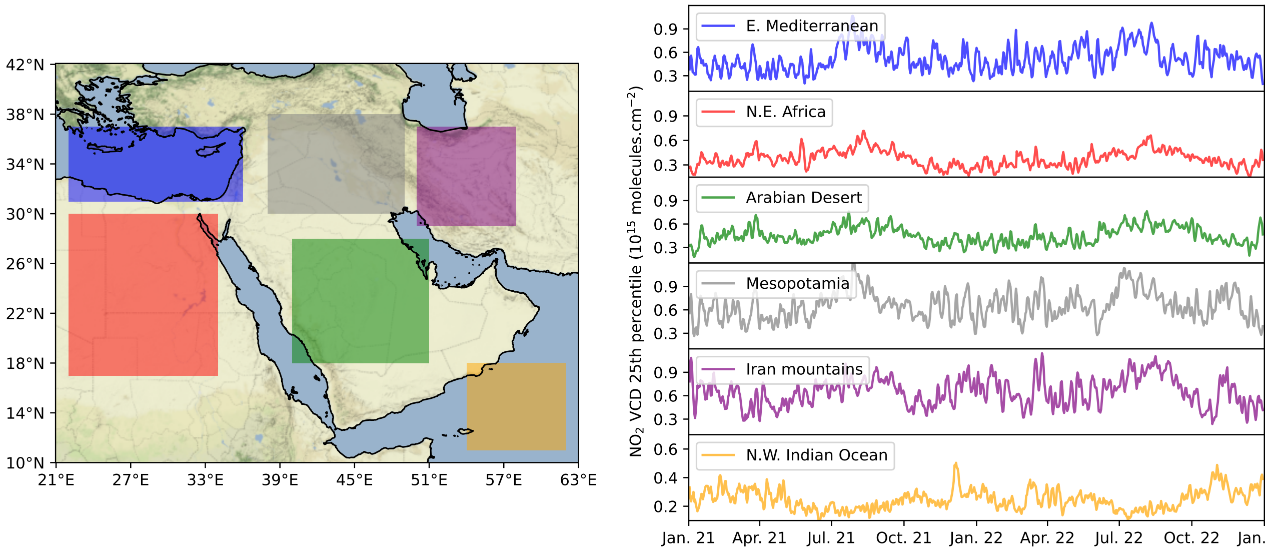

Figure 2.2: (left) Different large-scale areas in the EMME region used to calculate the NO_2 background as observed by TROPOMI, calculated each day as the mean value of NO_2 columns under the 25th percentile. (right) Corresponding time series for 2021 to 2022 (3-days moving average).

In the first five domains shown, there is little annual variability in the NO_2 background, with higher background concentrations during the summer months. The background is particularly low in the deserts (Sahara and Arabian Desert), probably due to the absence of natural sources of NO_2. Conversely, it is high in other areas, with a background sometimes exceeding the value of 1.0×10^{15} molecules.cm^{-2} in Mesopotamia and in Iran mountains. The domain of the EMME region corresponding to the north-east of the Indian Ocean has the lowest average background values, and shows a different annual cycle to the other zones (we have not tried to interpret this difference).

Overall, we can conclude from these time series that the mean natural NO_2 budget, which corresponds to natural processes mostly taking place in the higher troposphere, are responsible for a background higher during summer months, and with a mean value usually between 0.2 and $1.0{\times}10^{15}$ molecules.cm^{-2}. As a result, the detection and quantification of NO_x emissions in the region will be hampered for emitters producing a NO_2 content similar to this order of magnitude. Considering a signal-to-noise ratio as being "low" from the value of 2, we can expect difficulties in detecting emitters whose corresponding signal observed by TROPOMI is lower than $\sim 1.0{\times}10^{15}$ molecules.cm^{-2}. Considering this aspect will be particularly important for regions with small emitters, such as in Cyprus (Section 3.3) or for the characterisation of the traffic and shipping sectors (Section 3.5.1).

2.1.5 Diffuse sources and point sources

Interpretation of the results obtained from inversion using the flux-divergence method requires a prior theoretical understanding. The tracer emitted by a source, regardless of its size, is transported by the air flow. Its concentration is a passive scalar, which means it has no dynamical effect (such as buoyancy) on the fluid motion itself (Warhaft, 2000). Here, the velocity field $\vec{w}$ corresponds to the mean flow, and does not take into account the turbulent fluctuations whose description is necessary to precisely describe the movement of the fluid driven by inertia at any point in space. The fluctuations are defined as the expected value of the velocity field subtracted from the mean flow such that the corresponding time average equals zero, and while the mean flow is a predictable variables determined by dynamics laws, the turbulent fluctuations are regarded as stochastic variables (Adrian et al., 2000). At the scale of a TROPOMI pixel or in a reanalysis, the evaluation of the turbulent component is meaningless. However, the motion generated by turbulence is perceptible from space: eddies can be formed in turbulent regime and, due to the passive nature of the tracer, transport pollution around the source regardless of the mean flow direction (Cushman-Roisin, Beckers, 2011). Such phenomenon is called "eddy diffusion" and acts in a similar way as the molecular diffusion, but with an amplitude which is several orders of magnitude stronger than molecular diffusion. For NO_2, Palmes et al. (1976) derived a molecular diffusion coefficient of $K_m = 0.154$ cm^2.s^{-1} in air of 20°C and 1 atm), which is indeed lower than usual orders of magnitude of eddy turbulent diffusivities $K_e \sim 10^4$ m^2.s^{-1} (Haynes, Shuckburgh, 2000; Hegglin et al., 2005; Pisso et al., 2009). Molecular diffusion can therefore be neglected when studying such turbulent flows. The concentration pattern which is obtained from a passive tracer emitted by an isolated source under eddy diffusion in a Lagrangian frame of reference that moves with the mean wind is a Gaussian function whose standard deviation σ is proportional to the square root of both K_e and time.

Conversely, we can use an Eulerian approach and consider a theoretical isolated emitter in a 2-dimension, uniform and steady wind whose module is noted w_0. We can study the pollutant concentration profile along the streamline (i.e. parallel to the wind) passing by the centre of the emitter using only one axis described by the coordinate ξ. The combined effect of mean wind transport, chemical decay and eddy diffusion must be considered. The concentration profile can be reduced to a line density ω, which is described by a convolution of a truncated exponential function and a Gaussian function scaled by the total amount of pollutant $\mathcal{N}$ and shifted by a background concentration offset β. The exponential function ω_e describes transport and chemical decay:

$$\omega_e(\xi) = \begin{cases} \exp(-\frac{\xi}{\xi_0}), & \text{if } \xi > 0 \text{ (downwind).} \\ 0, & \text{if } \xi < 0 \text{ (upwind).} \end{cases} \tag{2.18}$$

Here ξ_0 is the distance over which the line density decreases by a factor of e (e-folding distance). This characteristic length represents the distance over which the pollutant is consumed along its transport by the wind. It represent the exponential decay of NO_2 due to the sink term in a moving frame of reference. This model is well suited to species consumed by a reaction with first-order kinetics, as explained in Equation 2.12, which is the case for NO_2. We can therefore link the lifetime τ of the species to the wind module w_0 as follows:

$$\xi_0 = w_0 \tau \tag{2.19}$$

Equation 2.18 and Equation 2.19 thus account for both the transport by the mean wind and the chemical decay along the streamline. On the other hand, a Gaussian function represents the spreading effect of turbulent mixing:

$$\omega_g(\xi) = \frac{1}{\sqrt{2\pi}\sigma} \exp(-\frac{\xi^2}{2\sigma^2}) \tag{2.20}$$

Here σ is the standard deviation of the Gaussian function. The line density of the plume is finally modelled as $\omega = \beta + \frac{\mathcal{N}}{\xi_0}\, \omega_e * \omega_g$ where $*$ is the convolution operator (the integral of $\omega_e * \omega_g$ is ξ_0). This results in the following profile, where the notation erfc stands for the complementary error function defined as $\mathrm{erfc}(\varsigma') = 1 - \frac{2}{\sqrt{\pi}} \int_0^{\varsigma'} e^{-\varsigma^2} \mathrm{d}\varsigma$:

$$\omega(\xi) = \beta + \frac{\mathcal{N}}{2\xi_0} \exp\left(-\frac{\xi}{\xi_0} + \frac{\sigma^2}{2\xi_0^2}\right) \mathrm{erfc}\left(-\frac{1}{\sqrt{2}}\left(\frac{\xi}{\sigma} - \frac{\sigma}{\xi_0}\right)\right) \tag{2.21}$$

The emissions of the source located at $\xi = 0$ are then obtained by $\mathcal{E} = \mathcal{N}/\tau$. The previous exponentially modified Gaussian (EMG) profile is well suited for "point-source" emissions, i.e. emissions that are localised in a narrow area. It is the case when the gas is produced by a single emitter in an isolated area, such as power plants or cement kilns that are several kilometers away from other human activities. For such emitters, the value of σ only accounts for turbulent diffusion, because the molecular diffusion is negligible. However, some emitters do not behave like such point sources. They can spread on distances that are larger than 50 km, which is more than the characteristic turbulent diffusion length (about 10 km). Such emitters can be modelled as the sum of several smaller emitters that could not be detected from space. It is the case of megacities, where traffic and residential emissions can overlap on more than thousands of square kilometers. In the case of NO_2, those "diffuse sources" can have associated emissions that are comparable to those of power plants or industrial facilities, but because they spread on a much wider area, the corresponding emissions per surface unit is much lower. For these sources, the value of σ account both the turbulent diffusion and the source extent.

Examples of the three functions ω_e, ω_g and ω are shown in Figure 2.3. The abscissa is the normalised curvline coordinate ξ and the ordinate the normalised line density. The source is placed at $\xi = 0$ and its emissions are normalised to 1. Background is reduced to $\beta = 0$. The e-folding distance is set to $\xi_0 = 20$ by setting wind module and lifetime parameters to $w_0 = 10$ and $\tau = 2$. The three cases differ only by the value of σ, and the extreme cases illustrate the "point source" and "diffuse source" behaviours. Note that the column peak is located slightly downwind the emitter (here to the right). Instead of being symmetrical, the concentration profile displays a "tail" pointing downwind (hence the common name "plume" for this type of profile).

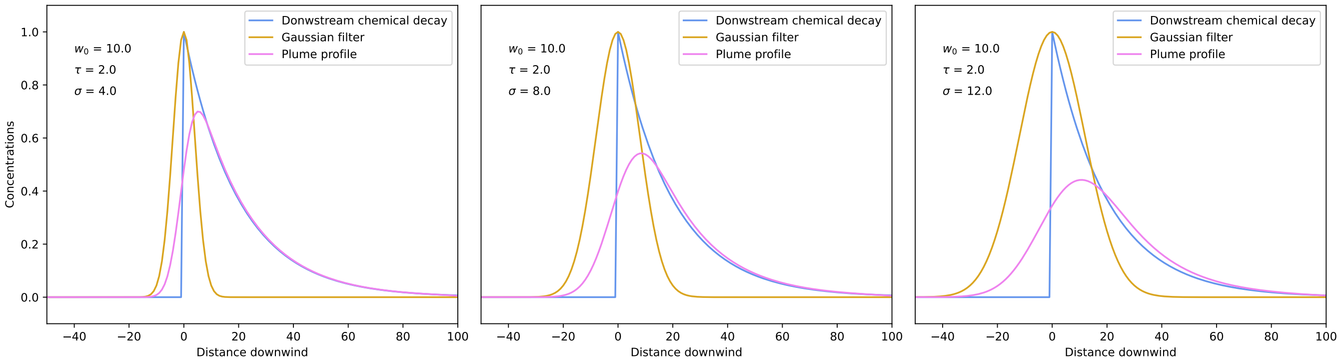

Figure 2.3: Theoretical illustration of the plume shape produced by an emitter with respect to its spatial extent along a streamline. With unchanged emissions, the emitter emits over a restricted area (left, characterisation of industrial facilities), an area of intermediate extent (centre), and a large area (right, characterisation of megacities). Emissions are modelled by a Gaussian whose standard deviation represents the spatial spread of emissions. Wind module is unchanged in all three cases.

Using the flux-divergence method, whose 1D-implementation corresponds to a simplification of the transport term div$(\Omega\vec{w})$ to $w_0\frac{\partial\Omega}{\partial\xi}$, we can compute the emissions corresponding to the concentration profiles in Figure 2.3. The calculation of the transport term, the sink term and the emissions are shown on Figure 2.4. The case on the left illustrates a point source: a Gaussian peak is centered around the source with the adequate value of σ. The result is similar for the case on the right, but the emissions are spread over a large distance due to the higher value of σ. Overall, the flux-divergence scheme has managed to reproduce the Gaussian behaviour entered as an input, but in the case of the point-source, this behaviour corresponds to turbulence mixing, while in the case of the diffuse source, it mostly corresponds to the spatial extent of the emitter.

Another distinctive feature of the point-source with respect to the diffuse source is the balance between the sink term and the transport term within the emissions. Figure 2.4 shows that an increase in the source extent goes together with a lowering of the transport term share within the emissions. Point sources are thus characterised by a dominance of the transport term with respect to the sink term, while diffuse sources are characterised by a dominance of the sink term. This behaviour has been described by Beirle et al. (2021).

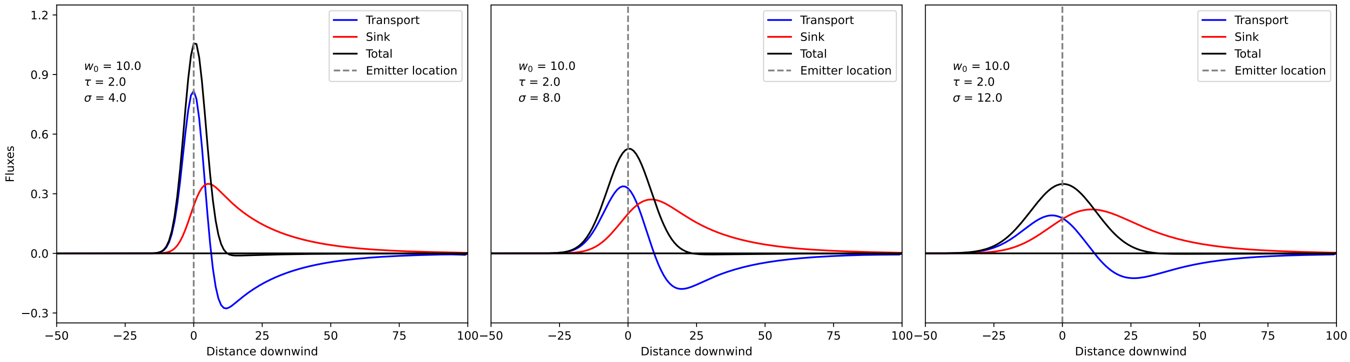

Figure 2.4: Theoretical illustration of the relative importance of the terms transport and sinks in calculating the total emissions of an emitter in relation to its spatial extent along a streamline. With unchanged emissions, the emitter emits over a restricted area (left, characterisation of industrial facilities), an area of intermediate extent (centre), and a large area (right, characterisation of megacities). Lifetime and wind module are unchanged in all three cases.

The properties illustrated in the 1D-representation of the flux-divergence method apply to the 2D domains provided by satellite observations: the mapping of NO_x emissions from NO_2 observations allow detecting the main emitters of a given region, and the analysis of transport and sink terms, provided that they are estimated correctly, allows identifying the behaviour (i.e. point source of diffuse source) of the observed sources. Note that in satellite images, the pixels are larger than source points but smaller than most of the megacities that act as diffuse sources. The spatial extent of the calculated emissions can therefore be artificially increased due to the resolution of the data, but their effect is more critical for point sources. Using Equation 2.17, Figure 2.5 and Figure 2.6 show examples of NO_x emissions calculated for a set of two close cement plants (Alarish Cement and Sinai White Cement Factory) in the Sinai peninsula in Egypt, and the city of Damascus, Syria. These two examples are chosen to illustrate the two behaviours: the two cement plants are less than 8 km apart and can be considered as a single emitter acting like a point source. Conversely, the urban area of Damascus extends over more than 800 km^2 and does not comprise any major industrial site, it acts like a diffuse source. Both emitters are isolated from other important sources, and the emissions are calculated for a day (i.e. using only one TROPOMI image) with a particularly clear sky. The horizontal wind field used to calculate the transport term, as well as temperature and OH concentration fields used to calculate the NO_2 lifetime, are taken from CAMS and ERA5, which are introduced in Section 2.3.1 and Section 2.3.2.

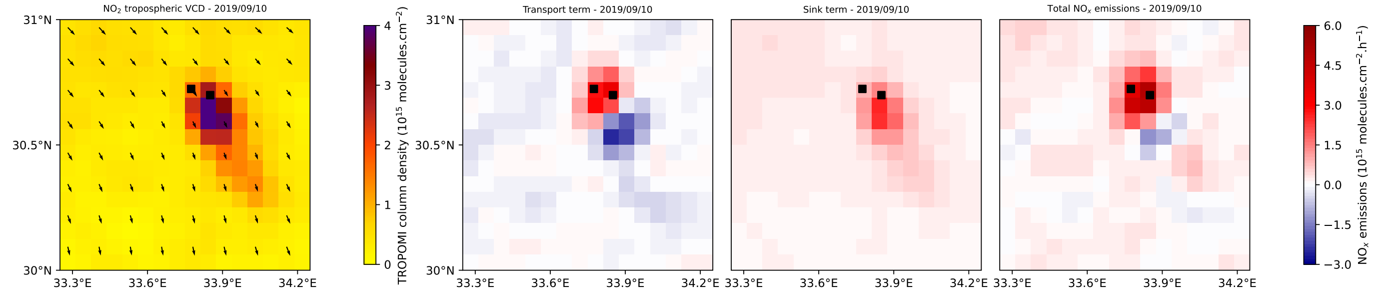

Figure 2.5: TROPOMI NO_2 tropospheric vertical columns for two cement plants in the Sinai region on September 10th 2019 (1st panel), as well as the transport term (2nd panel), sink term (3rd panel) and corresponding NO_x emissions (4th panel) using the flux-divergence method. The location of the cement plants are denoted with squares. The ERA5 wind field is added on the left panel and downscaled to a 0.0625°×0.0625° resolution.

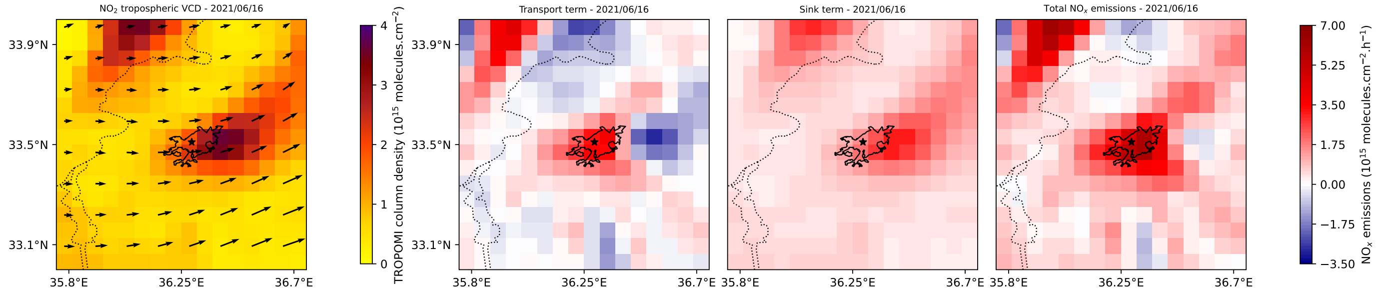

Figure 2.6: TROPOMI NO_2 tropospheric vertical columns for the city of Damascus, Syria, on June 16th 2021 (1st panel), as well as the transport term (2nd panel), sink term (3rd panel) and corresponding NO_x emissions (4th panel) using the flux-divergence method. The location of the city centre is denoted with a star and its urban extent is displayed. The ERA5 wind field is added on the left panel and downscaled to a 0.0625°×0.0625° resolution.

These two figures provide a 2D illustration of the theoretical behaviours highlighted with 1D profiles in Figure 2.4. For both cases, the transport term has the shape of a dipole oriented in the direction of the mean wind, with a positive pole above the source, and a negative pole downwind the source. Conversely, the sink term, which is proportional to the VCD, has the shape of a plume, with decreasing positive values downwind from the source. The negative pole of the transport term combines and compensates with the tail of the sink term profile, leading to near zero emissions downwind. The resulting emissions therefore have the shape of a disk above the emitter which supposedly has a Gaussian shape. For the Sinai cement plants and Damascus cases, the dipole/plume shape of the transport/sink terms are clearly visible. The Gaussian shape of the resulting emissions can be approximated in the case of the Sinai cement plants which act as a point source. In the case of Damascus, the urban sprawling is not circular, and a Gaussian shape is difficult to estimate. The two terms have similar values in the case of Damascus: in the 25 pixels around the city centre (which correspond approximately to the extent of the city), the transport term has an average value of 1.40×10^{15} molecules.cm^{-2}.h^{-1} while the sink term has an average value of 1.27×10^{15} molecules.cm^{-2}.h^{-1}. This balance constitutes an illustration of the theoretical profile on Figure 2.4 (right panel). For the cement plants in the Sinai region, if considered the 4 pixels with the highest emissions (which are also the closest to the emitter), the transport term has an average value of 2.85×10^{15} molecules.cm^{-2}.h^{-1} while the sink term has an average value of 1.48×10^{15} molecules.cm^{-2}.h^{-1}. The transport term thus account for about two thirds of the NO_x emissions budget. This predominance constitutes an illustration of the theoretical profile on Figure 2.4 (left panel). Generally speaking, the transport term accounts for most of the emissions in the case of a point source, and the amplitude of the effect increases with the output (capacity, production, etc.) of the source (Beirle et al., 2021). As a consequence, the effects of under-estimating or over-estimating the sink term, notably through a wrong parametrisation of the NO_2 lifetime, are less critical for a point source than for a diffuse source. Emission maps in both cases show numerical noise, which can go up to $\sim 1 \times 10^{15}$ molecules.cm^{-2}.h^{-1}, which is close to the average value of both terms. Assuming this noise is random and due to resolution effects and uncertainties in the estimation of the parameters used to calculate emissions, the best method to limit its effects is to average emissions. This method is commonly practiced using the flux-divergence scheme, and it provides consistent estimates of average emissions for a month or year. On the other hand, instantaneous emissions cannot be obtained. This type of averaging is done on Figure 2.7 which represents Riyadh, Saudi Arabia, for the year 2021. This example is interesting because the city comprises different power and cement plants in its neighbouring and already characterised by Beirle et al. (2019). It allows observing both behaviours mentioned previously.

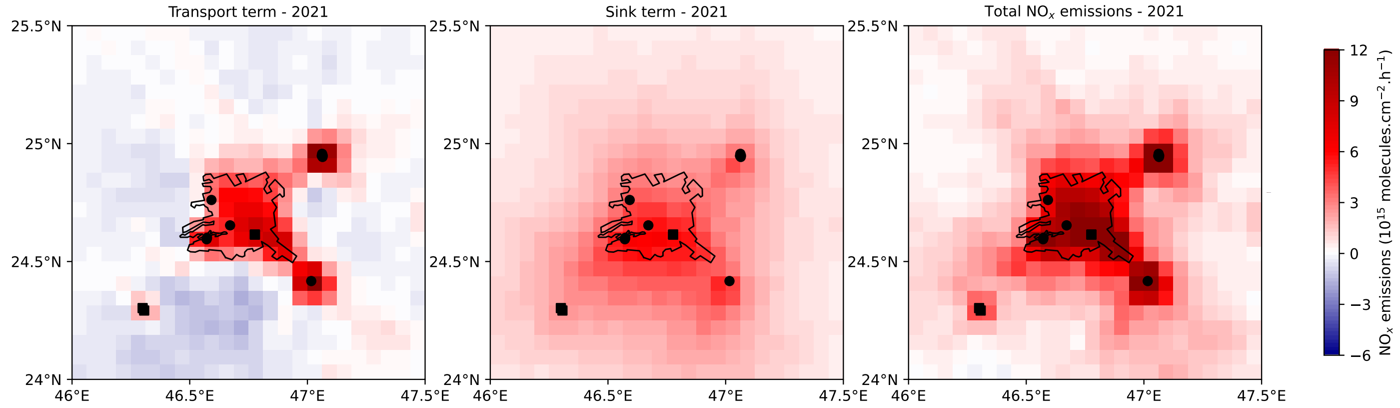

Figure 2.7: Mean transport term (left), sink term (centre) and corresponding NO_x emissions (right) calculated with the flux-divergence method for the city of Riyadh, Saudi Arabia in 2021. The location of the city centre is denoted with a star and its urban extent is displayed. The location of power plants and cement plants are displayed with rounds and squares respectively.

The estimations of average NO_x emissions in Riyadh illustrate the differences between types of emitters highlighted in section 2.1.5. We observe a transport term almost four times higher (between 9 and 13×10^{15} molecules.cm^{-2}.h^{-1}) than the corresponding sink term (between 3 and 5×10^{15} molecules.cm^{-2}.h^{-1}) at the combined cycle power plants to the north-west and south-west of the city centre, close to the behaviour shown in Figure 2.4 on the left. In contrast to these point sources, the north of the city, which does not contain any fossil fuel power stations, displays a transport term and a sink term of similar intensities (around 4×10^{15} molecules.cm^{-2}.h^{-1}), close to the behaviour shown in Figure 2.4 in the middle. The south of the city is very dense but also comprises power plants; it does not correspond to any typical behaviour. Accounting for the Gaussian nature of the emissions profile for point sources, the estimation of the NO_x emissions for the power plants in the north-east and south-east of the domain with a 1D Gaussian fit can be conducted (see Supplementary Materials, Figure A.3).

2.1.6 Vertical structure and topographic correction

Systematic artifacts of the transport term were reported over regions with complex topographies, with high tropospheric vertical column densities over mountainous regions. These high values can hinder the identification and quantification of NO_x point sources, possibly due to inaccurate mean wind fields over mountains (Beirle et al., 2021). However, a recent study by Sun (2022) shows that these patterns can also be caused by 3D transport effects which have been ignored in the simplified 2D approach which has been described so far. A "topography-wind" term can be introduced in order to correct for this effect:

$$\epsilon_{\text{correction}} = X_e \Omega \vec{w}_g \cdot \vec{\nabla} z_0 \tag{2.22}$$

Here $\vec{w}_g$ is the surface horizontal wind, $\vec{\nabla} z_0$ is the altitude gradient and X_e is the inverse scale height. The latter can be defined as the ratio between ground concentration and the total tropospheric column density, and it is used to model how the concentration of the species changes with altitude within the troposphere. Rather than parametrising this quantity, Sun (2022) used fitted values between 0.2 and 1.0 km^{-1} to derive NO_x emissions, which are obtained by correcting Equation 2.17 into:

$$E = \mathcal{L}(D + S + \epsilon_{\text{correction}}) \tag{2.23}$$

This corrective term is not used in this thesis but the implications of not accounting for vertical effects are discussed with regard to the results described in Section 3.1 and Section 3.3.

2.1.7 OH feedback and model resolution

As shown in Section 1.2.2, NO_x significantly impacts the ozone production. It also plays an important role in aerosol formation through its interaction with hydroxyl radical OH, hydroperoxyl radical HO_2 and organic peroxy radicals RO_2 (Murphy et al., 2006). The concentration of OH radical, which is crucial in removing NO_x during daytime, is closely tied to the concentration of NO_x itself. Therefore, accurately quantifying the removal rate of NO_x requires a model that can effectively distinguish NO_x levels near sources to background levels. Observations of NO_2 columns (Heue et al., 2008), in situ measurements (Russell et al., 2010) and simulations (Cohan et al., 2006; Loughner et al., 2007) indicate that this transition can occur at scales as small as 10 km. However, uncertainties in our understanding of atmospheric reactions or their representation in models can undermine the accuracy of inferred emissions. For instance, research has shown that modeled ozone production is highly dependent on model resolution due to its nonlinear relationship with NO_x concentration.

Valin et al. (2011) employed an analytical solution of the NO_x-OH-HO_2-RO_2 steady-state relationship to determine OH concentrations and simulated the removal of NO_2 by OH downwind sources using 1-D and 2-D plume models at different spatial resolutions. Figure 2.8 displays the relationship between OH and NO_2 derived from this steady-state relationship, along with the corresponding NO_2 lifetime according to Murphy et al. (2006). Decreasing high NO_2 levels (red) leads to increased OH and a shorter NO_2 lifetime, whereas reducing low NO_2 levels (blue) results in reduced OH and a longer NO_2 lifetime. The crucial aspect of this relationship is that intermediate NO_2 levels (green) are associated with higher OH feedbacks, with a maximum corresponding to NO_2 lifetimes of about two hours. On spatial scales, such a lifetime is equivalent to decay lengths between 5 and 50 km depending on mean wind module. Failing to accurately resolve the NO_2 gradients between low or high NO_2 levels and intermediate NO_2 levels leads to a wrong estimation of the OH feedback, and subsequently, biases in NO_2 lifetime. In cases where NO_2 distribution is misrepresented due to coarse model resolution, the biases in OH feedback, NO_2 lifetime, and total NO_2 concentration become significant.

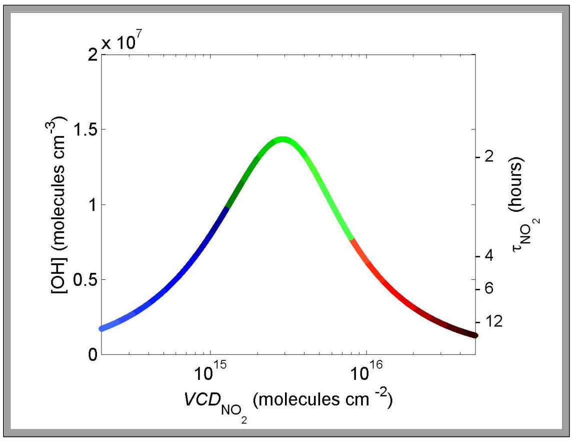

Figure 2.8: Steady state OH concentration (left axis) and corresponding NO_2 lifetime (right axis) versus boundary layer NO_2 column, assuming a 1-km well-mixed boundary layer. The color scheme corresponds to regions of high NO_2 (red), where OH is low, intermediate NO_2 (green), where OH is high, and low NO_2 (blue), where OH is low. Figure extracted from Valin et al. (2011).

Valin et al. (2011) also constructed a model for which NO_2 is emitted at the corner of a 1024-km domain and transported at a constant rate. The model was run with different emission rates, representing high, intermediate, and low NO_2-OH feedback regimes, and using different east-west resolutions while fixing the dimensions perpendicular to the flow at 1 km (north-south and vertical). Steady-state simulations in the 1-D model reveal that inaccurate resolution of NO_2 gradients results in biased OH levels, as well as mis-representation of NO_2 lifetimes and concentrations. For instance, when a source producing high emissions is computed at high resolution, OH is significantly suppressed and the associated lifetime is high, while the use of a coarser resolution averages NO_2 over the entire domain, enhancing OH and lowering the NO_2 lifetime. The NO_2 levels are thus biased-low NO_2. Such inaccuracies can lead to domain-total NO_2 biases exceeding 50% at coarse resolutions. On the other hand, for lower emissions, the NO_2 decays rapidly at high resolution due to high OH concentration, but for coarser resolution, the NO_2 is averaged over the domain, resulting in lower OH and higher lifetimes. A positive bias in NO_2 levels is therefore encountered. For an intermediate source of NO_2, sharp gradients cannot be adequately resolved with coarse resolution. The biases observed in NO_2 predictions for an intermediate source behave similarly to those of a large source at finer resolutions (less than 16 km approximately) and a small source at coarser resolutions. Generally speaking, biases are moderate (10–30%) at intermediate resolutions, primarily caused by numerical resolution diluting NO_2 at the edge of the plume. When the model resolution becomes significantly larger than the plume itself, OH feedbacks are significantly distorted compared to a resolved calculation of the plume.

Insights can be further derived from a 2-D model, considering horizontal diffusion and different source distributions. In their model, Valin et al. (2011) introduced a point source (2×2 km^2) and a diffuse source (96×96 km^2), with various emission rates representing high, intermediate, and low NO_2-OH feedback regimes. The model incorporated diffusion rates of 10 m^2.s^{-1} and fixed vertical layer dimensions at 1 km. Steady-state simulations reveal that a large point source of NO_2 is OH-suppressing and long-lived at high resolution, while experiencing high OH and being short-lived at coarse resolutions. The wide distribution of NO_2 and corresponding OH feedbacks in the resolved plume are grossly mispredicted at coarse resolution, leading to biases in domain-averaged NO_2. Similarly, over a small source, the opposite effect occurs, with high OH concentration and short NO_2 lifetime at high resolution, but low OH and long NO_2 lifetime at coarser resolutions, resulting in highly biased domain-averaged NO_2 predictions. Simulations using emissions from a diffuse source exhibit relatively modest biases, following a similar pattern as those over a point source. The biases over a diffuse source are smaller due to the fact that coarse resolutions are more capable of characterizing the NO_2 distribution and corresponding OH feedbacks over the wider plume compared to a point source which exhibits strong NO_2 gradients.

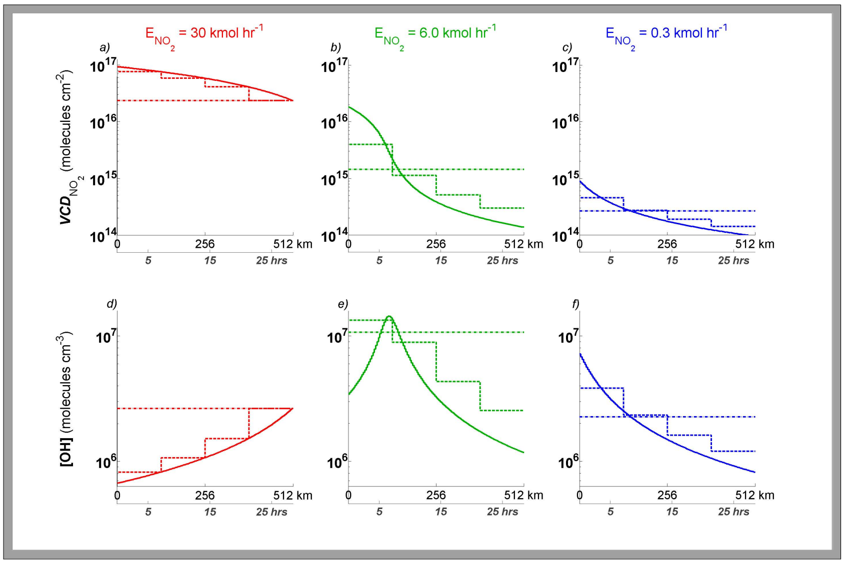

Figure 2.9: NO_2 column predicted in a 1-D plume model (east-west) at 2 km (solid), 128 km (dashed), and 512 km model resolutions (dash-dot) for (a) a large, (b) intermediate, and (c) small source of NO_2 and (d–f) the corresponding OH feedback. The color-scheme corresponds to NO_2-OH feedback regimes depicted in Figure 2.8. Horizontal (north-south) and vertical layers are fixed at 1 km thickness for all resolutions. Figure extracted from Valin et al. (2011).

To summarise, biases in NO_2 predicted in the presence of a constant OH field (without NO_2-OH feedback) are negligible across the entire domain but significant near the source. These biases result from the inability to resolve gradients for a short-lived species such as NO_2 on a coarse grid, and are negligible in regions larger than the spatial scale of chemical decay. However, when NO_2-OH chemical feedbacks are accounted for, biases depend on NO_x emissions, and their magnitude is greater when a coarser resolution is used. To mitigate these issues, a dataset for OH concentration (or NO_2 lifetime, alternatively) should have a resolution that can resolve NO_2 gradients and chemical feedbacks near emission sources. The use of a dataset that do not meet this criterion will result in large uncertainties in the estimation of NO_x emissions. This is explicitly true for point sources, for which horizontal gradients of NO_2 and OH are sharp. Conversely, using a low-resolution OH dataset could be computationally intensive and require advanced modelling techniques. This comprehension of the factors influencing the resolution effects of NO_x and the use of fine-resolution data, which has been supported by further studies (Li et al., 2023a), is of crucial importance when applied to satellite retrievals. A comparison of seasonal NO_2 column densities and OH concentrations is displayed for the EMME region in the Supplementary Materials.

2.2 Alternative methods to derive emissions from column densities

2.2.1 Comparison with an exponentially-modified Gaussian function

Another method to estimate NO_x emissions and lifetimes from satellite NO_2 column densities is based on line densities, i.e. integrated tropospheric columns perpendicularly to the wind direction and comparing the NO_2 decay profile along the streamline to the EMG function that has been introduced in Section 2.1.5. Here a modified version is used to account for a possible difference between the location of the source μ and the the middle of the streamline $\xi = 0$:

$$\omega(\xi) = \beta + \frac{\mathcal{N}}{2\xi_0} \exp\left(\frac{\mu - \xi}{\xi_0} + \frac{\sigma^2}{2\xi_0^2}\right) \operatorname{erfc}\left(-\frac{1}{\sqrt{2}}\left(\frac{\xi - \mu}{\sigma} - \frac{\sigma}{\xi_0}\right)\right) \tag{2.24}$$

The method aims at estimating emissions of a given source, and do not allow mapping emissions at the scale of a region. It has been introduced by Beirle et al. (2011) and refined by later studies (Valin et al., 2013; Lange et al., 2021; Griffin et al., 2021; Lama et al., 2022). In this method, satellite retrievals are rotated around the selected source with the corresponding reanalysis wind data to a common wind direction resulting in an upwind–downwind pattern. The NO_2 column of each pixel is converted into a NO_x column, and the mean NO_x distribution is calculated. To reduce the influence of possible surrounding sources, the line density is only calculated in a sector around the source, which does not cut the plume and thereby misses emissions. Typical values used for the sector size are between ± 15 and ± 70 km across the plume, depending on its width, and up to 200 km upwind and up to 400 km downwind of the source, depending on plume length and the presence of other neighbouring sources. Finally, the obtained profile is compared to the EMG function given by Equation 2.24; parameters β, $\mathcal{N}$, ξ_0, μ and σ are derived from the comparison. Using prior knowledge on the mean wind module above the emitter w_0 and the NO_x:NO_2 ratio $\mathcal{L}$, the lifetime can be calculated as $\tau = \xi_0/w_0$ according to Equation 2.19, and the total emissions can then be calculated as $\mathcal{E} = \mathcal{L}\mathcal{N}/\tau$. Additional filtering, on wind speed or direction, can be used to enhance the results (Beirle et al., 2011). The method is usually performed on mean profiles, but if the conditions are favorable (e.g. clear-sky, homogeneous and strong wind conditions), even a single overpass can deliver valuable results (Lorente et al., 2019; Goldberg et al., 2019b). Figure 2.10 illustrates the use of this method for the city of Riyadh observed on October 28th 2022. The wind module and the NO_x:NO_2 ratio are derived from ERA5 and CAMS data which are introduced in Section 2.3.1 and Section 2.3.2.

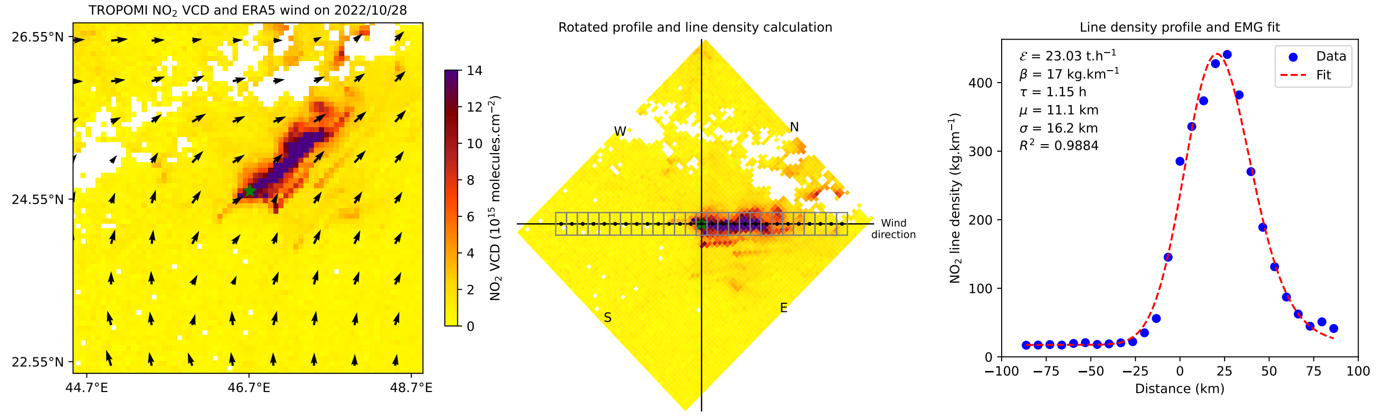

Figure 2.10: (left) TROPOMI NO_2 tropospheric vertical column over Riyadh and corresponding ERA5 horizontal wind. White pixels corresponds to retrievals with low-quality data ($q_a < 0.75$) or no data. (middle) Plume rotation with its wind direction around the centre of the source to an upwind-downwind pattern. The grey boxes indicate the sector of ± 20 km around the source relevant for the emission and lifetime estimates. (right) NO_2 line density as a function of distance to the source calculated for the ± 20 km sector (blue dots) and fit results (red line) with estimated NO_x emissions and lifetime. The city centre is denoted with a green star.

The EMG fit method is particularly efficient for intensive and isolated pollution emitters in a homogeneous wind, because these conditions allow observing plumes with a high signal-to-noise ratio and a regular decay along the streamline. Sources in coastal and mountainous regions with inhomogeneous terrain are more difficult to treat, as those features result in inhomogeneous wind patterns, which are more difficult to interpret and lead to larger uncertainties in the NO_x emissions and lifetimes. For sources in densely populated areas such as China or India, the influence of large NO_x-emitting sources nearby resulted in low contrast of the NO_2 column amount between the target and the local background (Lange et al., 2021). As a result, it might be considered as less useful than the flux-divergence method when trying to detect and map NO_x emissions. However, it provides, through the study of isolated and powerful emitters, a comparison which allows validating emissions and NO_2 lifetimes inferred by the flux-divergence method. Such a comparison is conducted taking Riyadh as a test case in Section 3.1.6.

2.2.2 Other alternative methods

The flux-divergence method and the EMG fit method have been presented here to infer NO_x emissions from NO_2 observations. Other methods exist, and they all have their advantages and drawbacks. This section aims at highlighting four of these other methods: the source pixel method, the integrated mass enhancement method, the constrained linear variational method and the cross-sectional flux method. Formulas inherent to these methods will not be proven.

Source pixel method

The source pixel method compares different satellite-observing configurations. It has been used by Jacob et al. (2016), and by Varon et al. (2018) in a comparative article for methane. In this method, emissions are inferred from enhancements of columns in the source pixel relative to the local background. For a square observation pixel of dimension ℓ containing a point source in a uniform wind speed w_0, emissions $\mathcal{E}$ are calculated from the mean source pixel enhancement $\Delta\Omega$, the surface pressure p, the acceleration of gravity g and the column of dry air Ω_{air} (expressed in mass terms) as:

$$\mathcal{E} = \frac{w_0 \ell p}{g \Omega_{\text{air}}} \Delta\Omega \tag{2.25}$$

The source pixel method is not optimal for many reasons. Indeed, the source pixel retrieval method only considers the column enhancement over the point source pixel, thus inferring the emission rate from ventilation of that pixel by the local wind. It assumes that the near-field plume is diluted over the source pixel and neglects information from the plume downwind. This can be an effective method when pixel resolution is coarse, so that most of the information is in the source pixel and the mean wind across the pixel can be well defined (Buchwitz et al., 2017). However, it does not exploit the information from downwind pixels, where most of the plume mass typically resides, and neglects the source pixel ventilation due to turbulent horizontal diffusion rather than transport by the mean wind. In addition, the instantaneous wind w_0 may have large uncertainty for small pixels because the turbulence cannot be properly parameterised on the small scale of instantaneous plumes. The method is also vulnerable to systematic errors in the column enhancement retrieved over the source pixel (e.g., due to different reflectance properties of the emitter compared to the surrounding area) and errors in the local background estimate. Finally, it is only designed to infer emissions from a source that has been detected already, and cannot serve as an emissions mapping method.

Integrated mass enhancement method

The integrated mass enhancement method relates the emissions from a source to the total plume mass detected downwind of the source. Following Frankenberg et al. (2016), it is based on an empirical linear relationship the emissions of a source and its corresponding integrated mass enhancement. For an observed column plume comprising n_p pixels of dimension ℓ (the corresponding columns are denoted $(\Omega_i)_{1 \leq i \leq n_p}$), the latter is defined as $\ell^2 \sum_{i=1}^{n_p} \Omega_i$. Fundamentally, the relationship between the latter quantity and the emissions are calculated using the residence time τ of the pollutant in the detectable plume: $\mathcal{E} = \frac{1}{\tau} \ell^2 \sum_{i=1}^{n_p} \Omega_i$. One can express τ dimensionally in terms of an effective wind speed w_0 and a plume size L as $\tau = L/w_0$. The emissions are therefore derived as:

$$\mathcal{E} = \frac{w_0}{L}\ell^2 \sum_{i=1}^{n_p} \Omega_i \tag{2.26}$$

Here, w_0 and L would have simple physical meanings of wind speed and plume length if dissipation of the plume occurred by uniform transport to a terminal distance downwind of the source. But the actual mechanism for plume dissipation is turbulent diffusion, which takes place in all directions. w_0 and L must therefore be viewed as operational parameters to be related to observations of wind speed and plume extent. The detectable plume size L depends on the wind speed and total emissions, introducing non-linearity in Equation 2.26. Moreover, as this method has been designed for the estimation of methane emissions (Varon et al., 2018; Cusworth et al., 2020), it is less suitable for gases with shorter lifetimes, for which the uncertainty on the plume length is higher. Finally, this method suffers the same drawbacks as the source pixel method: it is designed to infer emissions from an identified source and cannot serve as a mapping method.

Constrained linear variational method

The constrained linear variational method[†] comes from the comparison between simulations of pollution NO_x levels in CTMs with a variety of in situ and satellite observations (Jaeglé et al., 2005; Lamsal et al., 2011; Zhu et al., 2021). This method relies on the fact that satellite observations of tropospheric NO_2 columns are strongly related to surface NO_x emissions due to the short NO_x lifetime combined with the high NO_2:NO_x ratio in the boundary layer. By using a chemistry transport model inferring NO_2 columns from NO_x emissions, two simulations can be conducted, one with NO_x emissions from a given year and another with perturbed NO_x emissions in order to establish the relationship between changes in surface NO_x emissions and changes in tropospheric NO_2 columns (Walker et al., 2010; Lamsal et al., 2011):

$$\frac{\Delta E}{E} = \gamma \frac{\Delta \Omega}{\Omega} \tag{2.27}$$

Here γ is a unitless trend factor that describes how a change in NO_x emissions changes the NO_2 columns. It reflects the feedback of NO_x emissions on NO_x chemistry. Using such a relationship and a reference period for NO_x emissions and NO_2 columns, the emissions from any period can be derived from the observations of NO_2 columns of the same period. This simple method, however, relies heavily on the CTM used to derive maps for the γ factor and on the reference period for emissions. It also assumes that relative variations of NO_2 columns vary linearly with respect to relative variations of NO_x emissions. Such a strong hypothesis is not verified for important variations due to non-linearities in NO_x chemistry. Nevertheless, this method presents the main advantage of inferring emissions without prior detection of emitters, allowing a large-scale mapping of the emissions.

Cross-sectional flux method

The cross-sectional flux method is described by Kuhlmann et al. (2021). It accounts for both the exponential decay of the observed species downwind the source and the observed Gaussian behaviour along each point of the streamline passing through the source. The plume is split into sub-polygons of about 5 km intervals in the downstream direction and the corresponding cross-section perpendicular to the wind direction is calculated with a Gaussian fit. The emissions of the sources are then derived from the integral of the cross-section. For short-lived gases, an exponentially decaying curve is fitted to the observed estimates. Since this method takes into account both the exponential decay of the species studied and its Gaussian spread, it is similar to the EMG method, except that this is done in two stages (unlike the EMG method, which uses a single fit function). The advantage of the cross-section flux method is that it provides a better representation of the cross-sectional structure of the plumes observed. On the other hand, it is more sensitive to variations along the plume. A light version of this

---

[†] The method does not seem to have a specific name in scientific literature: the term "constrained linear variational" has thus been coined here.

method exists with a technical difference. Following Zheng et al. (2020) and Chevallier et al. (2022), the Gaussian fitting procedure to compute line densities is applied to larger data slices centered on the enhancements and orthogonal to the wind direction. The emissions are then similarly computed as the product of the line densities by the effective wind speed. For short-lived gases, emissions obtained at the enhancements are multiplied by an exponentially decaying function of assumed lifetimes.

It is worth noting that the source pixel, integrated mass enhancement and cross-sectional flux methods have been widely used to infer emissions from instantaneous satellite observations, while the the exponentially-modified Gaussian, flux-divergence and the constrained linear variational methods were originally based on averaging NO_2 satellite data over long periods of time (Walker et al., 2010; Beirle et al., 2011, 2019). However, the latter can conceptually be applied on instantaneous satellite observations as well. Indeed, the previous generation of NO_2 observing satellites (e.g. SCIAMACHY and OMI), often requires averaging (via over-sampling) to improve the precision and the spatial resolution. On the other hand, emission estimation methods based on the analysis of individual emission plumes have been mostly applied to long-lived greenhouse gases such as carbon dioxide and methane, which do no require adjustment for the lifetime. The improved spatial resolution provided by TROPOMI now constitutes a basis to compare all these different methods.

2.3 Estimation of parameters

This section presents the datasets used to estimate the parameters involved in Equation 2.10 and Equation 2.16. These datasets are widely used in the studies that will be presented in the next chapter. Some of them were also used in the examples presented on Figure 2.5 and Figure 2.6.

2.3.1 ERA5

ERA5 is the fifth generation reanalysis dataset produced by the European Centre for Medium-Range Weather Forecasts (ECMWF) for climate and weather (Hersbach et al., 2020). This product is commonly used for plume analysis (Chevallier et al., 2020; Lange et al., 2021; Maasakkers et al., 2022; Lin et al., 2023). Hourly ERA5 data are gridded over 37 pressure levels from 1000 to 1 hPa. Pressure levels ranging from 1000 hPa to 850 hPa are used. The temporal resolution is one hour. The spatial resolution is $0.25° \times 0.25°$. The reanalysis is updated daily, with a maximum latency of 5 days for the production of the reanalysis (with corrections occurring up to 3 months later). The wind fields used are a temporal interpolation of the 2 closest reanalyses (that of the hour before and that of the hour after). To be used with the re-gridded TROPOMI NO_2 vertical column density maps, the hourly values of the dataset have been linearly interpolated to the Sentinel-5P orbit timestamp and re-gridded to a lower resolution ($0.0625° \times 0.0625°$ or $0.1° \times 0.1°$, depending on the study).

The ERA5 data can be compared to other datasets to analyse the mean trends in wind direction. For instance, the previous generation of reanalysis dataset, ERA-Interim, can be used (Berrisford et al., 2009). The Modern-Era Retrospective analysis for Research and Applications, version 2 (MERRA-2), produced by the NASA Global Modeling and Assimilation Office, can also be used (Bosilovich et al., 2015). Those two datasets have coarser resolutions ($0.75° \times 0.75°$ and $0.625° \times 0.5°$ respectively). The horizontal resolution is the most limiting aspect of the wind products, especially in areas with high topography for which the mean wind can vary on horizontal scales lower than the average size of a TROPOMI pixel. In the EMME region, this limitation concerns mountainous countries, such as Iran, Lebanon or Türkiye.

2.3.2 CAMS

The Copernicus Atmospheric Monitoring Service (CAMS) global near-real-time service provides analyses and forecasts for reactive gases, greenhouse gases and aerosols. Data is gridded on 25 vertical pressure levels with a horizontal resolution of 0.4°×0.4° and a temporal resolution of 3 hours (Huijnen et al., 2019). From this dataset, we use:

- The OH concentration, for the calculation of the sink term (Equation 2.16).
- The temperature, for the calculation of the kinetic constant of the reaction between NO_2 and OH (Equation 2.16).
- The planetary boundary layer height, which is used as the scale along which other parameters are vertically averaged. This parameter does not appear directly in the equations.
- NO and NO_2 concentrations, used to calculate the ratio between NO_x and NO_2 through the Leighton relationship (Equation 1.9).

To be used with re-gridded TROPOMI NO_2 vertical column density maps, the hourly values of the dataset have been linearly interpolated to the Sentinel-5P orbit timestamp and re-gridded to a lower resolution (0.0625°×0.0625° or 0.1°×0.1°, depending on the study).

The flux-divergence method having been presented in detail, the following chapter presents the results of applying this method to the EMME region in order to determine its potential, but also its limitations. Three case studies are carried out for Egypt, Qatar and Cyprus. The results are analysed in terms of trends, sectors of activity, and more generally in terms of the specific socio-economic drivers of the region, with a particular emphasis on characterising emissions from megacities and power plants, as well as their annual and weekly variations.

Chapter 3

Results - NO_x emissions in the EMME region

This chapter presents the application of the flux divergence method on three different countries of the EMME region: Egypt, Qatar and Cyprus. The three studies resulted in the publication/submission of articles in peer-reviewed journals. They highlight a progressive improvement of the method. The results were compared with inventories and/or reported emissions to evaluate the relevance of the model. The chapter also includes a last section that presents an overview of the NO_x emissions in the EMME region and the applicability limits of the flux-divergence scheme with TROPOMI observations.

3.1 Estimation of NO_x emissions in Egypt with the flux-divergence method

3.1.1 Presentation of the article

This article on NO_x emissions in Egypt was the most important step in the development of the flux-divergence method. Initially, the resolution used for the re-gridding of the TROPOMI data was 0.1°×0.1°, which made co-localisation with other datasets (CAMS, ERA5) easier to implement. Here, the NO_2 background was processed after calculation of emissions using a mask. Such a background estimation has advantages and disadvantages compared to a background calculated directly from concentrations, and the reviews received after first submission of the article later led to prefer a concentration-based background. In this article, a comparison was made between the NO_2 lifetime estimated by the formula of Burkholder et al. (2020) and that derived from the method of comparing a plume with an EMG function fit, with the aim of verifying the reliability of the CAMS NRT forecast data over the EMME region. Although the correlation between the two quantities was low, the comparison provided sufficient agreements to consider the OH product from CAMS reliable in the EMME region. This study also includes a vertical sensitivity test. By evaluating emissions using parameters (wind and OH, NO and NO_2 concentrations) estimated close to the ground or at higher altitudes, it was shown that the flux-divergence model is sensitive to vertical variations. This highlights the importance of the a priori NO_2 vertical distribution within the TROPOMI columns product when estimating NO_x emissions. Finally, this study is, within the thesis, a first comparison between emissions estimated by remote sensing and inventory emissions. However, this study does not include any in-depth sectoral analysis: due to the particular nature of Egypt, which is a country where the large majority of the industrial facilities, as well as human settlements, are located in the narrow region of the Nile, emissions from different sectors overlap most of the time. The extreme behaviours of point source and diffuse emitters, highlighted in Figure 2.4, cannot be characterised here.

This article has been published under the name "**Quantifying NO_x emissions in Egypt using TROPOMI observations**" on September 7th 2022 in the journal Atmospheric Chemistry and Physics (ACP) from the editor Copernicus of the European Geosciences Union (EGU). Authors that participated to this work are **Anthony Rey-Pommier** (LSCE, The Cyprus Institute), Frédéric Chevallier

(LSCE), Philippe Ciais (LSCE, The Cyprus Institute), Grégoire Broquet (LSCE), Theodoros Christoudias (The Cyprus Institute), Jonilda Kushta (The Cyprus Institute), Didier Hauglustaine (LSCE) and Jean Sciare (The Cyprus Institute). The article can be accessed at: `https://acp.copernicus.org/articles/22/11505/2022/acp-22-11505-2022.html`.

The results of this study have been presented at the 2nd international conference on Climate Change in the Mediterranean and Middle East (October 2021, Nicosia, Cyprus), at the Climate and atmosphere research and innovation in the Eastern Mediterranean and Middle East workshop (November 2022, Nicosia, Cyprus), and at the EGU General Assembly 2023 (April 2023, Vienna, Austria). Figures, numbering of subsections and notations appearing in the following Section have been slightly modified in order to be consistent with the rest of this document. On figures, such changes only concern colorbars and dataset names. To be consistent with other articles, NO_x emissions have also been expressed in mass terms as NO_2 (rather than in NO in the original article).

3.1.2 Abstract

Urban areas and industrial facilities, which concentrate the majority of human activity and industrial production, are major sources of air pollutants, with serious implications for human health and global climate. For most of these pollutants, emission inventories are often highly uncertain, especially in developing countries. Spaceborne measurements from the TROPOMI instrument, onboard the Sentinel-5P satellite, are used to retrieve nitrogen dioxide (NO_2) column densities at high spatial resolution. Here, we use two years of TROPOMI retrievals to map nitrogen oxides ($NO_x = NO + NO_2$) emissions in Egypt with a top-down approach using the continuity equation in steady state. Emissions are expressed as the sum of a transport term and a sink term representing the three-body reaction comprising NO_2 and hydroxyl radical (OH). This sink term requires information on the lifetime of NO_2, which is calculated with the use of the CAMS near-real-time temperature and OH concentration fields. We compare this derived lifetime with the lifetime inferred from the fitting of NO_2 line density profiles in large plumes with an exponentially modified Gaussian function. This comparison, which is conducted for different samples of NO_2 patterns above the city of Riyadh, provides information on the reliability of the CAMS near-real-time OH concentration fields; it also provides some hint on the vertical levels that best represent typical pollution sources in industrial areas and megacities in the Middle East region. In Egypt, total emissions of NO_x are dominated by the sink term, but they can be locally dominated by wind transport, especially along the Nile where human activities are concentrated. Megacities and industrial regions clearly appear as the largest sources of NO_x emissions in the country. Our top-down model infers emissions with a marked annual variability. By looking at the spatial distribution of emissions at the scale of different cities with different industrial characteristics, it appears that this variability is consistent with national electricity consumption. We detect lower emissions on Fridays, which are inherent to the social norm of the country, and quantify the drop in emissions in 2020 due to the COVID-19 pandemic. Overall, our estimations of NO_x emissions for Egypt are 7.0% higher than the CAMS-GLOB-ANT_v4.2 inventory, and significantly differ in terms of seasonality.

3.1.3 Introduction

Economic growth in developing countries has led to a strong increase of urban air pollution (Baklanov et al., 2016). Among the different pollutants, nitrogen oxides are key species. They are generally the products of fuel combustion, such as the burning of hydrocarbons in the air at high temperature. The main sources of these compounds are vehicle engines, but also heavy industrial facilities such as power plants, iron and steel mills (Tang et al., 2020) and cement kilns (Kim et al., 2020a). Their accumulation in the lowest layers of the troposphere contributes to the formation of smog and acid rain (Singh, Agrawal, 2007). They also have a significant effect on human health, as they can cause various respiratory diseases (EPA, 2016). To deal with these phenomena, national and regional governments generally enact a series of air pollution control strategies, which typically take the form of bans on certain polluting technologies, with the aim of reducing the concentration of pollutants at the local level to targets that must be achieved within a given timeframe. These strategies, which also help driving technological innovation, have had a significant effect in Europe (Crippa et al., 2016).

In Egypt, population growth, urbanisation, socio-economic development and the associated increase in the vehicle fleet led to a major degradation of air quality in the last decades, especially in highly populated areas such as Greater Cairo and the Nile Delta (El-Magd et al., 2020) which gather the majority of the population. The Ministry of State for the Environment has thus initiated new policies that aim to reduce pollution levels throughout the country, through technical mitigation of emissions, emission standards for vehicles and intersectoral collaboration (UNEP, 2015). However, Egypt, like most developing countries, lacks the local infrastructure to access detailed information on technical factors such as energy consumption or fuel type and technology, leading to discrepancies in inventories (Xue, Ren, 2012). As a consequence, the monitoring of emissions, which is important to evaluate the effects of air pollution control policies, is of limited reliability.

To overcome the uncertainties in the emission inventories, the use of independent observations systems is becoming increasingly prevalent. In this study, we investigate the use of satellite remote sensing of atmospheric concentrations to improve the quantification of NO_x emissions in Egypt. Spectrally resolved satellite measurements of solar backscattered radiation enable the quantification of NO_2 and other trace gases absorbing in the ultraviolet and visible spectral ranges based on their characteristic spectral absorption patterns. Tropospheric vertical column densities, i.e. vertically integrated NO_2 concentrations in the troposphere, have been providing information on the spatial distribution of tropospheric NO_2 at global scale for nearly 30 years, allowing the identification of different sources of NO_x and the quantification of the associated emissions (Leue et al., 2001; Martin et al., 2003; Mijling, Van Der A, 2012; de Foy et al., 2015; Goldberg et al., 2019b; Beirle et al., 2019; Lorente et al., 2019; Lange et al., 2021). In October 2017, the Sentinel-5P satellite was launched. Its main instrument is the TROPOspheric Monitoring Instrument (TROPOMI), which provides tropospheric NO_2 column densities at high spatial resolution with a large swath width and with a daily frequency (Veefkind et al., 2012). By applying the steady-state continuity equation (Beirle et al., 2019; Lama et al., 2020), it is possible to build a top-down model that directly quantifies NO_x emissions from these NO_2 column densities, provided that some key parameters (wind, temperature, hydroxyl radical concentration and concentration ratio between NO_x and NO_2) are correctly estimated. This model is used to quantify the anthropogenic NO_x emissions in Egypt for a 2-year period, from November 2018 to November 2020.

This paper is organised as follows: Section 3.1.4 provides a description of the datasets used in this study. Section 3.1.5 explains the build-up and the limits of the top-down approach used to quantify NO_x emissions in Egypt. It also presents a method for validating the model parameters by using NO_2 line density profiles over Riyadh, Saudi Arabia. Section 3.1.6 presents the analysis of this validation method. It presents the location of the main NO_x sources in Egypt and evaluates the vertical sensitivity of the model. It also assesses the ability of the model to show less human activity on Fridays and during the lockdown that took place during the COVID-19 pandemic. It finally confronts the inferred emissions with different inventories in terms of amplitude and seasonality. Section 3.1.7 presents our conclusion and general remarks.

3.1.4 Instrumentation and data

3.1.4-A TROPOMI NO_2 retrievals

The TROPOspheric Atmosphere Monitoring Instrument (TROPOMI), onboard the European Space Agency's (ESA) Sentinel-5P (S-5P) satellite, provides measurements for atmospheric composition. TROPOMI is a spectrometer observing wavelengths in the infrared, visible and ultraviolet light at around 13:30 local time. The UV-Vis spectral band at 405-465 nm is used to retrieve NO_2. Other spectral bands are used to observe methane, formaldehyde, sulphur dioxide, carbon monoxide and ozone, as well as aerosols and cloud physical properties. The very high spatial resolution offered by TROPOMI (originally 3.5×7 km^2 at nadir, improved to 3.5×5.5 km^2 since 6 August 2019) provides unprecedented information on tropospheric NO_2. Its large swath width (~ 2600 km) makes it possible to construct NO_2 images on large spatial scales. Those images greatly improve the potential for detecting highly localised pollution plumes above the ground, identifying small-scale emission sources but also estimating emissions from megacities, industrial facilities and biomass burning. We use TROPOMI NO_2 retrievals (L2 data, OFFL stream, product version 1.0.0 and 1.1.0 successively) from November 2018 to November 2020 over Egypt. We also use them over Saudi Arabia, and more specifically over the city of Riyadh, to evaluate the reliability of other parameters. This will be explained in Section 3.1.6-A Both countries have an arid climate, which offers a large number of clear-sky days throughout the year, enabling the calculation of monthly averages based on more than 20 observations. They are also the host to many large plumes of pollutants due to high human concentrations along rivers and around megacities, which allows us to observe high NO_2 concentration patterns with a high signal-to-noise ratio. TROPOMI products provide a quality assurance value q_a, which ranges from 0 (no data) to 1 (high-quality data). For our analysis of concentrations, we selected NO_2 retrievals with q_a values greater than 0.75, which systematically correspond to clear-sky conditions (Eskes et al., 2019b). TROPOMI soundings are gridded at a spatial resolution of $0.1° \times 0.1°$ with daily coverage. This resolution is lower than that of the instrument; the gridding thus provides a grid for which most NO_2 columns correspond to one or more measurements. The observed plumes remain correctly resolved. Cells without measurements are infrequent, which facilitates the calculation of derivatives.

3.1.4-B Wind data

The horizontal wind $\vec{w} = (w_x, w_y)$ is taken from the European Centre for Medium-Range Weather Forecasts (ECMWF) ERA5 data archive (fifth generation of atmospheric reanalyses) at a horizontal resolution of $0.25°\times0.25°$ on 37 pressure levels (Hersbach et al., 2020). The hourly values have been linearly interpolated to the TROPOMI orbit timestamp and re-gridded to a $0.1°\times0.1°$ resolution.

3.1.4-C CAMS real-time fields

The Copernicus Atmospheric Monitoring Service (CAMS) global near-real-time service provides analyses and forecasts for reactive gases, greenhouse gases and aerosols on 25 pressure levels with a horizontal resolution of $0.4°\times0.4°$ and a temporal resolution of 3 hours (Huijnen et al., 2016). For the calculation of NO_x emissions from TROPOMI observations, we use CAMS concentration fields of nitrogen oxides (NO and NO_2) and hydroxyl radical (OH). We also use the CAMS temperature field T. NO and NO_2 concentrations are used to account for chemical processes that take place in polluted air. Anthropogenic activities produce mainly NO, which is transformed into NO_2 by reaction with ozone O_3. NO_2 is then photolyzed during the day, reforming NO (Seinfeld, 1989). This photochemical equilibrium between NO and NO_2 can be highlighted with the NO_x:NO_2 concentration ratio, whose value depends on local conditions, allowing to perform a conversion from NO_2 production to NO_x emissions. The reason for the use of OH is different. OH is the main oxidant that controls the ability of the atmosphere to remove pollutants such as NO_2 (Logan et al., 1981). It is mainly produced during daylight hours by interaction between water and atomic oxygen produced by ozone dissociation (Levy, 1971). In air that is directly influenced by pollution, another source of OH is due to a reaction between NO and HO_2. This reaction, referred to as the NO_x recycling mechanism, illustrates the nonlinear dependence of the OH concentration on NO_2 (Valin et al., 2011; Lelieveld et al., 2016). Since the OH lifetime is typically of less than a second, its concentration in the troposphere is very low and difficult to measure. As a consequence, global analyses, which estimate OH concentrations from other variable species (Li et al., 2018; Wolfe et al., 2019), provide a representation for OH concentrations with high associated uncertainties. Therefore, the CAMS OH concentrations are used here to account for the

NO_2 oxidation to form nitric acid (HNO_3), whose representation is explained in Section 3.1.5-A Finally, the temperature field is used to control variations in the kinetic parameters (Burkholder et al., 2020). The hourly values are also linearly interpolated to the TROPOMI orbit timestamp and re-gridded to a 0.1°×0.1° resolution.

3.1.4-D Background removal

Detecting traces of anthropogenic emissions in TROPOMI NO_2 images is not a straightforward process. The NO_2 signal from a sparsely populated area or a small industrial facility may be covered by numerical noise or by the signal generated by natural NO_x emissions. In the absence of anthropogenic sources, TROPOMI observes NO_2 concentrations which constitute a tropospheric background of $\sim 0.5\times10^{15}$ molecules.cm^{-2}. At the global scale, this background is the result of different sources. In the lower troposphere, natural NO_x emissions are mostly due to fires and soil emissions (Yienger, Levy, 1995; Hoelzemann et al., 2004). In the upper troposphere however, sources include lightning, convective injection and downwelling from the stratosphere (Ehhalt et al., 1992), but the factors controlling the resulting concentrations are poorly understood. According to state-of-art estimates, anthropogenic NO_x accounts for most of the emissions at the global scale, whereas natural emissions from fires, soils and lightning are less significant at the global scale and do not exceed a share of 35% combined (Jaeglé et al., 2005; Müller, Stavrakou, 2005), although associated errors can be very high. In eastern China, the non-anthropogenic share of total NO_x emissions is variable but does not exceed 20% (Lin, 2012). Egypt being a desertic region and not very conductive to lightning, we expect the share of those non-anthropogenic emissions to be smaller. To estimate anthropogenic NO_x emissions, it is therefore necessary to remove this share.

With an atmospheric lifetime of about a few hours, the presence of NO_2 is relatively short. Consequently, the majority of NO_2 is not transported far downwind from its sources. Thus, near-surface NO_2 concentrations are generally high over industrial facilities and densely populated areas that need to be identified. Because Egypt's population is almost entirely located along the Nile River and its delta, the study of NO_x emissions in this country cannot therefore be reduced to the study of a small number of point sources, as it would be the case for several other parts of the Middle East region, and must be carried out in the form of a mapping of the country. Further discussion is provided in Section 3.1.4-D. To identify urban areas in Egypt, we use the Socioeconomic Data and Applications Center (SEDAC) GRUMP (Global Rural-Urban Mapping Project) data archive, which comprises eight global datasets, including a population density grid provided at a resolution of 30 arc seconds, with population estimates normalised for the year 2000 (CIESIN, 2019). We combine this database with field data giving the location of industrial facilities from energy-intensive industries in the region (data have been retrieved from the Global Energy Observatory for oil and gas-fired power plants, from IndustryAbout for aluminium and iron smelters, from the work of Elvidge et al. (2016) for flaring sites, and from the work of Steven J. Davis and Dan Tong for cement plants; links at the end of this article).

These datasets are used to remove the non-anthropogenic part of the NO_x emissions signal. We conduct this removal by subtracting the mean emissions over areas without human activity from the mean emissions over industrial and densely populated areas. In order to perform this distinction between these two types of areas, our study is carried out using a mask within a 0.1°×0.1° grid. A grid cell is considered to be part of the mask if it has a population density higher than a threshold of 100 hab.km^{-2}, or if its centre is close to an industrial facility. Otherwise, the cell is considered to be part of the "background", i.e. outside the mask. In order to avoid any smearing that would correspond to abnormally high emissions outside urban and industrial centres (which can happen if the wind is poorly estimated), transition cells (in the immediate vicinity of the mentioned mask cells) are also considered to be mask cells. Figure 3.1 shows the distinction between mask cells and background cells on our domain in Egypt that lies between parallels 23°N and 32°N and meridians 29°E and 34°E. Most of the mask cells are located in the Nile area. Some mask cells are also found on the coast or in isolated parts in the desert. They correspond to remote industrial facilities, including major flaring sites, or sparsely populated industrial centres such as Ain Sokhna's industrial area. The domain comprises $n_m = 949$ mask cells and $n_b = 3692$ background cells. The mathematical description of the background removal is outlined in Section 3.1.5-D.

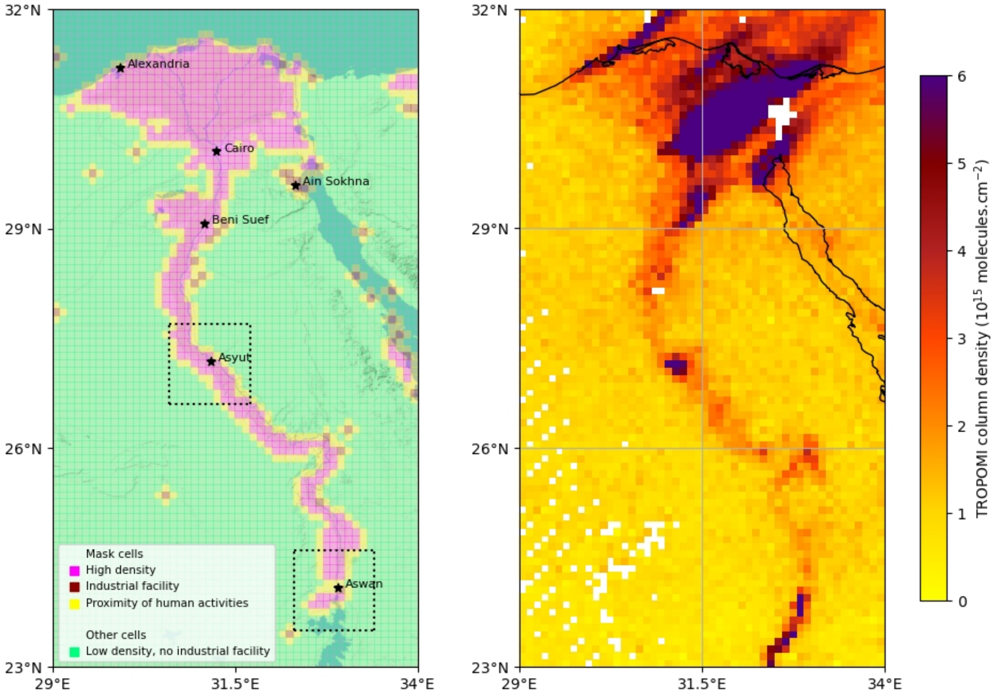

Figure 3.1: (left) Part of Egypt centered on Nile River. Within this domain, pink cells represent locations with an average human density above 100 hab.km^{-2}, brown cells represent locations with industrial facilities outside cities, and yellow cells represent locations in their vicinity. These cells constitute the mask used to calculate anthropogenic emissions. Outside this mask, green cells represent areas which do not correspond to any of the three criteria, considered to be void of human activity. Five larges cities in the country and the industrial area of Ain Sokhna are denoted with stars. Two smaller domains centered around the cities of Asyut and Aswan are represented with dotted lines; their use is presented in Section 3.1.6-F. (right) TROPOMI observation of NO_2 slant column densities above Nile valley on 3 January 2019. White pixels correspond to areas with low quality data ($q_a < 0.75$) or no data.

3.1.4-E Emission inventories

We compare TROPOMI-derived NO_x emissions to the Emissions Database for Global Atmospheric Research (EDGARv5.0) for 2020 and the CAMS global anthropogenic (CAMS-GLOB-ANT_v4.2) emissions inventory released in 2020. Both datasets provide 0.1°×0.1° gridded emissions for different sectors on a monthly basis. EDGARv5.0 emissions are based on activity data (population, energy production, fossil fuel extraction, industrial processes, agricultural statistics, etc.) derived from the International Energy Agency (IEA) and the Food and Agriculture Organization (FAO), corresponding emission factors, national and regional information on technology mix data and end-of-pipe measurements. The inventory covers the years 1970-2015 and differs from the previous version EDGARv4.3.2 which does not use splitting factors derived from the Energy Information Administration (EIA) data on fuel consumption of coal, oil and natural gas for specific countries (Crippa et al., 2020). CAMS-GLOB-ANT_v4.2 is developed within the framework of the Copernicus Atmospheric Monitoring Service (Granier et al., 2019). For this inventory, NO_x emissions are based on various existing sectors in the EDGARv4.3.2 emissions from 2000-2012 which are used as a basis for 2010 emissions and are extrapolated to the current year using 2011-2014 sector-based trends from the Community Emissions Data System (CEDS) inventory (Hoesly et al., 2018). From one inventory to another, the names and definitions of the sectors may vary. In EDGARv5.0 and CAMS-GLOB-ANT_v4.2, the emissions for a given country are derived from the type of technologies used, the dependence of emission factors on fuel type, combustion conditions, as well as activity data and low resolution emission factors (Janssens-Maenhout et al., 2019).

3.1.5 Method

3.1.5-A Calculation of NO_2 production from TROPOMI observations

As a first step, we use tropospheric NO_2 vertical column densities Ω_{NO_2} to derive top-down NO_2 production maps. Vertical column densities Ω_{NO_2} are obtained from TROPOMI slant column densities using an air mass factor (AMF) which is also provided by TROPOMI. Previous studies have shown that the use of the AMF is a source of structural uncertainty in NO_2 retrievals (Boersma et al., 2004; Lorente et al., 2017). In polluted environments, this source of uncertainty becomes non-negligible. Here, the AMF does not vary much temporally throughout the studied period, and is around 1.6 for mask cells and around 1.9 for background cells. The difference between the two types of cells is probably due to a different albedo between the urban environment and desert areas. Using the horizontal wind $\vec{w}$, the NO_2 flux is given as $\Omega\vec{w}$. The divergence of this flux can be added to the local time derivative $\frac{\partial \Omega}{\partial t}$ to balance NO_2 sources E_{NO_2} and sinks S according to the continuity equation:

$$\frac{\partial \Omega}{\partial t} + \mathrm{div}(\Omega\vec{w}) = E_{NO_2} - S \tag{3.1}$$

In steady state, the time derivative disappears and the mass balance is reduced to three terms. The NO_2 production can thus be estimated by taking the combined effect of atmospheric transport losses and the different sinks. For the transport term, we calculate numerical derivatives with a fourth-order central-finite difference scheme for each cell of the domain. Moreover, since the local overpass time of TROPOMI occurs is in the middle of the day, NO_2 losses are largely dominated by the three-body reaction involving NO_2 and OH (Seinfeld, 1989). Two channels have been identified for this reaction (Burkholder et al., 2020), leading to the production of nitric acid HNO_3 and pernitrous acid HOONO (Equation 1.13 and Equation 1.14):

$$\mathrm{NO_2 + OH + M \rightarrow HNO_3 + M} \tag{3.2}$$

$$\mathrm{NO_2 + OH + M \rightarrow HOONO + M} \tag{3.3}$$

For the OH concentrations that are considered in this region ($1-20\times10^6$ molecules.cm^{-3}), the reactions above follow first order kinetics. The total sink term can therefore be calculated as $S = \Omega_{NO_2}/\tau$ with:

$$\tau = \frac{1}{k_{\mathrm{mean}}(T, [\mathrm{M}])[\mathrm{OH}]} \tag{3.4}$$

τ appears here as the characteristic mixed lifetime of NO_2 in the atmosphere. The reaction rate k_{mean} characterises the reactions between NO_2 and OH and depends on atmospheric conditions. (Burkholder et al., 2020) provide a general expression of this rate as a function of both temperature T and total air concentration [M]. Note that HOONO can be rapidly decomposed back to NO_2 and OH in the lower troposphere. We assume here that this decomposition is slow and does not affect the NO_2 horizontal gradients. Both pathways are therefore taken into account, and the value of k_{mean} represent the total loss of NO_2 due to OH, with a contribution of the HOONO forming reaction between 5 to 15% under atmospheric conditions (Sander et al., 2011; Nault et al., 2016). Thus, the NO_2 production can be calculated as the sum of a transport term and a sink term:

$$E_{NO_2} = \mathrm{div}(\Omega\vec{w}) + \Omega/\tau \tag{3.5}$$

The treatment for NO_x removal is simplified here. NO_x concentrations are influenced by other sinks. (Stavrakou et al., 2013) showed that the reaction between NO_2 and OH forming HNO_3 accounted for most of total NO_x loss at the global scale, but with high uncertainties associated with other sinks. Here, the features of the climate in Egypt during daytime hinder many processes to have a significant effect. The following NO_x sinks, which can be of notable importance at the global scale, are not taken into account here:

- NO_2 deposition through the leaf stomata of vegetation. This sink can be significant in forested areas. In Egypt, the leaf area index is very low, except in the croplands of the Nile Delta where it is comparable to that of southern Europe or the western United States (Fang et al., 2019), for which the corresponding lifetime was of about 10-100 h (Delaria et al., 2020), i.e. about an order of magnitude larger than the lifetimes calculated here. To our knowledge, there are no studies focusing on the corresponding lifetimes for croplands, and we therefore do not take this sink into account.

- NO_x oxidation by organic radicals to produce alkyl and multifunctional nitrates (Sobanski et al., 2017). This sink increases with the concentration of volatile organic compounds (VOC), whose presence cannot be excluded in Egypt. Different models have estimated low biogenic isoprene emissions in the region (Wiedinmyer et al., 2006; Guenther et al., 2006). These emissions are concentrated around the Nile River and its delta, and do not exceed 15 $mg.m^{-2}.day^{-1}$. They are certainly noticeable and higher in summer than in winter, and contrast with the rest of the country, but they remain low compared to other regions in the world. They are, for instance, about an order of magnitude lower than in the forested areas of the eastern US, where the corresponding sink accounts for between 30% and 60% of the total NO_x sink (Romer Present et al., 2020). Furthermore, at large NO_2 concentrations (compared to VOC concentrations), the share of this sink in the total NO_x loss is weakened compared to that of HNO_3 (Romer Present et al., 2020). The effect of biogenic emissions of VOC can therefore be considered minor. However, VOC emissions can also be of anthropogenic origin, especially in urban areas, where they are difficult to estimate. To our knowledge, there is no study evaluating the competition of the two sinks in Egypt or in a region with similar features and we therefore do not account for this reaction in our calculations.

- NO reaction with HO_2 to produce nitric acid (Butkovskaya et al., 2005), whose yield is strongly enhanced in presence of water vapour (Butkovskaya et al., 2009). Here, we neglect this reaction as the corresponding reaction rate is lower by a factor 3 to 8 in dry conditions (Butkovskaya et al., 2005).

- NO conversion to NO_3, the latter being in thermal equilibrium with NO_2 and N_2O_5. This sink, which takes place via heterogeneous processes, has a significant contribution during nighttime in the Mediterranean region (Friedrich et al., 2021), is neglected at 13:30 when OH is close to its daily maximum.

- NO_2 reversible reaction with peroxyacetyl radical to produce peroxyacetylnitrate (Moxim et al., 1996). In the Nile Delta region, PAN concentrations in the lower troposphere are significantly below the global average (Fischer et al., 2014), possibly due to high temperatures favoring short PAN lifetimes. Moreover, its production peaks in the late afternoon and early evening (Seinfeld, 1989). We therefore do not consider this sink in the representation of NO_x emissions at 13:30.

- NO_2 uptake onto black carbon particles (Longfellow et al., 1999). This uptake is of limited amount in the Mediterranean region (Friedrich et al., 2021).

All these processes not being accounted for, the reaction between NO_2 and OH is the only sink that is considered in our calculations to provide an indication of NO_x emissions. Section 3.1.6-G details the consequences of not considering these various minor sinks on the results.

3.1.5-B Interpolation to daily average emissions

All parameters are evaluated at 13:30 local time, which means that the NO_2 production is calculated at the same moment. In Egypt, the maximum and minimum electricity consumption are reached around 20:00 and 6:00 local time respectively, and inter-daily consumption differences have been weakened by the increasing sales of air conditioning and ventilation systems in the past decades (Attia et al., 2012). The daily load profiles provided by the National Egyptian Electricity Holding Company show that the mean daily electricity consumption corresponds approximately to the consumption at 13:30 in the country (EEHC, 2021). The difference between the two quantities being small both in summer (about +2 to -3%) and winter (about -2 to -6%), we consider our inferred emissions as representative of the average activity in Egypt at any time of the year. This assumes that electricity consumption dominates the emissions of the country, or that the other emitting sectors have a similar daily profile. This can be justified. According to CAMS-GLOB-ANT_v4.2, the power sector accounts for 50 to 60% of total NO_x emissions in Egypt. EDGARv5.0 presents a lower share (40 to 45% of total emissions). Moreover, for both inventories, the transport sector accounts for the majority of the remaining emissions. According to the traffic congestion index in Cairo (`https://www.tomtom.com/en_gb/traffic-index/cairo-traffic/`), the congestion level around 13:30 seems to be slightly higher than during the morning peak, but lower than the during night peak. Traffic emissions at this moment of the day could therefore be representative of the average traffic emissions as well.

3.1.5-C Validation of CAMS OH concentration using line density calculations for Riyadh

When the transport term is integrated over large spatial scales, it cancels out due to the mass balance in the continuity equation between NO_2 sources and NO_2 sinks. At first order, the integration of the inferred emissions over the whole domain (of about 490,000 km^2) thus reflects chemical losses of the sink term. In this term, the NO_2 lifetime calculation involves the reaction rate k_{mean}, whose annual variability is low due to small changes in Egyptian midday temperatures throughout the year, and OH concentration, whose annual variability is highly marked. In Egypt, tropospheric OH concentrations, which are strongly correlated with solar ultraviolet radiation (Rohrer, Berresheim, 2006) and NO_x emissions, are higher in summer than in winter. To ensure an appropriate representation of the OH field by CAMS data, we select a large number of TROPOMI images characterised by a homogeneous wind field, in which we calculate the NO_2 lifetime according to Equation (3.11), where [OH] corresponds to the near-real-time CAMS data and k_{mean} is calculated with the formula from Burkholder et al. (2020). We compare this value with the lifetime determined by a method initially developed by Beirle et al. (2011), and expanded by Valin et al. (2013) by introducing a rotation of the image to refine the chemical lifetime. This method consists in fitting an exponentially modified Gaussian function (EMG) to NO_2 line density profiles. These profiles correspond to the integrated NO_2 columns along the mean wind direction in the pollution pattern and centered around the source. They are obtained by rotating TROPOMI images in the mean wind direction and using the values of the nearest columns in a 100 km^2 area. Line density profiles are generated on a span of 300 km. An example is given in Figure 3.3. Within the average profile, the NO_2 burden and lifetime can be derived from the parameters that describe the best statistical fit. The EMG model is expressed as follows (Lange et al., 2021):

$$\omega(\xi|\beta,\mathcal{N},\xi_0,\mu,\sigma) = \beta + \frac{\mathcal{N}}{2\xi_0}\exp\left(\frac{\mu-\xi}{\xi_0}+\frac{\sigma^2}{2\xi_0^2}\right)\operatorname{erfc}\left(-\frac{1}{\sqrt{2}}\left(\frac{\xi-\mu}{\sigma}-\frac{\sigma}{\xi_0}\right)\right) \tag{3.6}$$

Here, ξ is the distance in the downwind-upwind direction, β is the NO_2 background, $\mathcal{N}$ is the total number of NO_2 molecules observed in the vicinity of the point source, ξ_0 is the e-folding distance downwind, representing the exponential length scale of NO_2 decay, μ is the location of the apparent source relative to the centre of the point source, and σ is the standard deviation of the Gaussian function, representing the length scale of Gaussian smoothing. Using a non-linear least squares fit, we estimate the five unknown parameters: $\mathcal{N}$, β, ξ_0, μ and σ. From the mean wind module w_0 in the domain, the mean effective NO_2 lifetime τ_{fit} can be estimated using the fitted parameters:

$$\tau_{\text{fit}} = \frac{\xi_0}{w_0} \tag{3.7}$$

The geography of Egypt does not suit the method described here. The Egyptian population is contiguously concentrated along the Nile, which makes it difficult to define point sources isolated from human activity. Furthermore, large isolated cities such as Alexandria or Suez are too close to the coast for the wind to be considered homogeneous. We therefore use the city of Riyadh, Saudi Arabia (24.684°N, 46.720°E) to perform the comparison between the CAMS-induced lifetime and the fit-obtained lifetime. Riyadh has been the focus of anterior studies (Valin et al., 2013; Beirle et al., 2019), and is particularly suitable for several reasons. Firstly, Riyadh is a city within the latitudinal extend of Egypt (1600 km from Cairo) with a climate which is similar to the typical Egyptian climate. Secondly, NO$_2$ tropospheric columns over Riyadh are high ($\sim 9{\times}10^{15}$ molecules.cm^{-2}), leading to retrievals with a high signal-to-noise ratio. Thirdly, Riyadh is far from the coast, and its flat terrain makes the surrounding wind fields rather homogeneous during most of the year.

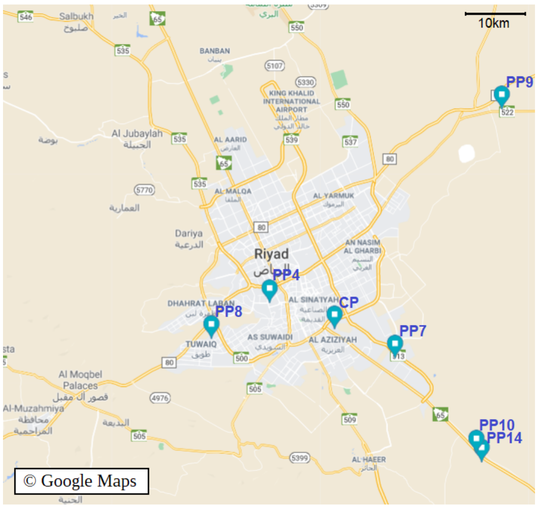

Figure 3.2: Map of Riyadh's city centre with the surrounding power plants (PP4, 7, 8, 9, 10 and 14) and cement plant (CP). The map has been extracted from © Google Maps.

As the fitting algorithm is very sensitive to any disturbance that might be induced by NO$_2$ production from other point sources, it is necessary to identify heavy industrial facilities in the area. Riyadh is also an industrial area, with several power plants located close to the city centre. Figure 3.2 shows the location of the most important emitters in the region, which include five gas-fired power plants (PP7, PP8, PP9, PP10 and PP14), one oil-fired power plant (PP4) and one cement plant (CP). The five gas power plants, with a total capacity of more than 10 GW, are located in the periphery of the city. These power plants are sufficiently far away from the city centre for TROPOMI to distinguish their own emissions from those of Riyadh's centre with a resolution of 0.1°×0.1°, which is not the case for CP and PP4 which are located in the city centre. It is therefore appropriate to restrict the study of NO$_2$ patterns over Riyadh to days for which the emissions from the city centre and those from the gas power plants do not overlap. This is the case when the wind blows steadily and homogeneously in a north-south direction. Within about 150 km around the city centre, we thus calculate the average wind given by ERA5 and consider the observation as reliable if the mean angle $\langle\alpha\rangle$ of the observations deviates by less than 40° from the north or the south, with a standard deviation σ_α of less than 36°. This condition generally leads to a selection of observations with large wind speeds, low winds speeds being often associated with more variable directions. This ensures the NO$_2$ decay to be dominated by chemical removal and not by the variability of the wind (Valin et al., 2013). Finally, we select observations with clear-sky conditions downstream of the flow (with at least 80% downstream cells with $q_a > 0.75$).

Our 0.1°×0.1° gridding ensures that retrieved lifetimes are governed by physical decay of NO_2 and not an artifact of the spatial resolution (Valin et al., 2011). The fitting procedure is very sensitive to the wind direction. Instead of manually correcting the ERA5 wind field for individual NO_2 patterns, the curve fitting is performed for every sample with three different rotation angles, corresponding to the wind direction with a correction of $-10°$, $0°$ or $10°$. A record is kept if one of these three fits leads to a correlation with the corresponding NO_2 line density whose coefficient is greater than 0.97. Among the remaining samples, we keep those with a value of τ_{fit} greater than 1.0 h (considered sufficiently high to be relevant). An example of curve fitting is given in Figure 3.3.

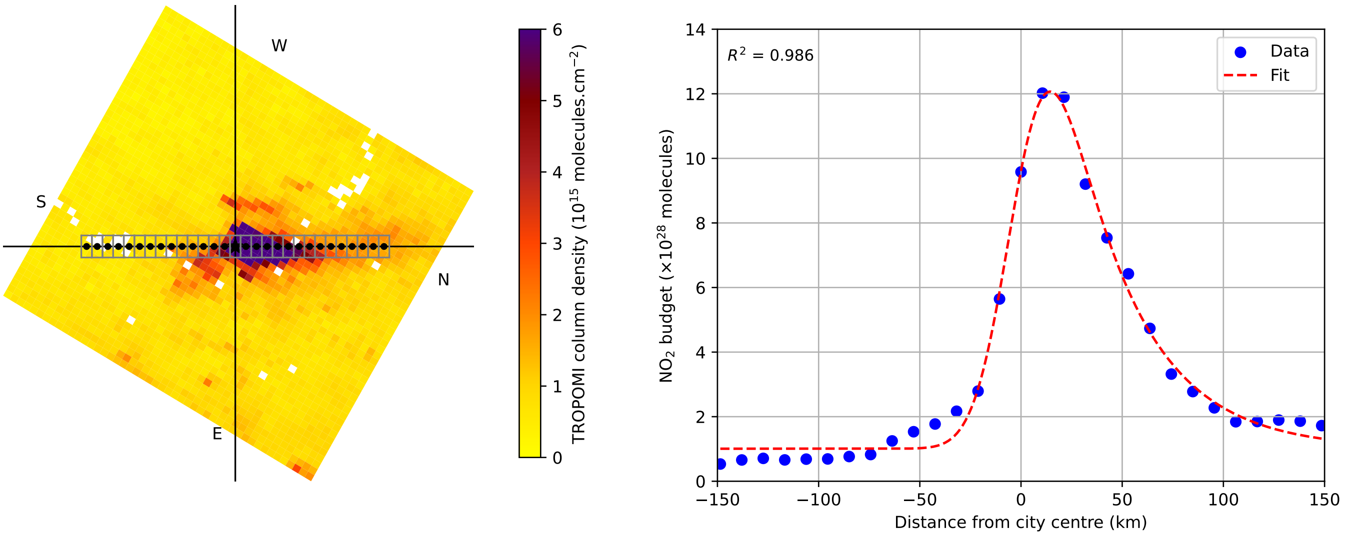

Figure 3.3: Estimation of the NO_2 lifetime from a pattern above Riyadh on 11 March 2020: (left) NO_2 plume rotated with its wind direction around the source (star) to an upwind-downwind pattern. Grey boxes centered around black points indicate the extent of the spatial integration of NO_2 columns to obtain the NO_2 line density. Values of cardinal points are noted in black. (right) Corresponding line densities (points) representing the downwind evolution of NO_2 as function of the distance to the city centre, and the corresponding fit according to the EMG function (dashed line).

The phenomena under study here take place in the planetary boundary layer (PBL), which in this region has a midday height of about 2 km (Filioglou et al., 2020). TROPOMI observations only provide information on the total NO_2 content of the tropospheric column, without providing information on the vertical distribution of concentrations. Extracting emissions from concentrations therefore requires a selection on the height at which wind, temperature and OH data are taken. Lama et al. (2020) and Lorente et al. (2019) conducted similar studies using the boundary layer average wind, while Beirle et al. (2019) chose a vertical level of about 450 m above ground. Because vertical transport of NO_x, which is emitted mainly from combustion engines and industrial stacks, is generally minor compared to horizontal transport, NO_x is confined to the first few hundred metres above ground level. Using PBL-averaged data poses a problem of consistency as wind, temperature and OH concentration values significantly vary within the PBL. As a consequence, we compare the CAMS-induced lifetime τ and the fit-induced lifetime τ_{fit} using the parameters ($\vec{w}$, [OH] and T) at two different vertical levels: a medium level $\mathcal{A}$ at 925 hPa (about 770 m above ground level), and a bottom level $\mathcal{B}$ at 987.5 hPa (about 210 m). These levels are interpolated from four and two ECMWF or CAMS consecutive pressure levels respectively (1000-850 hPa for level $\mathcal{A}$ and 1000-975 hPa for level level $\mathcal{B}$). Most mask cells having an altitude between 0 and 150 m, the corresponding pressure variations are small (up to $\sim$ 16 hPa), which allows us to neglect the effects of topography on the position of pressure levels. Figure 3.4 sums up the selection method for the comparison of lifetimes.

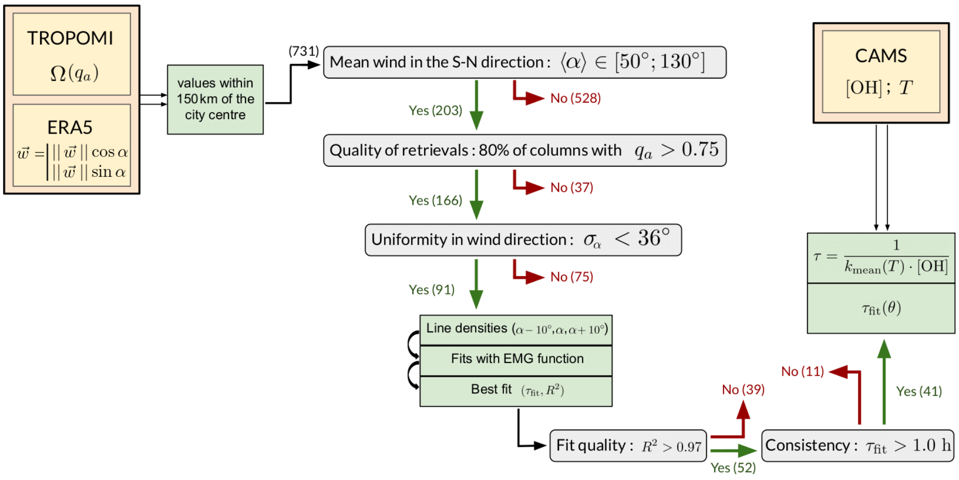

Figure 3.4: Selection method for NO_2 patterns over Riyadh. Datasets (yellow-orange) are used to calculate the quantities (light green) that are submitted to different tests (grey). 731 patterns are progressively conserved (green arrows) or rejected (red arrows). At each stage, the number of conserved or rejected patterns are noted within brackets (the value is only given for calculations performed at level $\mathcal{B}$). This selection process compares the lifetimes estimated by the EMG function fitting with TROPOMI line density profiles to the lifetimes calculated according to Equation (3.11) with CAMS data.

3.1.5-D Calculation of anthropogenic NO_x emissions and comparison with inventories

We calculate NO_x emissions on the entire domain from NO_2 production by using CAMS NO and NO_2 concentrations. These are not intended to replace TROPOMI observations; they are used to apply the concentration ratio $[NO_x]/[NO_2] = ([NO]+[NO_2])/[NO_2]$ to account for the conversion of NO_2 to NO and vice versa. As diurnal NO concentrations in urban areas generally range from 10 to 150 ppb (Khoder, 2009), the characteristic stabilization time of this ratio never exceeds a few minutes (Graedel et al., 1976; Seinfeld, Pandis, 2006). This time being lower than the order of magnitude of the inter-mesh transport time (about 30 min considering the resolution used and the mean wind module in the region), we can reasonably neglect the effect of the stabilization time of the conversion factor on the total composition of the emissions and treat each cell of the grid independently from its neighbours. Beirle et al. (2019) found an annual average of 1.32 for this conversion factor, but CAMS data shows small deviations from this value over Egyptian urban areas. We therefore calculate NO_x emissions for each cell of the domain as follows:

$$E_{NO_x} = \frac{[NO_x]}{[NO_2]} E_{NO_2} \tag{3.8}$$

For convenience, quantities $\frac{[NO_x]}{[NO_2]}\text{div}(\Omega_{NO_2}\vec{w})$ and $\frac{[NO_x]}{[NO_2]}\Omega_{NO_2}/\tau$ represent the respective contributions of the transport and the sink terms to total NO_x emissions. We finally obtain the emissions related to human activity $E^{\text{ant}}_{NO_x}$ by removing the arithmetic mean value of NO_x emissions above background cells from total emissions:

$$E^{\text{ant}}_{NO_x} = E_{NO_x} - \frac{1}{n_b}\sum_{i=1}^{n_b} E_{NO_x,i} \tag{3.9}$$

These removed emissions are linked to the NO_2 background estimated by TROPOMI. This background, which is mostly located in the upper troposphere, is inconsistent with the use of other parameters which are calculated in the lower troposphere. As such, these emissions do not correspond to anthropogenic emissions, but they provide the value of what must be substracted from the estimates to obtain emissions related to human activity. Such a removal assumes that other processes involved in NO_x budgets lead to similar emissions inside and outside the mask, which is not evident, as the majority of background cells are located in the desert or the ocean while the majority of mask cells are located near the Nile River. However, as the processes involved in natural NO_x sources lead to emissions much smaller than anthropogenic emissions in polluted areas, we neglect this difference in the following calculations. An alternative would be to calculate an average concentration for the background cells and subtract the corresponding value from the column densities before calculating the emissions. This would pose further reliability problems: for instance, very high NO_2 concentrations could appear outside the mask due to wind transport (an example is shown on Figure 3.1). They would lead to an overestimation of the NO_2 background and thus to an underestimation of the anthropogenic emissions.

Neglecting the part of the country that lies outside the domain, total emissions from the anthropogenic activity of Egypt can then be obtained by integrating $E_{\mathrm{NO_x}}^{\mathrm{ant}}$ on the whole domain. For robust statistics, these derived emissions can be averaged monthly, enabling a month-by-month comparison with bottom-up inventories. The linearity of the averaging processes ensures the interchangeability of temporal and spatial averages. A monthly average is relevant because it aggregates enough data to limit the impact of the outliers due to uncertainties in wind and OH representation. In addition, it enables the study of monthly NO_x emission profiles which reflect changes in human activities throughout the year due to temperature changes, economic constraints and cultural norms.

3.1.6 Results and discussion

3.1.6-A Line densities and NO_2 lifetime

We compare the results of the TROPOMI line densities fits for Riyadh to the lifetime calculated by Equation (3.11) using CAMS OH data. The two years of TROPOMI observations (from November 2018 to November 2020) provide a wide variety of profiles. For level $\mathcal{B}$, Figure 3.4 also provides the number of samples that are being kept at each stage of the process. Of the 731 observations available, 203 have a wind direction in the cone with a north-south orientation with an aperture of 40° (i.e. between 340° and 20° or between 160° and 200°). Of the remaining observations, 166 occured with a sufficiently clear sky to be retained. The criterion of weak variability for the wind direction brings to 91 the number of observations that are kept by the method. On these 91 observations, the line density profiles are calculated and the fits applied. According to Equation (3.7), the lifetime is calculated using the mean wind module around the point source. The two lifetimes are calculated with the parameters taken at the medium level $\mathcal{A}$ or at the top level $\mathcal{B}$. Of the 91 fits obtained, 51 are of high quality (correlation coefficient between fit function and line density profile greater than 0.97) for level $\mathcal{A}$ and 52 for level $\mathcal{B}$. 39 of these fits lead to a lifetime τ_{fit} greater than 1.0 h for level $\mathcal{A}$ and 41 for level level $\mathcal{B}$. All remaining samples correspond to atmospheric conditions with moderate to fast winds, with a module ranging between 2 and 11 $\mathrm{m.s^{-1}}$ (with an average of 5.9 $\mathrm{m.s^{-1}}$) for level $\mathcal{A}$ and between 3 and 8 $\mathrm{m.s^{-1}}$ (with an average of 5.4 $\mathrm{m.s^{-1}}$) for level $\mathcal{B}$. These lifetimes are compared to the corresponding lifetimes obtained from CAMS data in Figure 3.5, which is divided into seasons for a more convenient comparison. The use of level $\mathcal{A}$ leads to notable underestimations of the NO_2 lifetime in autumn compared to the lifetime calculated with the fitting method. This same level leads to lifetime overestimations in winter. This trend is not found with the use of level $\mathcal{B}$, which leads to a better reproduction of the lifetimes calculated with the fitting method for the available seasons. Figure 3.5 shows a linear regression between the two calculated lifetimes. The results are scattered, with a correlation coefficient higher for level $\mathcal{B}$ (0.408) than for level $\mathcal{A}$ (0.220). When the intercept of the regression line is forced to zero, the resulting slope is closer to 1 for level $\mathcal{B}$ (0.998) than for level $\mathcal{A}$ (1.071).

Although both correlations are weak, level $\mathcal{B}$ leads to a better match between the lifetime calculated with Equation (3.11) and the lifetime calculated from line densities. The results that are presented in the following sections (except for Section 3.1.6-C) are therefore results of calculations performed with parameters ($\vec{w}$, [OH], T and $[NO_x]/[NO_2]$) estimated at level $\mathcal{B}$. Nevertheless, it should be noted that no summer observations were included in the comparison. The main reason for this is the wind direction: of the 188 summer days observed, 178 have a mean wind direction outside the north-south cone over central Riyadh. On the remaining ten days (one for summer 2019 and nine for summer 2020), the ERA5 wind direction is too variable for the fit to be considered relevant, or the fit results in a correlation coefficient below 0.97. It is not clear how correctly the NO_2 lifetime would be calculated during both summer periods by Equation (3.11). With OH concentrations being the main driver of this lifetime, we cannot assess the relevance of the representation of OH concentrations by CAMS data during summer days in the study.

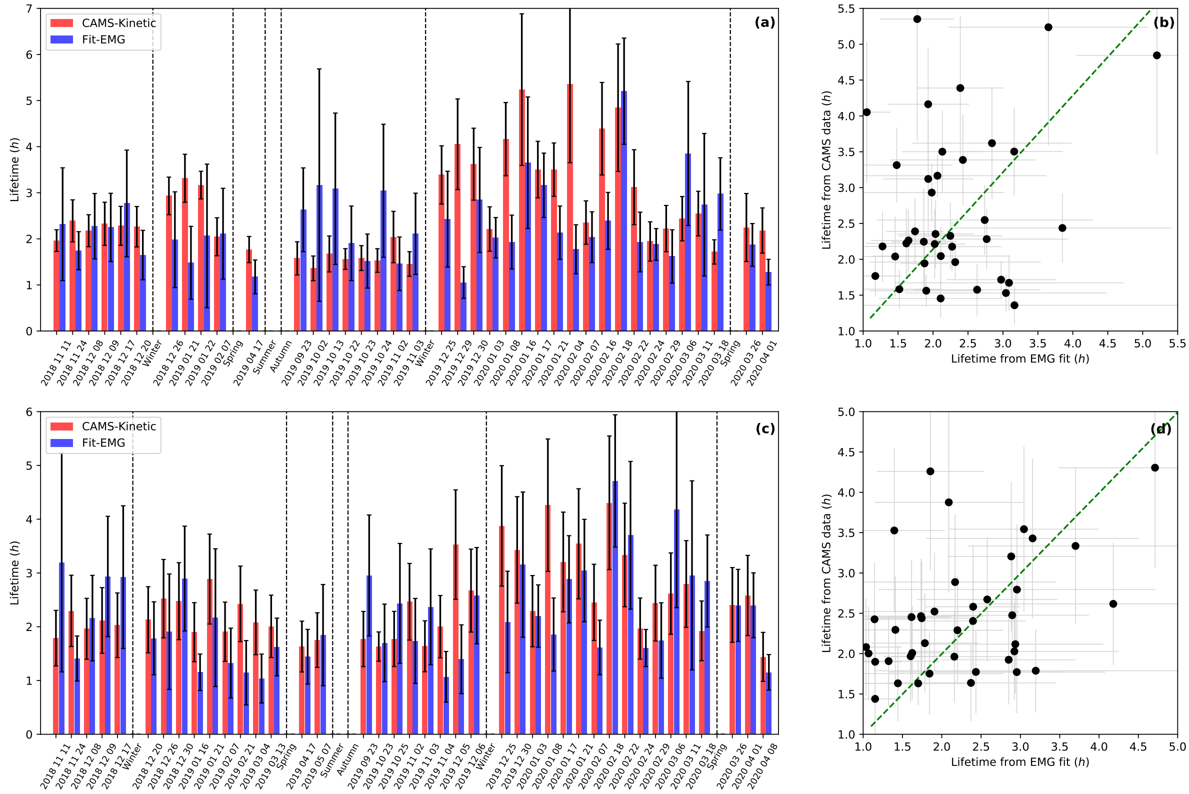

Figure 3.5: (left) Comparison between CAMS-derived NO_2 lifetimes and lifetimes from NO_2 line density fittings with EMG function above Riyadh city centre, for level $\mathcal{A}$ (a) and $\mathcal{B}$ (c). The samples presented correspond to patterns in clear-sky conditions for which the mean wind is in the north-south direction with a low variance, and for which the correlation between line density profile and fit gives a correlation coefficient of more than 0.97 and a lifetime of more than 1.0 h. NO_2 patterns do not have these conditions during the summers of 2019 and 2020. Dashed lines separate the groups of observations by season. (right) Comparison between the two calculated lifetimes for level $\mathcal{A}$ (b) and $\mathcal{B}$ (d). A linear regression with an intercept forced to be zero is displayed with a green dashed line.

3.1.6-B Mapping of Egypt's NO_x emissions

As a first step, we try to map NO_x emissions in Riyadh using parameters estimated at level $\mathcal{B}$. For the period from December 2017 to October 2018 and using a constant lifetime of 4 h, Beirle et al. (2019) estimated at 6.66 kg.s^{-1} the emissions of the corresponding urban area, and a mean rate density of about 3.7 µg.m^{-2}.s^{-1} for power plants PP9 and PP10/14, the transport term accounting for about 80 to 90% of this budget. Using the same domain for December 2018 to October 2019 with our method, we found a mean lifetime of 2.94 h and mean emissions of 5.92 kg.s^{-1} for the urban area. We also found smaller rate densities for the power plants (about 3.4 µg.m^{-2}.s^{-1} for PP9 and 3.0 µg.m^{-2}.s^{-1} for PP10/14), with a smaller contribution of the transport term (about 70%). Despite differences in resolution, AMF calculation, lifetime variability and background removal, the two methods give similar results.

The top-down emission model is then applied to the Egyptian domain with CAMS OH concentration and temperature fields for lifetime calculations. For each cell, NO_x emissions are calculated according to Equation (3.8), resulting in a mapping of Egypt's emissions. The obtained values are averaged monthly from November 2018 to November 2020. Figure 3.6 shows a composition of the emissions map with the transport term and the sink term for the months of January and July 2019. The corresponding anthropogenic emissions, calculated according to Equation (3.9), are added. The Nile appears on transport term maps: the divergence calculation complies with what is expected from a line of emitters, i.e. a clear separation of zones of positive divergence from zones of negative divergence with a separation line corresponding to the course of the river. The fact that areas of negative and positive divergence are respectively located to the east and the west of the river is the result of the zonal component of the wind being positive most of the time. Some point sources like Cairo, Alexandria, Asyut or Aswan are easily identifiable. The sink term, directly proportional to the TROPOMI column densities, also highlights these cities. However, unlike the transport term, which has a similar spatial pattern from month to month, the sink term is clearly stronger in summer than in winter. This is mainly due to a higher lifetime in winter than in summer (4.94 h on average in January 2019 and 2.62 h in July 2019) while the average TROPOMI NO_2 concentrations are slightly higher during winter (1.071×10^{15} molecules.cm^{-2} for January 2019 and 0.899×10^{15} molecules.cm^{-2} for July 2019). Over the whole domain, the mean transport term varies throughout the studied period between -0.014×10^{15} molecules.cm^{-2}.h^{-1} (December 2019) and 0.015×10^{15} molecules.cm^{-2}.h^{-1} (May 2020). Thus, it hardly contributes to the NO_x emission budget, the mean chemical sink term alone varying between 0.223×10^{15} molecules.cm^{-2}.h^{-1} (December 2019) and 0.534×10^{15} molecules.cm^{-2}.h^{-1} (September 2020).

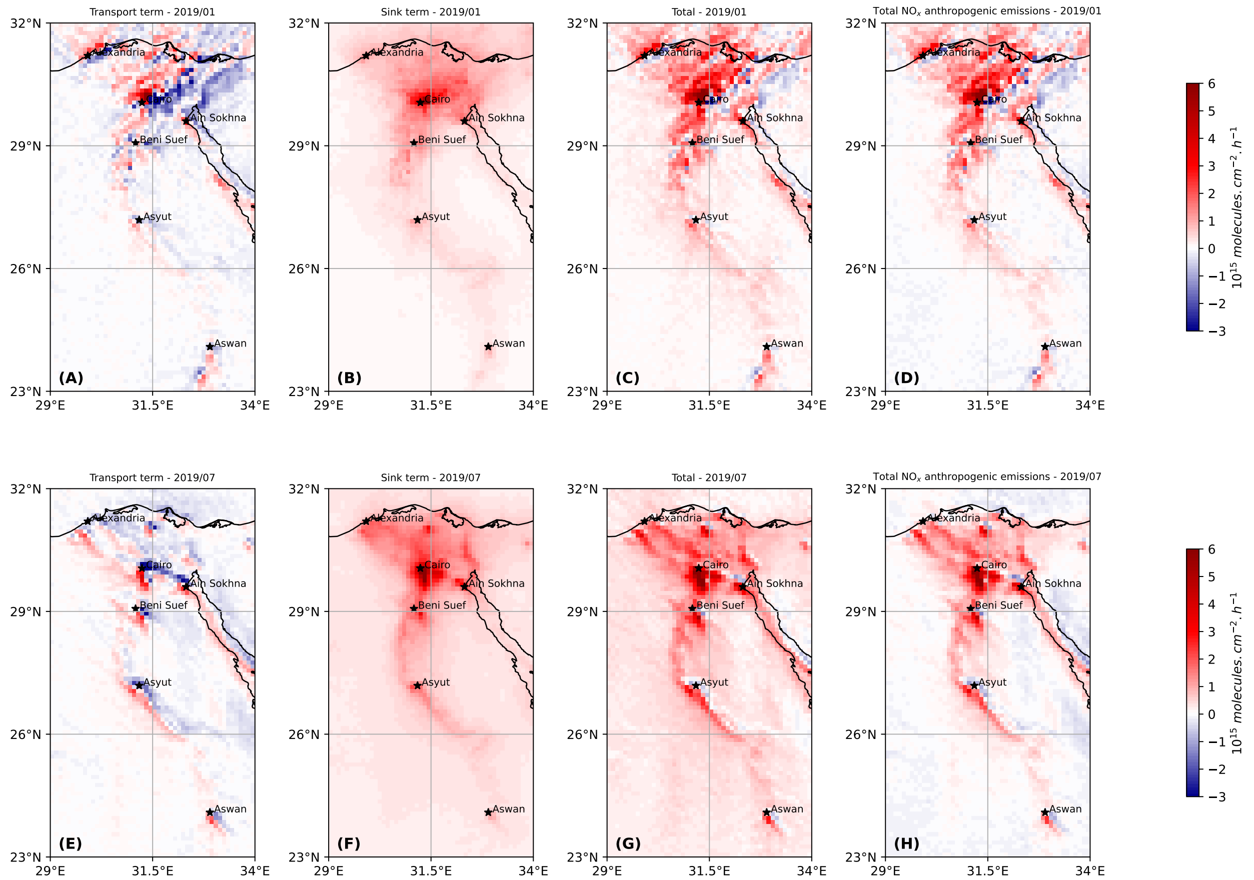

Figure 3.6: NO_x emissions above most of the Egyptian territory: (top) transport term (A), sink term (B), resulting emissions (C), and the corresponding anthropogenic emissions after non-anthropogenic background removal (D) for January 2019 (top) and corresponding values (E, F, G, H) for July 2019.

Several cities in the country appear as the main emitters of the country, such as Cairo, Alexandria, Beni Suef, Asyut or Aswan. The industrial area of Ain-Sokhna, located southwest of Suez, also appears as a main emitter. Table 3.1 compares the monthly values for the sink term and the absolute value of the transport term above five major cities of the country, with populations ranging from 200,000 to 20 million inhabitants, as well as Ain-Sokhna's area. The mean values for TROPOMI column densities are also provided. According to the results, the capital city of Cairo is by far the largest emitter in the country, largely due to its large population, resulting in high traffic emissions, but also to its intensive industrial activity. Alexandria, the country's second largest city, is not necessarily the second largest emitter, as its emissions are comparable to those of smaller cities such as Beni Suef or Asyut. However, the three cities concentrate a large amount of industrial activity: Alexandria hosts several oil and gas power plants and a small number of cement factories, while Beni Suef is close to several oil and gas power plants and hosts several flaring sites. Similarly, the city centre of Asyut is close to three oil and gas-fired power plants and a cement factory. This seems to indicate that industrial activity might be the main cause of NO_x emissions differences between these cities, before population size. This explains why NO_x emissions from these three cities are comparable to those of the industrial area of Ain Sokhna, which includes several cement facilities, iron smelters and oil and gas plants. It might also explain why Aswan, which has a population that is comparable to Beni Suef or Asyut, but which does not have any major industrial site, has slightly lower emissions than the two other cities. An additional analysis of the differences between Asyut and Aswan is provided in Section 3.1.6-F. Finally, the Gulf of Suez displays relatively large emissions, which might be attributed to the shipping sector, the region being a major gateway for international trade. Because it also hosts several flaring sites, these emissions might also be due to the oil and gas extraction activity.

City	**Population density**	**Jan. 2019**			**Jul. 2019**		
		VCD Ω	Transport	Sink	VCD Ω	Transport	Sink
	(habitants per square kilometer)	($\mathcal{M}_{NO_2}$.cm^{-2})	($\mathcal{M}_{NO_x}$.cm^{-2}.h^{-1})		($\mathcal{M}_{NO_2}$.cm^{-2})	($\mathcal{M}_{NO_x}$.cm^{-2}.h^{-1})	
Cairo	18,064	9.415	2.903	3.684	5.618	2.022	4.879
Alexandria	9,133	3.034	1.179	0.975	1.674	0.410	1.421
Asyut	1,644	1.708	0.679	0.718	2.137	1.236	1.520
Aswan	319	0.976	0.182	0.473	0.871	0.308	0.523
Beni Suef	2,056	2.950	0.548	1.080	2.321	0.428	1.591
Ain Sokhna	5	3.133	1.256	1.115	2.561	1.346	1.757

Table 3.1: Comparison between the transport term and the sink term above different cities in Egypt, as well as the industrial region of Ain Sokhna located 45 km southwest of Suez for January and July 2019. TROPOMI vertical NO_2 columns, NO_x emissions and population densities correspond to average values within 18 km from the city centre. Unit $\mathcal{M}$ stands for a quantity of 10^{15} molecules (NO_2 or NO_x).

Although these cities and areas can be described as high-emission sites, the term responsible for these emissions differ from one site to the other. Figure 3.7 shows the contribution of the transport term (taken in absolute value) to total emissions for January and July 2019. Because wind fields are relatively homogeneous along the Nile on spatial scales of less than 100 km, NO_2 concentration gradients perceived by TROPOMI in the region mainly contribute to the increase of the transport term which can reach similar values as the sink term. However, it is never significantly higher than the sink term: due to a spread of the emissions over large urban areas, the behaviour of these cities is therefore different from that of a point source for which the transport term would be very high (Beirle et al., 2021).

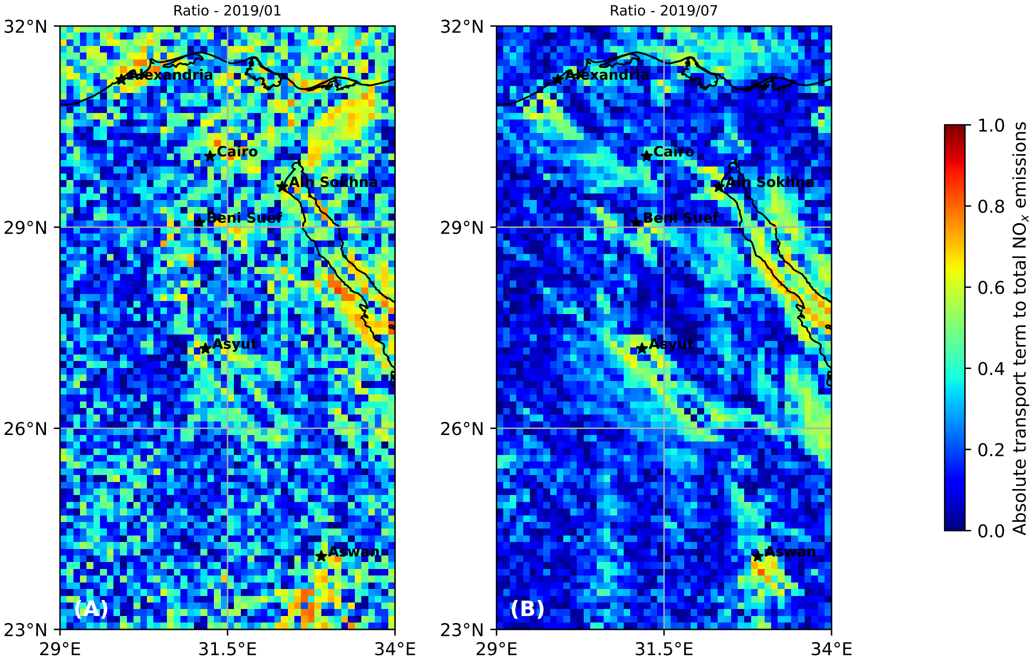

Figure 3.7: Share of the absolute value of the transport term in the sum of the sink term and the absolute value of the transport term above most of Egypt's territory, indicating the local importance of the transport term in NO$_x$ emissions above mask cells. The average of this ratio is shown for January 2019 (A) and July 2019 (B).

Desert areas such as the Libyan Desert, the Eastern Desert and the Sinai region, (located respectively to the west, east and northeast of the Nile) show a very low value for the transport term compared to the sink term, due to the homogeneity of both the wind field and the detected NO$_2$ concentrations in these areas. In the case of the Gulf of Suez, the transport term can be 1 to 2 times higher than the sink term, which varies between 0.4 and 1.2×10^{15} molecules.cm^{-2}.h^{-1}. Those values are slightly higher than the average emissions above background cells areas due to the sink term (about $0.2 - 0.6\times10^{15}$ molecules.cm^{-2}.h^{-1}), but remain quite low compared to the emissions in large cities. This relative predominance of the transport term is explained by a visible gradient of the TROPOMI NO$_2$ column densities. The region thus acts as a very thin line of emitters. Nevertheless, this predominance might also be partly due to a poor representation of the wind field. The low resolution of ERA5 (about 26 km in this region, which is the same order of magnitude as the width of the channel) may misrepresent the wind near the coast, creating artificial gradients.

3.1.6-C Vertical analysis

Here we investigate the influence of the choice of the vertical level in the representation of the different model parameters. This influence is of considerable importance, as NO$_x$ sources in urban areas can be located at different altitudes. For instance, emissions from the road sector from tailpipes are located at ground level, whereas NO$_x$ from power plants and industrial facilities can be emitted from stacks, which are usually located between 50 and 300 m above ground level. Section 3.1.6-A results showed that level $\mathcal{B}$ was more appropriate for the representation of the NO$_2$ lifetime. This level is therefore chosen as a reference for the comparison. We study the effect of a transition from level $\mathcal{B}$ to level $\mathcal{A}$ for each of the 3 parameters involved in the representation of the sink term, i.e. temperature T, hydroxyl radical concentration [OH] and concentration ratio [NO$_x$]/[NO$_2$]. The results for the averages over mask cells and background cells are given for the months of January, April, July and October 2019 in Table 3.2. As the wind field is only involved in the transport term whose spatial integration nearly leads to zero, the influence of this parameter is not studied.

		Sink term (10^{15} molecules.cm^{-2}.h^{-1})							
level $\mathcal{B}$ (987.5 hPa)	**level $\mathcal{A}$ (925 hPa)**	Jan. 19 (MASK)	Jan. 19 (BKGD)	Apr. 19 (MASK)	Apr. 19 (BKGD)	Jul. 19 (MASK)	Jul. 19 (BKGD)	Oct. 19 (MASK)	Oct. 19 (BKGD)
T, [OH], $\frac{[NO_x]}{[NO_2]}$	-	0.859	0.253	1.072	0.345	1.125	0.376	0.932	0.277
[OH], $\frac{[NO_x]}{[NO_2]}$	T	0.899 (+4.7%)	0.264 (+4.2%)	1.127 (+5.2%)	0.361 (+4.6%)	1.185 (+5.3%)	0.394 (+4.9%)	0.887 (+4.8%)	0.264 (+4.5%)
T, $\frac{[NO_x]}{[NO_2]}$	[OH]	0.769 (-10.5%)	0.219 (-13.6%)	1.013 (-5.5%)	0.324 (-6.0%)	1.129 (+0.4%)	0.375 (-0.3%)	0.853 (-8.5%)	0.251 (-9.5%)
T, [OH]	$\frac{[NO_x]}{[NO_2]}$	0.872 (+1.6%)	0.257 (+1.4%)	1.094 (+2.1%)	0.352 (+2.0%)	1.143 (+1.6%)	0.383 (+1.9%)	0.904 (+3.1%)	0.271 (+2.2%)

Table 3.2: Analysis of the effect of a vertical change in the parameters used to estimate the mean sink term in NO_x emissions: temperature, hydroxyl radical concentration, and NO_x:NO_2 concentration ratio. The comparison is conducted between the estimated quantities at level $\mathcal{B}$ and level $\mathcal{A}$ for mask cells (MASK) and background cells (BKGD) for January, April, October and July 2019. Values within brackets represent the variation from the base case for which all quantities are estimated at level $\mathcal{B}$.

The transition to level $\mathcal{A}$ generally results in a decrease in temperature, leading to an increase in the reaction rate k_{mean} and thus an increase in the emissions from the sink term. This transition has only a small influence on the total NO_x emission estimates, with mask and background cells emissions increasing by 4 to 6%. The influence of OH goes in the opposite direction: its concentration decreases with altitude, weakening the sink term. This weakening is particularly visible during winter months, for which the emissions are lower by up to 14%. In summer however, the effect is hardly noticeable. Finally, the influence of the NO_x:NO_2 ratio is negligible on the NO_x emission estimates. Thus, the transition to level $\mathcal{A}$ results in an increase in the sink term of 1 to 4%, due to a decrease in both concentrations of NO and NO_2 with respect to the vertical but with a greater decrease for NO_2. This vertical study confirms the crucial importance of the OH concentration for the accurate representation of NO_x emissions. It appears here as an important driver of the sink term, which is much more sensitive to vertical differences than temperature or the NO_x:NO_2 concentration ratio.

3.1.6-D Weekly cycle

In Egypt, the official rest day is Friday, and the economic activity of the country is a priori lower during this day than during the other days of the week. We therefore try to characterise this feature, by evaluating the weekly cycle of NO_x emissions. We use the TROPOMI-inferred emissions to obtain averages per day of the week. We use the quality assurance q_a of TROPOMI retrievals to ignore the days for which more than 20% of the domain has low-quality data (this happens 43 times in 2018/2019 and 28 times in 2019/2020). Such a filtering avoids accounting for the days when a large part of the urban and industrial areas are covered by clouds. However, it misses situations where small clouds are localised over large emitters, in which case the corresponding emissions are under-estimated. Figure 3.17 shows the resulting daily emissions for the period November 2018 - November 2019 and November 2019 - November 2020. NO_x emissions are expressed as NO_2 and in kilotons per day. A Friday minimum is observed, defining a weekly cycle. This trend is also observed for mean NO_2 column densities, for which no intra-weekly variation is observed. Over the 2018-2019 period, Fridays have average emissions of 1.244 ± 0.626 kt, which is lower than average emissions for the rest of the week, which reach 1.529 ± 0.817 kt. A similar trend is observed in 2019-2020, for which the average for Fridays is 1.079 ± 0.547 kt and the average for other days is 1.412 ± 0.688 kt. The difference in emissions between the two periods is due to smaller emissions in December 2019, January 2020 and February 2020 that are discussed in Section 3.1.6-D. On average, Friday emissions correspond to a ratio of 0.83:7 (i.e. a value of 0.83 after normalisation on the seven days of the week) for the entire domain. This result is consistent with the values obtained by Stavrakou et al. (2020), who used TROPOMI data and another emission model to calculate a ratio of 0.71:7 for Cairo and 0.89:7 for Alexandria in 2017.

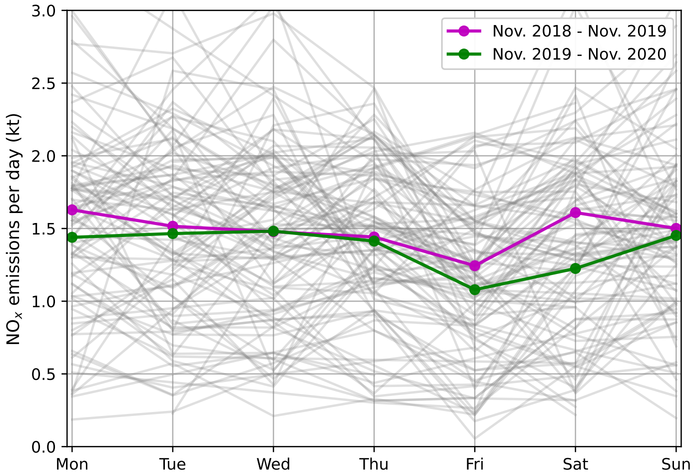

Figure 3.8: Weekly profiles of anthropogenic NO_x emissions for Egypt using TROPOMI observations in 2018-2019 (purple line) and 2019-2020 (green line). Thin grey lines represent individual weeks. Days for which less than 80% of the domain counts low quality observations ($q_a < 0.75$) are not represented.

3.1.6-E Impacts of lockdown during COVID-19

The ongoing global outbreak of COVID-19 forced many countries around the world to implement unprecedented public health responses, including travel restrictions, quarantines, curfews and lockdowns. Such measures have helped to counter the spread of the virus and have, meanwhile, caused high reductions in global demand for fossil fuels (IEA, 2020). They also led to a fall in the levels of NO_2 and other air pollutants across the globe (Venter et al., 2020; Bauwens et al., 2020; Gkatzelis et al., 2021). To prevent the spread of COVID-19, Egyptian authorities ordered a partial lockdown from March 15th till June 30th 2020, closing all public areas (e.g. sport centres, nightclubs, restaurants and cafes) and suspending religious activities in all mosques and churches throughout the country. They also implemented more drastic measures such as a full lockdown during Easter (April 20th) and Eid (May 23rd to May 25th), before lifting some restrictions on June 1st (Hale et al., 2021). In addition to the effect of containment on the activity of the country, the global decline in consumption led to a drop in the production of certain industrial products.

Several studies have estimated the impact of these events on the air pollution levels in the urban centres of the country : from in-situ measurements, El-Sheekh, Hassan (2021) estimated that NO_2 concentrations had dropped by 25.9% in Alexandria's city centre after the start of the lockdown on March 13th, while Abou El-Magd, Zanaty (2020) used OMI retrievals to estimate a 45.5% reduction of NO_2 concentrations for the entire country during the spring compared to 2018 and 2019 average values. However, due to a changing lifetime of NO_2, reductions in the concentrations of NO_2 might not be entirely due to a decrease in NO_x emissions, which leads us to focus on the variation of NO_x emissions during this singular period. Using our top-down emission model, reductions in total NO_x emissions of 20.1%, 11.8% and 13.5% are observed for the months of March, April and May 2020 compared to the equivalent months in 2019. This drop of emissions in 2020 compared to 2019 calculated by the model also correspond to a decrease in observed NO_2 columns: TROPOMI retrievals above mask cells show a decrease in NO_2 column densities of 21.6% over the same period. However, these effects observed for the months of March, April and May 2020 are not repeated in June 2020, for which emissions show an increase of 15.8% compared to June 2019. This rise is largely the result of an increase in the difference between average estimates inside and outside the mask. Indeed, emissions within the mask in June 2020 are higher than those of June 2019, due to an increase in TROPOMI concentrations above mask cells (+7.7%) while the NO_2 lifetime is almost unchanged (+3.3%). Emissions outside the mask varies in the opposite direction: a decrease in TROPOMI background concentrations (-5.4%) is observed while NO_2 lifetime increases strongly (+16.0%). This increase in June emissions seems to indicate that the lift on restrictions allowed a catch-up of the economic activity which was sufficiently strong to generate higher emissions in 2020 than in 2019. Note that CAMS OH concentrations during the lockdown periods do not show significant variations from previous years, although concentration values are slightly lower in 2020 than in 2019 (about 5.5% lower over the mask cells for the period March/April/May). The near-real-time CAMS system did not take into account the decrease in anthropogenic emissions in the representation of its OH concentrations. However, the satellite constraints inherent in the system may have modulated the lockdown effects locally or globally. Given the non-linearity of the chemistry but also given the large reactivity of OH with other species whose concentrations have varied differently during the lockdown, it is difficult to determine how these observations have impacted OH concentrations.

3.1.6-F Annual cycle and comparison to inventories

Here, we attempt to compare our TROPOMI-derived NO_x emissions in Egypt to emissions from CAMS-GLOB-ANT_v4.2 and EDGARv5.0 inventories. Figure 3.9 shows the total anthropogenic NO_x emissions over the mask cells from November 2018 to November 2020, calculated according to Equation (3.9). As indicated in Section 3.1.5-B, the emissions, calculated at 13:30 local time, are representative of the average daily consumption in Egypt. The total calculated for each month therefore corresponds to the NO_x production by human activities in the country. After aggregating the different sectors of activity, CAMS and EDGAR inventories directly provide the anthropogenic NO_x emissions over the same domain. All NO_x emissions are expressed in mass terms as NO_2. We note that the EDGAR inventory does not cover the period 2018-2020 (the last available year of the inventory is 2015). On Figure 3.9, EDGAR emissions corresponding to the period between November 2013 and November 2015 are displayed.

Figure 3.9: (top) Comparison of TROPOMI-derived anthropogenic NO_x emissions in Egypt (light blue), with the corresponding emissions from EDGAR (green with stripes) and CAMS (yellow) inventories. EDGAR data is shown for comparison purposes and covers the years 2013-2015. (bottom) TROPOMI-derived anthropogenic NO_x emissions for the cities of Asyut (dark red) and Aswan (light blue). The corresponding domains are displayed on Figure 3.1.

TROPOMI-derived emissions are higher than the CAMS inventory estimates. The top-down model estimates total NO_x emissions of 1069.7 kt over the 24 months, which is 70.4 kt higher than CAMS for the same period (999.3 kt). This difference is primarily localised in the first 12 months, for which TROPOMI-inferred emissions are always higher than the inventories and show higher values in summer than during the rest of the year. The next 12 months show similar emissions in summer but much lower values in winter. In particular, the difference is significant in December 2019 and January 2020 (respectively 56.5% and 66.5% of CAMS levels). These emissions also contrast with other winter emissions, with a total of 48.6 kt for December 2019–January 2020 against 81.7 kt for December 2018–January 2019 and 88.5 kt for 2020-12/2021-01. In the computations, this drop for winter 2019/2020 is mainly due to a relatively low value of the OH concentration which reaches 4.61×10^6 molecules.cm^{-3} on average for December 2019 and January 2020, with 4.29×10^6 molecules.cm^{-3} above mask cells and 4.69×10^6 molecules.cm^{-3} over background cells. They were respectively 5.29, 5.74 and 5.18×10^6 molecules.cm^{-3} for the previous year (2018-12/2019-01) and 5.11, 4.90 and 5.16×10^6 molecules.cm^{-3} for the subsequent year (2020-12/2021-01). A decrease in tropospheric columns (-18.5% for mask cells and -7.6% for background cells compared to winter 2018/2019) also contributes to this drop. The accuracy of the inferred emissions for winter 2019/2020 can therefore be questioned.

At first sight, the annual variability of TROPOMI-inferred emissions, which describes a one-year cycle with higher emissions in summer, seems to be correlated with power emissions which dominate the use of fossil fuels in Egypt (Abdallah, El-Shennawy, 2020). These power emissions are due to the country's residential electricity consumption (Attia et al., 2012; Elharidi et al., 2013; Nassief, 2014). They also meet the needs of industry. Summer peaks in electricity consumption are mostly driven by temperature, as illustrated by the increasing sales of air conditioning and ventilation systems for several decades (Wahba et al., 2018). The use of air conditioning in cars, which requires an additional amount of fuel, could also contribute to the increase of NO_x emissions in summer. To support this hypothesis, we use our model on two smaller domains centered around the two cities of Asyut and Aswan. The corresponding domains are displayed on Figure 3.1. Both cities have similar demographic features, with populations of about 467,000 and 315,000 inhabitants in 2021 and human densities of about 3,000 and 1,600 inhabitants per square kilometer respectively. However, their industrial features largely differ. There is no large fossil fuel-fired power plant in Aswan, where most of the electricity is produced by a hydroelectric dam, whereas Asyut counts three oil and gas power plants of various capacities (90, 650 and 1500 MW) in its urban area. Both cities have a cement plant, but the one in Asyut has a larger production capacity (5.7 Mt.yr^{-1} in Asyut, 0.8 Mt.yr^{-1} in Aswan). Our model is used following the same procedure as for the main domain. The background removal is done at the scale of the country. A seasonal cycle appears for Asyut, with a minimum for winter months and a maximum for summer months. This cycle seems slightly shifted from the one observed for the entire country, for which May emissions are as important as those of summer months. We also note that the decrease in emissions for winter 2019/2020 is less marked than for the emissions of the whole country, and of a similar value to the previous winter. This suggests that national NO_x emissions are indeed lower during winter, but that the values obtained for winter 2019/2020 are particularly low. We also find that the seasonality of the emissions is more pronounced for the Asyut domain than for the country as a whole. The case of Aswan is different. Emissions within the corresponding domain are significantly lower than for Asyut. The signal-to-noise ratio being higher, it is difficult to characterise an annual cycle, but the results do not seem to indicate low emissions in winter and high emissions in summer. This identification of a seasonal cycle identical to that of the entire country for a city with several power plants, and the absence of such a cycle in a city without any, strengthens the hypothesis that the power sector plays a major role in Egyptian NO_x emissions.

We note that some features of the industrial activities in the country might be counteracting this trend. For some sectors such as cement or steel, production is lower in summer, due to the physical wear experienced by workers due to heat, but also due to certain periods of leave. Given the importance of industrial activities in the production of NO_x shown in Section 3.1.6-B, this aspect cannot be neglected.

The transport sector could also counteract the observed trend: although the use of air conditioning in cars increase NO_x emissions of the sector, the observed mean traffic in the country is higher between November and February and lower between June and August, especially in Cairo which gathers most of the population. In the absence of additional data, it therefore seems difficult to conclude on the amplitude of the seasonal cycle produced by our top-down model. This caution is all the more necessary as CAMS and EDGAR show seasonal cycles for NO_x emissions, with different dynamics than those displayed by TROPOMI emissions: while the EDGAR inventory predicts a maximum of emissions in December or January and a minimum in April, the CAMS inventory shows two local maxima each year in May and November and two local minima in February and September. The amplitude of the corresponding cycles is much lower in those inventories, representing 14.2% of the average value for emissions estimates for EDGAR and 12.4% for CAMS. Those values must be compared to the amplitude displayed by TROPOMI-inferred emissions, for which the maximum/minimum ratio is about 1.8 if winter 2019/2020 is excluded, and 2.7 if it is included.

3.1.6-G Uncertainties and assessments of results

The estimation of NO_x emissions is based on the use of several quantities with varying uncertainties. The error bars shown in Figure 3.5 and Figure 3.9 are thus calculated from uncertainty statistics whose references are presented in this section. Since these references do not specify the exact nature of these statistics, we assume they correspond to standard deviations. The uncertainty of tropospheric NO_2 columns under polluted conditions is dominated by the sensitivity of satellite observations to lower tropospheric air masses, expressed by the tropospheric AMF. The column relative uncertainty due to the AMF is of the order of 30% (Boersma et al., 2004). Sentinel-5P validation activities indicate that TROPOMI tropospheric NO_2 columns are systematically biased low by about 30%-50% over cities (Verhoelst et al., 2021), which is most likely related to the a priori profiles used within the operational retrieval that do not reflect well the NO_2 peak close to ground. For the Middle East region, the impact of the a priori profile is less critical, as surface albedo is generally high and cloud fractions are generally low. Thus, we expect no such bias, and consider a relative uncertainty of 30% for the tropospheric column. Other uncertainties must be taken into account: the transition from NO_2 TROPOMI columns to NO_x emissions requires parameters which appear in Equation (3.11) and Equation (3.10). For wind module, uncertainties are generally of about 1 $m.s^{-1}$ for components taken at precise altitudes (Coburn, 2019; Beirle et al., 2019). Here, we assume an uncertainty of 3 $m.s^{-1}$ for both zonal and meridional wind components. For [OH], the analysis of different methods conducted by Huijnen et al. (2019) showed smaller differences for low latitudes than for extratropics, but still significant. We thus take a relative uncertainty of 30% for OH concentration. For the reaction rate k_{mean}, the value of the corresponding relative uncertainty has been estimated by Burkholder et al. (2020). Finally, we use the sensitivity tests performed in Section 3.1.6-C to assess the uncertainty associated with the choice of the vertical level. The cumulative effects on the final emissions of the three parameters studied, in particular the OH concentration, lead to a relative uncertainty that varies from month to month between 7 and 18%. The propagation of these different uncertainties on the monthly estimates of NO_x emissions in Egypt leads to an expanded uncertainty between 47 and 51%. For lifetimes calculated with the EMG function fitting, the corresponding expanded uncertainty ranges between 18% and 79%.

We acknowledge the fact that our treatment of NO_x is simplified. Many minor sinks highlighted in Section 3.1.5-A are not taken into account. In particular, anthropogenic VOC emissions, which remove NO_x from the atmosphere, compete with the oxidation by OH for the representation of NO_x loss. These emissions are difficult to estimate and the corresponding sink is complex to model. Taking this reaction into account would a priori lead to a strengthening of the sink term and thus to an increase of the NO_x emissions estimates. Moreover, due to the coarse resolution of CAMS data, OH gradients might also be underestimated, especially in the southern part of the domain, leading to a local underestimation of the sink term and the corresponding emissions. Other assumptions in the model are also simplifications. For instance, obtaining anthropogenic emissions by subtracting the average emissions over background cells assumes that the non-anthropogenic sources of NO_2 are similar inside and outside the mask, which is not true, since a large part of the mask cells correspond to croplands. For these cells, soil emissions may play a non-negligible role in the natural NO_2 budget. As a consequence, mean background emissions that are removed from NO_x emissions estimates above mask cells might be underestimated. Finally, the reliability of the data used can be questioned. The representation of the wind is crucial to avoid creating artificial patterns in the transport term. The OH concentration, which is proportional to the intensity of the sink term, is also important. We have shown that OH concentrations are partially responsible for an important drop in NO_x emissions in the winter of 2019/2020 that may be unrealistic. Because this decrease is largely due to variations in OH concentrations provided by CAMS, whose reliability has been evaluated for Riyadh, then the transposability hypothesis between Riyadh and Egypt may be subject to further discussion.

3.1.7 Conclusions

In this study, we investigated the potential of a top-down model of NO_x emissions based on TROPOMI retrievals at high resolution over Egypt. The model is based on the study of a transport term and a sink term that requires different parameters to be calculated. Among those parameters, the concentration in OH, involved in the calculation of the NO_2 mixed lifetime, is of fundamental importance. The comparison between NO_2 lifetimes derived from OH concentrations and NO_2 lifetimes derived from EMG function fittings of line density profiles shows that the OH concentration provided by CAMS is reasonably reliable for the country. Parameters are taken in the first 200 m of the planetary boundary layer, because it is where OH shows the best consistency. However, the vertical sensitivity linked to this parameters remains high. Results illustrate the importance of the transport term at local scale, which is of the same order of magnitude as the sink term above large cities and industrial facilities; it ceases to be relevant only at the scale of the whole country. The top-down model is able to characterise declines in human activities due to restrictions during the COVID-19 pandemic or to Friday rest. It also estimates higher emissions during summer. These high emissions may be interpreted by a higher consumption of electricity driven by air-conditioning during hot days, but it remains unclear whether this pattern clearly reproduces changes in human activity, in particular because the emission inventories show different seasonalities. These inventories also differ in the amount of total emissions: the average value for TROPOMI-derived NO_x emissions is 7.0% higher than CAMS-GLOB-ANT_v4.2 estimates. This discrepancy could be resolved by comparing the results of the model and inventory estimates to industrial production or electricity consumption data at the scale of countries or regions.

Here, our estimation of NO_x emissions benefited from favorable conditions. Egypt has a desertic climate, allowing to neglect many NO_x loss mechanisms for the sink term calculation, a flat terrain on most of its territory, limitating wind field errors for the transport term calculation, and a large population concentrated in a small number of cities, providing NO_2 maps with large signal-to-noise ratios above urban and industrial areas. For other regions of the world that do not have such features, the method presented here must be modified accordingly. However, we expect this method to be applicable to most countries similar to Egypt without substantial changes. For Middle East countries, this study thus demonstrates the potential of TROPOMI data for evaluating NO_x emissions. More generally, it demonstrates the importance of the contribution of independent observation systems to overcome the weaknesses of emission inventories, provided that the local chemistry is well understood and modelled. The development of similar applications for different species is likely to allow a better monitoring of global anthropogenic emissions, therefore helping companies and countries to report their emissions of air pollutants and greenhouse gases as part of their strategies and obligations to tackle air pollution issues and climate change.

Data availability

The TROPOMI NO_2 product is publicly available on the TROPOMI Open hub (`http://www.tropomi.eu/data-products/data-access`, TROPOMI Data Hub, 2022). The offline mode (OFFL) data of versions 1.0.0 to version 1.1.0 were used. CAMS data can be downloaded from the Copernicus Climate Data Store (`https://ads.atmosphere.copernicus.eu/cdsapp#!/home`, ECMWF, 2022a). The European Centre for Medium-Range Weather Forecasts (ECMWF) ERA5 reanalysis be downloaded from the Copernicus Climate Data Store (`https://cds.climate.copernicus.eu/cdsapp#!/dataset/reanalysis-era5-pressure-levels-monthly-means`, ECMWF, 2022b). The Global Rural-Urban Mapping Project (GRUMP) dataset is available from the NASA Socioeconomic Data and Applications Center at `https://sedac.ciesin.columbia.edu/data/collection/grump-v1` (SEDAC, 2017). Ground data for Egypt can be taken from `http://globalenergyobservatory.org/` (Global Energy Observatory, 2022) for oil and gas power plants and from `https://eogdata.mines.edu/download_global_flare.html` (Earth Observation Group, 2021) for flaring sites. CAMS-GLOB-ANT_v4.2 data are available at `https://eccad3.sedoo.fr/#CAMS-GLOB-ANT` (ECCAD-AERIS, 2022). EDGAR v5.0 Global Air Pollutant Emissions are provided by `https://edgar.jrc.ec.europa.eu/overview.php?v=50_AP` (European Commission, 2022).

Author contributions

AR analysed the data, prepared the main software code and wrote the paper. FC provided the TROPOMI NO_2 data product and corresponding gridded maps. PC contributed to building the database of emitters for Egypt. DH contributed to the interpretation of the use of OH for NO_x loss. GB, TC, JK and JS contributed to the improvement of the method and the interpretation of the results. All authors read and agreed on the published version of the paper.

Competing interests

The contact author has declared that none of the authors has any competing interests. Copernicus Publications remains neutral with regard to jurisdictional claims in published maps and institutional affiliations.

Acknowledgements

The authors would like to thank Steven J. Davis (University of California, Irvine) and Dan Tong (Tsinghua University) for their contribution to the construction of our emitter database.

Financial support

This research has been supported by the Horizon 2020 (EMME-CARE (grant n°856612)).

3.2 Estimation of NO_x emissions in Qatar and comparison with electricity data

3.2.1 Presentation of the article

This article on NO_x emissions in Qatar aimed to provide a different analysis to that carried out for Egypt. Where a sectoral analysis of NO_x emissions in Egypt was difficult, Qatar had several isolated emitters (a group of similar gas-fired power stations in the north-east and cement works in the west). This sectoral analysis was all the more interesting as the country's electricity production by power station was available. A concrete estimate of an emission factor therefore represented an interesting added value. Comparing the emissions obtained was also a challenge, as the country had not reported on its domestic NO_x emissions for more than a decade. Compared with the study of emissions in Egypt, the method was slightly modified: the TROPOMI data were gridded at a higher resolution (from $0.1°\times0.1°$ to $0.0625°\times0.0625°$), and the NO_2 background was calculated here directly by estimating the lowest column densities, and the ratio between NO_x and NO_2 had to be set at 1.32 due to structural weaknesses in the CAMS data in this region.

This article has been published under the name "**Detecting nitrogen oxide emissions in Qatar and quantifying emission factors of gas-fired power plants - A four-years study**" on October 30th 2023 in the journal Atmospheric Chemistry and Physics (ACP) from the editor Copernicus of the European Geosciences Union (EGU). Authors that participated to this work are **Anthony Rey-Pommier** (LSCE, The Cyprus Institute), Frédéric Chevallier (LSCE), Philippe Ciais (LSCE, The Cyprus Institute), Theodoros Christoudias (The Cyprus Institute), Jonilda Kushta (The Cyprus Institute), I. Safak Bayram (University of Strathclyde) and Jean Sciare (The Cyprus Institute). The article can be accessed at: `https://acp.copernicus.org/articles/23/13565/2023/acp-23-13565-2023.html`.

The results of this study have been presented at the Climate and atmosphere research and innovation in the Eastern Mediterranean and Middle East workshop (November 2022, Nicosia, Cyprus), and at the EGU General Assembly 2023 (April 2023, Vienna, Austria). Figures, numbering of subsections and notations appearing in the following Section have been slightly modified in order to be consistent with the rest of this document. On figures, such changes only concern colorbars and dataset names.

3.2.2 Abstract

Nitrogen oxides ($NO_x = NO + NO_2$), produced in urban areas and industrial facilities (particularly in fossil fuel-fired power plants), are major sources of air pollutants, with implications for human health, leading local and national authorities to estimate their emissions using inventories. In Qatar, these inventories are not regularly updated, while the country is experiencing fast economic growth. Here, we use spaceborne retrievals of nitrogen dioxide (NO_2) columns at high spatial resolution from the TROPOMI instrument to estimate NO_x emissions in Qatar from 2019 to 2022 with a flux-divergence scheme, according to which emissions are calculated as the sum of a transport term and a sink term representing the three-body reaction comprising NO_2 and hydroxyl radical (OH). Our results highlight emissions from gas power plants in the north-east of the country, and from the urban area of the capital Doha. The emissions from cement plants in the west and different industrial facilities in the south-east are underestimated, due to frequent low-quality measurements of NO_2 columns in these areas. Our top-down model estimates a weekly cycle with lower emissions on Fridays compared to the rest of the week, which is consistent with social norms in the country, and an annual cycle with mean emissions of 9.56 kt per month for the four-year period. These monthly emissions differ from CAMS-GLOB-ANT_v5.3 and EDGARv6.1 global inventories, for which the annual cycle is less marked and the average emissions are respectively 1.67 and 1.68 times higher. Our emission estimates are correlated with local electricity

generation, and allow to infer a mean NO_x emission factor of 0.557 $t.GWh^{-1}$ for the three gas power plants in the Ras Laffan area.

3.2.3 Introduction

Nitrogen oxides are reactive trace gases that can be converted into other chemical species, including ozone and fine particulate matter. Emissions of NO_x can originate from natural sources (from fires, lightning and soils), but the majority originates from anthropogenic sources, such as vehicle engines and heavy industrial facilities like power plants, steel mills and cement kilns (Vuuren, 2011). High levels of NO_x in the troposphere contribute to the formation of acid rain and smog. They also have a significant effect on human health by causing various respiratory diseases (Bovensmann et al., 1999; Burnett et al., 2004; EPA, 2016; He et al., 2020). To limit those impacts, national and regional governments generally enact a series of air pollution control strategies, which generally take the form of proscriptions on certain polluting technologies, with the aim of reducing the concentration of pollutants at the local level to targets that must be reached within a given timeframe. In the Middle East region, such mitigation strategies are quite recent. The region is thus experiencing increasing levels of NO_x pollution from anthropogenic sources (Osipov et al., 2022), with levels that remain high by international standards (Lelieveld et al., 2015). During the last two decades, Qatar experienced a rapid development based on oil and gas, leading to a degradation of air quality (Mansouri Daneshvar, Hussein Abadi, 2017). However, no official report concerning emissions of pollutants has been publicly available in the last 12 years.

Spectrally resolved satellite measurements of solar backscattered UV-Visible radiation enable the quantification of NO_2 in the atmosphere. Such measurements have been providing information on the spatial distribution of tropospheric NO_2 for more than 20 years, allowing the identification of many NO_x sources globally (Richter, Burrows, 2002; Celarier et al., 2008). In October 2017, the Sentinel-5 Precursor satellite was launched. Its main instrument is the TROPOspheric Monitoring Instrument (TROPOMI), which provides daily tropospheric NO_2 column densities at high spatial resolution with a large swath width. Columns images can then be used to retrieve NO_x emissions with the use of the continuity equation in steady state. This scheme, known as flux-divergence, requires the use of other physical quantities. In this study, we use this method to quantify the emissions in Qatar based on retrievals from 2019 to 2022 and overcome the absence of recent reporting.

This article is organised as follows: Section 3.2.4 provides a description of Qatar and its main emission sources. Section 3.2.5 provides a description of the datasets used in this study. Section 3.2.6 presents the flux-divergence method to infer NO_x emissions at the scale of the country. Section 3.2.7 presents the spatial distribution of NO_x emissions and their seasonal variations. It also presents the limitation of our method to infer emissions for areas above which TROPOMI measurements are often of low quality. Section 3.2.8 confronts our estimated emissions to local electricity generation and existing global inventories to provide a sectoral approach of NO_x emissions. Section 3.2.9 presents the limits and the uncertainties of the model, and Section 3.2.10 our concluding remarks. For the purposes of our study, NO_x emissions are expressed as NO_2 throughout this article.

3.2.4 General features of Qatar and overview of reported NO_x emissions in 2007

Qatar is a country with an area of 11,600 km^2, located on the northeast coast of the Arabian Peninsula. The country shares its sole terrestrial border with Saudi Arabia in the south, and has maritime boundaries with Bahrain in the west, Iran in the north and the United Arab Emirates in the east. Qatar has the third largest proven natural gas reserves in the world and non-negligible oil reserves (EIA, 2021). Since 1973, oil and gas revenues increased dramatically, making the country the third largest exporter of natural gas (OPEC, 2020). The resulting economic growth raised Qatar to one of the countries with the highest per capita incomes in the world. Between 2001 and 2019, the average gross domestic product growth rate of the country was 9.1 % (World Bank, 2022), driven by the exploitation of the oil and gas fields, which account for 85 % of its exports and over 60 % of its gross domestic product. The exploitation of such oil and gas resources is a source of air pollution, due to NO_x emissions during the incomplete combustion of hydrocarbons. The power sector, which is dominated by gas power plants, as well as the transport sector, are thus important contributors to the NO_x levels throughout the country. Other sectors, such as cement production, also contribute to the total NO_x budget. Little information is available on the country's emissions and the share of these different sectors. The last official communication dates back to 2011 for emissions in 2007, and uses the IPCC Common Reporting Format sector classification (UNFCCC, 2011). It estimates total emissions of 163 kt (assumed to be expressed as NO_2), with the following shares:

- **Power generation**: There are several gas-fired power plants in Qatar which, until the end of 2022, provided all the electricity in the country, with a generation that increased from 4.5 TWh in 1990 to 48 TWh in 2021 (EIA, 2022). According to the report for emissions in 2007, they produced 32.03 kt of NO_x, which corresponded to 19.7 % of the country's total emissions. The report indicates an emission factor equal to 0.109 $t.TJ^{-1}$ or 0.392 $t.GWh^{-1}$, which is a low but realistic emission factor for an electric mix dominated by gas. More recent data on NO_x emissions from the power sector are not available.

- **Cement production**: The country has three cement production sites. According to the report for emissions in 2007, cement production was responsible for 23.4 % of the country's total NO_x emissions. It should be noted that due to the high temperatures in summer, outdoor activities at the productions sites are reduced, which can result in lower activity between June and September.

- **Road transport**: According to the report for emissions in 2007, the road transport sector accounted for 22.7 % of the country's total NO_x emissions (27.6 % for the total transport sector). Fuel sales do not seem to have any annual seasonality (Al-Attiyah Foundation, 2018): the corresponding NO_x emissions are therefore not variable with seasons. However, they may change gradually with the nature of the vehicle fleet, which includes a growing number of diesel vehicles.

- **Manufacture of Solid Fuels and Other Energy Industries**: This sector includes upstream oil and gas activities and processing operations. Most of historical upstream operations took place in the Dukhan field, located in the west of the country, but the majority of the extraction currently takes place offshore in the North Field, which is one of the largest non-associated gas fields in the world. According to the report for emissions in 2007, these activities accounted for 25.7 % of the country's NO_x emissions.

Figure 3.10 shows the locations of the industrial facilities in Qatar which are likely to emit significant amounts of NO_x. Four regions can be distinguished. The west of the country comprises two large-capacity cement plants (7.0 $Mt.yr^{-1}$ and 5.0 $Mt.yr^{-1}$). The south-east includes a gas power plant, a cement plant and an aluminium smelter, while the north-east comprises the industrial area of Ras Laffan, including three gas power plants. Finally, the urban area of Doha, in the centre-east of the country, concentrates the majority of the population, as well as five gas power plants.

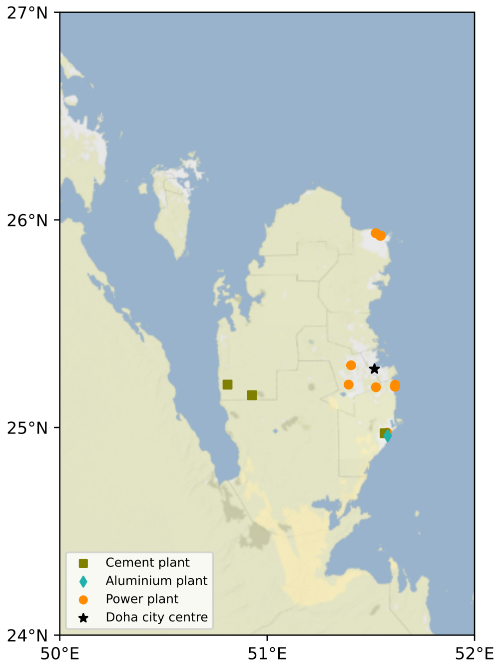

Figure 3.10: Location of the main industrial facilities (cement kilns, power plants and aluminium smelters) in Qatar. Urban areas are displayed in gray and Doha's city centre is denoted with a star. Industrial facilities and cities in other countries are not displayed. Map tiles by Stamen Design under CC BY 3.0. Data © OpenStreetMap contributors.

3.2.5 Instruments and data

3.2.5-A TROPOMI NO_2 retrievals

NO_2 can be observed from space with satellite instruments based on its strong absorption features in the 400–465 nm wavelength region (Vandaele et al., 1998). By comparing observed spectra with a reference spectrum, the amount of NO_2 in a portion of the atmosphere between the instrument and the surface can be derived. The TROPOspheric Monitoring Instrument (TROPOMI), onboard the European Space Agency's (ESA) Sentinel-5 Precursor (S-5P) satellite, is one of those instruments, providing daily measurements of NO_2 around 13:30 local time (LT). Its high spatial resolution (originally 3.5×7 km^2 at nadir, improved to 3.5×5.5 km^2 since 6 August 2019) allows to observe some of the fine-scale structure of NO_2 pollution, such as within cities (Beirle et al., 2019; Demetillo et al., 2020), or near power plants and industrial facilities (Shikwambana et al., 2020; Saw et al., 2021). Tropospheric vertical column densities (VCDs, or simply "columns") are provided by the algorithm after measurement by the instrument, which represents the vertically integrated number of NO_2 molecules per surface unit between the surface and the tropopause. An algorithm also provides an air mass factor (AMF), which is used to convert slant column densities into vertical column densities. This factor depends on many parameters, including the albedo of the viewed surface, the vertical distribution of the absorber and the viewing geometry. It is a source of structural uncertainty in NO_2 measurements (Boersma et al., 2004; Lorente et al., 2019), which becomes non-negligible in polluted environments. The large swath width of the instrument (∼2600 km) makes it possible to construct NO_2 images of VCDs on large spatial scales. We use TROPOMI NO_2 retrievals from 2019 to 2022 (S5P-PAL reprocessed data with processor version 2.3.1 from January 2019 to October 2021, OFFL stream with processor version 2.3.1 from November 2021 to October 2022, and OFFL stream with processor version 2.4.0 from November 2022 to December 2022) over Qatar. The arid climate of the country, which offers a large number of clear-sky days throughout the year, enables the calculation of monthly averages based on multiple observations. Its intensive anthropogenic activity, concentrated on a small number of areas, allows to observe high NO_2 concentration patterns. Due to its short lifetime (about 1 to 10 hours), background NO_2 levels can be orders of magnitude lower than levels near polluted areas. Pollution patterns are therefore characterised by large signal-to-noise ratios above main emitters. Finally, TROPOMI products provide a quality assurance value q_a, which ranges from 0 (no data) to 1 (high-quality data). For our analysis of concentrations, we selected NO_2 retrievals with q_a values greater than 0.75, which systematically correspond to clear-sky conditions (Eskes et al., 2022), and gridded these retrievals at a spatial resolution of 0.0625°×0.0625°. From August 2019, this resolution is lower than that of the instrument, thus providing a grid for which NO_2 VCDs correspond to one or more measurements. The observed plumes remain correctly resolved.

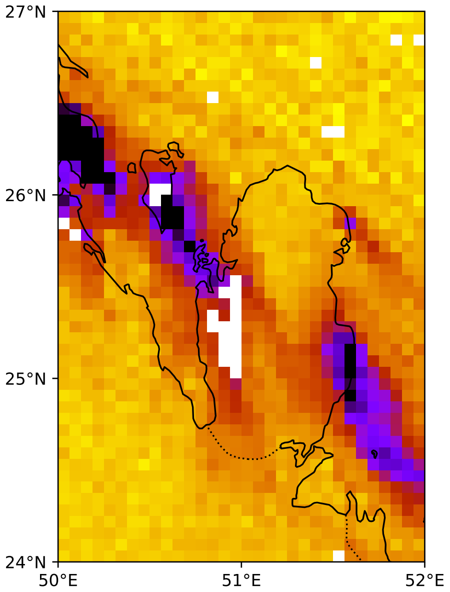

Figure 3.11: TROPOMI observation of NO_2 column densities above Qatar on December 12th 2019. White pixels correspond to areas with low-quality data ($q_a < 0.75$) or no data.

The domain of interest extends between the meridians 50°E and 52°E and between the parallels 24°N and 27°N. TROPOMI tropospheric columns show polluted areas, such as the Ras Laffan area, but also the large urban area of Doha. Observed VCDs are high (5 to 30×10^{15} molecules.cm^{-2}), which facilitates the observation of NO_2 plumes. An example of a TROPOMI image is provided in Figure 3.11. Within the domain, the meridional component of the wind is generally oriented towards the south. The zonal component varies throughout the year. Strong wind events can cause the pollution from Bahrain to reach the coasts of Qatar. Finally, several areas in the west of the country are not visible by TROPOMI most of the time, because the quality of the corresponding measurements is too low. This phenomenon, which is also present in the east of the country (slightly south of downtown Doha) but with a smaller spatial extent, is studied in details in Section 3.2.7-C.

3.2.5-B ERA5

The horizontal wind vector field $\vec{w} = (w_x, w_y)$ is taken from the European Centre for Medium-Range Weather Forecasts (ECMWF) ERA5 data archive (fifth generation of atmospheric reanalyses) at a horizontal resolution of 0.25°×0.25° on 37 pressure levels (Hersbach et al., 2020). The hourly values have been linearly interpolated to the TROPOMI orbit timestamp and re-gridded to a 0.0625°×0.0625° resolution.

3.2.5-C CAMS real-time fields

The Copernicus Atmospheric Monitoring Service (CAMS) global near-real-time service provides analyses and forecasts for reactive gases, greenhouse gases and aerosols. Data is gridded on 25 vertical pressure levels with a horizontal resolution of 0.4°×0.4° and a temporal resolution of 3 hours (Huijnen et al., 2019). Here, CAMS concentration fields of hydroxyl radical (OH) are used to calculate NO_2 sinks from TROPOMI observations. We also use CAMS temperature field T to account for the the reaction rate for HNO_3 production through the calculation of the NO_2 lifetime according to Burkholder et al. (2020). The hourly values are also linearly interpolated to the TROPOMI orbit timestamp and re-gridded to a 0.0625°×0.0625° resolution.

3.2.5-D Inventories

The Emissions Database for Global Atmospheric Research (EDGARv6.1) and the CAMS global anthropogenic emissions (CAMS-GLOB-ANT_v5.3) are global inventories that provide 0.1°×0.1° gridded emissions for different sectors on a monthly basis. EDGARv6.1 emissions are based on activity data (population, energy production, fossil fuel extraction, industrial processes, agricultural statistics, etc.) derived from the International Energy Agency (IEA) and the Food and Agriculture Organization (FAO), corresponding emission factors, national and regional information on technology mix data and end-of-pipe measurements. The inventory covers the years 1970-2018. CAMS-GLOB-ANT_v5.3 is developed within the framework of the Copernicus Atmospheric Monitoring Service (Granier et al., 2019). For this inventory, NO_x emissions are based on various sectors in the EDGARv5.0 emissions up to 2015 which are extrapolated to 2021 using sectorial trends from the Community Emissions Data System (CEDS) inventory (Hoesly et al., 2018) up to 2019. From one inventory to another, the names and definitions of the sectors may differ. In EDGARv6.1 and CAMS-GLOB-ANT_v5.3, the emissions for a given country are derived from the type of technologies used, the dependence of emission factors on fuel type, combustion conditions, as well as activity data and low-resolution emission factors (Janssens-Maenhout et al., 2019).

3.2.5-E Electricity consumption and production data

As the power sector is one of the main drivers of NO_x, we use electricity production and consumption data at several time scales, detailed in Section 3.2.7-E. Daily load profiles from February 2016 to January 2017 are taken from Bayram et al. (2018) and used to calculate monthly ratios between the average power demand and the power demand during the overpass of TROPOMI. These ratios are assumed to be valid from 2019 to 2022. We also use monthly electricity generation time series from 2019 to 2022, which are provided by the Qatar Ministry of Development Planning and Statistics (PSA, 2023). From 2019 to 2021, these time series can be completed with monthly reports from Kahramaa, which transmits and distributes the electricity generated by each of the country's power plants with great accuracy (Kahramaa, 2023). The corresponding data for 2022 is not available yet.

3.2.6 Method

3.2.6-A Mask and background removal

In satellite retrievals, the NO_2 signal from a sparsely populated area or a small industrial facility may be difficult to identify due to high noise levels or natural emissions. As a consequence, detecting traces of non-natural emissions in TROPOMI NO_2 images is not a straightforward process. In the absence of anthropogenic sources, the NO_2 columns that are observed constitute a tropospheric background that varies between 0.2 and 1.0×10^{15} molecules.cm^{-2}. At the global scale, this background is mostly due to soil emissions in the lower troposphere (Yienger, Levy, 1995; Hoelzemann et al., 2004). In the upper troposphere, NO_2 sources include lightning, convective injection and downwelling from the stratosphere (Ehhalt et al., 1992), but the factors controlling the resulting concentrations are poorly understood. According to state-of-art estimates, anthropogenic NO_x accounts for most of the emissions at the global scale, whereas natural emissions from fires, soils and lightning are smaller (Jaeglé et al., 2005; Müller, Stavrakou, 2005; Lin, 2012). In Qatar, the desert climate limits lightning and fire, and the share of the corresponding emissions within the background is thus expected to be low. As a first step, we estimate this background by excluding the part of the domain which is outside the territory of Qatar, as well as other regions with human activity, which include Bahrain and the neighbouring part of Saudi Arabia. The remaining pixels constitute an "external mask" within which we calculate the 5th percentile of the TROPOMI columns. The corresponding value is defined as the tropospheric background. Figure 3.12 displays the external mask, as well as an "internal mask" that gathers only pixels above Qatar's territory. This external mask is used in Section 3.2.7 and Section 3.2.8.

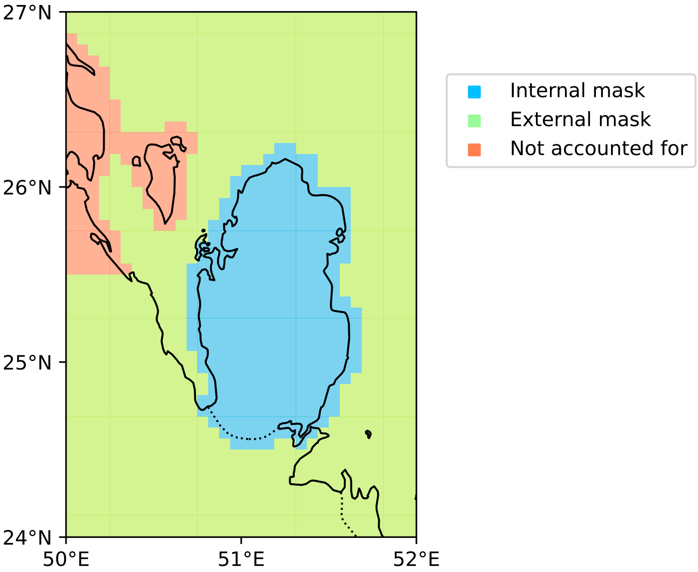

Figure 3.12: Masks used for NO_x emissions estimates: Green cells are used to estimate the NO_2 tropospheric background that is removed from vertical column densities before calculation of emissions (external mask). Blue cells are used to count NO_x emissions attributable to Qatar (internal mask). Orange cells, which cover urban and industrial areas from other countries, are not considered.

3.2.6-B Flux-divergence method

As a second step, we derive top-down NO_2 production maps with the flux-divergence method, which has originally been proposed by Beirle et al. (2019). It consists in applying the continuity equation in steady state as:

$$E_{NO_2} = \mathrm{div}(\Omega \vec{w}) + \Omega / \tau \tag{3.10}$$

The previous equation highlights a transport term $D = \mathrm{div}(\Omega \vec{w})$, obtained by multiplying NO_2 VCDs with horizontal wind speeds and the NO_2 sinks $S = \Omega/\tau$. As the local overpass time of TROPOMI is close to 13:30 LT, sinks are dominated by the chemical loss due to the reactions of NO_2 with OH (leading to formation of HNO_3), which can be described by the chemical lifetime τ as:

$$\tau = \frac{1}{k_{\mathrm{mean}}(T, [\mathrm{M}])[\mathrm{OH}]} \tag{3.11}$$

Here k_{mean} is the kinetic reaction rate that characterises the different first-order reactions between NO_2 and OH. Burkholder et al. (2020) provide a general expression of this reaction rate with respect to atmospheric conditions (temperature T and total air concentration [M]).

In the atmosphere, OH is a dominant oxidant species. It is mainly produced during daylight hours by interaction between water and atomic oxygen produced by ozone dissociation (Levy, 1971), and its concentration is therefore are strongly correlated with solar ultraviolet radiation (Rohrer, Berresheim, 2006). The direct measurement of OH is possible using spectroscopic methods but the spatial representativeness of the data is limited due to its short lifetime. Most global analyses thus estimate OH budgets from other variable species (Li et al., 2018; Wolfe et al., 2019) with high associated uncertainties (Huijnen et al., 2019). In polluted air, another mechanism for OH production is the reaction between NO and HO_2. This reaction, referred to as the NO_x recycling mechanism, illustrates the non-linear dependence of the OH concentration on NO_2 (Valin et al., 2011; Lelieveld et al., 2016). Here, considering OH as the only sink assumes other sinks are negligible. We consider such an approximation as valid (Rey-Pommier et al., 2022). This hypothesis can be validated a posteriori by analysing the calculated NO_x emission maps and verifying the absence of highly negative emissions (which would correspond, all other things being equal, to an underestimation of the sink term) or emissions having the shape of a plume (which would correspond, all other things being equal, to an overestimation of the sink term).

Finally, it should be noted that anthropogenic combustion activities produce mainly NO, which is transformed into NO_2 by reaction with ozone O_3. NO_2 is then photolyzed during the day, reforming NO (Seinfeld, 1989). This photochemical equilibrium between NO and NO_2 can be highlighted with the concentration ratio $\mathcal{L} = [NO_x]/[NO_2]$. NO_x emissions are therefore obtained by multiplying NO_2 production E_{NO_2} by $\mathcal{L}$. As diurnal NO concentrations in urban areas are generally above 20 ppb, the characteristic stabilization time of this ratio never exceeds a few minutes (Graedel et al., 1976; Seinfeld, Pandis, 2006). This time being lower than the order of magnitude of the inter-mesh transport time (about 30 min considering the resolution used and the mean wind module in the region), we can reasonably neglect the effect of the stabilization time of the conversion factor on the total composition of the emissions and treat each cell of the grid independently from its direct environment. In Rey-Pommier et al. (2022), this ratio was estimated using the CAMS NO and NO_2 concentration fields in Egypt. For Qatar, CAMS data show many outliers for these concentration fields: for some pixels, NO concentrations can be equal to zero. They can be also two times higher than NO_2 concentrations in places without any significant feature that would explain it. We therefore do not use these fields and choose a fixed value of 1.32 for this ratio, as used by Beirle et al. (2019). After removal of outliers in the statistics, CAMS values for $\mathcal{L}$ suggest that the average value for this ratio ranges between 1.17 and 1.60 with small spatial variations.

Through the OH concentration, we enable a variability in the chemical lifetime. This variability is not allowed in the original version of the first-divergence method by Beirle et al. (2019), which relied on heavy averaging over time to infer emissions at the scale of cities and power plants. Here, seasonal and spatial variations of lifetimes are resolved, thus limiting the errors in the estimation of the daily sink term. Although errors remain high when estimating daily emissions, averaged monthly emissions are correctly resolved above the main emitters.

3.2.7 Results

3.2.7-A Selection of TROPOMI images and averages

We apply Equation 3.10 to daily TROPOMI images and average the resulting emissions to obtain monthly daytime emissions. This process can be hindered due to the presence of poor quality measurements that prevent the calculation of the divergence in the transport term each day. This happens when a significant part of the country is covered by clouds. Furthermore, the resolution used to grid data (0.0625°×0.0625°, i.e. about 6.3×6.9 km^2 in this region) is lower than the initial resolution of TROPOMI (3.5×7 km^2 until 6 August 2019). For the first eight months of this study, our gridding therefore results in maps having many pixels without data. In the process of estimating mean monthly emissions, we consider these two situations and do not take into account in the averaging the days for which corresponding TROPOMI images have more than 70 % of the territory of Qatar (defined by the internal mask) without data or with poor quality data ($q_a < 0.75$). Furthermore, Bahrain is located 30 km away from Qatar, and the centres of the capitals of the two countries are separated by about 130 km. Pollution from Bahrain, which is usually transported to Qatar, can reach Doha during strong wind events. In such situations, the errors in ERA5 can alter the estimation of the transport term and thus the NO$_x$ estimates. As a consequence, we also remove days with high wind speeds in the Bahrain/Qatar direction , i.e. days for which the average wind over Bahrain and the marine area between the two countries has a speed higher than 30 km.h^{-1} and an angle between -15° (E$\frac{1}{4}$SE) and -75° (S$\frac{1}{4}$SE). The choice of these thresholds are discussed in the Supplementary Materials. Figure 3.13 shows the amount of days considered in the calculation of the average emissions of a given month between 2019 and 2022. It also shows the number of days that have been discarded and the reasons for the corresponding discards.

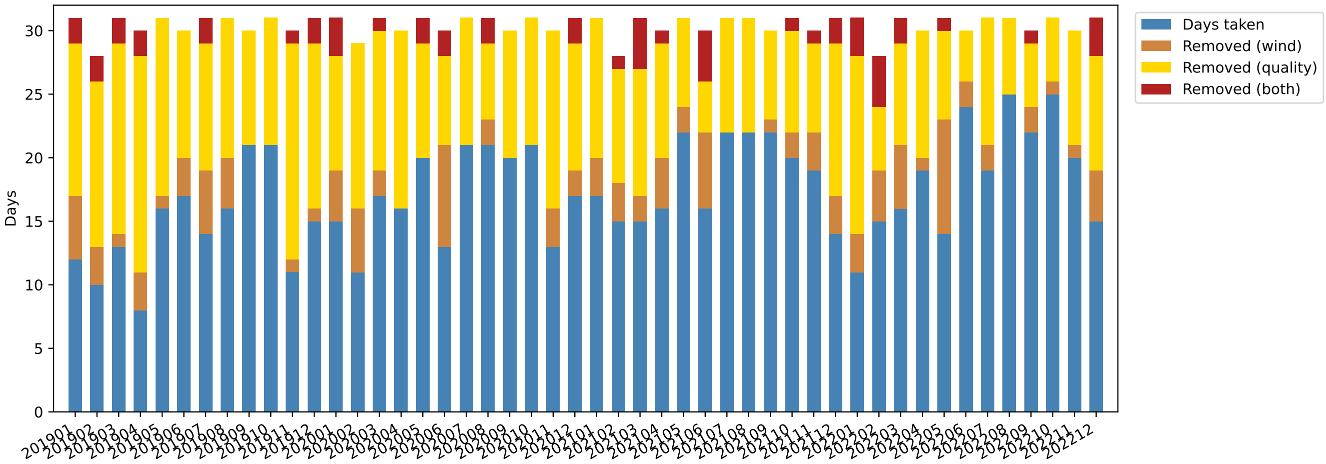

Figure 3.13: Number of days involved in the mean monthly estimates of NO$_x$ emissions (blue) and days that have been discarded due to strong winds blowing from Bahrain to the south-east (brown), large areas within the internal mask with low-quality data (yellow), or both (red).

Here, monthly average emissions are calculated with between 8 and 25 days of TROPOMI images, with low values for the seven first months of the study due to the lower resolution of TROPOMI during this period. Excluding these months, averages are calculated with 17.9 days. Cases for which too many pixels are not observed by TROPOMI in the internal mask occur more frequently than cases with strong winds from Bahrain. Overall, we consider most of the inferred monthly averages to be robust. However, at the small scale, there are a small number of pixels with a constant absence of reliable VCD estimations due to low-quality measurements, resulting with pixels having estimations of NO$_x$ with a poor reliability. The treatment of such pixels is precised in Section 3.2.7-C.

3.2.7-B Spatial distribution of NO$_x$ emissions

We use the flux-divergence model to obtain NO$_x$ emission maps within our domain. For each applicable day (as described in Section 3.2.7-A), a background is calculated using the external mask and daily emissions are estimated. These daily emissions are then averaged to obtain a representation of the emissions at 13:30 LT on a monthly scale. For October 2022, a maximum of 25 daily emissions have been average to calculate the corresponding mean monthly emissions map, which is displayed in Figure 3.14. When the transport term is integrated over large spatial scales, it cancels out due to the mass balance in the continuity equation between NO$_2$ sources and NO$_2$ sinks. Although the sink term is responsible for most of the total NO$_x$ budget within the domain, the transport term can reach high values at small scale, highlighting hotspots where emissions are concentrated. Such hotspots comprise gas power plants in the north-eastern part of the country and industrial facilities in the south-east. High emissions are also observed in Doha, but in that case, the sink term accounts for most of the NO$_x$

budget due to the spread of sources in the urban area. The west part of the country, where two cement plants are located, also shows significant emissions. High emissions outside of Qatar are observed in the urban areas of Manama (Bahrain) and Dammam (Saudi Arabia). In the south-eastern corner of the domain, an area of high emissions also seems to stand out from the desert. This area corresponds to a cross-border centre between Saudi Arabia and the United Arab Emirates. It is possible that an important road traffic there is responsible for such emissions, but we have no information to support this hypothesis. Finally, we observe high emissions at sea, up to about 30 km from the east coast of the country. These emissions, of about 2.0×10^{15} molecules.cm^{-2}.h^{-1}, cannot be solely attributed to shipping activity (Rey-Pommier et al., 2022). Because in this region, the centre of the 40 km × 44 km CAMS pixel is close to the coast, the NO_2 lifetime is probably underestimated. The rest of the domain has relatively low emissions, which is consistent with the absence of major sources of NO_x.

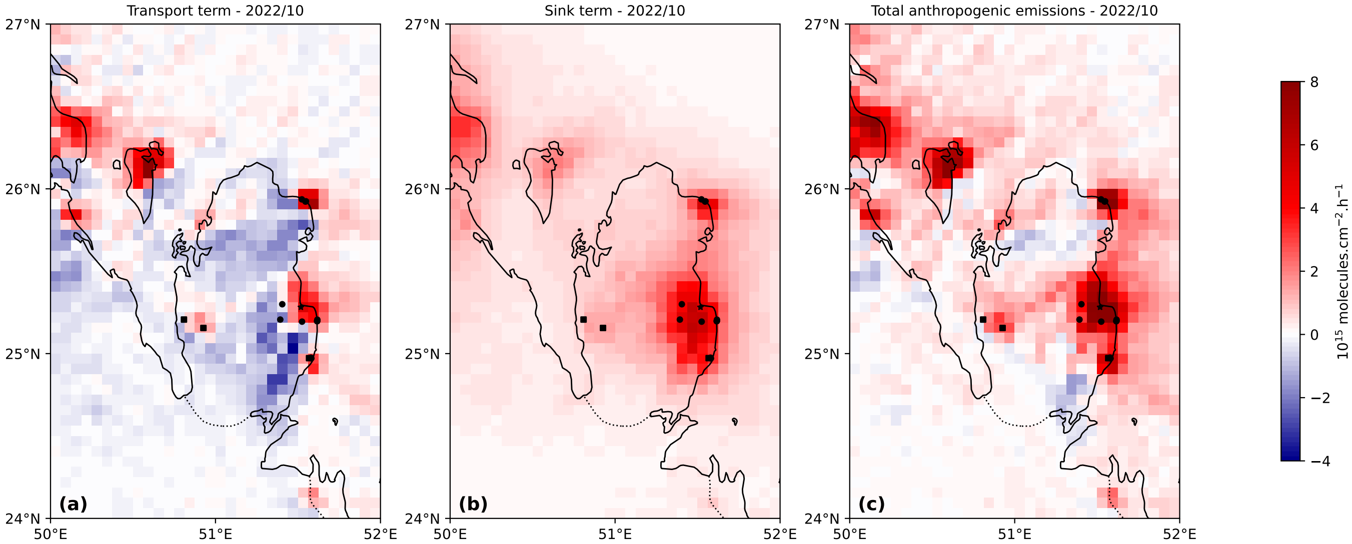

Figure 3.14: Mean NO_x emissions above Qatar (13:30 LT): transport term (a), sink term (b), and resulting emissions (c) for October 2022. Power plants are denoted with dots, cement plants with squares, and Doha's city centre with a star.

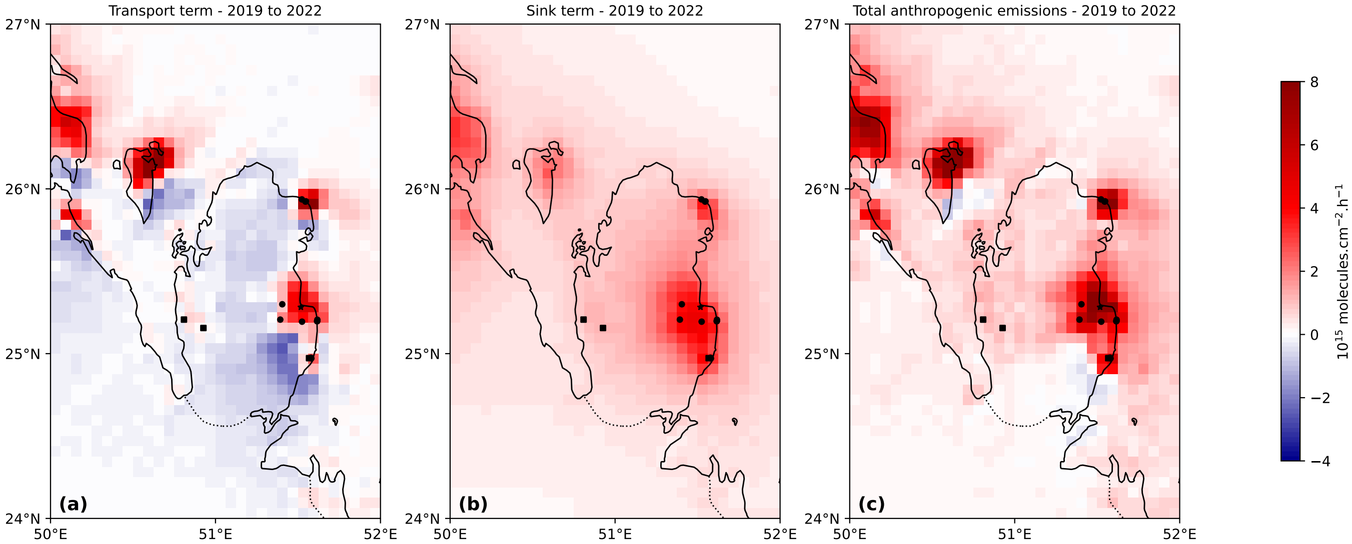

Figure 3.15: Mean NO_x emissions above Qatar (13:30 LT): transport term (a), sink term (b), and resulting emissions (c) for the 2019-2022 period. Power plants are denoted with dots, cement plants with squares, and Doha's city centre with a star.

Nevertheless, it can be noted that inferred emissions in the domain remain relatively noisy. From monthly maps, we calculate average emissions at 13:30 for the period 2019-2022, which are displayed on Figure 3.15. The hotspots identified earlier remain visible with a improved signal-to-noise ratio. In particular, emissions in the north-east region are superior to 3.0×10^{15} molecules.cm^{-2} for only 7 pixels, which are among the pixels closest to the power plants in the region. In the eastern part of the country, NO_x emissions reflect the main directions of urban expansion in Doha (from the coast towards the west and the southwest), with emissions ranging from 2×10^{15} molecules.cm^{-2}.h^{-1} to 10×10^{15} molecules.cm^{-2}.h^{-1}. The desert areas display very low emissions (about 0.2×10^{15} molecules.cm^{-2}.h^{-1}), indicating a slight overestimation of the average sink term or an underestimation of the NO_2 background. Emissions at sea remain abnormally high on the east coast, but the effect is lower than what is observed on Figure 3.14. However, unlike for October 2022, for which the emissions from cement plants could be identified, we observe low emissions in the western part of the country.

3.2.7-C Availability of TROPOMI data above industrial sites

High-quality measurements by TROPOMI are infrequent above the western and south-eastern part of Qatar, with pixels regularly corresponding to measurements with $q_a < 0.75$. For these pixels, the inferred emissions are only calculated with an average over a very small number of measurements. In many cases, no measurements are available, and emissions can not be attributed to the pixels. Figure 3.16 shows the mean TROPOMI coverage over the domain for year 2020 counted as fraction of days with $q_a < 0.75$ within the year. In addition to the west and south-east (corresponding to the southern part of Doha) already identified, the north-east is also affected, but to a lesser extent. This situation is the same for years 2019 and 2021, and the identified areas have a fraction of observable days lower than 40 %. The situation is different for year 2022, during which the west has a fraction of about 70 % and the south-east 50 % (see Supplementary Materials). The effect on total inferred emissions is not negligible, since pixels that are concerned include intensive emitters, such as an industrial area in the south-east and the two large cement plants in the west. For instance, during the 36 months of the period 2019-2021, inferred emissions above these cement plants are lower than 1.5×10^{15} molecules.cm^{-2}.h^{-1} for 8 months and greater than this value for 8 months. Emissions could not be inferred for at least one of the plants for the remaining 20 months. Conversely, emissions could be inferred for 10 months out of 12 in 2022, and they were higher than 1.5×10^{15} molecules.cm^{-2}.h^{-1} for 6 of those months. In the TROPOMI products, the value of q_a includes automated quality assurance parameters related to different algorithms concerning the presence of clouds, aerosol particles, pressure levels and other physical quantities. For situations with $q_a < 0.75$, retrievals are only sensitive to the NO_2 concentrations above the clouds and will depend on model assumptions for the missing part. They still contain useful information, but this information should be carefully interpreted. Here, all areas that are affected by these low values are located near the coasts. These areas are not characterised by persistent clouds, but they are all located within or close to urban or industrial centres, in which aerosol emissions can be high. However, other regions in Qatar and the neighbouring countries are characterised by high emissions of aerosols without q_a values being particularly high there. For instance, many studies have been providing estimates of NO_x emissions in Riyadh (Beirle et al., 2019) without indicating anything similar. We observe that these high frequencies of low q_a values are found in several urban and industrial areas on both coasts of the Persian Gulf (especially in Saudi Arabia, United Arab Emirates and Iran). This suggests that the identified persistent low values for q_a come from the calculation of one or several quality assurance parameters. Because the areas displaying low values usually have a rectangular shape, it also suggests a low resolution for these parameters.

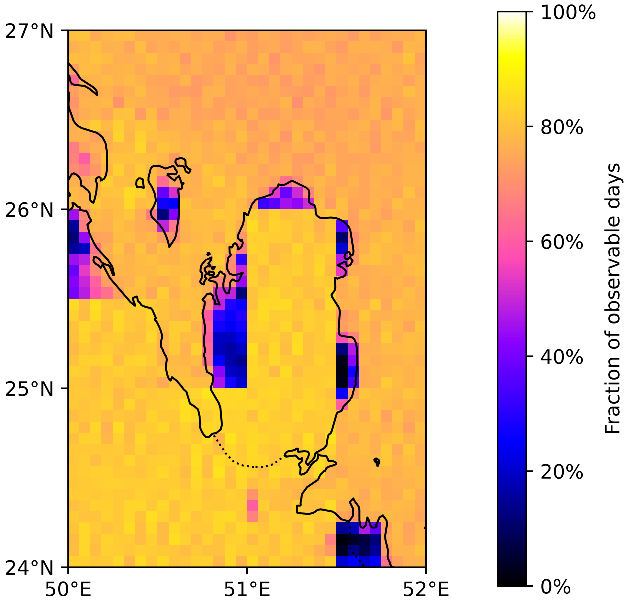

Figure 3.16: TROPOMI observation density for 2020.

Here, we observe that the use of the OFFL stream (version 2.3.1) from November 2021 to October 2022 generates less pixels for which the value of q_a falls below 0.75 than the use of the S5P-PAL data from January 2019 to October 2021. Furthemore, the last two months of 2022, calculated with the version 2.4.0 of the NO_2 product (operational since July 2022), do not show any area with particularly low quality flag values (see Supplementary Materials). The latest version of the user manual indicates that in this last version, the surface albedo climatology (SAC) used in the NO_2 fitting window and derived from OMI and GOME-2 was replaced by a SAC derived from TROPOMI observations (Eskes et al., 2022). This new TROPOMI SAC is consistently applied in the cloud fraction, the cloud pressure retrievals, and in the air-mass factor calculation. In the low-q_a areas identified on Figure 3.16, it is therefore possible that high levels of aerosol-generating industrial activities, in a small number of pixels in the grid, results in a value of q_a below 0.75 in those pixels, but also in all the surrounding pixels due to the low resolution of the parameter responsible for exceeding the threshold, without these pixels being located over particularly emissive zones. This effect would be absent in the version 2.4.0 of the TROPOMI product. For the first 34 months of our study, the calculated monthly emissions for these areas would be then underestimated, because they would correspond to the days with low industrial activity.

To evaluate the impact of this effect, we apply the same model using a threshold value of q_a corresponding to 0.7. This includes many pixels that would be rejected with a threshold of 0.75. As the TROPOMI manual recommends not to use this threshold level, we do not consider these emissions to be representative of human activity in Qatar, and they are not treated as emissions estimates. Nevertheless, it allows us to evaluate the effect of non-detection of cement plants and power plants in the south-east of the domain. The use of a threshold value of $q_a = 0.7$ increases the inferred fluxes by 43.8 % above cement plants in the west, and by 33.4 % above the industrial area in the south-east. Fluxes for the Ras Laffan area in the north and central Doha, which are less affected by the effect described here, are increased by 2.6 % and 3.0 % respectively. It is difficult to determine whether these increases are realistic because they were obtained using columns where NO_2 might have been estimated above aerosol and cloud layers. However, they indicate that our model, ran with TROPOMI data before November 2021, leads to a systematic underestimation of NO_x emissions in two of the four most NO_x-intensive areas of the country. We note however that on average, these increases are compensated: with a threshold of $q_a = 0.7$, total fluxes within the internal mask are reduced by 2.1% because fluxes outside the main emissive areas, which comprises most of the mask, are reduced by about 17%.

3.2.7-D Weekly cycle

In Qatar, the official rest day is Friday, and the economic activity of the country is lower during this day than during the other days of the week. We therefore try to characterise this feature, by evaluating the weekly cycle of NO_x emissions. We use the TROPOMI-inferred emissions to obtain averages per day of the week. We use the flux-divergence method to calculate the emissions within the internal mask. We remove the days for which most of the area contains poor quality measurements and those for which the wind from Bahrain blows to the south-east, in the same way as it was conducted in Section 3.2.7-A.

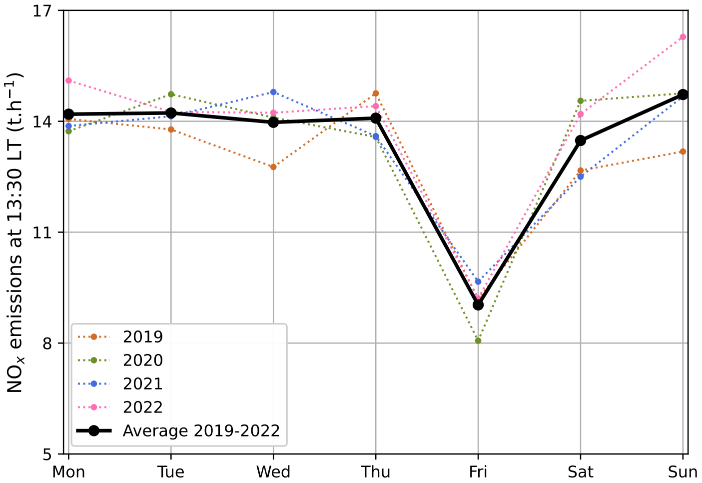

Figure 3.17: Mean weekly profiles of anthropogenic NO_x emissions at 13:30 LT in Qatar using TROPOMI observations for 2019 to 2022. The average emissions for the four-year period is displayed with the black line.

For a given day, the empty pixels (i.e. those to which it was not possible to assign emissions) are filled with the average of the emissions obtained for the remaining pixels. This choice leads to an underestimation of the emissions when the main emitting areas are covered by clouds or aerosols, and to an overestimation in the opposite case. To limit this effect, we remove from our estimate of annual averages the emissions below the 5th percentile and above the 95th percentile. Figure 3.17 shows the resulting daily emissions for the four-year period. Each year, a Friday minimum is observed, defining a weekly cycle. This trend is also observed for mean NO_2 column densities, but not for OH concentrations. It is also more pronounced for residential areas for which the Friday activity is 40% lower than the weekly average. Conversely, the effect is weaker above the power plants in the north of the country, which are located more than 30 km away from major residential areas (see Supplementary Materials). At the scale of the country, Fridays have average emissions of 9.04 $t.h^{-1}$, which is lower than average emissions for the rest of the week, which reach 14.15 $t.h^{-1}$. In Middle-Eastern countries, this "week-end" effect had already been inferred from satellite measurements by Stavrakou et al. (2020) and Rey-Pommier et al. (2022), and from ground measurements by Butenhoff et al. (2015) on NO_2 concentrations, but with a lower difference between Fridays and the other days.

3.2.7-E Scaling of emissions and annual cycle

In this study, we estimate the emissions at around 13:30 LT, which corresponds to the moment when TROPOMI overpasses the country. However, anthropogenic activity is not uniform throughout the day, and the emissions inferred from parameters calculated at 13:30 do not correspond to the average emissions of the country. Using the power consumption data from Bayram et al. (2018), Figure 3.18 shows the mean load curve for the country on April 2016, July 2016, October 2016 and January 2017. These curves show that the average power injected into the grid is slightly lower than the power injected at 13:30. The ratio between the two powers is minimal in June and reaches 0.911, and maximal in February where it reaches 0.976 (see Supplementary Materials). Moreover, according to the traffic congestion index in Doha (Tomtom, 2023), the road traffic around 13:30 shows a congestion peak, slightly lower than the other peaks that occur at the beginning and the end of daytime. This suggests that the average emissions from the road transport sector are also close to those at 13:30, with a similar ratio to that of the power sector.

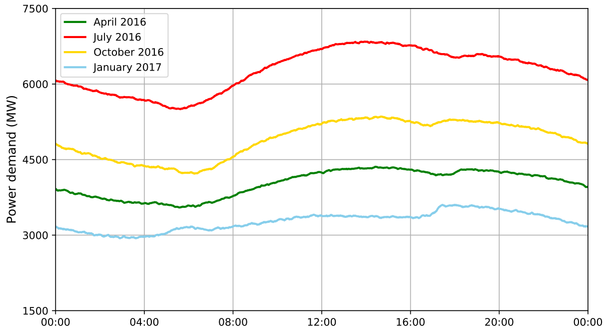

Figure 3.18: Monthly mean power demand in Qatar for four different months in 2016-2017.

We therefore re-scale the inferred NO_x emissions at the scale of the country by multiplying the monthly estimate for 13:30 with the power ratio to estimate mean monthly emissions. We acknowledge this is a simplification: the power sector has a variable emission factor due to the different technologies in the power plants that are used to respond to the electricity demand over the year, and the road congestion level does not necessarily reflect traffic emissions. Moreover, other sectors, such as cement production, whose seasonality is unknown to us, might behave differently.

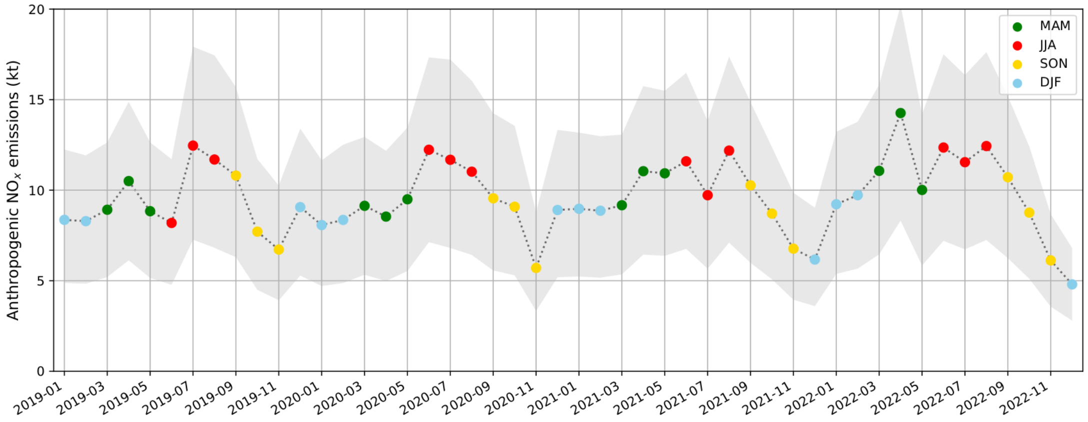

Figure 3.19: Total TROPOMI-derived anthropogenic NO_x emissions in Qatar from 2019 to 2022 using the flux-divergence method. The colors are used to illustrate seasonal variations.

Within the internal mask, Figure 3.19 shows total NO_x emissions in Qatar using our method. Since the NO_2 background has been removed from VCD calculations, the total NO_x budget calculated for each month corresponds to the NO_x production by human activities. The annual variability is marked, with higher emissions in summer and lower emissions in winter. On average, NO_x emissions reach 9.56 kt per month. With mean emissions of 9.29 kt and 10.08 kt, 2019 and 2022 appear to be the years with lowest and highest mean emissions respectively. No seasonal cycle seems to appear for VCDs, except above the greater Doha area which undergoes NO_2 levels that are about 23% higher than the 2019-2022 average from October to January, while they are 27% lower from June to August. To obtain the observed cycle in NO_x emissions, these differences in VCDs over Doha suggest a more intense oxidation in summer, which is captured by higher OH values for summer months. This is consistent with nonlinear effects in the NO_2 loss rate, with an absolute growth rate higher for OH than for NO_2

VCDs at high NO_2 levels inside the plume (Valin et al., 2011). However, because wind speeds tend to be higher during summer in Qatar, the observed variations in VCDs over Doha can also be partially explained by a spread of the pollution beyond the shores of the country. The uncertainties, detailed in Section 3.2.9, are higher for the months for which emissions could not be attributed for the western and south-eastern parts of the territory. This hinders year-on-year comparisons. Consequently, although emissions in the March/April/May (MAM) 2020 period are 96 % and 87 % of the level of emissions in MAM 2019 and MAM 2021 respectively, we can not assert whether this effect can be attributed to the restrictions put in place from March to May 2020 to tackle the Covid-19 pandemic. This caution is all the more necessary as these restrictions have been less stringent than in other countries (Hale et al., 2021). Similarly, higher emissions during 2022 could be due to the different values reached by q_a in the 2.4.0 version of the TROPOMI product with respect to the 2.3.1 version. However, it can not be excluded that these higher emissions were due to a more intense activity in 2022 in the context of organising the FIFA World Cup.

3.2.8 Comparison with air pollution inventories and electricity generation data

As Qatar is a small country with an undiversified economy, the annual cycle of the TROPOMI-inferred emissions can be interpreted. Reported emissions reached 163 kt in 2007, but a significant part did not take place within the terrestrial borders of the country. To compare such reported emissions with those calculated within the internal mask, emissions from upstream oil and gas operations (41.86 kt), which mostly take place offshore, must be removed from the previous budget. We also remove emissions from navigation (4.35 kt), civil aviation (3 kt) and fugitive emissions (4.28 kt). Reported terrestrial emissions therefore reach the approximate value of 109.51 kt for 2007, i.e. an average of 9.13 kt per month, with the main NO_x emitting sectors being power generation, transport and cement. Total emissions, as well as and their share in the total NO_x budget, may have varied since then. This section confronts our estimated emissions with local electricity generation and existing global inventories in order to provide a sectoral approach of NO_x emissions and their annual variability.

3.2.8-A Comparison with electricity generation data

In Qatar, all electricity production comes from gas-fired power plants, with three plants located in the north-east (Ras Laffan area). Other gas power plants are located in the urban area of Doha and in the south-east of the country. Figure 3.20 shows the total electricity production and the share of the power plants in Ras Laffan between 2019 and 2021 as provided by Kahramaa. Data regarding the electricity generation by power plant in 2022 is not yet available. The electricity generation is 2 to 2.5 times higher during summer months than during winter months. This increased generation is mostly due to the use of air conditioning (Gastli et al., 2013), which is also captured on Figure 3.18.

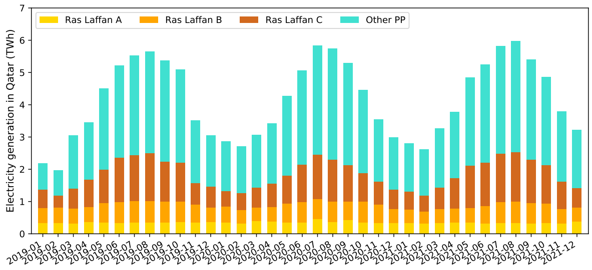

Figure 3.20: Electricity generation in Qatar from 2019 to 2021 according to the Planning and Statistics Authority reports. Generation from to the three Ras Laffan power plants, in the north-eastern part of the country, are displayed in yellow, orange and brown, while generation from other power plants are displayed in light blue.

The inferred emissions have a behaviour that is similar to electricity generation, with higher emissions in the warmer months. The comparison of the time series of NO_x emissions and the electricity generation data for the four-years period provides a correlation coefficient of $R^2 = 0.400$. This value is relatively low, but it should be noted that monthly emission maps can be very noisy due to averaging over too few days. For instance, on April 2019, the spatial distribution of emissions for this month shows non-negligible emissions in the central part of the country where no significant emitter is located. We can therefore consider that the average is not calculated with enough data to limit noise effects. When we only keep in the analysis the mean monthly emissions calculated on the basis of more than 18 days (the average over the 4-year period being 17.1), 19 points out of 48 are retained and the correlation is improved, with a coefficient which then reaches $R^2 = 0.657$, with a slope of 1.773 $t.GWh^{-1}$. This value would be equal to the emission factor of the power sector, provided that it was the only source of variable NO_x emissions during the months that are considered. This value must therefore be considered as an upper limit estimate. Figure 3.21 shows the comparison between electricity generation and emissions in the two cases. The points that are retained in the second case mostly correspond to months with high emissions, notably in autumn. Among these 19 points, only 2 correspond to winter or spring months (December to May) whereas 7 correspond to summer months (June to August) and 10 to autumn months (September to November).

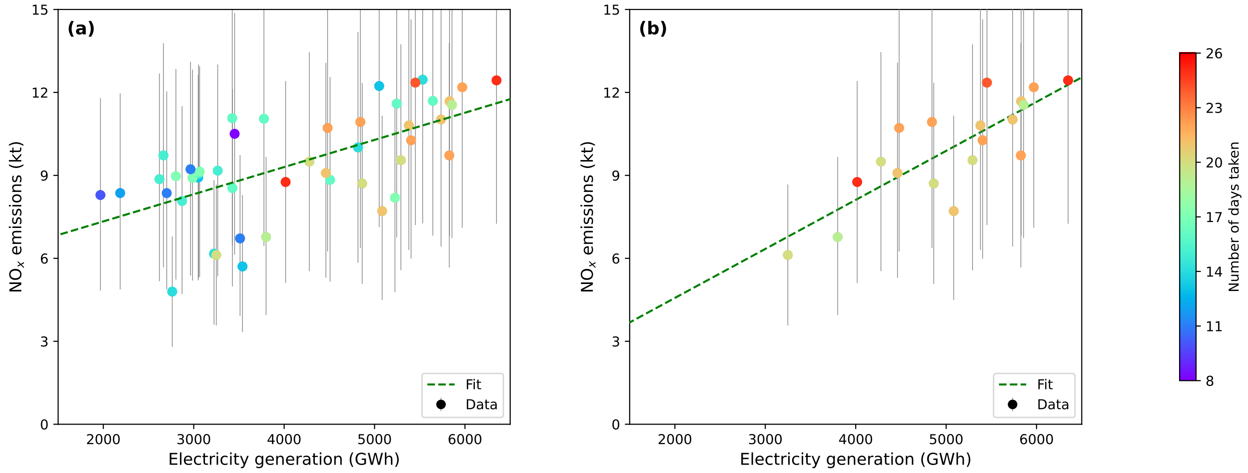

Figure 3.21: Comparison between monthly TROPOMI-derived NO_x emissions for the entire Qatar territory and corresponding electricity generation according to Planning and Statistics Authority reports. A linear regression between the two datasets is displayed with a green dashed line. (a) All months in the period 2019-2022 are included. (b) Months that are included are those for which inferred total emissions have been obtained with an averaging of 18 daily emissions or more. The color scale represents the number of days involved in the calculation of points.

The improved correlation must be interpreted with caution, but it might be possible that other NO_x-producing sectors have a seasonality which is the opposite to that of the power sector. If the transport sector has no particular seasonal cycle, it is possible that industry has a higher production during winter and spring months, leading to higher industrial NO_x emissions during this period. As mentioned before, mid-day temperatures in summer are high in Qatar, preventing labor in outdoor activities, and this interpretation could be investigated. With the exception of the two cement plants in the west of the country, most of the industries are located in the urban area of Doha or Ras Laffan, where emissions from several sectors overlap over distances smaller than the resolution of TROPOMI.

The method can also be applied to a smaller area of the domain. The north-eastern part of the country is interesting in this respect: it is very sparsely populated and the human activity there is mainly associated with oil and gas activities and the production of electricity. In this region, three power plants (Ras Laffan A, B and C) have a total capacity of 3.35 GW, and are responsible of about 45 % of the total electricity generation throughout the year, as shown on Figure 3.20. These power plants are independent water and power plants (IWPPs), serving as both desalination plants and power plants. Other than these plants, the region also has gas liquefaction facilities, as Qatar is a major producer of LNG. Refineries are also present. In the life cycle of gas, only extraction and combustion are high NO_x-emitting processes: emissions from midstream (liquefaction and transport) and downstream (refining) activities are 20 to 30 times lower per unit of fuel (Marais et al., 2022). As the oil and gas extraction processes are located outside this area (mostly offshore), it can be considered that the majority of the NO_x emitted in this region come from the combustion of gas in the power plants. This is not the case for other power plants in the country, which are located in urban areas where emissions from different sectors overlap. We focus on this area and calculate the corresponding monthly emissions. The three power plants are located within the same pixel, and the difficulty for TROPOMI to visualise this region with good quality measurements is less pronounced than for other regions identified in Section 3.2.7-C. Because Ras Laffan plants are not the only ones participating in the country's electricity generation, the use of load curves is not longer valid to infer total emissions on a given period, and only emissions at 13:30 can be considered. Assuming a correct calculation of emissions, the observed emissions display a Gaussian distribution around the power plants. Using a zonal cross-section of obtained emissions in a 28-km band centered around the mean latitude of the plants, we estimate the mean emissions by fitting a Gaussian curve $\mathcal{G}(\lambda) = e_0 + \frac{E_0}{\sigma\sqrt{2\pi}} \exp(-\frac{(\lambda-\lambda_0)^2}{2\sigma^2})$ on the profile, with e_0 the observed emissions above desert areas and seas, λ_0 the mean longitude of the power plants, σ the standard deviation (measured as an angle) and E_0 the total emissions. λ is the zonal angle. The best approximation is displayed on Figure 3.22.

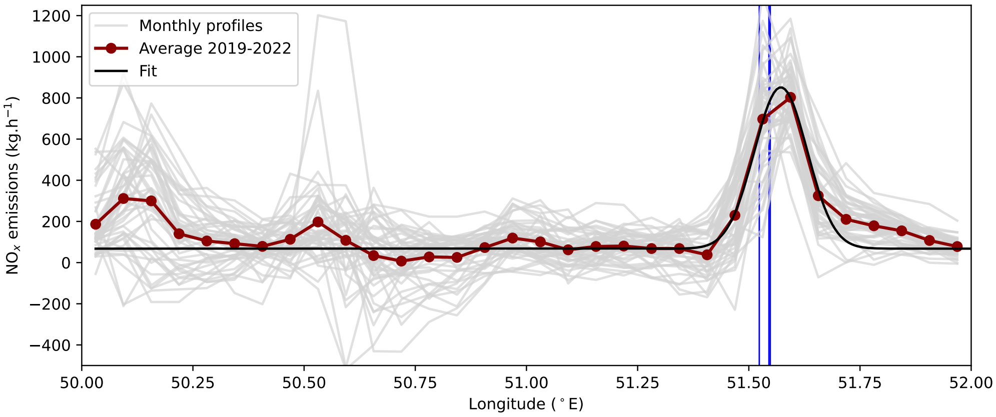

Figure 3.22: Zonal cross sections of 13:30 NO_x emissions at the latitude of Ras Laffan power plants. The average profile for 2019-2022 is displayed in red, and the corresponding Gaussian fit in black. Individual monthly profiles are displayed in light grey. The positions of the three power plants are marked with vertical blue lines.

Monthly profiles peak around the location of the power plants whose height vary without displaying any particular seasonality. The fit of the averaged profile leads to a low positive background of 67.8 kg.h^{-1} per unit of band surface, i.e. about 0.390 mg.m^{-2}.h^{-1}, and average emissions of 1.86 t.h^{-1} for the three power plants. This value has an order of magnitude similar to that of emissions for power plants in other regions estimated with the flux-divergence method (de Foy, Schauer, 2022; Sun, 2022). In particular, it corresponds approximately to the value reported by Beirle et al. (2023), which estimated an output of 1.81 t.h^{-1}, despite various differences in the parametrisation of the method.

Here, only a small part of the domain is considered, for which the power sector is by far the major contributor to NO_x emissions. It is therefore not necessary to consider the seasonality of the other sectors in the estimation of an emission factor, as it was done earlier when the emissions of the whole domain were considered. However, as the scaling assumption can no longer be used, other assumptions must be made. One assumption would be that these plants serve as intermediate-load power plants: 13:30 being a peak of consumption at any time of the year, the Ras Laffan plants would be running very close to their maximum capacity, and the annual variability of power generation by the three plants observed in Figure 3.20 would be due to the decrease of power generation during low demand hours. This would be consistent with the lack of seasonality detected in the monthly profiles in Figure 3.22. In this case, comparing the emissions at 13:30 with the total capacity of the plants provides an emission factor of 0.557 $t.GWh^{-1}$. As the total capacity is used in the calculation, this value must be considered as a lower limit estimate.

Another possible assumption is that the three plants are used as peak-load power plants: in this case, they would be used at 13:30 to respond to the daily peak. This use would increase with the height of the peak, and therefore with the temperature. In this case, the annual variability of power generation by the three plants would be due to their variable use at 13:30. The absence of a clear annual variability in our TROPOMI-inferred emissions would be explained by the large uncertainties in the calculation of our emissions, which concern only 6 pixels of our domain. Here, the large share of the three power plants in the electricity production seems to rule out a peak-load functioning. However, it is also possible that some of the plants correspond to different functions within the national grid.

3.2.8-B Comparison with emission inventories

We compare TROPOMI-derived NO_x emissions to inventory emissions in EDGARv6.1 (for 2018) and CAMS-GLOB-ANT_v5.3 (from 2019 to 2022). The two inventories provide 0.1°×0.1° sectorial gridded emissions on a monthly basis. After aggregating the different sectors of activity, CAMS-GLOB-ANT and EDGAR inventories directly provide the anthropogenic NO_x emissions over the same domain. Both inventories display NO_x emissions that are significantly higher than our estimates. According to CAMS-GLOB-ANT, the annual emissions for 2019, 2020, 2021 and 2022 are 191.7, 191.8, 192.5 and 193.7 kt respectively, whereas we only estimate emissions of 111.5, 111.8, 114.4 and 121.0 kt for these same years. According to EDGAR, NO_x emissions are even higher, reaching 193.8 kt in 2018. It should be noted that the same version of EDGAR estimates emissions of 111.1 kt in 2007, which is similar to the reported terrestrial emissions for the same year, as well as our estimated emissions for 2019-2022.

The sectoral shares of emissions estimated by EDGAR and CAMS-GLOB-ANT differ. In EDGAR, the transport sector accounts for 42 to 54 % of the emissions, whereas it has a nearly constant share of 50 % in CAMS-GLOB-ANT. In the remaining emissions, industry accounts for about 2.8 kt per month in both inventories. These emissions are slightly lower during summer which can be interpreted like a lower production due to a reduced outdoor activity at high temperatures. The corresponding share is more variable in EDGAR (between 13 and 23% of terrestrial emissions) than in CAMS-GLOB-ANT (about 17% of terrestrial emissions). These values are lower than reported industrial shares for 2007, where the cement sector alone accounted for 23.4% of total emissions. Finally, power sector emissions in both inventories account for a significant share of total emissions, but with a higher value for EDGAR (35 % of the total budget for 2018) than for CAMS-GLOB-ANT (32 % of total emissions in 2019-2022). The two values are respectively higher and lower than the reported share for power emissions, which was estimated at 28.1 % for terrestrial emissions in 2007. Another major difference concerns the seasonal cycle of those power emissions. The two inventories do not show any correlation with the corresponding electricity generation data. However, in 2018, EDGARv6.1 shows a pronounced variability, with extremes of 7.0 kt emitted in May and 3.5 kt in December (see Supplementary Materials). The ratio between these two values remains lower than the ratio between the extremes of the monthly electricity generations, which has varied between 2.2 and 2.8 over the last four years, but it highlights a difference with the previous version of EDGAR (EDGARv5.0) which showed almost no seasonality in power emissions. This lack of seasonality is also found in the emissions of CAMS-GLOB-ANT_v5.3, which uses EDGARv5.0 as a basis. We also note that while these seasonality differences between TROPOMI-inferred emissions and inventories were already highlighted for the previous versions of EDGAR and CAMS-GLOB-ANT in Egypt, the difference between mean annual NO_x emissions was much lower (Rey-Pommier et al., 2022).

3.2.8-C Emission factor for the power sector

The report for emissions in 2007 indicates an emission factor for the power sector of 0.392 $t.GWh^{-1}$, and the corresponding power plants are still operating today. In the previous sections, we estimated an emission factor of 1.773 $t.GWh^{-1}$ using all monthly emissions in the internal mask and assuming the power sector was the only source of variable NO_x emissions. We also estimated a value of 0.557 $t.GWh^{-1}$ for Ras Laffan power plants using mean emissions at 13:30 under the hypothesis of a intermediate-load power plant functionning. To infer emission factors from inventory estimates, power emissions in EDGAR and CAMS-GLOB-ANT and total electricity generation provided by the Planning and Statistics Authority (PSA) between 2018 and 2022 can also be used to infer emission factors of 1.406 $t.GWh^{-1}$ and 1.219 $t.GWh^{-1}$ respectively. Table 3.3 summarises all the different emission factors that have been calculated. Even though EDGAR's emission factor is particularly high compared to other estimates, the five listed values are plausible, as the majority of gas-fired power plants have a NO_x emission factor value between 0.1 and 10 $t.GWh^{-1}$ (Miller, 2004).

Year(s)	**Source**	**Data for NO_x emissions**	**Data for power**	**Method**	**Emission factor ($t.GWh^{-1}$)**
2007	All PPs	Reported emission factor (Initial National Communication to the UNFCCC)			0.392
2018	All PPs	EDGARv6.1 inventory NO_x emissions	Annual power generation (PSA)	Ratio between total power emissions and electricity generation	1.406
2019-2022	All PPs	CAMS-GLOB-ANT_v5.3 inventory NO_x emissions	Monthly power generation (PSA)	Ratio between total power emissions and electricity generation	1.219
2019-2022	Internal mask	Monthly TROPOMI-inferred NO_x emissions	Monthly power generation (PSA)	Linear fit between monthly power emissions and electricity generation	1.773
2019-2022	Ras Laffan power plants	13:30 TROPOMI-inferred NO_x emissions	Power plant capacities (PSA)	Gaussian fit of zonal cross-section for Ras Laffan power plants	0.557

Table 3.3: NO_x emission factors for electricity production inferred from different sources and methods. The value is calculated from monthly emissions and electricity generation, fluxes at 13:30 and capacities or directly reported by Qatar authorities.

The comparison between these different emission factors should be made with caution. The factor reported by the report for 2007 emissions takes into account all of the power plants in the country, the oldest having been built in 1980. Moreover, some units of one of the Ras Laffan plants were built between 2010 and 2011, i.e. after the publication of the report. It is also possible that other power plants have been upgraded in the last years. Finally, the reported emission factor for 2007 accounts for the public electricity production and the water production, but the monthly reports from Kahramaa do not specify whether the electricity generation from the Ras Laffan power plants account for the large amount of electricity that is used in desalination processes (Kahramaa, 2023). Monthly reports show that the water production from the IWPPs in the country does not have a clear annual cycle, the production generally ranging between 50 and 60 millions of cubic meters per month in the entire country. The amount of electricity needed for this water production varies with the technologies used in the IWPPs, and accounts for about 20 % of the consumption in total electricity (Okonkwo et al., 2021). Consequently, if the electricity used for water production is not accounted for in the electricity generation for monthly reports, then all inferred emission factors are overestimated.

3.2.9 Uncertainties and assessment of results

The long time series of average NO_2 concentrations in cities in several countries with similar economic and industrial developments (Dubai, Manama, Kuwait City) show a stagnation of NO_x levels over the period 2005-2014 (Lelieveld et al., 2015). It is therefore not clear whether the NO_x emissions of the country in 2019-2022 have increased from their value in 2007, as suggested by CAMS and EDGAR, or decreased, as our TROPOMI-based estimates seem to suggest. We do not know exactly how parameters in EDGARv6.1 and CAMS-GLOB-ANT_v5.3 are estimated in order to calculate NO_x emissions, which means we cannot conduct a discussion on such bottom-up estimates accordingly. However, we can identify several factors that could influence of our top-down NO_x emissions. The following aspects can be considered:

- As discussed in Section 3.2.7-C, a large portion of the territory, which includes some of the most emissive facilities in the country, is not visible by TROPOMI with high-quality data, and emissions from very emissive pixels might be underestimated. As this situation only occurs from 2019 to 2021, the magnitude of the induced underestimation is the difference between inferred emissions in 2022 and inferred emissions in 2019-2021, i.e. about 6 %.

- TROPOMI retrievals are sometimes biased due to poor estimation of the air mass factor or local effects under particular vertical distribution conditions (Griffin et al., 2019; Lorente et al., 2019; Judd et al., 2020; Wang et al., 2021a). It should be noted that the latest versions of TROPOMI (v2.x) have tropospheric VCDs that are between 10 % and 40 % larger than the first versions (v1.x), depending on the level of pollution and season (Van Geffen et al., 2022). The chemical transport model TM5, which is used in the retrieval of the operational TROPOMI data, has been shown to under-estimate surface level pollution while over-estimating NO_2 at higher levels above the sea (Latsch et al., 2023; Rieß et al., 2023). Such a bias is probably not negligible and probably accounts for significant part of the difference between our estimates and inventories, but also within our estimates, as surface albedo values differ between desert areas and urban zones.

- The vertical levels on which parameters in Equation 3.10 are estimated might be incorrect. Most studies use values averaged within the planetary boundary layer, which is higher in summer (Lorente et al., 2019; Lama et al., 2020), or averaged within a fixed vertical layer (Beirle et al., 2019). Here, we interpolated the fields of $\mathbf{w}$, T and [OH] using the first pressure levels in ERA5 and CAMS at a mean pressure of 987.5 hPa. As Qatar is a flat country, this level corresponds to an altitude between 220 and 250 m. Because vertical transport of NO_x, which is emitted mainly from combustion engines and industrial stacks, is generally minor compared to horizontal transport (Sun, 2022), NO_x is confined to these first hundred metres above ground level. In Egypt, Rey-Pommier et al. (2022) have shown that the consideration of higher levels decrease mean temperature which tends to increase emissions, balanced by the decrease of mean OH concentrations with altitude which tends to decrease the sink. The net effect would be a decrease of emissions of a few percents during most of the year.

- The NO_x:NO_2 ratio might locally be underestimated. The conversion of NO to NO_2 by the reaction with O_3 is balanced by the photolysis of NO_2 which reforms NO, leading to a stabilisation of the ratio a few kilometers downwind the source. The stationary regime can also be displaced by the presence of volatile organic compounds. Near important sources of emissions, which mainly produce NO, a high NO_x:NO_2 ratio should be expected. We can therefore consider that for pixels containing hotspots close to their boundaries, such as power plants, it should be much higher than the chosen value of 1.32 (Hanrahan, 1999; Goldberg et al., 2022), leading to an underestimation of our emissions locally. With power plants concentrating a large share of the NO_x emissions in our study, this effect is probably not negligible and probably accounts for a large part of the difference between our estimates and inventories.

- The sink term might be underestimated or overestimated. If the transport term is assumed to be estimated correctly, an underestimation of the sink term would lead to significant negative emissions in many parts of the domain, while an overestimation would lead to non-emitting areas with NO_x emissions that are higher than noise. None of these effects seem to appear for averaged emissions for the 2019-2022 period, but monthly maps show significant portions of the territory with negative emissions in winter and spring months, while summer months display abnormally high emissions over deserts and seas. Those effects are not visible for most of the autumn months. We can therefore assume that the sink term is slightly underestimated in winter and spring months and overestimated in summer months, due to errors in the estimation of OH in CAMS and/or the presence of additional sinks in summer. Accounting for this effect would not change the averaged emissions for the period 2019-2022, but would reduced the seasonality observed on Figure 3.15. The emission factor calculated from emissions in the internal mask would also be reduced.

These effects must be taken into account for understanding the differences between our model, reported emissions and inventory emissions. The uncertainties used here must also be considered. NO_x emissions, as estimated with the flux-divergence method, are calculated with the use of several quantities. The uncertainty ranges shown in Figures 3.19 and 3.21 are calculated from uncertainty statistics whose references are presented in this section, assuming that they correspond to standard deviations. The uncertainty of tropospheric NO_2 columns under polluted conditions is dominated by the sensitivity of satellite observations to air masses in the lower troposphere, expressed by the AMF, and the corresponding relative uncertainty is of the order of 30 % (Boersma et al., 2004), and is likely related to the a priori profiles used within the operational retrieval that do not reflect well the concentration peak of NO_2 near the ground. For the Middle East region, the impact of the a priori profile is less critical, as surface albedo is generally high and cloud fractions are generally low. Thus, we do not expect a bias of this importance, and consider a relative uncertainty of 30 % for the tropospheric column as reasonable. For wind module, we assume an uncertainty of 3 $m.s^{-1}$ for both zonal and meridional wind components. For OH concentrations, the analysis of different methods conducted by Huijnen et al. (2019) showed smaller differences for low latitudes than for extratropics, but still significant. We thus take a relative uncertainty of 30 % for OH concentration. For the reaction rate k_{mean}, we use the value of the corresponding relative uncertainty, as estimated by Burkholder et al. (2020).

3.2.10 Conclusion

In this study, we investigated the potential of a top-down model of NO_x emissions based on TROPOMI retrievals and a flux-divergence scheme applied at high resolution over Qatar for the last four years (2019-2022). This scheme requires different parameters to be calculated and consists in the calculation of a transport term that uses horizontal wind, and the calculation of a sink term that requires temperature data and OH concentration to illustrate the chemical loss of NO_x. Results illustrate the difference between localised and diffuse sources of NO_x. For diffuse sources such as the Doha urban area, the transport term and the sink term similarly contribute to the total NO_x budget, whereas the transport term is higher than the sink term for localised sources such as the gas power plants located in the north-east of the country. The emissions from other hotspots, such as cement plants in the west part of the country, could not be correctly estimated from 2019 to 2021 due to unavailability of high-quality TROPOMI retrievals. Our estimated NO_x emissions show a weekly variability which is consistent with the social norms of the country and an annual variability which is consistent with its electricity generation. In this study, estimated emissions are similar to reported emissions in 2007, but they are 1.67 times lower than emissions in the CAMS-GLOB-ANT_v5.3 inventory for 2019-2022 and 1.68 times lower than emissions in EDGARv6.1 for 2018. They have an annual cycle whose relative amplitude is higher than those two inventories. These notable differences may be subject to further discussion regarding sectoral activity data and emission factors used in global inventories. Finally, this study is also an attempt to retrieve the NO_x emission factor of the power sector. This top-down estimation is made possible by the desert features of Qatar, which allow to consider only one chemical sink, and also by the low diversity of its economy in which the power sector is the major source of variable NO_x. An emission factor is also estimated for a group of isolated gas power plants. The emission factors are 1.42 and 4.52 times higher than the value reported for 2007. Moreover, the emission factor of the entire power sector is higher than that of the three isolated gas power plants, indicating higher emission factors for other power plants in Doha. Although several limitations exist in the estimation of these results, we believe that such a calculation can be reproduced in other countries and for power plants that share similar characteristics. Overall, this study highlights the potential of TROPOMI to compensate for non-existent, inaccurate or outdated inventories by providing low-latency emissions estimates. The development of similar applications is likely to provide a better monitoring of global anthropogenic emissions, therefore helping countries to report their emissions of air pollutants and greenhouse gases as part of their strategies and obligations to tackle air pollution issues and climate change.

Code availability

Code will be made available on request.

Data availability

The TROPOMI Sentinel 5P Product Algorithm Laboratory (S5P-PAL) reprocessed data (processor version 2.3.1) from January 2019 to October 2020 has been used. The OFFL stream has been used afterwise, using processor versions 2.3.1 and 2.4.0 from November 2022. The TROPOMI NO_2 product is publicly available on the TROPOMI Open hub (`http://www.tropomi.eu/data-products/data-access`, TROPOMI Data Hub, 2022) while the S5P-PAL reprocessed data can be found on the S5P-PAL data portal (`https://data-portal.s5p-pal.com`, ESA, 2022). CAMS data can be downloaded from the Copernicus Climate Data Store (`https://ads.atmosphere.copernicus.eu/cdsapp#!/dataset/cams-global-atmospheric-composition-forecasts`, ECMWF, 2022a). The European Centre for Medium-Range Weather Forecasts (ECMWF) ERA5 reanalysis be downloaded from the Copernicus Climate Data Store (`https://cds.climate.copernicus.eu/cdsapp#!/dataset/reanalysis-era5-pressure-levels-monthly-means`, ECMWF, 2022b). Electricity generation data can be downloaded from The Planning and Statistics Authority Portal (`https://www.psa.gov.qa/en/statistics1/Pages/default.aspx`, last access: 31 January 2023), and from Kahramaa Portal (`https://www.km.qa/MediaCenter/Pages/Publications.aspx`, last access: 24 January 2023). Emissions reported for year 2007 is available on the UNFCCC website (`https://unfccc.int/resource/docs/natc/qatnc1.pdf`, last access: 26 August 2022). EDGARv6.1 emissions are provided by `https://edgar.jrc.ec.europa.eu/emissions_data_and_maps`. CAMS-GLOB-ANT_v5.3 emissions are available at `https://eccad3.sedoo.fr`.

Author contributions

AR analysed the data, prepared the main software code and wrote the paper. FC provided the TROPOMI NO_2 data product and corresponding gridded maps. ISB provided time series of electricity consumption. PC, TC, JK, and JS contributed to the improvement of the method and the interpretation of the results. All authors read and agreed on the published version of the paper.

Financial support

This study has been funded by the European Union's Horizon 2020 research and innovation programme under grant agreement N°856612 (EMME-CARE), and partially under grant agreement N°958927 (Prototype System for a Copernicus CO2 Service (CoCO2)).

Competing interests

The authors declare that they have no conflict of interest.

3.3 NO_x emission factors differences in Cypriot power plants

3.3.1 Presentation of the article

The study of NO_x emissions in Cyprus had three objectives. Firstly, it aimed to test the method in locations where it is limited, by the complex topography of Cyprus which makes it difficult to estimate transport due to the existence of non-uniform wind, but also by the low signal-to-noise ratio of NO_2 over the main emitters in Cyprus. Secondly, the existence of WRF-Chem simulations for Cyprus made it possible to test the method with a source of parameters (wind, OH concentration and NO_x/NO_2 ratio) other than the CAMS NRT data. Finally, the de facto separation of the island, which occurred almost five decades ago, led to substantial differences in economic and industrial trajectories between the north and the south and, as a results, in emission factor differences, which were interesting to investigate using satellite images. Identifying the differences in emission factors between a part of the island that is subject to EU standards and a part that is not could provide an illustration of a mode of economic development. Of course, the knowledge of the Cyprus Institute regarding the environmental, economic and industrial situation of the island provided a high-quality supervision of the study, leading to a thorough interpretation of the results. Few changes have been made to the main method.

The article presented here is a first draft and slight changes will certainly be necessary before it can be submitted to a journal. In particular, we plan to perform a vertical analysis of the parameters involved in the calculation of emissions, and we will try to compare the two wind datasets used in the study to in situ measurements. The journal in which we would like to publish it has not yet been chosen, but we plan a submission before the end of 2023. Authors that participated to this work are **Anthony Rey-Pommier** (LSCE, The Cyprus Institute), Theodoros Christoudias (The Cyprus Institute), Jonilda Kushta (The Cyprus Institute), Frédéric Chevallier (LSCE), Philippe Ciais (LSCE, The Cyprus Institute), Georges Georgiou (The Cyprus Institute), Florence Dubart (The Cyprus Institute), Angelos Violaris (The Cyprus Institute) and Jean Sciare (The Cyprus Institute).

The preliminary results of this study have been presented at the Climate and atmosphere research and innovation in the Eastern Mediterranean and Middle East workshop (November 2022, Nicosia, Cyprus), and at the EGU General Assembly 2023 (April 2023, Vienna, Austria). Numbering of subsections and notations appearing in the following Section have been slightly modified in order to be consistent with the rest of this document.

3.3.2 Abstract

Nitrogen oxides ($NO_x = NO + NO_2$) are produced in large quantities in urban areas and fossil fuel-fired power plants, contributing to local and regional pollution, with serious implications for human health. To implement air-quality policies, local and national authorities often rely on emission inventories. The island of Cyprus is de facto divided into two different political entities, and as a result, emissions inventories are not systematically available for the whole island, hindering an optimal monitoring of air quality. We map NO_x emissions in Cyprus for 2021 and 2022 using a flux-divergence scheme, using spaceborne retrievals of nitrogen dioxide (NO_2) columns at high spatial resolution from the TROPOMI instrument, as well as horizontal wind data to derive advection and hydroxyl radical concentration to derive chemical loss. These paraemeters are estimated using ECMWF data fields and WRF-Chem simulations. Taking advantage of the low emissions in Cyprus and dataset differences, we show that the flux-divergence method is limited by the resolution of wind and hydroxyl radical parameters, the signal-to-noise ratio of the observed tropospheric column densities, and the NO_x:NO_2 ratio above the main NO_x sources. We also provide an estimation of NO_x emissions for the five power plants of the island. For the power plants in the south, our estimated emissions are in the range of reported emissions and global/regional inventories, despite differences in annual seasonal cycles. For the power plants in the north, our estimated emissions are significantly higher than emissions in global/regional inventories. On average, power plants in the north have mean daytime emissions 1.8 times higher than

power plants in the south, despite a production capacity 3.6 times lower, illustrating the use of different norms, technologies and fuels in the two parts of the island.

3.3.3 Introduction

In most regions of the world, economic growth and development have resulted in a strong increase of urban air pollution (Baklanov et al., 2016). Among the different air pollutants, nitrogen oxides are crucial species, primarily generated through fuel combustion, such as the high-temperature combustion of hydrocarbons. These species predominantly emanate from vehicle engines and heavy industrial facilities, including power plants, iron and steel mills (Tang et al., 2020), and cement kilns (Kim et al., 2020a). Their accumulation in the lower tropospheric layers of the atmosphere plays a significant role in the formation of smog and acid rain (Singh, Agrawal, 2007), and their adverse impacts on human health, leading to various respiratory diseases, are significant (EPA, 2016). In response to these challenges, national and regional governments typically implement air pollution control strategies, often involving bans on specific polluting technologies. In the recent years, successful reduction of NO_x emissions occured in most developed countries (Crippa et al., 2016; Miyazaki et al., 2017), and later, China (de Foy et al., 2016), while other regions experienced a rise or stagnation of their emissions, such as the Eastern Mediterranean region (Lelieveld et al., 2015).

In this region, Cyprus is a special case. The island is de facto divided into two parts, the north and the south (Resolution 550, UN Security Council, 1984), which have followed different economic, political and industrial trajectories, resulting in different norms applying on the two sides of the island in terms of acceptable pollution levels and technologies that can be used. The sources of NO_x on the northern part of the island are not listed in all regional or global inventories. To overcome this absence in emission inventories, the use of independent observation systems is becoming increasingly prevalent.

Spectrally resolved satellite measurements of solar backscattered radiation enable the quantification of trace gases absorbing in the UV–visible spectral range based on their characteristic spectral absorption patterns. For these species, tropospheric vertical column densities, i.e. vertically integrated concentrations in the troposphere, have been providing information on the composition of the troposphere at a global scale for nearly 30 years. For NO_2, the use of such columns enabled the identification of different sources of NO_x and the quantification of the associated emissions (Leue et al., 2001; Martin et al., 2003; Mijling, Van Der A, 2012; de Foy et al., 2015; Goldberg et al., 2019b; Lorente et al., 2019). In October 2017, the Sentinel-5 Precursor satellite was launched. Its main instrument is the TROPOspheric Monitoring Instrument (TROPOMI), which provides tropospheric NO_2 column densities at high spatial resolution with a large swath width and a daily frequency (Veefkind et al., 2012). Additionally, inverse methods relying on such observations have proved in the recent years to provide reliable estimations for isolated emitters, provided that certain conditions are met. In particular, the use of tropospheric vertical column densities can be used to retrieve NO_x emissions with the use of the continuity equation in steady state (Beirle et al., 2019; Lama et al., 2020; Rey-Pommier et al., 2022; Beirle et al., 2023; de Foy, Schauer, 2022). This scheme, known as flux-divergence, requires the use of other physical quantities (wind, temperature, hydroxyl radical concentration and concentration ratio between NO_x and NO_2). In this study, we use this method to quantify the emissions of the five power plants of Cyprus, in the purpose of comparing the obtained estimates to reported emissions. We use the specific features of Cyprus, expressly its low NO_x emissions and its unreported sources, to illustrate the main limitations of the flux-divergence method.

This paper is organised as follows: Section 3.3.4 provides a description of the main NO_x emitters of the island, and Section 3.3.5 presents the datasets used in this study. Section 3.3.6 explains the flux-divergence method. Section 3.3.7 highlights the main limitations of the flux-divergence method by comparing different datasets, while Section 3.3.8 estimates NO_x emissions of the five power plants of the island and compares them to reported emissions and regional/global inventories. Section 3.3.9 presents our conclusion and general remarks.

3.3.4 General features of NO_x emitters in Cyprus

Cyprus is the third largest island in the Mediterranean (approximately 200 km in the east-west direction and 100 km in the north-south direction), located at the south of the Anatolian peninsula and the west of the Levant. It has a Mediterranean climate characterised by hot, dry summers and mild, wet winters. It counts two mountain ranges, the higher one being the Troodos, situated in the central part of the island and peaking at 1,952 meters above sea level, and the smaller one being the Kyrenia Range in the north. To the north-east of the island lies the Karpas peninsula, with its tip about 90 km from the coasts of Türkiye (to the north) and Syria (to the east). The northern part of the capital Nicosia and the northern part of the island is not controlled by the government of the republic of Cyprus, each side of the island counting about 920,000 (south) and 320,000 (north) inhabitants. Overall, the main sources of NO_x on the island are the following:

3.3.4-A Urban areas

Most of the Cypriot population is concentrated in cities. The two urban areas of Nicosia and Limassol are the largest, with about 327,000 and 184,000 inhabitants respectively. In addition to these two urban areas, the four urban areas of Famagusta, Kyrenia, Larnaca and Paphos account for more than 80% of the population. Here, only the urban areas of Nicosia and Limassol are large enough to be considered as significant NO_x hotspots, with emissions dominated by the traffic sector. The EC Global Human Settlement Layer (`https://ghsl.jrc.ec.europa.eu/download.php`) provides population maps at a regional scale, which allows the display of a population density map for the island.

3.3.4-B Power plants

Fossil fuel-fired power plants are important sources of NO_x. The island of Cyprus accounts for five power plants. Of these five power stations, three are located in the southern part. The oldest and smallest is the Moni Power Station, located about 15 km east of Limassol. It produces a negligible share of the country electricity, as it is used to respond to peaks in the electricity demand. The largest power plant is Vasilikos, located 10 km east of Moni, which was renovated after an incident in 2011. It is used as the baseload for power supply and produces about two thirds of the electricity in the southern part. The rest of the production is provided by the Dhekelia power plant, used for base and intermediate load, located within the British Sovereign Base Area of the same name. More information on these power plants can be found on the Electricity Authority of Cyprus (EAC) web page at: `https://www.eac.com.cy/EN/RegulatedActivities/Generation/aboutgeneration/Pages/default.aspx`. The two remaining power plants are located in the northern part of the island. The Teknecik plant is located about 13 km from the centre of Kyrenia, while the Kalecik-Tesisleri plant is located in the north-east of the island, far away from any significant urban centre. These two plants are not listed by the EAC, and the corresponding electricity production is unknown to them. However, their production capacities are known, and they are small compared to those of the power plants in the south of the island. Finally, there are interconnections between the northern and southern electricity grids, but the exchanges are relatively small compared to their respective productions. The characteristics of the five plants are summarised in Table 3.4, and their location are shown on Figure 3.23, along with the human density map of the island showing its main urban areas.

Name	**Location (°N, °E)**	**Capacity (MW)**	**Fuel**	**Date of commissioning**
Moni	(34.710, 33.183)	140	Diesel / Light Fuel Oil	1966
Vasilikos	(34.729, 33.290)	868	Diesel / Heavy Fuel Oil	2002
Dhekelia	(34.980, 33.746)	460	Heavy Fuel Oil / Light Fuel Oil	1982
Teknecik	(35.336, 33.460)	260	Diesel	NC
Kalecik	(35.330, 33.997)	148	Diesel	2003

Table 3.4: Location, capacity, fuel and age of the five power plants in Cyprus.

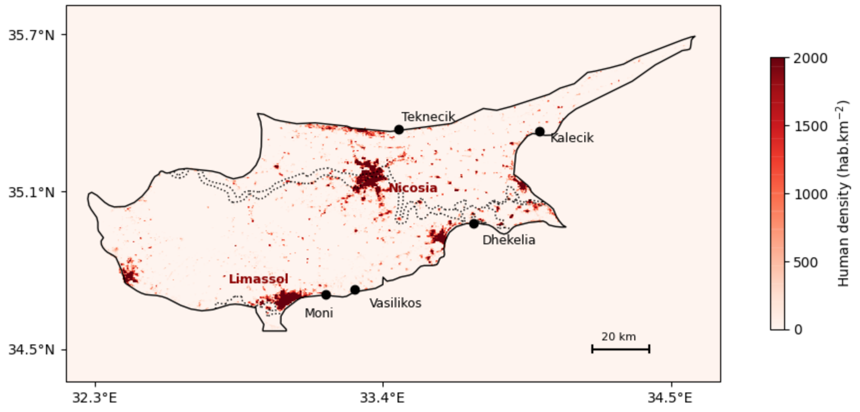

Figure 3.23: Human density settlement map showing the main urban areas and the location of the power plants in Cyprus.

3.3.4-C Other sources

Other industrial facilities are also large emitters of NO_x, such as cement plants and metal smelters. In Cyprus, the Vasilikos cement plant is the only one that has a production capacity high enough to generate pollution levels similar to those of a city or a power plant. It is therefore impossible to distinguish these two emitters from space with instruments having a coarser resolution than 2 km, which is approximately the distance between this cement plant and the Vasilikos power station.

3.3.5 Instrumentation and data

3.3.5-A TROPOMI NO_2 retrievals

NO_2 can be observed from space with satellite instruments based on its strong absorption features in the 400–465 nm wavelength region (Vandaele et al., 1998). By comparing observed spectra with a reference spectrum, the amount of NO_2 in a portion of the atmosphere between the instrument and the surface can be derived. The TROPOspheric Monitoring Instrument (TROPOMI), onboard the European Space Agency's (ESA) Sentinel-5 Precursor (S-5P) satellite, is one of those instruments, providing daily measurements of NO_2 around 13:30 local time (LT). Its high spatial resolution (3.5×5.5 km^2 since 6 August 2019) allows to observe some of the fine-scale structure of NO_2 pollution, such as within cities (Beirle et al., 2019; Demetillo et al., 2020), or near power plants and industrial facilities (Shikwambana et al., 2020; Saw et al., 2021). Tropospheric vertical column densities (VCDs, or simply "columns") are provided after measurement of total slant column densities with a Differential Optical Absorption Spectroscopy method. VCDs represent the vertically integrated number of NO_2 molecules per surface unit between the surface and the tropopause. An algorithm also provides an air mass factor, which is used to convert slant column densities into vertical column densities. This factor depends on many parameters, including the albedo of the viewed surface, the vertical distribution of the absorber and the viewing geometry. It is a source of structural uncertainty in NO_2 measurements (Boersma et al., 2004; Lorente et al., 2019), which becomes non-negligible in polluted environments. The large swath width of the instrument (~2600 km) makes it possible to construct NO_2 images of VCDs on large spatial scales. We use TROPOMI NO_2 retrievals from 2021 to 2022 (S5P-PAL reprocessed data with processor version 2.3.1 from May to October 2021 and OFFL stream with processor version 2.3.1 from November 2021 to October 2022) over Cyprus. The location of the country in the Eastern Mediterranean offers a large number of clear-sky days throughout the year, enabling the calculation of monthly averages based on multiple observations. However, the relatively low industrial activity of the country enables to observe NO_2 plumes only above the sites mentionned precedently, and often with levels that are close to those of the surrounding environment. Finally, TROPOMI products provide a quality assurance value, which ranges from 0 (no data) to 1 (high-quality data). For our analysis, we selected NO_2 retrievals with a quality assurance values greater than 0.75, which systematically corresponds to clear-sky conditions (Eskes et al., 2022), and gridded these retrievals at a spatial resolution of 0.0625°×0.0625°. This resolution is lower than that of the instrument, thus providing a grid for which NO_2 VCDs correspond to one or more observations. The observed plumes remain correctly resolved.

3.3.5-B CAMS and ERA5 real-time fields

The Copernicus Atmospheric Monitoring Service (CAMS) global near-real-time service provides analyses and forecasts for reactive gases, greenhouse gases and aerosols. Forecasts are gridded on 25 vertical pressure levels with a horizontal resolution of 0.4°×0.4° and a temporal resolution of 3 hours (Huijnen et al., 2019). NO_2, NO and OH concentration fields are used, as well as temperature. For wind data, the horizontal vector field $\vec{w} = (w_x, w_y)$ can be taken from the European Centre for Medium-Range Weather Forecasts (ECMWF) ERA5 data archive (fifth generation of atmospheric reanalyses) at a horizontal resolution of 0.25°×0.25° on 37 pressure levels (Hersbach et al., 2020). To adjust parameters to the NO_2 VCD format, parameters taken from CAMS and ERA5 data are linearly interpolated to the TROPOMI orbit timestamp and re-gridded to a 0.0625°×0.0625° resolution.

3.3.5-C WRF-Chem simulations

The Weather Research and Forecasting model coupled with Chemistry (WRF-Chem) version 3.9.1.1 has been used to perform 3 days ahead meteorological and air quality forecasts for years 2021 and 2022. The horizontal resolution of the domain is 2 km, focused over the island of Cyprus. 33 vertical layers are used (which correspond to altitudes between ground level and approximately 21 km above sea level), while adaptive time stepping is used in order to meet the Courant–Friedrichs–Lewy (CFL) stability criterion at each time step (Jacobson, 1999). In order to have optimal representation of the meteorological fields, physics parameterisations are used. They have been optimised for Cyprus by the Department of Meteorology for weather forecast and as well as physics parameterizations that have been shown by Zittis et al. (2014) to have the better performance in terms of simulating several meteorological variables, including air temperature over the Eastern Mediterranean and the Middle East region. Various gas-phase chemistry and aerosol mechanisms have different behaviour in terms of predicting the atmospheric concentrations of pollutants over specific regions. Detailed description of the model physics configuration is given in Georgiou et al. (2022). Initial and boundary conditions for meteorology are provided by the Global Forecast System (GFS). Boundary conditions for the gas-phase species and aerosols are provided by WACCM (Gettelman et al., 2019). Biogenic emissions are generated based on weather and land use data, using the Model of Emissions of Gases and Aerosols from Nature version 2.1 (MEGAN2.1) by Guenther et al. (2012). For anthropogenic emissions, a high-resolution emission inventory developed by Georgiou et al. (2020) is used. The power plants of Vasilikos and Dhekelia are represented, but the two power plants located in the northern part of the island are not included in the inventory. For these areas, the emission inventory takes into account the emissions from the EDGAR-HTAP global emission inventory. To adjust parameters to the NO_2 VCD format, horizontal wind, temperature, OH, NO and NO_2 concentrations as well as planetary boundary layer (PBL) height are linearly interpolated to the TROPOMI orbit timestamp and downscaled to a 0.0625°×0.0625° resolution.

3.3.5-D NO_x emission gridded inventories

Emissions inferred from TROPOMI data and parameters from WRF-Chem simulations and/or CAMS and ERA5 data are compared to corresponding sectoral NO_x emissions from three different inventories:

- The Emissions Database for Global Atmospheric Research (EDGARv6.1) is a global inventory providing 0.1°×0.1° gridded emissions of greenhouse gases and air pollutants. It covers different sectors on a monthly basis. It is based on activity data (population, energy production, fossil fuel extraction, industrial processes, agricultural statistics, etc.) derived from the International Energy Agency (IEA) and the Food and Agriculture Organization (FAO), corresponding emission factors, national and regional information on technology mix data and end-of-pipe measurements. The inventory covers the years 1970-2018.

- The CAMS global anthropogenic emissions (CAMS-GLOB-ANT_v5.3) is a global inventory providing 0.1°×0.1° gridded emissions. It is developed within the framework of the Copernicus Atmospheric Monitoring Service (Granier et al., 2019) providing monthly emissions and covers years until 2022. For this inventory, NO_x emissions are based on various sectors in the EDGARv5.0 emissions up to 2015 which are extrapolated to 2021 using sectorial trends from the Community Emissions Data System (CEDS) inventory (Hoesly et al., 2018) up to 2019.
- The CAMS regional inventory (CAMS-REG-v4), developed for the European domain (Kuenen et al., 2022), covers an 18-year time series (2000–2017) at a 0.05°×0.1° grid resolution above Europe to support air quality modelling. It includes major air pollutants, including NO_x, and relies on officially reported emission data by European countries to the UN Framework Convention on Climate Change, the Convention on Long-Range Transboundary Air Pollution, and the EU National Emission Ceilings Directive as the primary basis, and lacking data is filled using the Greenhouse gas Air pollution Interaction and Synergies (GAINS) model. The emissions are categorised by sectors, and point source emissions are mainly based on facility-level reports, supplemented with other data for power plants. For Cyprus, the two power plants located in the northern part of the island are not included in the inventory.

From one inventory to another, the names and definitions of the sectors may differ. In EDGARv6.1 and CAMS-GLOB-ANT_v5.3, the emissions for a given country are derived from the type of technologies used, the dependence of emission factors on fuel type, combustion conditions, as well as activity data and low-resolution emission factors (Janssens-Maenhout et al., 2019), while CAMS-REG-v4 uses emissions reported in 2019 from the Centre on Emission Inventories and Projections (CEIP) for the years 2000–2017.

3.3.6 Method

3.3.6-A The flux-divergence method

A two-dimension mass balance, expressed at the scale of a NO_2 column taken as a control volume, enables deriving the continuity equation for NO_2 linking its production E_{NO_2} and its loss S with its horizontal transport D. In steady state, this relationship is expressed locally as:

$$E_{NO_2} = D + S \tag{3.12}$$

The application of this method, called flux-divergence, to satellite retrievals, goes back to a study of Beirle et al. (2019), who used temporally-averaged VCDs from TROPOMI images to derive NO_x emissions.

3.3.6-B The transport term

Equation 3.12 highlights two terms. The first one is the transport term D which is obtained by multiplying NO_2 VCDs Ω with horizontal wind speeds to account for advection as $D = \mathrm{div}(\Omega \vec{w})$. The shape of the transport term that is associated with a plume representing the spreading of NO_2 from a source with the wind is the shape of a dipole oriented in the direction of the mean flow, with a positive pole above the source, and a negative pole downwind the source. For a given plume, the poor representation of wind speed leads to a mis-estimation of transport, but the expected profile, i.e. that of a dipole, remains represented. The estimation of the transport term thus significantly relies heavily on the representation of the wind angle. Errors are therefore expected to be higher in regions having winds that vary rapidly in time, or regions with complex horizontal wind variations, such as mountainous regions. In particular, situations where sub-grid scale-phenomena affecting the mean wind occur might display even higher errors in the estimation of the transport term.

3.3.6-C The sink term

The second term appearing in Equation 3.12 is the sink term S which represents the chemical loss of NO_2. It is usually simplified to $S = \Omega/\tau$ where τ is the effective lifetime of NO_2. During daytime, this chemical loss is dominated by the reaction of NO_2 with OH leading to formation of HNO_3 (Seinfeld, 1989), and the lifetime can be expressed as:

$$\tau = \frac{1}{k_{\mathrm{mean}}(T, [\mathrm{M}])[\mathrm{OH}]} \tag{3.13}$$

Here k_{mean} is the reaction rate that characterises the different reactions between NO_2 and OH. Burkholder et al. (2020) provide a general expression of this reaction rate with respect to atmospheric conditions (temperature T and total air concentration [M]). As the local overpass time of TROPOMI is close to 13:30 LT, the chemical loss is dominated by the reaction with OH.

The modelling of the sink term suffers from two limitations. Firstly, NO_x affects atmospheric composition through feedback on certain species, notably OH. The concentration of OH radical, whose reaction is the main NO_x sink, thus depends strongly on NO_x itself. To accurately quantify this removal rate, a model must therefore accurately resolve NO_x from its source to background. This can be criticial in resolving the NO_2 loss within plumes, whose length depend on wind conditions. Above this limit, biases increase with the resolution, and their direction depend on the mean NO_x budget (Valin et al., 2011).

Another difficulty in estimating the sink term is the consideration of additional reactions in the NO_2 loss. The particularity of Cyprus is that apart from Nicosia, its main emitters are located close to the coasts, with NO_x loss processes being different at sea and on land. In the Mediterranean basin, HNO_3 is the dominant component of total reactive nitrogen besides NO_x, supported by high OH levels reported in the Mediterranean Sea (Friedrich et al., 2021). However, NO_x sinks on land other than the OH-induced loss, that can be neglected in drier and hotter regions (Rey-Pommier et al., 2022), can be non-negligible in Cyprus during daytime. In particular, organic peroxy radicals can oxidise a significant amount of NO_x (Day et al., 2003), leading to the formation of peroxy nitrates. This other sink might be significant, since organic peroxy radicals can be formed by oxidation of volatile organic compounds, whose presence has been attested by measurements in the region (Debevec et al., 2017). Other NO_x loss can be attributed by the conversion of NO_2 to peroxyacetyl nitrate (Moxim et al., 1996). Here, we do not wish to complexify the modelling of the sink term and these minor sinks are not represented.

Finally, it must be noted that in the absence of anthropogenic sources, the NO_2 columns that are observed constitute a tropospheric background. At the global scale, this background is mostly due to soil emissions in the lower troposphere (Yienger, Levy, 1995; Hoelzemann et al., 2004). In the upper troposphere, NO_2 sources include lightning, convective injection and downwelling from the stratosphere (Ehhalt et al., 1992), but the factors controlling the resulting concentrations are poorly understood. In order not to account for this tropospheric background in the calculation of NO_x emissions, we remove from daily VCD maps the value of the lowest levels in the domain, defined here as the 10th percentile of observed VCDs. This removal is critical not to over-estimate the sink term, but relatively insignificant for the transport term, as wind divergence is close to zero.

3.3.6-D Upscaling NO_2 flow rates to NO_x emissions

Anthropogenic activities produce mainly NO, which is transformed into NO_2 by reaction with ozone O_3.

NO_2 is then photolyzed during the day, reforming NO (Seinfeld, 1989). This photochemical equilibrium between NO and NO_2 is accounted for in the model with the concentration ratio $\mathcal{L} = [NO_x]/[NO_2]$ which usually varies between 1.2 and 1.4, depending on local conditions. NO_x emissions are therefore obtained by multiplying NO_2 production E_{NO_2} by $\mathcal{L}$. As diurnal NO concentrations in urban areas are generally above 20 ppb, the characteristic stabilization time of this ratio never exceeds a few minutes (Graedel et al., 1976; Seinfeld, Pandis, 2006). This time being lower than the order of magnitude of the inter-mesh transport time (about 20 min considering the resolution used and the mean wind module in the region), it is possible to reasonably neglect the effect of the stabilization time of the conversion factor on the total composition of the emissions and treat each cell of the grid independently from its neighbours. Such a reasoning is no longer valid in the vicinity of emitters, where the stationary hypothesis is not necessarily verified, in which case the value of $\mathcal{L}$ may be significantly higher than 1.4. In the case of an emitter located in one pixel but close to another, it is no longer possible to treat the two pixels independently.

3.3.6-E Use of different datasets for the flux-divergence method

Overall, the NO_x emissions are derived from TROPOMI NO_2 columns with the flux-divergence method with the following equation:

$$E_{NO_2} = \mathcal{L}(\mathrm{div}(\Omega\vec{w}) + k_{\mathrm{mean}}(T, [\mathrm{M}])[\mathrm{OH}]\Omega) \tag{3.14}$$

As k_{mean} variations with temperature are small compared to those of VCD or hydroxyl radical throughout a year, the main parameters of Equation 3.14 are the horizontal wind $\vec{w}$, the OH concentration [OH], and the NO_x:NO_2 ratio $\mathcal{L}$, while the column Ω (with removed background) serves as the main variable. Here, we derive NO_x emissions using three sets of parameters:

- The first set (EC) is composed of parameters entirely taken from ECMWF datasets, i.e. CAMS near-real-time data and the ERA5 reanalysis, which are linearly interpolated to the TROPOMI orbit timestamp and downscaled to a 0.0625°×0.0625° resolution. The original resolution of the data is coarse: in particular, the original 0.4°×0.4° resolution of OH do not allow to resolve most plumes in Cyprus, due to the small spatial extent of the emitters. For the same reason, the NO_x:NO_2 ratio varies little from one pixel to another.

- The second set (WW) is composed of parameters entirely taken from WRF-Chem simulations, which are linearly interpolated to the TROPOMI orbit timestamp and upscaled to a 0.0625°×0.0625° resolution. The original high-resolution of the data enables resolving most plumes in Cyprus, but only for emitters that are represented. The representation of the emitters is more obvious for the NO_x:NO_2 ratio, as the power plants in the south generally have ratios above 1.5, which is not observed for the power plants in the north. The high-resolution horizontal wind enables observing wind variations at the scale of several kilometers, which can be induced by physical factors such as topography.

- The third set (EW) is composed of parameters entirely taken from WRF-Chem simulations, except wind which is taken from ERA5. This choice is justified a posteriori by noticing significant differences in wind angles between ERA5 data and WRF-Chem simulations, which is critical in the evaluation of the transport term. This aspect is discussed in Section 3.3.7.

To illustrate the differences between the parameters chosen in each set, Figure 3.24 displays the differences between CAMS/ERA5 data and WRF-Chem simulations observed for $\vec{w}$, [OH], and $\mathcal{L}$ on a given day. The corresponding TROPOMI vertical columns are added.

<table>
<tr><th>Parameters and variable</th><th>CAMS NRT & ERA 5</th><th>WRF-Chem simulations</th></tr>
<tr><td>Tropospheric vertical column densities</td><td colspan="2">
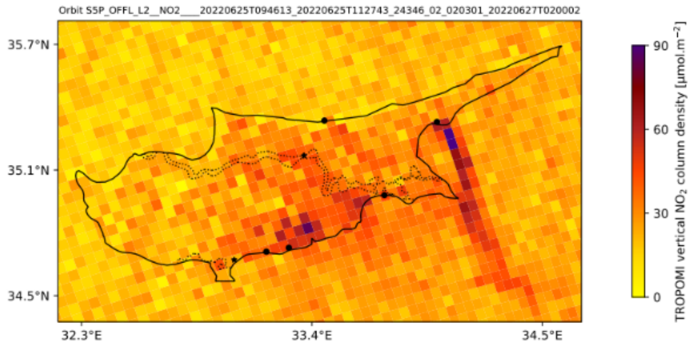

TROPOMI - around 13:30 LT - 3.5×5.5 km² maximum
</td></tr>
<tr><td>Horizontal wind</td><td>
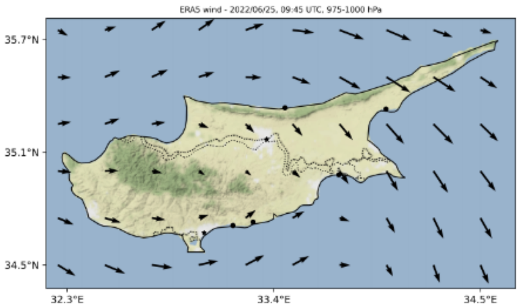

ERA5
1 h res. - 0.25°×0.25°
</td><td>
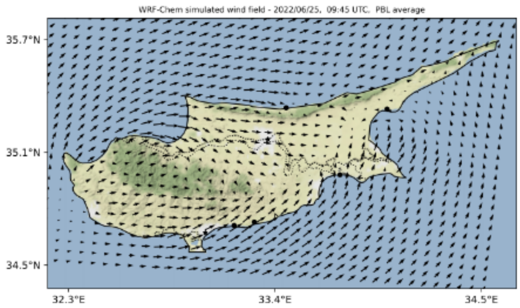

WRF-Chem
1 h res. – 2×2 km²
</td></tr>
<tr><td>Hydroxyl radical concentration</td><td>
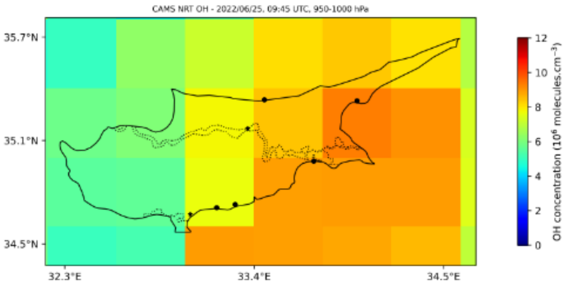

CAMS NRT
3 h res. - 0.25°×0.25°
</td><td>
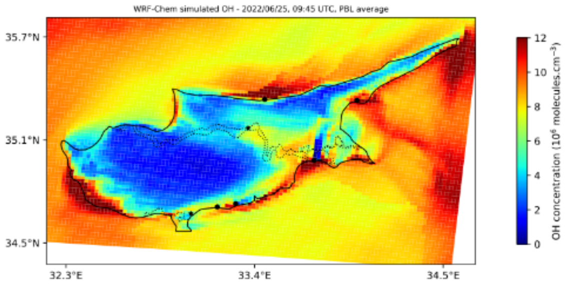

WRF-Chem
1 h res. – 2×2 km²
</td></tr>
<tr><td>NO_x:NO_2 ratio (derived from NO_2 and NO fractions)</td><td>
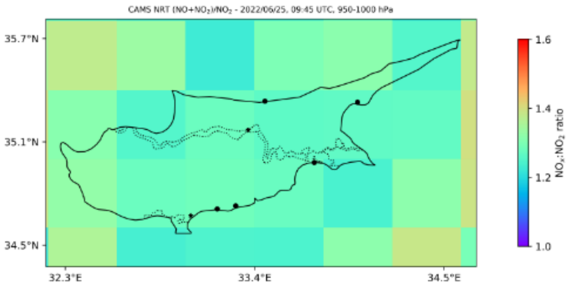

CAMS NRT
3 h res. - 0.25°×0.25°
</td><td>
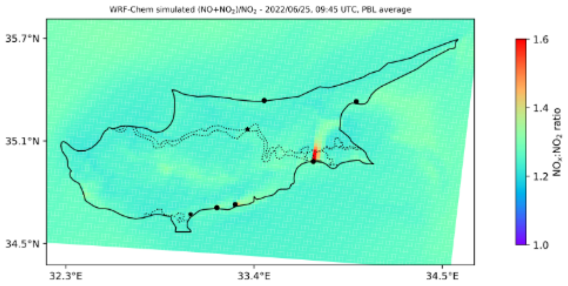

WRF-Chem
1 h res. – 2×2 km²
</td></tr>
</table>

Figure 3.24: Origin of the different parameters used in sets EC, WW and EW in the flux-divergence scheme to calculate NO_x emissions in Cyprus, displayed with their original resolution for June 25th, 2022. Power plants are denoted with dots while Nicosia and Limassol are denoted with stars.

3.3.7 Results

3.3.7-A Tropospheric background and NO_x signal-to-noise ratios above the main emitters of the island

In the TROPOMI retrievals, the NO_2 signal from a sparsely populated area or a small industrial facility may be covered by noise or by the signal generated by natural NO_x emissions. The noise is of the order of magnitude of the calculated tropospheric background, calculated here as the 10th percentile of the observed VCDs. In our domain, pixels having columns lower than this calculated background are mostly encountered at sea or above the Troodos mountain range. In the Eastern Mediterranean, measurements of air masses have inferred lower OH reactivity than in other neighbouring seas such as the Red Sea or the Persian Gulf, due to aged and cleaner air leading to higher NO_2 levels at sea (Pfannerstill et al., 2019). These high NO_2 concentrations at sea have also been reported by satellite data in the past (Richter et al., 2011). Such observations suggest lower signal-to-noise ratios for NO_2 signals for the power plants in Cyprus, in comparison to larger emitters or similar emitters that would be located elsewhere.

Here, we calculate mean TROPOMI NO_2 trospoheric column densities above five different regions of the domain: the urban area of Nicosia, the power plants of the northern part of the island (Teknecik and Kalecik), the power plants of the southern part (Moni, Vasilikos and Dhekelia), the Troodos mountain range (altitude above 1 km), and the surrounding sea (less than 60 km from the shores). Due to its proximity with the Moni and Vasilikos power plants, the urban area of Limassol is not represented. The five regions are characterised with differerent albedos, with lower values for the sea and the mountain and higher values for Nicosia. On Figure 3.25, the time series of these three type of emitters, as well as the calculated background, are compared with mean column densities above the surrounding sea and above the Troodos mountain, where no significant anthropogenic NO_x source is expected. To better visualise the NO_2 trend without accounting for weekly effects, seven-day moving averages are displayed. The origin of the abscissa is calculated as the average between the mean NO_2 above sea and mean NO_2 above mountains, which is particularly relevant for the study of the power plants that are located on shores.

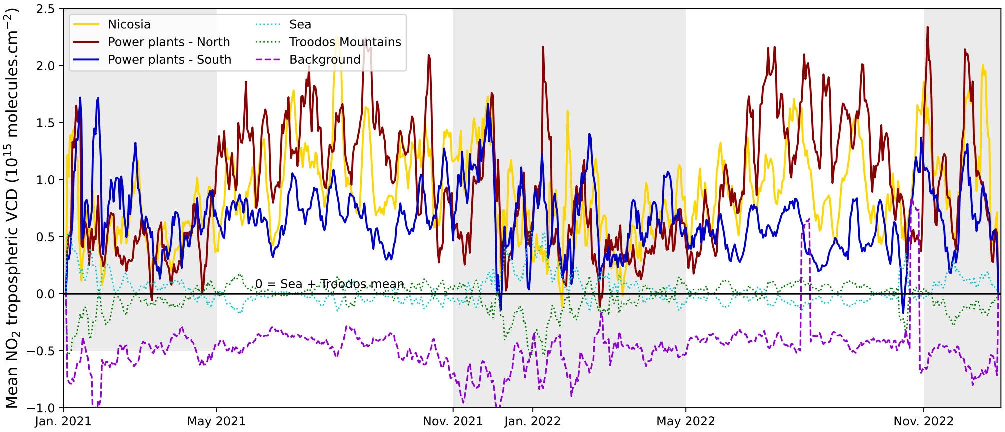

Figure 3.25: Difference between and the mean tropospheric vertical column densities above the main emitters in Cyprus (Nicosia, power plants in the north and the south of the country), and mean tropospheric vertical column densities above sea and mountain regions for 2021 and 2022 (seven-day moving averages). The difference between the calculated background (10th percentile of the domain) and the mean columns above sea and mountain regions is also shown with a dashed line.

The observed column densities show NO_2 levels above the main sources that are higher than the calculated background (we discard high levels encountered in September and October 2022 that seem to be outliers in the TROPOMI product). NO_2 columns above the sea are similar to NO_2 levels above the mountain, except during wintertime for which NO_2 columns at sea are higher. Moreover, the mean NO_2 level above sea and mountains is clearly lower than above emitters during summer, although important variations can be observed. Between November and May, NO_2 columns above sources can be similar to those above sea and mountains, indicating a very low signal-to-noise ratio. However, they remain noticeably superior than the calculated background, indicating a wide distribution of NO_2 columns far from the main sources. Considering the high uncertainties in the tropospheric columns, it is therefore not possible to distinguish emissions from the main sources in Cyprus from their close environment during approximately this half of the year. The following sections will thus focus on estimating monthly emissions for the remaining two 6-month periods (May-November 2021 and 2022). Note that although these months are the hottest in the year, they do not correspond to the months with the highest electricity consumption as in other Eastern Mediterranean countries (Yathreb, 2016) or Gulf countries (Gastli et al., 2013; Alktranee et al., 2020; Alfaoyzan, Almasri, 2023). In Cyprus, electricity consumption is the highest in summer, but the lowest in autumn and spring, as electricity consumption rises in winter due to heating demand (Solyali, Redfern, 2010; Kassem et al., 2020).

3.3.7-B Dataset differences

We use the flux-divergence model to calculate NO_x emissions in Cyprus using the three different sets (EC, WW and EW) Parameters are averaged within the planetary boundary layer, which is taken from WRF-Chem simulations. For each day, a background is calculated and daily emissions are estimated. These daily emissions are then averaged to obtain a representation of the emissions around 13:30 LT on a monthly scale. In the calculation of the average, we discard the days for which more than two thirds of the domain has low-quality data or no data by using the quality assurance value provided in the TROPOMI product. For the period under study, averages have thus been calculated using between 21 and 30 days per months, except for September and October 2022 for which outliers have been identified in TROPOMI NO_2 columns or WRF-Chem-simulated OH concentration and NO_x:NO_2 ratio (calculated with 12 days each).

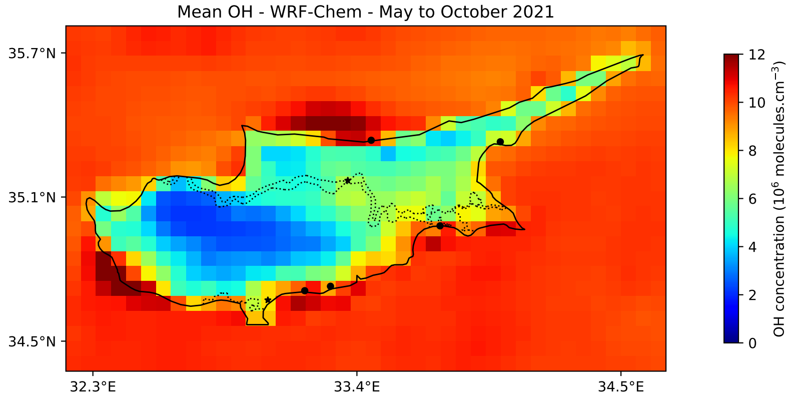

Figure 3.26: Mean PBL-averaged OH concentration above Cyprus for WRF-Chem simulations between May and October 2021. Power plants are denoted with dots while Nicosia and Limassol are denoted with stars.

The differences in the mapping of emissions lie in the differences between datasets. In particular, while the OH concentration of CAMS in the EC set is slightly higher on land than at sea, the OH concentration in the WRF-Chem simulations (sets WW and EW) is higher at sea. Figure 3.26 shows the mean OH concentration for the WRF-Chem simulations during the first period May-October 2021. These high OH concentrations at sea (usually between 8 and 14×10^6 molecules.cm^{-3}) are consistent with daytime NO_2 lifetimes found during the AQABA campaign (Friedrich et al., 2021). On land, concentrations are lower, and the areas that emit the most NO_x (the power plants and, to a lesser extent, the urban areas of Nicosia and Limassol) have higher OH concentrations than remote regions such as the Troodos mountains. Particularly high concentrations are calculated near the urban areas of Paphos and Kyrenia. Their origin is unclear, as these areas do not correspond to specific industrial installations, and might be the result of the accumulation of species on these coasts. It should however be noted that both CAMS data and WRF-Chem simulations show a similar mean annual cycle of OH with higher concentrations during summer months, which are consistent with the higher OH production with photochemical activity.

The differences are also significant in the horizontal wind field used to calculate the transport term. The linear interpolation carried out by downscaling the wind from ERA5 to a resolution of 0.0625°×0.0625° creates a regular field in the wind direction over the whole domain, whereas the upscaling of the WRF-Chem simulations preserves significant variations in angles on the grid. Figure 3.27 shows, for each pixel, the proportion of times that the wind in the two datasets differs by more than 30°. Generally speaking, the two datasets agree at sea and on the south coast of the island, with agreement between datasets 50 to 70% of the time. For the south coast, this proportion rises to 80% if the difference threshold is increased to 45°. The two datasets have slightly different angles on the north-west coast, where a difference is observed around 50% of the time with a threshold of 30 or 45°. Finally, the two datasets differ significantly along a 25 km-wide line, stretching from the centre of the Troodos massif to the Karpas Peninsula where the Kalecik power station is located. In this region, the two datasets agree only 15 to 30% of the time.

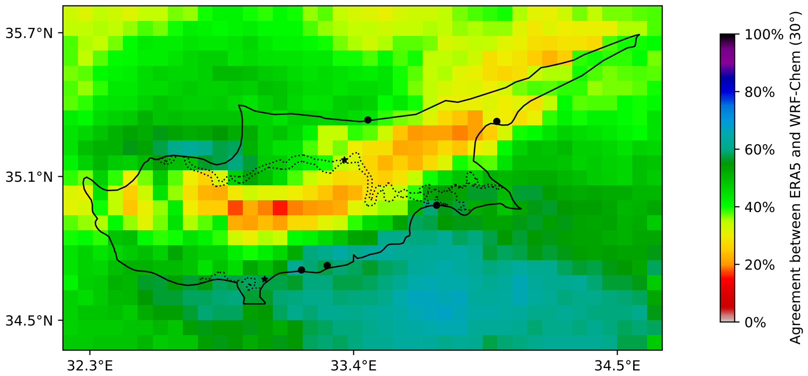

Figure 3.27: Frequency with which horizontal wind direction from ERA5 and WRF-Chem simulations agree (angle difference lower than 30°) between May and October 2022. Power plants are denoted with dots while Nicosia and Limassol are denoted with stars.

On this line, the differences between the two datasets are obtained because the smooth angle variations obtained by downscaling in ERA5 data do not correspond to the wind calculated by the WRF-Chem simulations, which frequently display drastic changes in angle direction over a few kilometres (as displayed, for instance, on Figure 3.24). This disagreement is important to take into account in our NO_x emission calculations, as the calculation of the transport term is very sensitive to wind angle, particularly for source points for which this term accounts for most of the NO_x budget.

3.3.7-C Mapping of NO_x emissions

NO_x emissions in Cyprus are mapped for the three datasets in Cyprus. Figure 3.28 shows the corresponding transport term, sink term and total emissions for May to October 2021. While we observe almost no emission above the Troodos mountain in the three cases, the sea surrounding the island displays relatively high emissions for sets WW and EW, i.e. sets for which WRF-Chem simulations have been used for OH concentrations. In these simulations, the OH budget is higher than in CAMS data and agree with observations (Friedrich et al., 2021), leading to higher calculated NO_x emissions up to 0.50×10^{15} molecules.cm^{-2}.h^{-1}. This points to a fault of our modelling; at sea, the reactivity of OH is lower, but the observed NO_2 levels remain low, which indicates a chemical loss through other processes. The urban areas of Nicosia and Limassol do not appear as significant emitters, and the power plants appear as the main sources of the island, with 6-month mean emissions that can go up to 2.50×10^{15} molecules.cm^{-2}.h^{-1}.

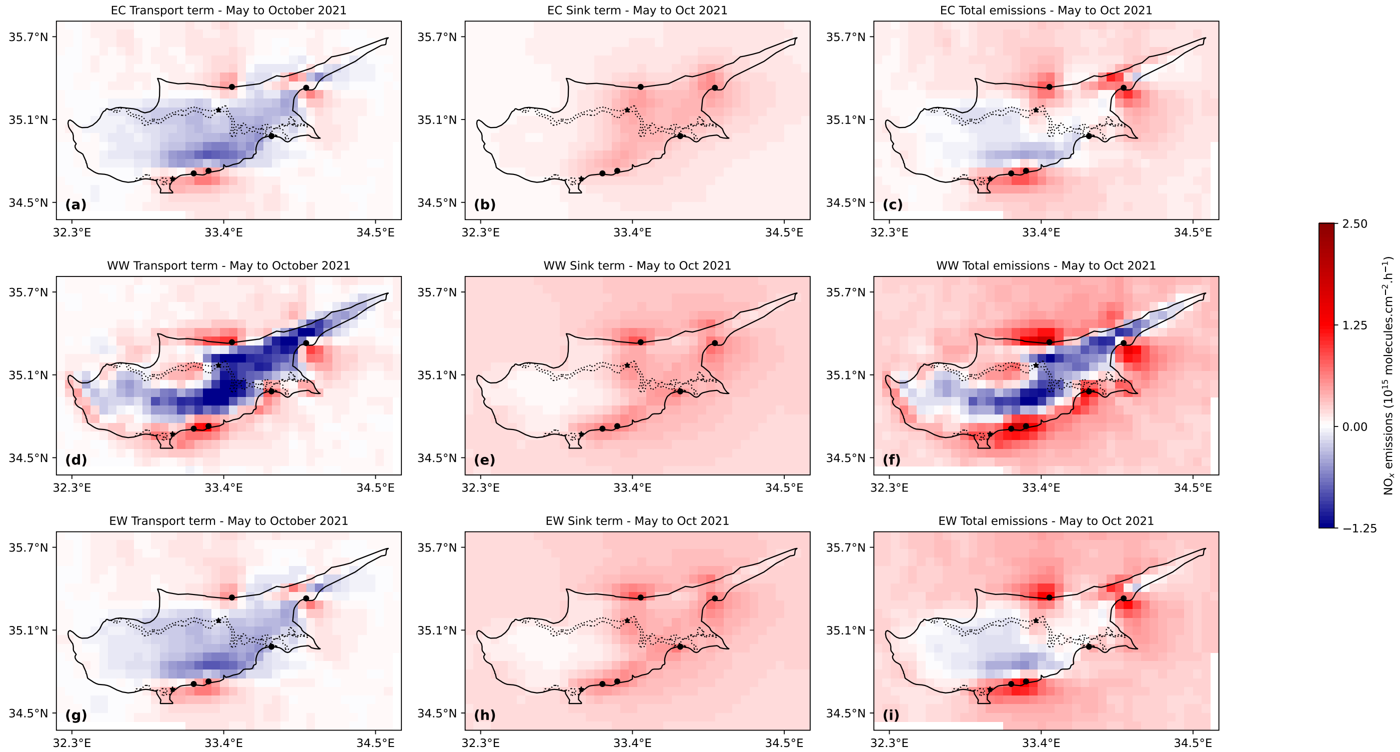

Figure 3.28: TROPOMI-derived mean daytime NO_x emissions for Cyprus (13:30 LT): transport term (left), sink term (middle), and resulting emissions (right) for May to October 2021, estimated with sets EC (a-c), WW (d-f) and EW (g-i). Power plants are denoted with dots, while Nicosia and Limassol urban centres are denoted with stars.

Although the sink term is responsible for most of the total NO_x budget within the domain, the transport term can reach high values at the smaller scale, highlighting hotspots where emissions are concentrated. Such hotspots comprise the power plants in the country, with the absolute transport term being on average 0.6 to 2.1 times higher than the sink term. However, this ratio varies with the used set and the considered power plant. Due to higher mean OH concentrations, the sink term is higher in the set EW compared to the set EC, leading to a lower transport-to-sink ratio. Conversely, a higher transport-to-sink ratio is calculated in set WW due to higher values of the transport term. Moreover, the set EW displays the lower differences between power plants in terms of transport-to-sink ratio, with Dhekelia, Teknecik, Kalecik and Vasilikos/Moni having a mean ratio of 0.68, 0.77, 0.98 and 1.27 respectively for the two 6-month periods. These values are lowered to 0.70, 1.30, 1.05 and 1.78 for set EC and 1.33, 1.44, 2.08 and 1.93 for set WW. They are lower than transport-to-sink ratio that had been observed in Qatar (Rey-Pommier et al., 2023), which can be explained by the lower capacity of the considered facilities (Beirle et al., 2023).

Another important feature common to these three mappings is the presence of negative values in total NO_x emissions. They are not realistic, and for a given pixel, such negative values appear when a negative value for the transport term (meaning that NO_x has been transported by the wind to the pixel) is not compensated by the sink term (which is always positive). This situation can occur when the absolute transport term is over-estimated, mainly due to errors in wind direction. However, when the transport term is correctly estimated, this situation can happen when the sink term is under-estimated, due to an under-estimation of OH or a neglect of additional sinks. For sets EC and EW, the observed negative values are located in the centre of the island and between Larnaca and the two power plants Moni and Vasilikos. Here, these negative values rarely exceed -0.4×10^{15}

molecules.cm^{-2}.h^{-1}. An increase of the sink term by 33% and 31% removes half of the pixels lower than -0.1×10^{15} molecules.cm^{-2}.h^{-1} in sets EC and EW respectively. Considering the latter value as a limit for emissions to be considered as residual, we can support the hypothesis of an underestimated sink term, to an extent which is consistent with the share of additional sinks mentioned in Section 3.3.6-C that have not been accounted for. However, negative values frequently exceed 1.0×10^{15} molecules.cm^{-2}.h^{-1} for set WW, and the increase of the sink term necessary to significantly lower the number of negative pixels is 151%, which is inconsistent with reported shares of the neglected NO_x sinks (Stavrakou et al., 2013). For this set, we can therefore conclude that the transport term is over-estimated. This over-estimation concerns pixels which, through the dipole shape taken by the transport term near emitters, are linked to pixels with negative values downstream. The shape taken by these pixels with negative values resembles the disagreement line between WRF-Chem simulations and ERA5 data highlighted on Figure 3.27. This comparison is only an outline of analysis, and a more detailed treatment of the sink term underestimation, including additional NO_x losses, would be necessary.

3.3.8 Comparison with regional and global inventories for power plants

3.3.8-A Observed cycle and difference between north and south power plants

We estimate monthly daytime emissions (around 13:30 local time) of the power plants on the island by summing the emissions of the 9 pixels closest to each plant, i.e. in a square of size 21×17 km^2. This length corresponds to the observed spread of emissions around an emitters, which accounts for both turbulent mixing an resolution effects. Due to their proximity, Vasilikos and Moni are counted as a single emitter but their sum is calculated on 12 pixels instead of 9. Figure 3.29 shows the monthly inferred emissions for the period between May 2021 and October 2022. Due to the low signal-to-noise ratio observed in Section 3.3.7-A, monthly emissions for the period November 2021 – April 2022 are too noisy be calculated, and the emissions over the period are averaged to a single point. The corresponding emissions from the different inventories are displayed (2018 for EDGARv6.1, 2021-2022 for CAMS-GLOB-ANT_v5.3 and 2018-2019 for CAMS-REG-v4). CARE-C reported emissions are also displayed for years 2018 and 2019. Emissions are expressed in mass terms as NO_2. In comparison with reported and inventory NO_x emissions, we interpret the TROPOMI-inferred emissions of each power plant as follows:

Vasilikos and Moni : The emissions calculated for both power plants are higher from June to August compared to the rest of the study period. Both 6-month periods show similar results, which can be interpreted as an increased electricity production to respond to the increased cooling demand. However, the amplitude of this annual cycle varies among the three sets, with the WW set displaying a particularly pronounced amplitude. CAMS-GLOB-ANT and CAMS-REG inventories also show a seasonal cycle, which is not the case for reported emissions and EDGAR emissions, for which the inter-monthly variations are relatively low. On average, emissions calculated by the EC (172 kg.h^{-1}) and EW (245 kg.h^{-1}) sets are similar to the average emissions from CAMS-REG (214 kg.h^{-1}), while the average emissions from the WW dataset (366 kg.h^{-1}) resemble those from CAMS-GLOB-ANT (349 kg.h^{-1}). Within these emissions, the contribution of Moni is unclear. This power plant is used to respond to peak electricity demands, which can occur during midday for the months under consideration. Due to the spreading of the emissions from Vasilikos, it is imposible to estimate whether this power plant is active or not by looking at gridded VCD maps. Additionally, the calculated emissions may also account for industrial cement production near both power plants. Therefore, the emissions calculated here may potentially be overestimated. Nevertheless, given the small size of the cement plant (with a capacity of 1.26 million tons per year), it is unlikely that its activity alone can explain the observed seasonal cycle.

Dhekelia : The emissions calculated with the EC and EW datasets are extremely low and similar to the reported emissions for 2018 and 2019 (between 58 and 65 $kg.h^{-1}$). These low emissions are not reflected in the inventories, which have levels similar to Vasilikos, despite Dhekelia having a lower production capacity. It is possible that NO_x filters have been installed for this power plant, significantly reducing its emissions. This reduction may not have been considered when constructing the inventories, which overestimate average emissions by calculating them based on the capacity and fuel of the power plant.

Teknecik : For all three datasets, a pronounced seasonal cycle is observed for the year 2021, with higher emissions during the summer months. This cycle does not appear to be replicated in 2022, except in the case of the WW dataset. However, an examination of the transport term near the power plant reveals negative emissions in its vicinity, suggesting possible errors that explain the high values calculated by this dataset. The seasonal cycle of 2021 is entirely absent from the CAMS-GLOB-ANT and EDGAR inventories, which are the only ones that represent this power plant. On average, the EC and EW datasets have emissions of 207 $kg.h^{-1}$ and 297 $kg.h^{-1}$ respectively, while the two inventories report emissions of 87 $kg.h^{-1}$ and 81 $kg.h^{-1}$ respectively. It is possible that the inventories mis-estimate the fuel used by this power plant and infer its emissions solely based on its capacity. Indeed, the emissions obtained from both inventories are similar to the emissions that would be obtained by applying the emission-to-capacity ratio of Vasilikos and Dhekelia. Finally, it should be noted that the WRF-Chem simulations do not represent this power plant and display a lower NO_x:NO_2 ratio (about 1.3) than the southern power plants (about 1.5). If the NO_x:NO_2 ratios of the southern power plants were applied to this plant, as well as to Kalecik, their emissions would increase by approximately 15%.

Kalecik : This power plant is located on the Karpas Peninsula, where differences in wind between ERA5 and WRF-Chem simulations are most noticeable, as shown in Figure 3.27. It is likely that both datasets inaccurately estimate the wind in this part of the island, leading to the unusual shape of the transport term around the power plant, as observed on Figure 3.28, which is characteristic of average emissions obtained when the wind is poorly represented. Nevertheless, it can be reasonably assumed that the emissions from the two inventories representing the power plant (CAMS-GLOB-ANT and EDGAR) underestimate its emissions for the same reasons as for Teknecik.

In general, inferred NO_x emissions are higher in the EW set than in the EC set, due to higher OH concentrations close to the coast and a higher NO_x:NO_2 ratio (for the power plants in the south) in the WRF-Chem simulations. Emissions estimated by the WW set are significantly higher for Vasilikos/Moni, Dhekelia and Teknecik, but this difference might be due to wind angle errors in WRF-Chem simulations. Those errors might also occur in the ERA5 reanalysis for Kalecik. Emissions from the power plants in the south are dominated by the Vasilikos power plant, whose emissions are higher during the summer. On average, the emissions from this plant are similar to those from Teknecik and slightly higher than Kalecik. The emissions from the power plants in the north are 1.8 times higher than those from the power plants in the south, despite a production capacity that is 3.6 times lower. This difference can be interpreted as due to two factors: the first is the quality of fuels used on either side of the island. The fuels used by the power plants in the north are of lower quality, as reported by the press (Cyprus Today, 2021), and therefore generate more NO_x per unit of fuel consumed. The second difference is in the technology used: in comparison with the power plants in the north, cleaner technologies might be used for Vasilikos, which was renovated in 2011, and for Dhekelia, whose engines were constructed in 2009 and 2010.

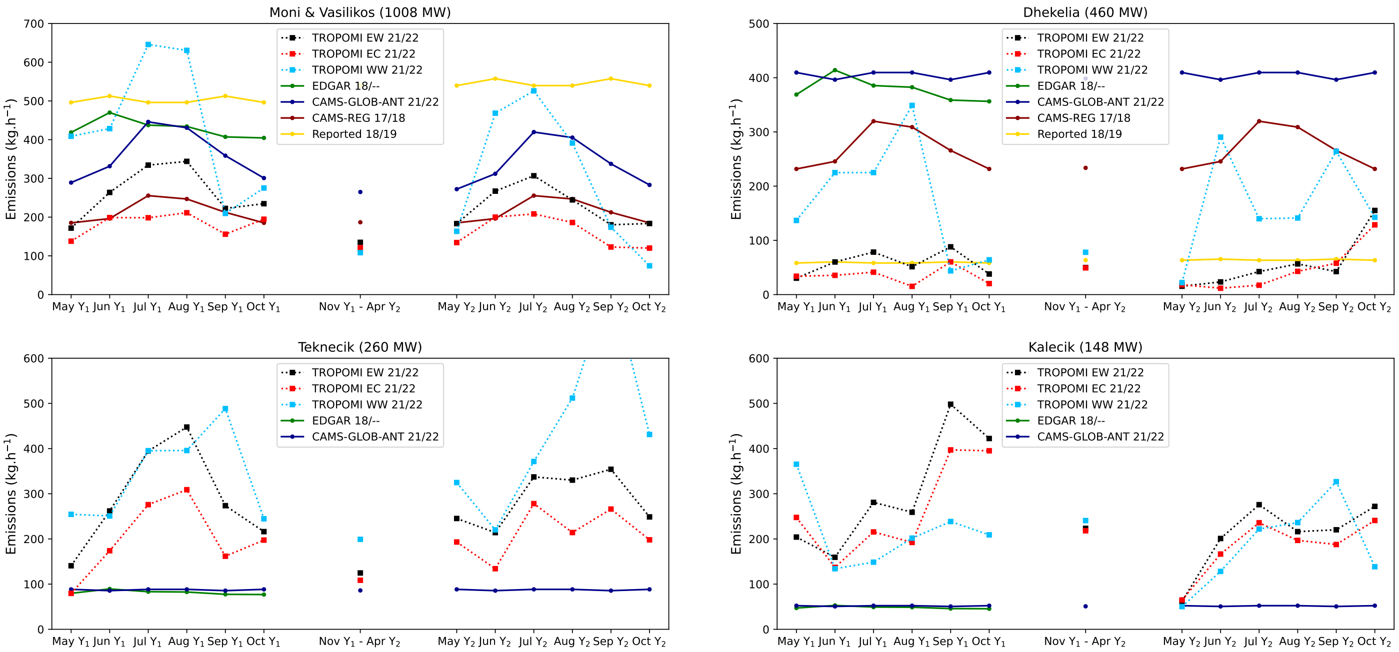

Figure 3.29: TROPOMI-derived mean daytime NO$_x$ emissions for power plants in Cyprus, estimated the datasets EW (black dotted), WW (light blue dotted) and EC (red dotted) between May 2021 and October 2022, compared to corresponding emissions in EDGARv6.1 for 2018 (green), CAMS-GLOB-ANTv5.3 for 2021/2022, CAMS-REG v4.2 for 2017/2018 and reported emissions for 2018/2019: Vasilikos and Moni (top left), Dhekelia (top right), Teknecik (bottom left) and Kalecik (bottom right). For each time series, Y$_1$ and Y$_2$ stand for the first and second year of the serie. Note that the range of the abscissa is different from one power plant to the other.

3.3.8-B Errors, uncertainties and assessment of results

In addition to the different error sources that vary from a power plant to the other, other aspects can be considered in the general uncertainties for the NO$_x$ emissions calculated with the flux-divergence method.

The first uncertainties to account for are those related to quantities used to calculate the emissions. TROPOMI retrievals are sometimes biased due to poor estimation of the air mass factor or local effects under particular vertical distribution conditions (Griffin et al., 2019; Lorente et al., 2019; Judd et al., 2020; Wang et al., 2021b). It should be noted that the latest versions of TROPOMI (v2.x) have tropospheric VCDs that are between 10% and 40% larger than the first versions (v1.x), depending on the level of pollution and season (Van Geffen et al., 2022). The chemical transport model TM5, which is used in the retrieval of the operational TROPOMI data, has been shown to under-estimate surface level pollution while over-estimating NO$_2$ at higher levels above the sea (Latsch et al., 2023; Rieß et al., 2023). In Cyprus, the albedos over the main power plants are relatively high, but because they are located near the sea, for which the albedo is lower, the impact of the a priori profile can be significant. We therefore consider a relative uncertainty of 40% for the tropospheric column. Uncertainties for the parameters involved in the calculation of NO$_x$ emissions must also be accounted for. For the wind module, uncertainties are generally of about 1 m.s^{-1} for components taken at precise altitudes (Coburn, 2019). Here, we assume an uncertainty of 4 m.s^{-1} for both zonal and meridional wind components averaged within the PBL in ERA5. For the OH concentration, the analysis of different methods conducted by Huijnen et al. (2019) showed smaller differences for low latitudes than for extratropics, but still significant. We thus take a relative uncertainty of 30% for OH concentration. For the reaction rate k_{mean}, the value of the corresponding relative uncertainty has been estimated by Burkholder et al. (2020). Using the transport-to-sink ratio for power plants highlighted in Section 3.3.7-C, the propagation of these different uncertainties on the monthly estimates of NO$_x$ emissions leads to an expanded uncertainty between 47% and 58% for sets EC and EW.

In addition to the uncertainties, systematic biases can arise due to the method used for our estimations. Here, the neglect of additional sinks in the NO_2 loss has already been discussed. Another bias can be the non-consideration of 3D transport. Indeed, the topography of Cyprus might be too complex to only account for 2D advection in the transport term. To capture these 3D transport effects, which can be particularly critical over mountainous regions, Sun (2022) introduced a corrective term parametrised by the ground wind, the inverse scale height of NO_2, and the altitude gradient. Here, although the island of Cyprus may show significant elevation gradients, these are relatively weak near the power plants, and the effect of this correction would be minor. Finally, the choice of the grid can also be called into question. In this research, spatial gradients were computed following the gridding of TROPOMI data onto a standard latitude-longitude 0.0625°×0.0625° grid. In contrast, de Foy, Schauer (2022) suggested the direct calculation of spatial gradients on the original TROPOMI grid (along-track and across-track). The primary advantage of calculating emissions directly on the TROPOMI grid lies in its ability to handle pixels with low-quality or no data (i.e. NO_2 retrievals with a quality insurance values lower than 0.75), resulting in lower discontinuities in the calculated derivatives. Here, we perform our averaging after calculation of the derivatives, and thus do not know how this grid change would affect our results.

Finally, other biases are in our comparison of daytime NO_x emissions inferred from TROPOMI observations and inventories, which calculate average emissions that are averaged throughout the month (i.e. accounting for daytime and nighttime emissions). Indeed, lower emissions cannot be excluded at night, highlighting the limitation of estimating total emissions over a long period using TROPOMI maps taken at one moment per day. A possibility would be to use the load curve to scale daytime emissions to total emissions, as it was done for Qatar (Rey-Pommier et al., 2023). This would not be possible for emissions from Teknecik and Kalecik, as their load curve is unknown here. It could theoretically be possible for Vasilikos/Moni, but the particular functioning of Moni, which is used to respond to peak electricity demands, as well as the spreading of the observed emissions between the two sources, makes it unfeasible in practice.

3.3.9 Conclusion

In this study, we investigated the potential of a top-down model of NO_x emissions based on TROPOMI retrievals and a flux-divergence scheme applied at high resolution over Cyprus. This scheme requires different parameters to be calculated and consists in the calculation of a transport term that uses horizontal wind, and the calculation of a sink term that requires temperature data and OH concentration to illustrate the chemical loss of NO_x. Emissions have been calculated with three different sets to assess the main limitations of the method. Our results show that lower NO_2 levels hinders the estimation of emissions from November to May. For the remaining period, we showed that the coarse resolution of CAMS near-real-time forecasts over power plants failed to represent the small-scale behaviour of OH, which is crucial to correctly estimate the sink term, but also the high NO_x:NO_2 ratio which is representative of the NO_x emitters. These parameters are better represented by WRF-Chem simulations, which agree with previous measurements conducted in the Eastern Mediterranean in the case of OH. However, high-resolution WRF-Chem simulations show mean wind fields whose angle vary rapidly in space, leading to large errors in the transport term that were lower when using the ERA reanalysis. Low emissions are calculated for the urban areas of Nicosia and Limassol. However, the power plants of Vasilikos and Moni, Teknecik and Kalecik appear as clear NO_x emitters, with high values for the transport term. For the six consecutive months under study, estimated daytime NO_x emissions show an annual variability for the five power plants in the country, with higher emissions during summer months. Noticing this trend is of high importance, since emission inventories and reported emissions do not systematically represent it. Moreover, this study shows that emissions for the power plants in the north of the island, when they are represented in inventories, are under-estimated. During these six months, they had mean daytime emissions 1.8 times higher than power plants in the south, despite a production capacity 3.6 times lower, i.e. an daytime emission factor 6.5 times higher while inventories represent similar emission factors for both sides of the island. Such a difference highlights the different paths followed by the two parts of the island in terms of used fuel and technologies, which are absent from inventories.

Several limitations exist in the estimation of these results, which do not allow a precise quantification of NO_x emissions without large associated uncertainties. However, they provide a more accurate representation of emissions in terms of average levels and seasonal cycles than air quality inventories, for which the smallest sources are often not reported or mis-represented, particularly in developing countries. As a consequence, we believe that such a qualitative analysis can be reproduced in other countries counting power plants with similar capacities, as a first step towards a better monitoring and reporting of anthropogenic emissions, as part of national and regional strategies to tackle air pollution issues and climate change.

Code availability

Code will be made available on request.

Data availability

The TROPOMI Sentinel 5P Offline Product (OFFL) and Product Algorithm Laboratory (PAL) have been used, using processor version 2.3.1. The TROPOMI NO_2 product is publicly available on the TROPOMI Open hub (`http://www.tropomi.eu/data-products/data-access`, TROPOMI Data Hub, 2022) while the S5P-PAL reprocessed data can be found on the S5P-PAL data portal (`https://data-portal.s5p-pal.com`, ESA, 2022). CAMS data can be downloaded from the Copernicus Climate Data Store (`https://ads.atmosphere.copernicus.eu/cdsapp#!/dataset/cams-global-atmospheric-composition-forecasts`, ECMWF, 2022a). The European Centre for Medium-Range Weather Forecasts (ECMWF) ERA5 reanalysis be downloaded from `https://cds.climate.copernicus.eu/cdsapp#!/dataset/reanalysis-era5-pressure-levels-monthly-means`. EDGARv6.1 emissions are provided by `https://edgar.jrc.ec.europa.eu/emissions_data_and_maps`. CAMS-REG-v4 and CAMS-GLOB-ANT_v5.3 emissions are available at `https://eccad3.sedoo.fr`.

Author contributions

AR analysed the data, prepared the main software code and wrote the paper. FC provided the TROPOMI NO_2 data product and corresponding gridded maps. GG provided the WRF-Chem simulations. FD and AV contributed to compare the inferred emissions with reported emissions for the power plants in the southern part of Cyprus. PC, TC, JK, and JS contributed to the improvement of the method and the interpretation of the results. All authors read and agreed on the published version of the paper.

Financial support

This study has been funded by the European Union's Horizon 2020 research and innovation programme under grant agreement N°856612 (EMME-CARE).

Competing interests

The authors declare that they have no conflict of interest. The authors would like to thank Ülkü Tasseven (The Cyprus Institute) for her help concerning informations for the power plants in the north.

3.4 Limitations of the method

This section presents the various limitations inherent to the quantification of NO_x emissions using satellite NO_2 observations, which have gradually become obvious through the development of the flux-divergence method. As such, this section is not a quantification of the uncertainties surrounding emissions, as these have already been highlighted in the three case studies carried out in this chapter. However, it presents various aspects to be taken into account for future quantifications, and suggests applicability criteria and possible improvements for future developments.

3.4.1 Limits in the TROPOMI *a priori* profiles and quality flags

The NO_2 columns being the main material in the estimation of NO_x emissions, the construction of the TROPOMI products is the first element to examine when considering the limitations of the flux-divergence method. Indeed, a large part of the uncertainties in the estimated NO_x outputs lies in the vertical tropospheric columns, which have been calculated from measurements of solar backscattered radiation using the DOAS method and data assimilation systems using the TM5-MP chemistry transport model. The coarse resolution of this model ($1° \times 1°$) can be a first limitation to effectively infer NO_x emissions, as shown for the case of Qatar. The TM5-MP profiles can be replaced by any other profile information, resulting in a new retrieved tropospheric NO_2 column. Douros et al. (2023) replaced the a priori TROPOMI OFFL NO_2 profile by high-resolution air quality forecasts for Europe. As compared to the standard TROPOMI NO_2 data, this new product was found to be biased-low by 5% to 12% for most European cities.

The air mass factor (AMF) itself can be replaced: for instance, Lama et al. (2022) re-calculated the AMF by replacing the tropospheric AMF of the original TROPOMI OFFL product by an AMF taken from WRF-Chem simulations. Similarly, Beirle et al. (2023) re-calculated the AMF above different emitters from the corresponding averaging kernel based on a delta-peak profile at plume height to better reflect the NO_2 distribution close to ground, which resulted in an AMF correction of about 1.61. Another option to reduce uncertainties in estimated average emissions would be to exclude TROPOMI data with the highest cloud radiance fractions, regardless of the value taken by the quality assurance flag q_a. For instance, Liu et al. (2023) excluded TROPOMI NO_2 data with cloud radiance fraction higher than 0.5 or greater in our analysis. However, for versions of the flux-divergence method where lifetime variability is not allowed and determined independently from NO_2 observations, this exclusion might lead to a bias in the NO_2 emissions, since it would remove scenes with lower lifetimes. A sensitivity analysis regarding the impact of clouds has been discussed by Liu et al. (2022).

3.4.2 Limits in the estimation of the sink term

Within the flux-divergence method, the accurate estimation of the sink term is crucial. It is generally responsible for the major portion of the annual observed variability in the estimated emissions, particularly those of diffuse emitters for which the sink term is typically greater than the transport term. Most of this variability is the result of the composition of an annual cycle of NO_2 concentrations (observed in the form of columns) and OH concentrations, with a relative amplitude of the corresponding annual cycles generally higher for OH than that of NO_2. For the OH concentration, a relative uncertainty of 30% has been used (Huijnen et al., 2016), representing the largest component of absolute uncertainty. Large errors in the annual cycle of OH, and therefore in the sink term, can thus be expected. In addition to these large-scale errors, an incorrect representation of the sink term can occur at the scale of a plume by not capturing the non-linear relationship between OH and NO_2. Two datasets have been employed throughout this thesis to estimate OH: the CAMS NRT data and WRF-Chem simulations for Cyprus. In the case of CAMS, the $0.4° \times 0.4°$ resolution may not always capture the NO_2 gradients adequately in plumes near a known emitter (Valin et al., 2011; Li et al., 2023a). Due to the non-linear relationship between NO_x and OH, this can lead to inaccurate sink term estimations within a plume, whose bias depends on the NO_x regime (low, intermediate, or high NO_2 levels). These biases in the representations of the OH field worsen when the location of emitters is unknown, causing OH levels to be incorrect by almost an order of magnitude, as it was observed in the case of WRF-Chem simulations for Cyprus above power plants.

The second difficulty in estimating the sink term is the consideration of additional reactions. It was demonstrated in Section 3.1.5 that reactions other than the oxidation by OH were reasonably negligible in the total NO_2 loss in Egypt. Generally speaking, this neglect is valid for areas in the EMME region with dry and warm climates that hinder most daytime reactions highlighted in Section 1.2.3-A. When it is not the case, the sink term can be under-estimated at a levels much higher than the residual noise observed in maps. In an environment with higher humidity rates, the reaction of NO with HO_2 might play a more significant role in chemical loss. In a cooler environment, the formation of PAN would also be less inhibited. Finally, most of the additional loss during daytime might be due to the reaction between NO_2 and organic peroxy radicals, whose yield is enhanced in areas with high levels of VOC emissions (such as forests for biogenic emissions and industrial/urban areas for anthropogenic emissions). Incorporating all these reactions would be complex, as it would require additional data for emissions estimation. The reliability and uncertainties of such data would need to be assessed for the concerned regions.

An alternative approach is to quantify the share of chemical loss not accounted for by the results provided by the current flux-divergence method. In areas far from human activities, there are no anthropogenic NO_x emissions, and natural emissions in the lower troposphere are low. As the sink term is always positive, zero emissions in pixels without anthropogenic emissions would correspond to a negative value for the transport term (indicating that any observed pollution there would result from the wind transporting pollution from areas with human activity). Thus, the neglected sink can be evaluated as the quantity needed to be added to the sink term to counterbalance the negative trend of the transport term away from these areas. Due to the residual noise observed in the maps provided by the flux-divergence method, this neglected sink would be assessed as an average value. Two hypotheses can be made to evaluate this quantity without needing to incorporate other datasets:

1. Additional sinks are proportional to tropospheric vertical columns. In this case, the sink term is modified by adding an additional lifetime τ_{add} as follows: $S = \Omega/\tau + \Omega/\tau_{\text{add}}$. This hypothesis is reasonable when all relevant additional reactions have first-order kinetics, which is the case for all reactions highlighted in Section F.

2. Additional sinks are proportional to the tropospheric vertical columns and the OH concentration. In this case, the sink term is modified by adding a multiplicative factor χ to the OH-driven sink as: $S = (1+\chi)\Omega/\tau$. This is a strong hypothesis, indicating a behavior of other species involved in NO_2 loss similar to that of OH (i.e., with non-linearities).

In both cases, this "boosted" sink term is ideally such that emissions are zero above zones without anthropogenic activity. Supposing other parameters are estimated correctly, the optimal values of τ_{add} or χ are thus given by:

$$\frac{1}{\tau_{\text{add}}} = \langle \frac{\text{div}(\Omega\vec{w})}{\Omega} - \frac{1}{\tau} \rangle_{\text{no activity pixels}} \tag{3.15}$$

$$\chi = -1 - \langle \frac{\text{div}(\Omega\vec{w})}{\Omega/\tau} \rangle_{\text{no activity pixels}} \tag{3.16}$$

In Cyprus, a similar calculation of χ has been performed (Section 3.3.7-C) but on all pixels of the domain (rather than those with low anthropogenic activity), and inferred a value of 33% when both the sink and the transport term were estimated using CAMS and ERA5 data. A wider study of the calculation of χ could inform us about the missing part of the NO_2 sink in the northern part of the EMME region.

3.4.3 Limits in the estimation of the transport term

The example of Cyprus shows that an accurate representation of the wind is critical to estimate the transport term correctly. For a given plume, the poor representation of wind speed leads to an under- or over-estimation of transport, but the expected profile, i.e. that of a dipole, remains represented. However, an incorrect representation of the wind direction, such as a non-alignment with the main direction of the plume, fails to represent this dipole shape. Negative values of transport maps are thus not coincident with high values of the sink term in the tail of the plume. This effect is highlighted on Figure 3.30, re-uses the example of the NO_x emissions estimated for the Sinai cement plants on a single day (for which the dipole shape of the transport term was correctly captured on Figure 2.5), but by adding an offset of 30, 90 and 180 degrees to the wind direction. The sink term remains unchanged. The results shows a mis-estimation of the emissions with the wrong wind fields, with high negative values near the emitter location that are not compensated by the sink term.

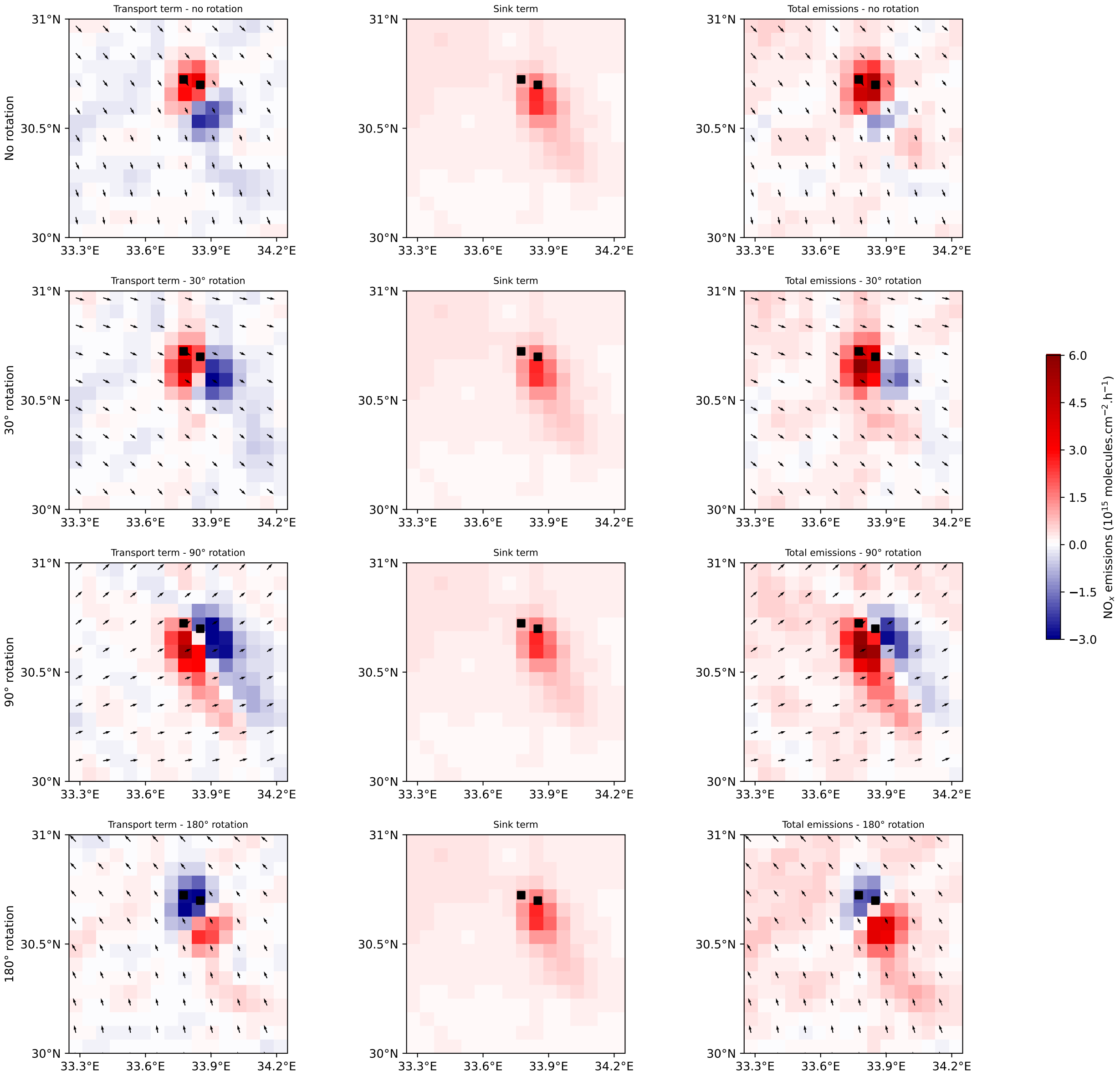

Figure 3.30: NO_x emissions of the Sinai cement plants on September 10th 2019 with an additional angle offset to the ERA5 wind field of 0°, 30°, 90° and 180° offset (from top to bottom). The sink term remains unchanged. The transport term (left), sink term (middle) and total emissions (right) are displayed, with the corresponding wind field on the transport and emissions maps. The location of the cement plants are denoted with squares.

The estimation of the transport term significantly thus relies heavily on the representation of the wind angle. Higher errors are therefore expected to be high in regions having winds that vary rapidly in time, or regions with complex horizontal wind variations, such as mountainous regions. In particular, situations where sub-grid scale-phenomena occur, such as mountain and sea breezes, but without being accounted for in reanalyses like ERA5 or simulations, might display even higher errors in the estimation of transported NO_x.

Another limitation on the accuracy of the transport term comes from the calculation of derivatives in the divergence operator. Theoretically, the derivatives are defined in the form of a limit. In practice, since physical quantities vary discretely in datasets (in our case from one pixel to another), derivatives are approximated by the growth rate. For a given function f, the second-order central-finite difference scheme gives an approximation of its derivative $\frac{\mathrm{d}f}{\mathrm{d}\xi}$ as the growth rate between points on a grid whose spacing is $\Delta\xi$:

$$\frac{\mathrm{d}f}{\mathrm{d}\xi}(\xi) \simeq \frac{f(\xi+\Delta\xi)-f(\xi-\Delta\xi)}{2\Delta\xi} \tag{3.17}$$

For this scheme, the error in the approximation of the derivative is proportional to $\Delta\xi^2$. Better approximations of the derivative are possible, and the fourth-order central-finite difference is regularly used:

$$\frac{\mathrm{d}f}{\mathrm{d}\xi}(\xi) \simeq \frac{-f(\xi+2\Delta\xi)+8f(\xi+\Delta\xi)-8f(\xi-\Delta\xi)+f(\xi-2\Delta\xi)}{12\Delta\xi} \tag{3.18}$$

For this scheme, the error in the approximation of the derivative is proportional to $\Delta\xi^4$. This means it is more accurate than the previous approximation (Yew, 2011). However, this calculation requires knowledge on the function f estimated at four different neighbouring points (i.e. eight points for a divergence operator in two dimensions), while the second-order central-finite difference scheme only requires estimates for two points (four for the divergence in two dimensions). For a given pixel, the use of the fourth-order difference makes the calculation of the divergence in the transport term more difficult, since data for the eight neighbouring pixels is required. For emitters close to areas with low-quality data or no data ($q_a < 0.75$), the flux-divergence method based on TROPOMI retrievals fails to estimate the transport of NO_2. It is thus critical in cloudy areas, which is not the case for most of the EMME region. This limitation can be considered insignificant when average emissions (i.e. monthly or annual emissions) need to be estimated, because a given region is never entirely covered by clouds for long periods of time. However, it becomes critical when emissions must be estimated for a single day. In this case, the use of the second-order central-finite difference scheme is more flexible, although with higher errors. The difference of the error magnitude between the two schemes seems low compared to the amplitude of the transport. For instance, in the case of the two cement plants in Sinai, already discussed in Section 2.5, both schemes were tested in the calculation of the transport term (see Supplementary Materials). Pixels that are closer to the emitters, which are also pixels with the highest absolute values, have an averaged contribution of 2.6×10^{15} molecules.cm^{-2}.h^{-1} for the fourth-order scheme and 2.2×10^{15} molecules.cm^{-2}.h^{-1} for the second-order scheme, i.e. a relative difference of 20%. Relative differences between 10 and 25% are generally found for different emitters and different averaging periods. For functions with rapid changes, the fourth-order scheme may yield larger absolute values than the second-order because it captures finer details, unless these details are not represented due to the coarse grid spacing. Here, the size of the TROPOMI pixels is of the order of magnitude of the NO_2 turbulent spreading, but it is the same order of magnitude as the plume length. The analysis of the amplitude of the transport term calculated with the fourth-order central-finite difference scheme, compared to the transport term than the second-order central-finite difference scheme, is yet to be conducted.

3.4.4 Vertical transport effects

Results obtained in Section 3.1.6-C showed that in Egypt, the flux-divergence model had low sensitivity to the vertical, with less than 10% changes when the parameters involved in the calculation of the sink term were estimated on different vertical layers. However, vertical effects regarding the transport of pollutants were not investigated. As mentioned in Section 2.1.6, the 2D-divergence approach fails to capture 3D transport effects, which can be particularly critical over mountainous regions. To account for those effects, Sun (2022) introduced a corrective term $\epsilon_{\text{correction}} = \Omega X_e \vec{w}_g \cdot \vec{\nabla} z_0$. It is possible to estimate the importance of this corrective term with respect to the others, i.e. the transport and sink terms. In particular, since both the corrective term and the sink terms are proportional to the tropospheric VCD, their absolute ratio can be easily expressed as:

$$\frac{|\epsilon_{\text{correction}}|}{|S|} = \frac{\Omega X_e |\vec{w}_g \cdot \vec{\nabla} z_0|}{\Omega/\tau} \sim \tau X_e w_g ||\vec{\nabla} z_0|| \tag{3.19}$$

Here w_g is the mean wind module at ground level. In the previous expression, the altitude gradient $||\vec{\nabla} z_0||$ is the only non-variable term. With typical values for inverse scale height $X_e \sim 0.3$ km^{-1}, ground wind $w_g \sim 20$ km.h^{-1} and lifetime $\tau \sim 4$ h, we obtain the typical altitude gradient value above which the corrective term has the same order of magnitude as the other terms as $||\vec{\nabla} z_0||_{\text{lim}} \simeq 0.042 = 42$ m.km^{-1}. Figure 3.31 shows the altitude gradient over the most mountainous parts of the EMME region. Countries such as Lebanon, Greece, Türkiye and Iran have gradients which are frequently higher than this critical value, but the rest of the EMME region generally displays gradients more than two times lower (we therefore prove a posteriori that estimating the correction term was not necessary for Egypt, Qatar and, to a certain extent, Cyprus, for which complex topography is mostly found far from NO_x sources). The gradient has been derived from re-gridded altitude maps from Smith, Sandwell (1997).

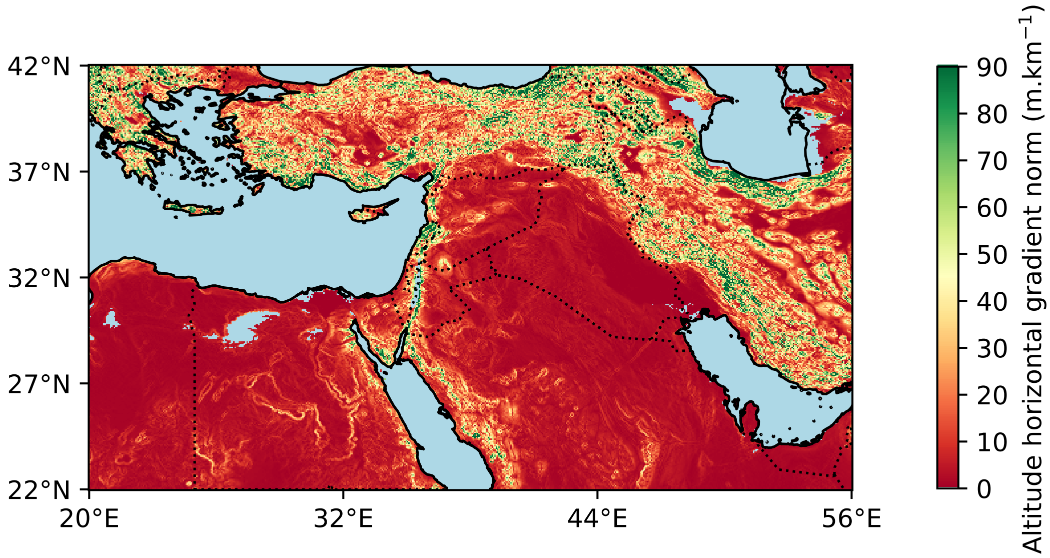

Figure 3.31: Horizontal gradient of the ground level on a 0.0625°×0.0625° grid for the northern half of the EMME region. The areas with an altitude below sea level are represented in light blue.

It can therefore be estimated that in the most mountainous areas, the use of the correction term is fundamental in order to obtain a correct estimate of NO_x emissions. For less steeply sloping areas, it would be lower than the sink term. Since most NO_x emitters have a transport term similar to or greater than the sink term (the latter in the case of a point-source emitter), the correction term would also be lower than the transport term. On the other hand, it is completely negligible in the calculation of emissions only for totally flat terrain. Overall, it is not sufficient, in most cases, to predict whether or not the correction term is negligible just by using altitude gradient data. The amplitude of this term will depend on the meteorological conditions, mainly the surface wind speed. It should also be noted that the calculation of the correction term itself involves a number of uncertainties. In reanalyses, surface winds generally present higher errors in complex terrain, due to the intricate interactions between the Earth surface and the lower atmosphere, which are significantly influenced by topography and temperature gradients. The resolution used here can be considered too coarse to effectively model such phenomena.

3.4.5 Overlapping of emissions

Quantifying the emissions from a NO_x emitter becomes more complicated when other emitters are located nearby, because their emissions can overlap. This situation of overlapping is extremely common. Indeed, major industrial sites are often situated in specialised regions because it offers several advantages, including the access to a skilled workforce, shared infrastructures (especially transportation networks) or economies of scale. Consequently, the case of a facility completely isolated from human activities is relatively rare. The most common case is that of industrial sites located near a city, adding an industrial layer to the emissions of the area. This corresponds to the majority of cities we have studied so far, making it impossible to achieve a sector-specific characterisation of NO_x emissions in these areas. Another common case is the one of industrial areas situated far from urban centers. In this case, characterisation of industrial emissions is possible, but these emissions encompass several different polluting sites. This is the case in the Ain Sokhna region in Egypt, identified in Section 3.1.6-B, which includes cement plants and a steel factory. It is also the case of the Ras Laffan region in Qatar, studied in Section 3.2.8-A. This case is the most interesting, because industrial emissions could be predominantly attributed to the power sector, allowing to characterise the emissions of the power sector and derive an emission factor. However, because the three power plants are located in the same pixel of the re-gridded VCD maps, their individual emission factor could not be estimated. The issue is the same for power plants that are separated by one or two pixels (i.e. about 14 km), because the spread of the emissions around the source overlap to extent that a distinction between the two sources is not possible. In Cyprus, this is the case for the Moni and Vasilikos power plants, separated by 10 km, which were considered as a single emitter.

A non-systematic overlap can also occur when two close emitters are located on the same streamline. This situation is common in Cyprus between the city of Limassol and the Moni/Vasilikos power plants (when the wind is in the east or west direction). In these cases, the plume resulting from these two emitters does not exhibit a decreasing shape downstream of the first emitter. Distinguishing the two sources is possible if the distance between them is greater than the order of magnitude of the observed emissions spreading (i.e., accounting for resolution effects) of emissions. Otherwise, the flux-divergence method will treat the two emitters as a single source with emissions peaking between the two emitters (see Supplementary Materials).

3.4.6 Scaling of NO_2 production to NO_x emissions

A large source of uncertainties comes from the calculation of the conversion of NO_2 production to NO_x emissions, which is necessary as satellites measure NO_2, whereas inventories report total NO_x emissions. Nitrogen oxides are mostly emitted in the form of NO, which is not observed by satellites. A typical assumption is that NO is quickly oxidized to NO_2 by reaction with ozone and the steady state NO:NO_2 ratio is reached within a few minutes. Many studies (Beirle et al., 2019; de Foy, Schauer, 2022) assume a photostationary state and use the steady-state daytime concentration ratio under typical urban conditions of $\mathcal{L} = 1.32$ based on Seinfeld, Pandis (2006). For Egypt, this ratio was calculated using CAMS NRT forecasts, and small deviations from the 1.32 value were found over urban areas. In Qatar, outliers were found using CAMS data and the value of 1.32 was used, which illustrates the need to appropriately account for the conversion from NO_2 to NO_x. Indeed, the photostationary state is a hypothesis which is potentially not verified on the scale of a NO_x source like a power plant stack. This possibility, which is supported by values of $\mathcal{L}$ higher than 1.6 in WRF-Chem simulations over power plants in the southern part of Cyprus, but also by Li et al. (2023b) who calculated values of $\mathcal{L}$ correlated with the combustion temperature and energy efficiency of large energy consuming sources in northern China with a median value of 3.3 for power plants, suggests that NO_x emissions inferred in Egypt and Qatar might be under-estimated.

Other phenomena can be taken into account to explain possible biases in the calculation of the NO_x:NO_2 ratio under the photostationary hypothesis: in environment with high pollution levels, the use of the Leighton relationship might not be valid due to the presence of other species like VOCs, influencing the balance between NO and NO_2. Specifically, the hydroxyl radical, capable of reacting with both VOCs and NO_x, can result in the generation of oxygenated VOCs. Simultaneously, it can facilitate the conversion of NO to NO_2 and the subsequent formation of ozone. To limit uncertainties in the calculation of NO_x emissions due to this factor, it is necessary to quantify the amplitude of the corresponding bias. Further studies estimating this ratio from different methods and at different spatial and temporal scales would therefore pave the way towards a more precise quantification of NO_x emissions.

3.5 Extension of the method

3.5.1 Estimation of traffic and shipping emissions

So far, NO_x emissions from power plants and cement plants have been estimated, mostly with the flux-divergence method. However, transport emissions also hold a significant share in the total anthropogenic NO_x budget. In urban areas, it can be the major source of NO_x, but those emissions overlap with emissions from other sectors. As a consequence, they cannot be isolated and characterised there. Nevertheless, terrestrial transport emissions (traffic) or maritime transport emissions (shipping) can be estimated in areas where they are the sole sources of NO_x. This is the case for major highways and shipping lanes. Most of the time, such routes can be identify on TROPOMI NO_2 VCD maps. For instance, Georgoulias et al. (2020) and Kurchaba et al. (2022) estimated NO_x emissions from individual ships, while Rieß et al. (2021) estimated that NO_x emissions from ships over European seas reduced by 20-25% during the COVID-19 pandemic. Here, Figure 3.32 provides an estimation of the emissions for two transport routes: the first one is a series of highways in Saudi Arabia that connect the coastal city of Jeddah to Riyadh via Mecca, and the second one is a shipping route that starts from the southern end of the Suez Canal (beginning of the Gulf of Suez) and crosses the Red Sea to the Bab-el-Mandeb strait, which opens into the Gulf of Aden. Emissions are calculated with the flux-divergence method using ERA5 data for wind and CAMS data for OH concentration, temperature and NO_x:NO_2 ratio. In both cases, the approximate coordinates of the routes are pre-entered, and the emissions for each segment of the route are calculated by considering the closest pixels within a radius of 40 km (6 pixels) for the shipping lane and 23 km (3-4 pixels) for traffic. The chosen radius roughly corresponds to the spatial extent of emissions observed on averaged emission maps, plus the size of one pixel. The lower spread of emissions on road lanes, compared to shipping lanes, might be due to the absence of infrastructure (i.e., highways) that constrain movement of individual sources, but it can also be due to differing wind and atmospheric conditions between the open sea and desert environments. It has been a posteriori verified that the entered path for both routes aligns with observed NO_x maps. A more precise estimation of emissions could directly use route coordinates. Moreover, in the case of the shipping route, the Suez Canal itself is not considered is the route due to its narrowness; the TROPOMI pixels would include emissions from other sectors, which we aim to avoid here.

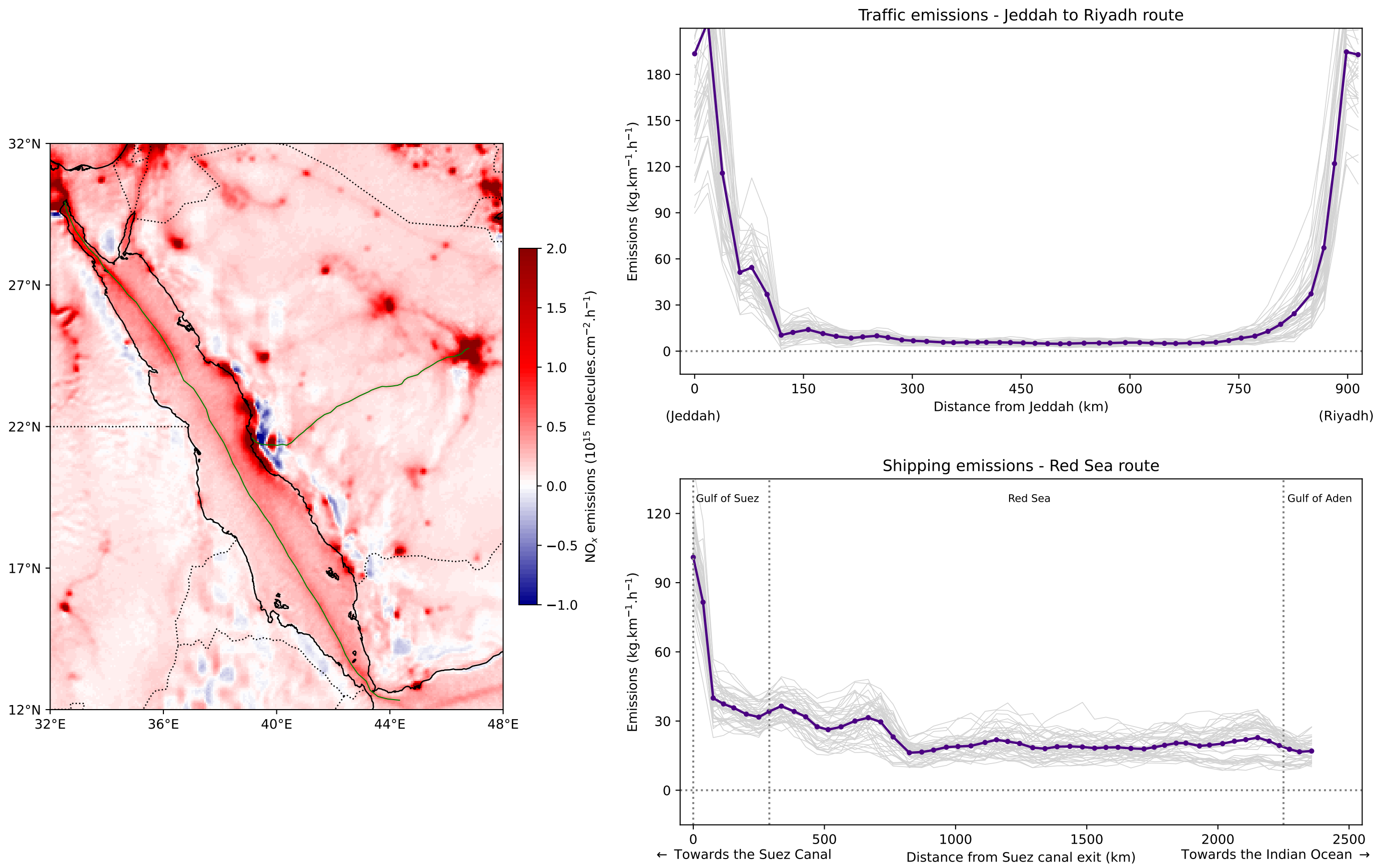

Figure 3.32: (left) Map of mean NO$_x$ TROPOMI-inferred daytime emissions from 2019 to 2022 and paths of routes. (right) NO$_x$ emissions for traffic along the terrestrial route from Jeddah to Riyadh (top) and for shipping along the maritime route from the Suez Canal to the Gulf of Aden (bottom). Monthly averages are shown in gray, while the 2019-2022 average is shown in purple. In the case of the maritime route, the entrance and exit of the Gulf of Suez, as well as the location of the Bab-el-Mandeb strait, are indicated with dashed lines.

The observed emissions are uniform along the roadway axis, at around 10 kg.km^{-1}.h^{-1}. This value is ten to twenty times lower than the line emission densities estimated in urban areas (Jeddah and Riyadh, at the ends of the profile). The profile of the shipping route also exhibits emissions that are significantly lower than in urban environments. Higher densities are observed within and immediately outside the Gulf of Suez at bout 30 kg.km^{-1}.h^{-1}, followed by a reduction to 20 kg.km^{-1}.h^{-1} during the majority of the crossing of the Red Sea. Such estimates provide original information on NO$_x$ emissions from cars on roads and ships on open sea. This information is potentially useful for authorities to help determine the (non-)compliance of companies and individuals with increasingly stringent NO$_x$ emission regulations on cars, trucks and ships. However, the estimation of such emissions face two major issues that must be accounting for when interpreting profiles such as shown here:

- The extremely low signal-to-noise ratio of the NO$_x$ signal makes the method heavily sensitive to the calculation of the background. Near highways and shipping lanes, the previous map show residual emissions that have the same order of magnitude as the calculated line emission densities for those routes. As a consequence, it can be difficult to interpret the obtained profiles. For instance, the comparison of mean profiles for March-April 2019, 2020 and 2021 shows a decrease in shipping emissions for a significant part of the Red Sea route in 2020, but not for the traffic emissions on the Jeddah-Riyadh axis. The low level of these emissions make it difficult to characterise a COVID-19 effect (see Supplementary Materials, Figure A.14).
- Uncertainties of the air mass factor are believed to be higher over sea than over land. Rieß et al. (2021) demonstrated that previous versions of TROPOMI, implemented with the older version

of the FRESCO cloud algorithm (Wang, Stammes, 2007), led to biases that underestimated columns over the sea. Additionally, Latsch et al. (2023) highlighted the significance of identifying genuine shipping signals in TROPOMI data to prevent unintentional interpretation of a priori information.

3.5.2 Combination with estimated activity from satellite RGB images

We have shown that the flux-divergence method allows to estimate NO_x emissions from an isolated industrial facility under certain conditions. However, random errors, arising mainly from the estimation of parameters involved in the method and the resolution of satellites, are responsible for considerable uncertainties, especially for emissions estimated for a single day. This is one of the reasons why a heavy averaging is carried out prior to or after the emission calculations through the flux-divergence method. In Qatar and Egypt, we have demonstrated the existence of annual and weekly cycles. In particular, the study of the emissions in Qatar identified a difference in the weekly cycle between urban areas and power plants, with a deeper Friday drop in urban areas as an illustration of the "week-end effect". Such cycles are much less obvious for industrial facilities, especially those not directly connected to urban activity such as power plants. Several polluting industrial sectors, like cement production, exhibit highly irregular output. In Section 3.2.8-A, emissions from the two cement plants in the west of Qatar were calculated on a monthly scale or over 4 years by averaging emissions from TROPOMI images, even when their activity was unknown. Generally speaking, characterising emissions from an industrial site involves averaging observed daily emissions when the facility is active with observed daily emissions when it is not, leading to a biased-low estimation of the NO_x output (in other words, the calculated emissions represent the average NO_x flow rate above the emitter but does not characterise the facility itself).

To counterbalance this effect and achieve accurate characterisation, inactive days need to be sorted out during emission averaging. To achieve this, a first option is to have additional information about the activity of the facility. Such activity data is hard to obtain, as it is typically known by the site operator. A second option is to filter daily images based on a threshold of observed VCDs above the site: images that are kept are those where pollution surpasses a certain level, defined, for instance, as a multiple of the local background or proportional to the production capacity of the site. This option is the simplest to implement, but it does not distinguish between days when an installation operates at full capacity and days when the production is reduced. A third option, accounting for the inter-daily variability of the production, involves a prior estimation of the activity through other satellite images. In the EMME region, previous studies have used other combination of satellite data to characterise the activity of industrial sites (Abeed et al., 2021). The example presented here is that of an association with visible images from the Sentinel-2 RGB product (Drusch et al., 2012), which is a composition of satellite images captured by the two ESA Sentinel-2 twin satellites (Sentinel-2A, launched in 2015, and Sentinel-2B, launched in 2017). This composition combines different spectral bands to create a visible color image with a ground spatial resolution of 10 meters. These images allow for detailed and realistic visualization of the land surface, ideal for monitoring environmental changes, land use, and natural resources. This Sentinel-2 product is widely used in mapping, resource management, crop monitoring, and other remote sensing applications. The two satellites in the constellation have a combined revisit period of 5 days at the equator. In a monitoring context, these images can be used to roughly quantify the activity of industrial facilities. For instance, if the industrial site possesses multiple emission stacks, a dimensionless estimate of activity can be calculated by counting the number of active stacks through smoke and steam detection, provided by color threshold or segmentation algorithms (Yogamangalam et al., 2013). Figure 3.33 provides an example of a 1320 MW hard coal power plant located near Sugözü, Türkiye (36.834°N, 35.880°E) observed by Sentinel-2 on June 9th 2022, and the detection of steam above the stack of the plant provided by a grey level threshold algorithm. Corresponding TROPOMI NO_x emissions are calculated for this day.

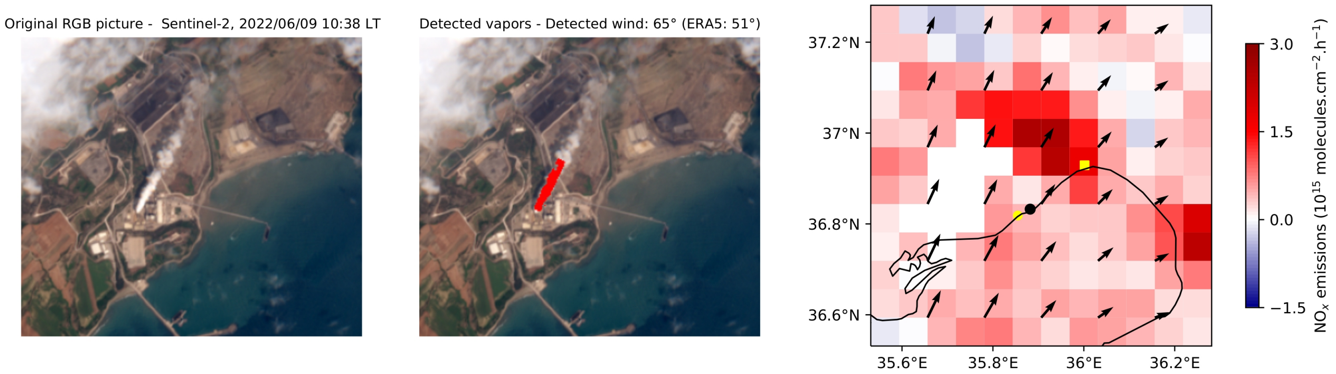

Figure 3.33: Sentinel-2 RGB images of the İsken Sugözü power plant (1st column) on July 9th 2022, and activity index estimation through steam detection (2nd column), with the downwind steam being identified in red. The corresponding NO_x emissions calculated with the flux-divergence method is added (3rd column). The location of a smaller power plant and a cement kiln are noted with a yellow circle and a yellow square respectively.

This method is only valid to infer emissions from a single isolated source, and cannot be used as a mapping method. Because it requires a prior knowledge of the asset whose emissions are estimated (vicinity with other emitters, number of stacks, fuel type, etc.), it cannot be used as a detection method either. Moreover, the daily monitoring is made impossible since both Sentinel-2 satellites have a revisit time of 5 days. The reduced scope of this method comes with additional limitations that arise when using Sentinel-2 images to estimate the activity of an industrial facility. Indeed, the detection of steam can be particularly difficult in hot weather, since a warmer air can hold more water vapor before reaching a point of saturation where condensation occurs. Conversely, the grey/black color of smoke can be confused with many elements of any industrial site, or even the surrounding terrain. Finally, Sentinel-2 images are limited by frequent or persistent cloud conditions that obstruct the view of the satellite. This limitation is common in remote sensing methods and is shared by many instruments (Chevallier et al., 2020). Refined segmentation algorithms, such as machine-learning-based methods, trained with segmented images (Wang et al., 2021b; Rahman et al., 2021) with different spectral bands, could provide an increasing efficiency of such methods in order to optimise the activity index upon which the averaging of NO_x emissions is calculated. Other limitations are linked to the timestamp differences of the satellites: because the overpass time of Sentinel-2 and Sentinel-5P are different, the activity detected on Sentinel-2 images might not reflect the activity when NO_2 columns are calculated by TROPOMI. This is particularly true for industrial facilities whose production is variable throughout the day, but also for power plants that are used to respond to electricity consumption peaks during the middle of the day at the TROPOMI overpass. For instance, it is impossible to affirm that the NO_x emissions calculated on Figure 3.33 during the overpass of Sentinel-5P correspond to the activity of the power plant identified by Sentinel-2 images, or if it corresponds totally or partially to the emissions of the cement plant located about 15 km to the north-east.

Chapter 4

Conclusion and perspectives

4.1 Conclusion

The purpose of this thesis was to take advantage of the climatic characteristics of the EMME region, as well as its high density of greenhouse gas and atmospheric pollutant emitters, to develop and apply an inverse modelling system for the systematic detection and analysis of atmospheric plumes originating from point sources and intense areas in TROPOMI images, enabling a trend analysis of the activity sectors and socio-economic drivers in the region. This work was motivated by the absence or the outdated nature of the emissions inventories in this part of the world, which can be explained by several different factors. Therefore, this work aimed to serve as a bridge between the different countries in the EMME region in their air quality monitoring strategy. Furthermore, because the emissions of certain atmospheric pollutants in a given sector are, to some extent, proportional to their CO_2 emissions, this work aimed to initiate the detection, mapping, and quantification of CO_2 emissions, ultimately leading to a reduction in greenhouse gas emissions as part of the EMME Climate Change Initiative.

The main challenge in developing such an emission detection system was the lack of prior knowledge about the location of emitters. Through data collection efforts, a list of emitters in the region could be obtained, but it remains incomplete and does not provide precise information on the temporal variation of emissions for each of its sources. The absence of NO_x emissions inventories forced us to turn to global inventories, CAMS-GLOB-ANT and EDGAR, and, for Cyprus, the regional European inventory CAMS-REG-ANT. Although these inventories provide valuable information about the order of magnitude of emissions and their general distribution, they suffer from three major drawbacks. The first drawback is the absence of consideration or inaccurate representation of some powerful emitters. In these inventories, emitters can be missing, or present with an incorrect location. Some industrial facilities are also recorded in inventories, but are no longer active. Finally, most emitters exist but their emissions are not precise, as they are partially represented through a uniformisation of reported emissions, i.e., a method that does not systematically distinguish between technologies used, and based on emissions that can be imprecise or outdated. The second drawback is the temporal resolution, with emissions only available monthly, which does not represent intra-daily and inter-weekly variations. This does not allow capturing the finest emission variations. The third drawback is the resolution, which prevents the characterization of the closest sources (two emitters side by side cannot be distinguished). Therefore, an alternative method that relies as little as possible on external data had to be found. By comparing several methods, we determined that the flux-divergence method was the best suited for the proposed objective. This method is based on the conservation of mass in steady-state conditions, expressing the emissions of any trace gas as the sum of a transport term and a sink term. In the case of quantifying NO_x emissions, several parameters are used, but four are fundamental:

- The column of NO_2 taken from TROPOMI products, resulting from Differential Optical Absorption Spectroscopy measurements of atmospheric slant columns, transformed into vertical tropospheric columns by an internal chemistry transport model, which allows capturing the fine-scale structure of the NO_2 distribution in the atmosphere through daily high-resolution observations of plumes.

- The average wind, which allows the analysis of the spread of plumes in space and the calculation of pollution transport from emitters.

- The concentration of OH, which is responsible for most of the chemical loss of NO_2 through a non-linear mechanism, allowing quantification of the lifetime of NO_2 in the atmosphere.

- The ratio between NO_x and NO_2 (i.e., the distribution between NO and NO_2), which depends on photochemical conditions, and allows the upscaling of calculated NO_2 flow rates to NO_x emissions.

The use of this method has proven to provide more accurate results than other direct inversion methods. It also enables the detection and estimation of emissions from smaller emitters, such as small gas power plants or medium-sized cities. Additionally, it has the advantage of allowing emissions mapping. However, although this method is less dependent on external datasets than others, it still relies on several modeled parameters. The first dependency is the chemistry transport model used by TROPOMI to calculate vertical tropospheric columns from measurements of slant atmospheric columns. This dependency is not negligible because the use of the air mass factor, which is derived from such models, is critical to infer the tropospheric NO_2 vertical column density. The second dependency is the concentration of OH, which is mainly determined by photochemical parameters but also by NO_x itself through a non-linear mechanism. Therefore, the lack of prior knowledge about the location of some emitters results in an mis-estimation of the OH field due to an underestimation of NO_x in the concerned area.

The flux-divergence method allows, for the most powerful isolated sources, and under regular wind conditions, an enhanced tracking of NO_x emissions. For these specific cases, the obtained emissions can be compared to other data sources (RGB images, activity data) and provide a precise monitoring of emissions. However, in most cases, such a monitoring is not possible, generally because the source is not isolated enough, because its emissions are not high enough in comparison to the observed background, or because the parameters involved in the calculation of emissions have too large errors. In most cases, these problems can be mitigated by averaging emissions. Monthly or annual emissions maps thus allow for a more comprehensive visualisation of the NO_x sources.

Three studies were conducted on different countries in the EMME region. The interest in studying Egypt lays in the diversity of NO_x-emitting sectors in the country and the unique distribution of emissions along the Nile and its delta with very intense emissions. Qatar is a simpler case, as all its emissions are located in the capital and two industrial areas in the north and west of the country, illustrating the extreme behaviours of emitters (diffuse source and point source respectively). Finally, Cyprus, with lower mean emissions in a more complex topography and a non-desert climate, represented a final case to evaluate the limits in the generalisation of the method. The de facto division of the island into two distinct political entities, each with different economic development trajectories, allowed for a illustration of the method going beyond the scientific interest. These three studies were partially complemented by applications of the method for the city of Riyadh. From these different examples, we can extract the following ten essential guidelines concerning the identification and measurement of NO_x emissions in the EMME region using the flux-divergence method with TROPOMI retrievals:

- NO_x emissions are well represented in most countries of the EMME region. The high resolution used in the method allows a clear identification of the positions of megacities, industrial areas, isolated emitters, maritime and terrestrial routes, which is not necessarily the case for NO_2 column density maps due to pollution transport that spread NO_2 concentrations much further than the source locations.

- The use of daily TROPOMI images enables the determination of trends at larger temporal scales: for each country of the region, weekly and annual trends, reflecting their social norms and industrial activities, can be derived.

- Under certain conditions, it is possible to characterise the emissions of a sector. The use of additional data, such as electricity generation, cement production or traffic intensity, enables to calculate emission factors for the power, traffic and shipping or cement sectors respectively.

- Due to their associated low signal-to-noise ratio in column densities, emissions of smaller cities are difficult to estimate (the term "small" is made vague on purpose, as it can refer to high urban sprawl, low emissions per capita or small total population).

- The transport term is more important for identifying emitters concentrated in small areas (point sources). Adding the sink term can cause a smearing effect, making it harder to identify smaller sources. Such an identification is all the more difficult as there is no reliable measure for NO_2 lifetime at the regional scale. If the method is used to quantify emissions however, much care must be put into the estimation of the sink term. As a consequence, the transport term dominates the NO_x budget for point sources, with the larger source of errors being the mean wind angle, while the sink term becomes more important for emitter extending in large areas (diffuse sources). In this case, the larger source of errors is the OH concentration field.

- Uncertainties arise regardless of the nature of the emitter. The uncertainty of tropospheric NO_2 columns under polluted conditions is dominated by the sensitivity of satellite observations to air masses near the ground, expressed by the air mass factor which is calculated with high uncertainties. Additionally, the conversion of NO_2 flow rates to NO_x emissions is often made under hypotheses that are not always verified near the largest point sources.

- The accuracy of the method is limited in areas with complex topography, where 3D transport cannot be simplified, as well as regions in which additional reactions leading to NO_x loss cannot be neglected.

- Estimated emissions exhibit differences with global emissions inventories, whether they concern the sectoral share of emissions or their annual variability, although the order of magnitude is the same. Moreover, the use of the flux-divergence method applied with TROPOMI observations enables to detect emitters that are not present in global inventories.

- An indication on the quality of NO_2 observations is required to prevent the estimation of emissions that are not consistent to the ground activity. In this regard, considerable improvements in the TROPOMI product (improvement of the resolution since August 2019, new product version 2.4.0 since July 2022, reprocessed PAL version for data between January 2019 and October 2021) enabled a better detection of emitters in the EMME region.

We hope that these insights will allow the method to be used more widely to better characterise the EMME region, especially for countries that have not been discussed as an example. We expect that through a more complex method, a reduction in modelling uncertainties will be possible, allowing its generalisation to other regions of the world.

4.2 Perspectives

This thesis work is part of an ongoing effort to better quantify greenhouse gas emissions and co-emitted species as part of the fight to improve air quality and tackle climate change. The three studies made it possible to implement and use the flux-divergence method to shed new light on the composition and distribution of NO_x emissions in the EMME region. Our method, which is based on several developments that have been carried out by anterior research, has been improved on the basis of the expertise of the supervisory team in terms on remote sensing methods, sectoral structure of NO_x emissions and climate features of the EMME region. In a similar way, this work might serve as a basis for new developments that will make it possible to further reduce the model uncertainties in the estimation of NO_x emissions, and extend the method to other regions of the world to improve air quality inventories, and possibly greenhouse gas inventories through a better understanding of the relation between NO_x and CO_2 in emission processes.

However, even if these future developments live up to their promises, satellite observations will probably not replace bottom-up inventories in the near future. Remote sensing methods suffer from the structural constraints that most satellites only measure atmospheric composition a few times per day or less. The one-day revisit time of Sentinel-5P already constituted a significant factor to improve remote sensing methods, since previous satellites had longer revisit times. To estimate daily emissions, remote sensing methods rely on models or assumptions to account for periods unobserved by satellites, leading to high uncertainties in the retrieved emissions. To counter this drawback, the use of geostationary satellites that constantly observe a portion of the Earth, such as Sentinel-4 for Europe and the Mediterranean, TEMPO for North America and GEMS for East Asia, will be a significant improvement, but assumptions would still be necessary to estimate nighttime trends. In addition to this structural constraint, the extended presence of clouds in many regions of the world often makes reliable emission estimations from instantaneous satellite observations impossible.

As a consequence, it is likely that direct inversions, on the basis on improved models, would be mostly relevant to estimate emissions that would serve as temporary substitutes for non-existent or outdated bottom-up inventories, especially in regions where model uncertainties are low or activity data is unknown. This is the case for most of the EMME region, but other regions can share the same features, such as Central Asia, North Africa and Southern Africa. Ultimately, these estimations of NO_x and CO_2 emissions can serve as a first step to establish national inventories for air quality and greenhouse gas emissions with low latency. As such, they would help local and national governments, but also industrial firms in polluting sectors, as part of their strategies and obligations to tackle local air pollution issues and mitigate climate change.

List of Figures

1.1 Historical total emissions in the EMME region by greenhouse gas (solid lines, left ordinate) and share of total world emissions (dashed lines, right ordinate). Data sources: country reported emissions from the PRIMAP-hist dataset version 2.3.1 (Gütschow et al., 2016). Figure extracted from Zittis et al. (2022) SI. 13
1.2 Year of last submission of GHG inventories in EMME countries (green). The last year for which emissions are estimated is also shown (yellow). This graph has been produced on July 21st 2023 based on available data at that time on the UNFCCC website. 16
1.3 Examples of NO_x pollution in four megacities of the EMME region, with clockwise from the top-left corner: Athens (extracted from Athanasios et al. (2015)), Istanbul (photographer: Dmitry Papkovich), Tehran (unknown source) and Dubai (unknown source). NO_2 is responsible for the reddish-brown color of the lower layers of the atmosphere. 19
1.4 Location of the main industrial facilities that produce nitrogen oxides (flaring sites, fossil fuel-fired power plants, aluminium smelters, steel mills and cement kilns) in the EMME region, along with the urban areas having more than 100,000 inhabitants. EMME countries are displayed in light orange. 21
1.5 Mean NO_x emissions in the EMME region for year 2018 estimated by bottom-up inventories EDGARv6.1 (left) and CAMS-GLOB-ANT_v5.3 (right). 22
1.6 Comparison of mean anthropogenic NO_x emissions from the EDGARv6.1 and CAMS-GLOB-ANT_v5.3 inventories in 2018. Each point represents a pixel of the gridded inventories in the EMME region. The colors indicates the sector with the highest emissions proportion among power generation, transportation, industry, and other sources (blue, grey, dark red and green respectively). When no sector accounts for more than 40% of the NO_x budget, the point is represented in yellow. The 1:1 ratio is represented with a dashed line (note the logarithmic scale). The corresponding domain lies between parallels 10°N and 42°N and meridians 21°E and 63°E. 22
1.7 Sketch of the NO_x chemistry in the troposphere during daytime (left) and nighttime (right). 29
1.8 Sketch of satellite reflectance measurement in a plane parallel atmosphere. The DOAS algorithm consists in measuring the light absorption along the optical path relevant to the slant column density (blue line) in order to derive the integrated content of absorbers in the corresponding vertical column from the ground ($z = 0$) to the top of the troposphere and the total atmosphere (purple line). 33
1.9 NO_2 tropospheric vertical column density on a Sentinel-5P orbit covering part of the EMME region on July 14th 2022 (L2 product, OFFL stream, processor version 2.3.1). White pixels correspond to areas with low-quality data or no data (with a quality assurance limit at 0.70, see Section 1.3.7). 35
1.10 Composite asynchronous map representing gridded mean TROPOMI nitrogen dioxide tropospheric vertical column density above the EMME region for July 1st 2022 to July 14th 2022 (L2 product, OFFL stream, processor version 2.3.1). White pixels correspond to areas with low-quality data or no data during the period (with a quality assurance limit at 0.75, see Section 1.3.7). 35
1.11 Total air mass factor (left) and tropospheric air mass factor (right) for a Sentinel-5P orbit over part of the EMME region on July 14th 2022 (L2 product, OFFL stream). Note that the colorbar bounds are different. 38
1.12 Example of TROPOMI averaging kernels for five pixels within the EMME region on July 14th 2022: pixels with low surface albedos (Nile Valley croplands and Mediterranean Sea), pixels with high surface albedos (Sahara Desert and Athens urban area) and pixel with an optically thick cloud characterised by $q_a < 0.75$ (over Crete). The pressure is normalised as a fraction of the standard pressure $p_0 = 1013.25$ hPa. Corresponding locations and vertical columns are shown on the left. 39
1.13 Mean seasonal differences in tropospheric vertical column densities between PAL and OFFL versions of TROPOMI data (PAL/OFFL-1) above the EMME region between September 2020 and August 2021. . . 41
1.14 Number of TROPOMI observations of NO_2 tropospheric columns above quality assurance value thresholds $q_{a,\mathrm{lim}} = 0.75$ and $q_{a,\mathrm{lim}} = 0.70$ for the Persian Gulf region in December 2020 (data product version 2.3.1) and December 2022 (OFFL product version 2.4.0). 42

2.1 Mass balance within a tropospheric column. 44

2.2 (left) Different large-scale areas in the EMME region used to calculate the NO_2 background as observed by TROPOMI, calculated each day as the mean value of NO_2 columns under the 25th percentile. (right) Corresponding time series for 2021 to 2022 (3-days moving average). . . . 47

2.3 Theoretical illustration of the plume shape produced by an emitter with respect to its spatial extent along a streamline. With unchanged emissions, the emitter emits over a restricted area (left, characterisation of industrial facilities), an area of intermediate extent (centre), and a large area (right, characterisation of megacities). Emissions are modelled by a Gaussian whose standard deviation represents the spatial spread of emissions. Wind module is unchanged in all three cases. . . . 50

2.4 Theoretical illustration of the relative importance of the terms transport and sinks in calculating the total emissions of an emitter in relation to its spatial extent along a streamline. With unchanged emissions, the emitter emits over a restricted area (left, characterisation of industrial facilities), an area of intermediate extent (centre), and a large area (right, characterisation of megacities). Lifetime and wind module are unchanged in all three cases. . . . 50

2.5 TROPOMI NO_2 tropospheric vertical columns for two cement plants in the Sinai region on September 10th 2019 (1st panel), as well as the transport term (2nd panel), sink term (3rd panel) and corresponding NO_x emissions (4th panel) using the flux-divergence method. The location of the cement plants are denoted with squares. The ERA5 wind field is added on the left panel and downscaled to a $0.0625° \times 0.0625°$ resolution. . . . 51

2.6 TROPOMI NO_2 tropospheric vertical columns for the city of Damascus, Syria, on June 16th 2021 (1st panel), as well as the transport term (2nd panel), sink term (3rd panel) and corresponding NO_x emissions (4th panel) using the flux-divergence method. The location of the city centre is denoted with a star and its urban extent is displayed. The ERA5 wind field is added on the left panel and downscaled to a $0.0625° \times 0.0625°$ resolution. . . . 51

2.7 Mean transport term (left), sink term (centre) and corresponding NO_x emissions (right) calculated with the flux-divergence method for the city of Riyadh, Saudi Arabia in 2021. The location of the city centre is denoted with a star and its urban extent is displayed. The location of power plants and cement plants are displayed with rounds and squares respectively. . . . 52

2.8 Steady state OH concentration (left axis) and corresponding NO_2 lifetime (right axis) versus boundary layer NO_2 column, assuming a 1-km well-mixed boundary layer. The color scheme corresponds to regions of high NO_2 (red), where OH is low, intermediate NO_2 (green), where OH is high, and low NO_2 (blue), where OH is low. Figure extracted from Valin et al. (2011). . . . 54

2.9 NO_2 column predicted in a 1-D plume model (east-west) at 2 km (solid), 128 km (dashed), and 512 km model resolutions (dash-dot) for (a) a large, (b) intermediate, and (c) small source of NO_2 and (d–f) the corresponding OH feedback. The color-scheme corresponds to NO_2-OH feedback regimes depicted in Figure 2.8. Horizontal (north-south) and vertical layers are fixed at 1 km thickness for all resolutions. Figure extracted from Valin et al. (2011). . . . 55

2.10 (left) TROPOMI NO_2 tropospheric vertical column over Riyadh and corresponding ERA5 horizontal wind. White pixels corresponds to retrievals with low-quality data ($q_a < 0.75$) or no data. (middle) Plume rotation with its wind direction around the centre of the source to an upwind-downwind pattern. The grey boxes indicate the sector of ± 20 km around the source relevant for the emission and lifetime estimates. (right) NO_2 line density as a function of distance to the source calculated for the ± 20 km sector (blue dots) and fit results (red line) with estimated NO_x emissions and lifetime. The city centre is denoted with a green star. . . . 56

3.1 (left) Part of Egypt centered on Nile River. Within this domain, pink cells represent locations with an average human density above 100 hab.km^{-2}, brown cells represent locations with industrial facilities outside cities, and yellow cells represent locations in their vicinity. These cells constitute the mask used to calculate anthropogenic emissions. Outside this mask, green cells represent areas which do not correspond to any of the three criteria, considered to be void of human activity. Five larges cities in the country and the industrial area of Ain Sokhna are denoted with stars. Two smaller domains centered around the cities of Asyut and Aswan are represented with dotted lines; their use is presented in Section 3.1.6-F. (right) TROPOMI observation of NO_2 slant column densities above Nile valley on 3 January 2019. White pixels correspond to areas with low quality data ($q_a < 0.75$) or no data. . . . 66

3.2 Map of Riyadh's city centre with the surrounding power plants (PP4, 7, 8, 9, 10 and 14) and cement plant (CP). The map has been extracted from © Google Maps. . . . 70

3.3 Estimation of the NO_2 lifetime from a pattern above Riyadh on 11 March 2020: (left) NO_2 plume rotated with its wind direction around the source (star) to an upwind-downwind pattern. Grey boxes centered around black points indicate the extent of the spatial integration of NO_2 columns to obtain the NO_2 line density. Values of cardinal points are noted in black. (right) Corresponding line densities (points) representing the downwind evolution of NO_2 as function of the distance to the city centre, and the corresponding fit according to the EMG function (dashed line). . . . 71

3.4 Selection method for NO_2 patterns over Riyadh. Datasets (yellow-orange) are used to calculate the quantities (light green) that are submitted to different tests (grey). 731 patterns are progressively conserved (green arrows) or rejected (red arrows). At each stage, the number of conserved or rejected patterns are noted within brackets (the value is only given for calculations performed at level $\mathcal{B}$). This selection process compares the lifetimes estimated by the EMG function fitting with TROPOMI line density profiles to the lifetimes calculated according to Equation (3.11) with CAMS data. 72

3.5 (left) Comparison between CAMS-derived NO_2 lifetimes and lifetimes from NO_2 line density fittings with EMG function above Riyadh city centre, for level $\mathcal{A}$ (a) and $\mathcal{B}$ (c). The samples presented correspond to patterns in clear-sky conditions for which the mean wind is in the north-south direction with a low variance, and for which the correlation between line density profile and fit gives a correlation coefficient of more than 0.97 and a lifetime of more than 1.0 h. NO_2 patterns do not have these conditions during the summers of 2019 and 2020. Dashed lines separate the groups of observations by season. (right) Comparison between the two calculated lifetimes for level $\mathcal{A}$ (b) and $\mathcal{B}$ (d). A linear regression with an intercept forced to be zero is displayed with a green dashed line. 74

3.6 NO_x emissions above most of the Egyptian territory: (top) transport term (A), sink term (B), resulting emissions (C), and the corresponding anthropogenic emissions after non-anthropogenic background removal (D) for January 2019 (top) and corresponding values (E, F, G, H) for July 2019. 75

3.7 Share of the absolute value of the transport term in the sum of the sink term and the absolute value of the transport term above most of Egypt's territory, indicating the local importance of the transport term in NO_x emissions above mask cells. The average of this ratio is shown for January 2019 (A) and July 2019 (B). 77

3.8 Weekly profiles of anthropogenic NO_x emissions for Egypt using TROPOMI observations in 2018-2019 (purple line) and 2019-2020 (green line). Thin grey lines represent individual weeks. Days for which less than 80% of the domain counts low quality observations ($q_a < 0.75$) are not represented. 79

3.9 (top) Comparison of TROPOMI-derived anthropogenic NO_x emissions in Egypt (light blue), with the corresponding emissions from EDGAR (green with stripes) and CAMS (yellow) inventories. EDGAR data is shown for comparison purposes and covers the years 2013-2015. (bottom) TROPOMI-derived anthropogenic NO_x emissions for the cities of Asyut (dark red) and Aswan (light blue). The corresponding domains are displayed on Figure 3.1. 80

3.10 Location of the main industrial facilities (cement kilns, power plants and aluminium smelters) in Qatar. Urban areas are displayed in gray and Doha's city centre is denoted with a star. Industrial facilities and cities in other countries are not displayed. Map tiles by Stamen Design under CC BY 3.0. Data © OpenStreetMap contributors. 88

3.11 TROPOMI observation of NO_2 column densities above Qatar on December 12th 2019. White pixels correspond to areas with low-quality data ($q_a < 0.75$) or no data. 89

3.12 Masks used for NO_x emissions estimates: Green cells are used to estimate the NO_2 tropospheric background that is removed from vertical column densities before calculation of emissions (external mask). Blue cells are used to count NO_x emissions attributable to Qatar (internal mask). Orange cells, which cover urban and industrial areas from other countries, are not considered. 91

3.13 Number of days involved in the mean monthly estimates of NO_x emissions (blue) and days that have been discarded due to strong winds blowing from Bahrain to the south-east (brown), large areas within the internal mask with low-quality data (yellow), or both (red). 93

3.14 Mean NO_x emissions above Qatar (13:30 LT): transport term (a), sink term (b), and resulting emissions (c) for October 2022. Power plants are denoted with dots, cement plants with squares, and Doha's city centre with a star. 94

3.15 Mean NO_x emissions above Qatar (13:30 LT): transport term (a), sink term (b), and resulting emissions (c) for the 2019-2022 period. Power plants are denoted with dots, cement plants with squares, and Doha's city centre with a star. 94

3.16 TROPOMI observation density for 2020. 96

3.17 Mean weekly profiles of anthropogenic NO_x emissions at 13:30 LT in Qatar using TROPOMI observations for 2019 to 2022. The average emissions for the four-year period is displayed with the black line. 97

3.18 Monthly mean power demand in Qatar for four different months in 2016-2017. 98

3.19 Total TROPOMI-derived anthropogenic NO_x emissions in Qatar from 2019 to 2022 using the flux-divergence method. The colors are used to illustrate seasonal variations. 98

3.20 Electricity generation in Qatar from 2019 to 2021 according to the Planning and Statistics Authority reports. Generation from to the three Ras Laffan power plants, in the north-eastern part of the country, are displayed in yellow, orange and brown, while generation from other power plants are displayed in light blue. 99

3.21 Comparison between monthly TROPOMI-derived NO_x emissions for the entire Qatar territory and corresponding electricity generation according to Planning and Statistics Authority reports. A linear regression between the two datasets is displayed with a green dashed line. (a) All months in the period 2019-2022 are included. (b) Months that are included are those for which inferred total emissions have been obtained with an averaging of 18 daily emissions or more. The color scale represents the number of days involved in the calculation of points. . . . 100

3.22 Zonal cross sections of 13:30 NO_x emissions at the latitude of Ras Laffan power plants. The average profile for 2019-2022 is displayed in red, and the corresponding Gaussian fit in black. Individual monthly profiles are displayed in light grey. The positions of the three power plants are marked with vertical blue lines. . . . 101

3.23 Human density settlement map showing the main urban areas and the location of the power plants in Cyprus. . . . 110

3.24 Origin of the different parameters used in sets EC, WW and EW in the flux-divergence scheme to calculate NO_x emissions in Cyprus, displayed with their original resolution for June 25th, 2022. Power plants are denoted with dots while Nicosia and Limassol are denoted with stars. . . . 115

3.25 Difference between and the mean tropospheric vertical column densities above the main emitters in Cyprus (Nicosia, power plants in the north and the south of the country), and mean tropospheric vertical column densities above sea and mountain regions for 2021 and 2022 (seven-day moving averages). The difference between the calculated background (10th percentile of the domain) and the mean columns above sea and mountain regions is also shown with a dashed line. . . . 116

3.26 Mean PBL-averaged OH concentration above Cyprus for WRF-Chem simulations between May and October 2021. Power plants are denoted with dots while Nicosia and Limassol are denoted with stars. . . . 117

3.27 Frequency with which horizontal wind direction from ERA5 and WRF-Chem simulations agree (angle difference lower than 30°) between May and October 2022. Power plants are denoted with dots while Nicosia and Limassol are denoted with stars. . . . 118

3.28 TROPOMI-derived mean daytime NO_x emissions for Cyprus (13:30 LT): transport term (left), sink term (middle), and resulting emissions (right) for May to October 2021, estimated with sets EC (a-c), WW (d-f) and EW (g-i). Power plants are denoted with dots, while Nicosia and Limassol urban centres are denoted with stars. . . . 119

3.29 TROPOMI-derived mean daytime NO_x emissions for power plants in Cyprus, estimated the datasets EW (black dotted), WW (light blue dotted) and EC (red dotted) between May 2021 and October 2022, compared to corresponding emissions in EDGARv6.1 for 2018 (green), CAMS-GLOB-ANTv5.3 for 2021/2022, CAMS-REG v4.2 for 2017/2018 and reported emissions for 2018/2019: Vasilikos and Moni (top left), Dhekelia (top right), Teknecik (bottom left) and Kalecik (bottom right). For each time series, Y_1 and Y_2 stand for the first and second year of the serie. Note that the range of the abscissa is different from one power plant to the other. . . . 122

3.30 NO_x emissions of the Sinai cement plants on September 10th 2019 with an additional angle offset to the ERA5 wind field of 0°, 30°, 90° and 180° offset (from top to bottom). The sink term remains unchanged. The transport term (left), sink term (middle) and total emissions (right) are displayed, with the corresponding wind field on the transport and emissions maps. The location of the cement plants are denoted with squares. . . . 127

3.31 Horizontal gradient of the ground level on a $0.0625° \times 0.0625°$ grid for the northern half of the EMME region. The areas with an altitude below sea level are represented in light blue. . . . 129

3.32 (left) Map of mean NO_x TROPOMI-inferred daytime emissions from 2019 to 2022 and paths of routes. (right) NO_x emissions for traffic along the terrestrial route from Jeddah to Riyadh (top) and for shipping along the maritime route from the Suez Canal to the Gulf of Aden (bottom). Monthly averages are shown in gray, while the 2019-2022 average is shown in purple. In the case of the maritime route, the entrance and exit of the Gulf of Suez, as well as the location of the Bab-el-Mandeb strait, are indicated with dashed lines. . . . 132

3.33 Sentinel-2 RGB images of the İsken Sugözü power plant (1st column) on July 9th 2022, and activity index estimation through steam detection (2nd column), with the downwind steam being identified in red. The corresponding NO_x emissions calculated with the flux-divergence method is added (3rd column). The location of a smaller power plant and a cement kiln are noted with a yellow circle and a yellow square respectively. . . . 134

A.1 Seasonal maps of tropospheric vertical NO_2 column densities from TROPOMI above the EMME region on a $0.0625° \times 0.0625°$ grid. The logarithmic scale and the choice of colors (blue: low pollution; green: intermediate pollution; red: high pollution) refer to Figures 2.8 and 2.9 from Valin et al. (2011) to illustrate the three different regimes in the NO_x-OH non-linear relationship. . . . 171

A.2 Seasonal maps of PBL-averaged OH concentrations from CAMS NRT data estimated at 12:00 UTC above the EMME region with a $0.4° \times 0.4°$ horizontal resolution. . . . 172

A.3 Estimation of the NO_x emissions of the two fuel-fired power plants in the east of Riyadh using averaged meridional cross-section profiles from 2019 to 2022. The latitude of the two power plants is given with dotted lines and the Gaussian fit is provided with a solid black line. 173
A.4 Mean NO_x emissions above Qatar (13:30 LT): transport term (a), sink term (b), and resulting emissions (c) for years 2019 to 2022 (top to bottom). Power plants are denoted with dots, cement plants with squares, and Doha with a star. 174
A.5 Comparison between TROPOMI observation densities for different periods between 2019 and 2022 with a quality threshold of $q_{a,\mathrm{lim}} = 0.75$ (left) and $q_{a,\mathrm{lim}} = 0.70$ (right). The corresponding TROPOMI version is indicated for each period. 176
A.6 Annual mean emissions at 13:30 for years 2019 to 2022 (left to right) with quality flag threshold equal to $q_{a,\mathrm{lim}} = 0.75$. 177
A.7 Annual mean emissions at 13:30 for years 2019 to 2022 (left to right) with quality flag threshold equal to $q_{a,\mathrm{lim}} = 0.70$. 177
A.8 Mean weekly profiles for NO_2 tropospheric vertical columns, OH concentration and NO_x emissions for the entire country (left), the Ras Laffan power plants in the north (middle), and the Greater Doha area (right). The 2019-2022 average is given and represented by the 100% line. 178
A.9 Monthly terrestrial NO_x emissions in Qatar for year 2018 in EDGARv6.1 by sector 179
A.10 Monthly terrestrial NO_x emissions in Qatar for years 2019 to 2022 in CAMS-GLOB-ANT_v5.3 by sector. 179
A.11 Map of annual NO_x emissions in Qatar for years for EDGARv6.1 within the internal mask for the power (left), transport (middle) and industry (right) sectors. 180
A.13 Transport term for the NO_x emissions estimated for two cement plants in the Sinai region on September 10th 2019 with derivatives calculated with a second-order central-finite difference order approximation (left), a fourth-order central-finite difference order approximation (middle), and the corresponding difference (right). The location of the cement plants are denoted with squares. 180
A.12 Dimensionless theoretical illustration of the estimation of emissions from two overlapping sources. The transport and sink terms, as well as total emissions, are calculated along a streamline. With unchanged emissions, both emitters emit over a restricted area (left, characterisation of industrial facilities), an area of intermediate extent (centre), and a large area (right, characterisation of megacities). Lifetime and wind module are unchanged in all three cases. From top to bottom, the distance between emitters increases. All cases are denoted with corresponding distance between emitters $\Delta\xi$, emissions extent $\sigma_{1,2}$ and ratio $\Delta\xi/\sigma_{1,2}$. 181
A.14 NO_x emissions for traffic along the terrestrial route from Jeddah to Riyadh (top) and for shipping along the maritime route from the Suez Canal to the Gulf of Aden (bottom) for the March-April period in 2019, 2020 and 2021. To represent the level of residual emissions, the 10th and 90th percentiles of the emissions within a 80 km radius are represented with a shaded area for each point of the route (these points are represented on Figure 3.32). 182

List of Tables

1.1 Different technical features of different instruments measuring nitrogen dioxide column densities onboard satellites launched in the last 30 years. 37

3.1 Comparison between the transport term and the sink term above different cities in Egypt, as well as the industrial region of Ain Sokhna located 45 km southwest of Suez for January and July 2019. TROPOMI vertical NO_2 columns, NO_x emissions and population densities correspond to average values within 18 km from the city centre. Unit $\mathcal{M}$ stands for a quantity of 10^{15} molecules (NO_2 or NO_x). 76

3.2 Analysis of the effect of a vertical change in the parameters used to estimate the mean sink term in NO_x emissions: temperature, hydroxyl radical concentration, and NO_x:NO_2 concentration ratio. The comparison is conducted between the estimated quantities at level $\mathcal{B}$ and level $\mathcal{A}$ for mask cells (MASK) and background cells (BKGD) for January, April, October and July 2019. Values within brackets represent the variation from the base case for which all quantities are estimated at level $\mathcal{B}$. 78

3.3 NO_x emission factors for electricity production inferred from different sources and methods. The value is calculated from monthly emissions and electricity generation, fluxes at 13:30 and capacities or directly reported by Qatar authorities. 103

3.4 Location, capacity, fuel and age of the five power plants in Cyprus. 109

A.0 Acronyms and abbreviations used multiple times in the thesis. 170

A.1 Ratio between mean daily power demand and power demand at 13:30 LT, averaged for each month between February 2016 and January 2017 and expected to be valid from 2019 to 2022. 178

Bibliography

Abdallah Lamiaa, El-Shennawy Tarek. Evaluation of CO2 emission from Egypt's future power plants // Euro-Mediterranean Journal for Environmental Integration. 2020. 5, 3. 1–8. (page 81).

Abdelsattar Amal, Al Nadhairi Rahma, Hassan Ali N. Space-based monitoring of NO2 levels during COVID-19 lockdown in Cairo, Egypt and Riyadh, Saudi Arabia // The Egyptian Journal of Remote Sensing and Space Science. 2021. 24, 3. 659–664. (page 19).

Abeed Rimal, Clerbaux Cathy, Clarisse Lieven, Van Damme Martin, Coheur Pierre-François, Safieddine Sarah. A space view of agricultural and industrial changes during the Syrian civil war // Elem Sci Anth. 2021. 9, 1. 000041. (page 133).

Abou El-Magd Islam, Zanaty Naglaa. Impacts of short-term lockdown during COVID-19 on air quality in Egypt // The Egyptian Journal of Remote Sensing and Space Science. 2020. (pages 19 and 79).

Adrian RJ, Christensen KT, Liu Z-C. Analysis and interpretation of instantaneous turbulent velocity fields // Experiments in fluids. 2000. 29, 3. 275–290. (page 48).

Al-Attiyah Foundation . Gear change: Vehicle fuel efficiency in the GCC, `https://www.abhafoundation.org/media-uploads/rpapers/Research%20series-17-Date-01-2018-Fuel%20Efficiency%20GCC.pdf`. 2018. (page 87).

Alfaoyzan Faouzan Abdulaziz, Almasri Radwan A. Benchmarking of energy consumption in higher education buildings in Saudi Arabia to be sustainable: Sulaiman Al-Rajhi University case // Energies. 2023. 16, 3. 1204. (page 117).

Alghamdi MA, Khoder M, Harrison Roy M, Hyvärinen A-P, Hussein T, Al-Jeelani H, Abdelmaksoud AS, Goknil MH, Shabbaj II, Almehmadi FM, others . Temporal variations of O3 and NOx in the urban background atmosphere of the coastal city Jeddah, Saudi Arabia // Atmospheric Environment. 2014. 94. 205–214. (page 30 and 30).

Alktranee Mohammed HR, Al-Yasiri Qudama, Sahib Mortda M. Power output enhancement of grid-connected PV system using dual-axis tracking // Renewable Energy and Environmental Sustainability. 2020. 5. 8. (page 117).

Almazroui Mansour. Changes in temperature trends and extremes over Saudi Arabia for the period 1978–2019 // Advances in Meteorology. 2020. 2020. 1–21. (page 14).

Almazroui Mansour, Islam M Nazrul, Dambul Ramzah, Jones PD. Trends of temperature extremes in Saudi Arabia // International Journal of Climatology. 2014. 34, 3. 808–826. (page 14).

Alpert P, Ben-Gai T, Baharad A, Benjamini Y, Yekutieli D, Colacino M, Diodato L, Ramis C, Homar V, Romero R, others . The paradoxical increase of Mediterranean extreme daily rainfall in spite of decrease in total values // Geophysical research letters. 2002. 29, 11. 31–1. (page 14).

Anenberg Susan C, Miller Joshua, Minjares Ray, Du Li, Henze Daven K, Lacey Forrest, Malley Christopher S, Emberson Lisa, Franco Vicente, Klimont Zbigniew, others . Impacts and mitigation of excess diesel-related NOx emissions in 11 major vehicle markets // Nature. 2017. 545, 7655. 467–471. (page 19).

Athanasios Valavanidis, Vlachogianni Thomais, Loridas Spyridon, Fiotakis Constantinos. Atmospheric Pollution in Urban Areas of Greece and Economic Crisis. // Trends in air quality and atmospheric pollution data, research and adverse health effects. 2015. (pages 19 and 139).

Atkinson R., Baulch D. L., Cox R. A., Crowley J. N., Hampson R. F., Hynes R. G., Jenkin M. E., Rossi M. J., Troe J.:. Task Group on Atmospheric Chemical Kinetic Data Evaluation, Data Sheet NOx 24. 2013. (page 25).

Atkinson Roger. Atmospheric chemistry of VOCs and NOx // Atmospheric environment. 2000. 34, 12-14. 2063–2101. (page 27).

Attia Shady, Evrard Arnaud, Gratia Elisabeth. Development of benchmark models for the Egyptian residential buildings sector // Applied Energy. 2012. 94. 270–284. (pages 69 and 81).

Baklanov Alexander, Molina Luisa T, Gauss Michael. Megacities, air quality and climate // Atmospheric Environment. 2016. 126. 235–249. (pages 62 and 108).

Batchelor George Keith. An introduction to fluid dynamics. 1967. (page 45).

Baukal Charles. Everything you need to know about NOx // Metal finishing. 2005. 103, 11. 18–24. (page 20).

Bauwens M, Compernolle S, Stavrakou T, Müller J-F, Van Gent J, Eskes H, Levelt Pieternel Felicitas, A R van der, Veefkind JP, Vlietinck J, others . Impact of coronavirus outbreak on NO2 pollution assessed using TROPOMI and OMI observations // Geophysical Research Letters. 2020. 47, 11. e2020GL087978. (page 79).

Bayram Islam Safak, Saffouri Faraj, Koc Muammer. Generation, analysis, and applications of high resolution electricity load profiles in Qatar // Journal of Cleaner Production. 2018. 183. 527–543. (pages 90, 97, and 178).

Beer . Bestimmung der Absorption des rothen Lichts in farbigen Flüssigkeiten // Annalen der Physik. 1852. 162, 5. 78–88. (page 31).

Beirle S, Borger C, Dörner S, Li A, Hu Z, Liu F, Wang Y, Wagner T. Pinpointing nitrogen oxide emissions from space, Sci. Adv., 5, eaax9800. 2019. (pages 46, 52, 59, 63, 63, 70, 71, 72, 74, 82, 88, 91, 92, 92, 95, 104, 108, 110, 112, and 130).

Beirle Steffen, Boersma K Folkert, Platt Ulrich, Lawrence Mark G, Wagner Thomas. Megacity emissions and lifetimes of nitrogen oxides probed from space // Science. 2011. 333, 6050. 1737–1739. (pages 56, 56, 59, and 69).

Beirle Steffen, Borger Christian, Dörner Steffen, Eskes Henk, Kumar Vinod, Laat Adrianus de, Wagner Thomas. Catalog of NOx emissions from point sources as derived from the divergence of the NO2 flux for TROPOMI // Earth System Science Data. 2021. 13, 6. 2995–3012. (pages 50, 52, 53, and 76).

Beirle Steffen, Borger Christian, Jost Adrian, Wagner Thomas. Improved catalog of NOx point source emissions (version 2) // Earth System Science Data. 2023. 15, 7. 3051–3073. (pages 40, 101, 108, 119, 125, and 173).

Belda Michal, Holtanová Eva, Halenka Tomáš, Kalvová Jaroslava. Climate classification revisited: from Köppen to Trewartha // Climate research. 2014. 59, 1. 1–13. (page 14).

Benkovitz Carmen M, Scholtz M Trevor, Pacyna Jozef, Tarrasón Leonor, Dignon Jane, Voldner Eva C, Spiro Peter A, Logan Jennifer A, Graedel TE. Global gridded inventories of anthropogenic emissions of sulfur and nitrogen // Journal of Geophysical Research: Atmospheres. 1996. 101, D22. 29239–29253. (page 21).

Berchet A, Pison I, Chevallier F, Paris J-D, Bousquet P, Bonne J-L, Arshinov M Yu, Belan BD, Cressot C, Davydov DK, others . Natural and anthropogenic methane fluxes in Eurasia: a mesoscale quantification by generalized atmospheric inversion // Biogeosciences. 2015. 12, 18. 5393–5414. (page 17).

Berezin EV, Konovalov IB, Ciais Philippe, Richter A, Tao S, Janssens-Maenhout Greet, Beekmann M, Schulze E-D. Multiannual changes of CO2 emissions in China: indirect estimates derived from satellite measurements of tropospheric NO2 columns // Atmospheric Chemistry and Physics. 2013. 13, 18. 9415–9438. (page 18).

Berner Robert A. The long-term carbon cycle, fossil fuels and atmospheric composition // Nature. 2003. 426, 6964. 323–326. (page 12).

Berrisford Paul, Dee DPKF, Fielding Keith, Fuentes Manuel, Kallberg P, Kobayashi Shinya, Uppala Sakari. The ERA-interim archive // ERA report series. 2009. 1. 1–16. (page 59).

Boersma KF, Eskes HJ, Brinksma EJ. Error analysis for tropospheric NO2 retrieval from space // Journal of Geophysical Research: Atmospheres. 2004. 109, D4. (pages 33, 39, 67, 82, 88, 105, and 110).

Boersma KF, Vinken GCM, Eskes HJ. Representativeness errors in comparing chemistry transport and chemistry climate models with satellite UV–Vis tropospheric column retrievals // Geoscientific Model Development. 2016. 9, 2. 875–898. (page 37).

Bosilovich Michael G, Lucchesi Rob, Suarez M. MERRA-2: File specification. 2015. (page 59).

Bouguer Pierre. Essai d'optique sur la gradation de la lumière. 1729. (page 31).

Bovensmann Heinrich, Burrows JP, Buchwitz M, Frerick Johannes, Noel Suresh, Rozanov VV, Chance KV, Goede APH. SCIAMACHY: Mission objectives and measurement modes // Journal of the atmospheric sciences. 1999. 56, 2. 127–150. (pages 33, 37, and 86).

Browne EC, Cohen RC. Effects of biogenic nitrate chemistry on the NOx lifetime in remote continental regions // Atmospheric Chemistry and Physics. 2012. 12, 24. 11917–11932. (page 28).

Buchwitz Michael, Schneising Oliver, Reuter Maximilian, Heymann Jens, Krautwurst Sven, Bovensmann Heinrich, Burrows John P, Boesch Hartmut, Parker Robert J, Somkuti Peter, others . Satellite-derived methane hotspot emission estimates using a fast data-driven method // Atmospheric Chemistry and Physics. 2017. 17, 9. 5751–5774. (page 57).

Burkholder JB, Sander SP, Abbatt JPD, Barker JR, Cappa C, Crounse JD, Dibble TS, Huie RE, Kolb CE, Kurylo MJ, others . Chemical kinetics and photochemical data for use in atmospheric studies; evaluation number 19. 2020. (pages 46, 61, 65, 67, 67, 69, 82, 90, 91, 105, 113, and 122).

Burnett Richard T, Stieb Dave, Brook Jeffrey R, Cakmak Sabit, Dales Robert, Raizenne Mark, Vincent Renaud, Dann Tom. Associations between short-term changes in nitrogen dioxide and mortality in Canadian cities // Archives of Environmental Health: An International Journal. 2004. 59, 5. 228–236. (page 86).

Burns Douglas A, Aherne Julian, Gay David A, Lehmann Christopher. Acid rain and its environmental effects: Recent scientific advances // Atmospheric Environment. 2016. 146. 1–4. (page 24).

Burrows John P, Weber Mark, Buchwitz Michael, Rozanov Vladimir, Ladstätter-Weißenmayer Annette, Richter Andreas, DeBeek Rüdiger, Hoogen Ricarda, Bramstedt Klaus, Eichmann Kai-Uwe, others . The global ozone monitoring experiment (GOME): Mission concept and first scientific results // Journal of the Atmospheric Sciences. 1999. 56, 2. 151–175. (page 37).

Butenhoff Christopher L, Khalil M Aslam K, Porter William C, Al-Sahafi Mohammed Saleh, Almazroui Mansour, Al-Khalaf Abdulrahman. Evaluation of ozone, nitrogen dioxide, and carbon monoxide at nine sites in Saudi Arabia during 2007 // Journal of the Air & Waste Management Association. 2015. 65, 7. 871–886. (pages 19, 25, 30, 30, 30, and 97).

Butkovskaya NI, Kukui Alexandre, Pouvesle N, Le Bras Georges. Formation of nitric acid in the gas-phase HO2+NO reaction: Effects of temperature and water vapor // The Journal of Physical Chemistry A. 2005. 109, 29. 6509–6520. (pages 27, 68, and 68).

Butkovskaya Nadezhda, Kukui Alexandre, Le Bras Georges. Pressure and temperature dependence of ethyl nitrate formation in the C2H5O2+ NO reaction // The Journal of Physical Chemistry A. 2010. 114, 2. 956–964. (page 27).

Butkovskaya Nadezhda, Rayez Marie-Thérèse, Rayez Jean-Claude, Kukui Alexandre, Le Bras Georges. Water vapor effect on the HNO3 yield in the HO2+NO reaction: experimental and theoretical evidence // The Journal of Physical Chemistry A. 2009. 113, 42. 11327–11342. (pages 27 and 68).

Caloiero Tommaso, Veltri Simone, Caloiero Paola, Frustaci Francesco. Drought analysis in Europe and in the Mediterranean basin using the standardized precipitation index // Water. 2018. 10, 8. 1043. (page 14).

Eastern Mediterranean and Middle East Climate Change Initiative: Report of the Task Force on the Built Environment. // . 2021. (page 12).

Carmona I, Alpert P. Synoptic classification of moderate resolution imaging spectroradiometer aerosols over Israel // Journal of Geophysical Research: Atmospheres. 2009. 114, D7. (page 14).

Castellanos Patricia, Boersma K Folkert. Reductions in nitrogen oxides over Europe driven by environmental policy and economic recession // Scientific reports. 2012. 2, 1. 265. (page 19).

Celarier EA, Brinksma EJ, Gleason JF, Veefkind JP, Cede A, Herman JR, Ionov Dimitri, Goutail Florence, Pommereau J-P, Lambert J-C, others . Validation of Ozone Monitoring Instrument nitrogen dioxide columns // Journal of Geophysical Research: Atmospheres. 2008. 113, D15. (page 86).

Chakraborty D, Park J, Lin Ming-Chang. Theoretical study of the OH+ NO2 reaction: formation of nitric acid and the hydroperoxyl radical // Chemical physics. 1998. 231, 1. 39–49. (page 27).

Chanda A, Robbins J, Mackay GI, Nadler SD, Schiff HI. Optical remote sensing measurements using a UV DOAS system. 1997. (page 32).

Chevallier Frederic, Broquet Grégoire, Zheng Bo, Ciais Philippe, Eldering Annmarie. Large CO2 emitters as seen from satellite: comparison to a gridded global emission inventory // Geophysical Research Letters. 2022. 49, 5. e2021GL097540. (pages 17 and 59).

Chevallier Frédéric, Zheng Bo, Broquet Grégoire, Ciais Philippe, Liu Zhu, Davis Steven J, Deng Zhu, Wang Yilong, Bréon François-Marie, O'Dell Christopher W. Local anomalies in the column-averaged dry air mole fractions of carbon dioxide across the globe during the first months of the coronavirus recession // Geophysical research letters. 2020. 47, 22. e2020GL090244. (pages 59 and 134).

Clugston Michael, Flemming Rosalind. Advanced chemistry. 2000. (page 24).

Coburn Jacob J. Assessing wind data from reanalyses for the upper midwest // Journal of Applied Meteorology and Climatology. 2019. 58, 3. 429–446. (pages 82 and 122).

Cohan Daniel S, Hu Yongtao, Russell Armistead G. Dependence of ozone sensitivity analysis on grid resolution // Atmospheric Environment. 2006. 40, 1. 126–135. (page 53).

Compernolle Steven, Verhoelst Tijl, Pinardi Gaia, Granville José, Hubert Daan, Keppens Arno, Niemeijer Sander, Rino Bruno, Bais Alkis, Beirle Steffen, others . Validation of Aura-OMI QA4ECV NO2 climate data records with ground-based DOAS networks: the role of measurement and comparison uncertainties // Atmospheric Chemistry and Physics. 2020. 20, 13. 8017–8045. (page 38).

Cox Lyndon. Nitrogen oxides (NOx) why and how they are controlled. 1999. (pages 20, 24, and 30).

Cramer Wolfgang, Guiot Joël, Fader Marianela, Garrabou Joaquim, Gattuso Jean-Pierre, Iglesias Ana, Lange Manfred A, Lionello Piero, Llasat Maria Carmen, Paz Shlomit, others . Climate change and interconnected risks to sustainable development in the Mediterranean // Nature Climate Change. 2018. 8, 11. 972–980. (page 15).

Crippa M, Guizzardi D, Muntean M, Schaaf E, Solazzo E, Monforti-Ferrario F, Olivier JGJ, Vignati E. Fossil CO2 emissions of all world countries // Luxembourg: European Commission. 2020. 1–244. (pages 21 and 66).

Crippa Monica, Janssens-Maenhout Greet, Dentener Frank, Guizzardi Diego, Sindelarova Katerina, Muntean Marilena, Van Dingenen Rita, Granier Claire. Forty years of improvements in European air quality: regional policy-industry interactions with global impacts // Atmospheric Chemistry and Physics. 2016. 16, 6. 3825–3841. (pages 19, 63, and 108).

Cushman-Roisin Benoit, Beckers Jean-Marie. Introduction to geophysical fluid dynamics: physical and numerical aspects. 2011. (page 48).

Cusworth Daniel H, Duren Riley M, Thorpe Andrew K, Tseng Eugene, Thompson David, Guha Abhinav, Newman Sally, Foster Kelsey T, Miller Charles E. Using remote sensing to detect, validate, and quantify methane emissions from California solid waste operations // Environmental Research Letters. 2020. 15, 5. 054012. (page 58).

Cyprus Today . Teknecik power plant "needs to have a filter", `https://cyprustodayonline.com/cyprus-today-august-21-2021-pdfs` // Cyprus Today. 2021. 2021-08-21. (page 121).

Day Douglas A, Dillon Michael B, Wooldridge Paul J, Thornton Joel A, Rosen Rebecca S, Wood Ezra C, Cohen Ronald C. On alkyl nitrates, O3, and the "missing NOy" // Journal of Geophysical Research: Atmospheres. 2003. 108, D16. (pages 27 and 113).

Debevec Cécile, Sauvage Stéphane, Gros Valérie, Sciare Jean, Pikridas Michael, Stavroulas Iasonas, Salameh Thérèse, Leonardis Thierry, Gaudion Vincent, Depelchin Laurence, others . Origin and variability in volatile organic compounds observed at an Eastern Mediterranean background site (Cyprus) // Atmospheric Chemistry and Physics. 2017. 17, 18. 11355–11388. (page 113).

Dee Dick P, Uppala S M, Simmons Adrian J, Berrisford Paul, Poli Paul, Kobayashi Shinya, Andrae U, Balmaseda MA, Balsamo G, Bauer d P, others . The ERA-Interim reanalysis: Configuration and performance of the data assimilation system // Quarterly Journal of the royal meteorological society. 2011. 137, 656. 553–597. (page 37).

Delaria Erin R, Place Bryan K, Liu Amy X, Cohen Ronald C. Laboratory measurements of stomatal NO2 deposition to native California trees and the role of forests in the NOx cycle // Atmospheric Chemistry and Physics. 2020. 20, 22. 14023–14041. (pages 29 and 68).

Demetillo Mary Angelique G., Navarro Aracely, Knowles Katherine K., Fields Kimberly P, Geddes Jeffrey A., Nowlan Caroline R., Janz Scott J, Judd Laura M, Al-Saadi Jassim, Sun Kang, McDonald Brian C., Diskin Glenn S., Pusede Sally E. Observing nitrogen dioxide air pollution inequality using high-spatial-resolution remote sensing measurements in Houston, Texas // Environmental Science & Technology. 2020. 54, 16. 9882–9895. (pages 88 and 110).

Dickerson Russell R, Stedman Donald H, Delany Anthony C. Direct measurements of ozone and nitrogen dioxide photolysis rates in the troposphere // Journal of Geophysical Research: Oceans. 1982. 87, C7. 4933–4946. (page 25).

Dirksen Ruud J, Boersma K Folkert, Eskes Henk J, Ionov Dmitry V, Bucsela Eric J, Levelt Pieternel F, Kelder Hennie M. Evaluation of stratospheric NO2 retrieved from the Ozone Monitoring Instrument: Intercomparison, diurnal cycle, and trending // Journal of Geophysical Research: Atmospheres. 2011. 116, D8. (page 37).

Donat MG, Peterson TC, Brunet M, King AD, Almazroui Mansour, Kolli RK, Boucherf Djamel, Al-Mulla Anwar Yousuf, Nour Abdourahman Youssouf, Aly Ahmed Attia, others . Changes in extreme temperature and precipitation in the Arab region: long-term trends and variability related to ENSO and NAO // International Journal of Climatology. 2014. 34, 3. 581–592. (page 14).

Douros John, Eskes Henk, Geffen Jos van, Boersma K Folkert, Compernolle Steven, Pinardi Gaia, Blechschmidt Anne-Marlene, Peuch Vincent-Henri, Colette Augustin, Veefkind Pepijn. Comparing Sentinel-5P TROPOMI NO 2 column observations with the CAMS regional air quality ensemble // Geoscientific Model Development. 2023. 16, 2. 509–534. (page 125).

Drusch Matthias, Del Bello Umberto, Carlier Sébastien, Colin Olivier, Fernandez Veronica, Gascon Ferran, Hoersch Bianca, Isola Claudia, Laberinti Paolo, Martimort Philippe, others . Sentinel-2: ESA's optical high-resolution mission for GMES operational services // Remote sensing of Environment. 2012. 120. 25–36. (page 133).

Duncan Bryan N, Prados Ana I, Lamsal Lok N, Liu Yang, Streets David G, Gupta Pawan, Hilsenrath Ernest, Kahn Ralph A, Nielsen J Eric, Beyersdorf Andreas J, others . Satellite data of atmospheric pollution for US air quality applications: Examples of applications, summary of data end-user resources, answers to FAQs, and common mistakes to avoid // Atmospheric environment. 2014. 94. 647–662. (page 31).

EIA . Natural gas, `https://www.eia.gov/international/data/world/natural-gas/dry-natural-gas-reserves`. 2021. (page 86).

EIA . Analysis - Energy Sector Highlights, `https://www.eia.gov/international/data/country/QAT`. 2022. (page 87).

EMME-CCI . EMME Climate Change Initiative, `https://emme-cci.org/`. 2022. (page 12).

EPA US. Integrated science assessment for oxides of nitrogen–health criteria // US Environmental Protection Agency, Washington, DC. 2016. (pages 62, 86, and 108).

Ehhalt DH, Drummond JW. The tropospheric cycle of NOx // Chemistry of the Unpolluted and Polluted Troposphere: Proceedings of the NATO Advanced Study Institute held on the Island of Corfu, Greece, September 28–October 10, 1981. 1982. 219–251. (page 28).

Ehhalt Dieter H, Rohrer Franz, Wahner Andrea. Sources and distribution of NOx in the upper troposphere at northern mid-latitudes // Journal of Geophysical Research: Atmospheres. 1992. 97, D4. 3725–3738. (pages 47, 65, 90, and 113).

Einstein A. Über einen die Erzeugung und Verwandlung des Lichtes betreffenden heuristischen Gesichtspunkt (1905) 47-62 // Annalen der Physik. 1905. 6. 132–148. (page 31).

Einstein A. Zur Quantentheorie der Strahlung // Physikalische Zeitschrift. 1917. 18. 121–128. (page 31).

El Kenawy Ahmed M, Lopez-Moreno Juan I, McCabe Matthew F, Robaa SM, Domínguez-Castro Fernando, Peña-Gallardo Marina, Trigo Ricardo M, Hereher Mohamed E, Al-Awadhi Talal, Vicente-Serrano Sergio M. Daily temperature extremes over Egypt: Spatial patterns, temporal trends, and driving forces // Atmospheric Research. 2019. 226. 219–239. (page 19).

El-Magd Abou, Zanaty Naglaa, Ali Elham M, Irie Hitoshi, Abdelkader Ahmed I, others . Investigation of aerosol climatology, optical characteristics and variability over Egypt based on satellite observations and in-situ measurements // Atmosphere. 2020. 11, 7. 714. (page 63).

El-Sheekh Mostafa M, Hassan Ibrahim A. Lockdowns and reduction of economic activities during the COVID-19 pandemic improved air quality in Alexandria, Egypt // Environmental Monitoring and Assessment. 2021. 193, 1. 1–7. (page 79).

Eldering A, Wennberg PO, Crisp D, Schimel DS, Gunson MR, Chatterjee A, Liu J, Schwandner FM, Sun Y, O'dell CW, others . The Orbiting Carbon Observatory-2 early science investigations of regional carbon dioxide fluxes // Science. 2017. 358, 6360. eaam5745. (page 17).

Elharidi Aly Mohamed Aly Hassan, Tuohy Paul Gerard, Teamah M. Facing the growing problem of the electric power consumption in Egyptian residential building using building performance simulation program // Building simulation Cairo 2013 conference. 2013. (page 81).

Elvidge Christopher D, Zhizhin Mikhail, Baugh Kimberly, Hsu Feng-Chi, Ghosh Tilottama. Methods for global survey of natural gas flaring from visible infrared imaging radiometer suite data // Energies. 2016. 9, 1. 14. (pages 20 and 65).

Eskes H, Geffen J van, Boersma F, Eichmann KU, Apituley A, Pedergnana M, Sneep M, Veefkind JP, Loyola D. Sentinel-5 Precursor/TROPOMI Level 2 Product User Manual Nitrogen Dioxide. 2022. (pages 41, 89, 96, and 111).

Eskes HJ, Boersma KF. Averaging kernels for DOAS total-column satellite retrievals // Atmospheric Chemistry and Physics. 2003. 3, 5. 1285–1291. (page 39).

Eskes HJ, Eichmann KU, Lambert JC, Loyola D, Veefkind JP, Dehn A, Zehner C. S5P Mission Performance Centre Nitrogen Dioxide [L2$_{N}O2]Readme.1,00.2019a.(page40)$.

Eskes HJ, Eichmann KU, Lambert JC, Loyola D, Veefkind JP, Dehn A, Zehner C. S5P Mission Performance Centre Nitrogen Dioxide [L2_NO2] Readme // Royal Netherlands Meteorological Institute (KNMI) De Bilt, the Netherlands, version. 2019b. 1, 00. (page 64).

Eskes Henk, Geffen Jos van, Sneep Maarten, Veefkind Pepijn, Niemeijer Sander, Zehner Claus. S5P Nitrogen Dioxide v02. 03.01 intermediate reprocessing on the S5P-PAL system: Readme file. 2021. (pages 41 and 173).

Fabry Ch, Buisson H. Étude de l'extrémité ultra-violette du spectre solaire // J. phys. radium. 1921. 2, 7. 197–226. (page 32).

Fang Hongliang, Baret Frederic, Plummer Stephen, Schaepman-Strub Gabriela. An overview of global leaf area index (LAI): Methods, products, validation, and applications // Reviews of Geophysics. 2019. 57, 3. 739–799. (page 68).

Filioglou Maria, Giannakaki Elina, Backman John, Kesti Jutta, Hirsikko Anne, Engelmann Ronny, O'Connor Ewan, Leskinen Jari TT, Shang Xiaoxia, Korhonen Hannele, others . Optical and geometrical aerosol particle properties over the United Arab Emirates // Atmospheric Chemistry and Physics. 2020. 20, 14. 8909–8922. (page 71).

Finné Martin, Woodbridge Jessie, Labuhn Inga, Roberts C Neil. Holocene hydro-climatic variability in the Mediterranean: A synthetic multi-proxy reconstruction // The Holocene. 2019. 29, 5. 847–863. (page 14).

Fischer EV, Jacob Daniel James, Yantosca Robert M, Sulprizio Melissa Payer, Millet DB, Mao Jiandong, Paulot F, Singh HB, Roiger Anke, Ries L, others . Atmospheric peroxyacetyl nitrate (PAN): a global budget and source attribution // Atmospheric Chemistry and Physics. 2014. 14, 5. 2679–2698. (page 68).

Fisher Jenny A, Jacob Daniel J, Travis Katherine R, Kim Patrick S, Marais Eloise A, Chan Miller Christopher, Yu Karen, Zhu Lei, Yantosca Robert M, Sulprizio Melissa P, others . Organic nitrate chemistry and its implications for nitrogen budgets in an isoprene-and monoterpene-rich atmosphere: constraints from aircraft (SEAC 4 RS) and ground-based (SOAS) observations in the Southeast US // Atmospheric chemistry and physics. 2016. 16, 9. 5969–5991. (page 28 and 28).

Fonseca Ricardo, Francis Diana, Nelli Narendra, Thota Mohan. Climatology of the heat low and the intertropical discontinuity in the Arabian Peninsula // International Journal of Climatology. 2022. 42, 2. 1092–1117. (page 14 and 14).

Founda D, Giannakopoulos C, Pierros F, Kalimeris A, Petrakis M. Observed and projected precipitation variability in Athens over a 2.5 century period // Atmospheric Science Letters. 2013. 14, 2. 72–78. (page 14).

Fowler David, Coyle Mhairi, Skiba Ute, Sutton Mark A, Cape J Neil, Reis Stefan, Sheppard Lucy J, Jenkins Alan, Grizzetti Bruna, Galloway James N, others . The global nitrogen cycle in the twenty-first century // Philosophical Transactions of the Royal Society B: Biological Sciences. 2013. 368, 1621. 20130164. (page 23).

Francis Diana, Temimi Marouane, Fonseca Ricardo, Nelli Narendra R, Abida Rachid, Weston Michael, Whebe Youssef. On the analysis of a summertime convective event in a hyperarid environment // Quarterly Journal of the Royal Meteorological Society. 2021. 147, 734. 501–525. (page 14).

Frankenberg Christian, Thorpe Andrew K, Thompson David R, Hulley Glynn, Kort Eric Adam, Vance Nick, Borchardt Jakob, Krings Thomas, Gerilowski Konstantin, Sweeney Colm, others . Airborne methane remote measurements reveal heavy-tail flux distribution in Four Corners region // Proceedings of the national academy of sciences. 2016. 113, 35. 9734–9739. (page 57).

Freiwan Muwaffaq, Kadioğlu Mikdat. Climate variability in Jordan // International Journal of Climatology: A Journal of the Royal Meteorological Society. 2008. 28, 1. 69–89. (page 14).

Friedrich Nils, Eger Philipp, Shenolikar Justin, Sobanski Nicolas, Schuladen Jan, Dienhart Dirk, Hottmann Bettina, Tadic Ivan, Fischer Horst, Martinez Monica, others . Reactive nitrogen around the Arabian Peninsula and in the Mediterranean Sea during the 2017 AQABA ship campaign // Atmospheric Chemistry and Physics. 2021. 21, 10. 7473–7498. (pages 19, 68, 68, 113, 117, and 118).

Galloway James N, Townsend Alan R, Erisman Jan Willem, Bekunda Mateete, Cai Zucong, Freney John R, Martinelli Luiz A, Seitzinger Sybil P, Sutton Mark A. Transformation of the nitrogen cycle: recent trends, questions, and potential solutions // Science. 2008. 320, 5878. 889–892. (page 23).

Gastli Adel, Charabi Yassine, Alammari Rashid A, Al-Ali Ali M. Correlation between climate data and maximum electricity demand in Qatar. 2013. 565–570. (pages 99 and 117).

Georgiou George K, Christoudias Theodoros, Proestos Yiannis, Kushta Jonilda, Pikridas Michael, Sciare Jean, Savvides Chrysanthos, Lelieveld Jos. Evaluation of WRF-Chem model (v3. 9.1. 1) real-time air quality forecasts over the Eastern Mediterranean // Geoscientific Model Development. 2022. 15, 10. 4129–4146. (page 111).

Georgiou George K, Kushta Jonilda, Christoudias Theodoros, Proestos Yiannis, Lelieveld Jos. Air quality modelling over the Eastern Mediterranean: Seasonal sensitivity to anthropogenic emissions // Atmospheric Environment. 2020. 222. 117119. (page 111).

Georgoulias Aristeidis K, Boersma K Folkert, Van Vliet Jasper, Zhang Xiumei, Zanis Prodromos, Laat Jos de, others . Detection of NO2 pollution plumes from individual ships with the TROPOMI/S5P satellite sensor // Environmental Research Letters. 2020. 15, 12. 124037. (page 131).

Gettelman A, Mills MJ, Kinnison DE, Garcia RR, Smith AK, Marsh DR, Tilmes S, Vitt F, Bardeen CG, McInerny J, others . The whole atmosphere community climate model version 6 (WACCM6) // Journal of Geophysical Research: Atmospheres. 2019. 124, 23. 12380–12403. (page 111).

Gholami Hamid, Mohammadifar Aliakbar, Bui Dieu Tien, Collins Adrian L. Mapping wind erosion hazard with regression-based machine learning algorithms // Scientific Reports. 2020. 10, 1. 20494. (page 14).

Gkatzelis Georgios I, Gilman Jessica B, Brown Steven S, Eskes Henk, Gomes A Rita, Lange Anne C, McDonald Brian C, Peischl Jeff, Petzold Andreas, Thompson Chelsea R, others . The global impacts of COVID-19 lockdowns on urban air pollutiona critical review and recommendations // Elementa: Science of the Anthropocene. 2021. 9, 1. (page 79).

Goldberg Daniel L, Harkey Monica, Foy Benjamin de, Judd Laura, Johnson Jeremiah, Yarwood Greg, Holloway Tracey. Evaluating NOx emissions and their effect on O3 production in Texas using TROPOMI NO2 and HCHO // Atmospheric Chemistry and Physics. 2022. 22, 16. 10875–10900. (page 104).

Goldberg Daniel L, Lu Zifeng, Oda Tomohiro, Lamsal Lok N, Liu Fei, Griffin Debora, McLinden Chris A, Krotkov Nickolay A, Duncan Bryan N, Streets David G. Exploiting OMI NO2 satellite observations to infer fossil-fuel CO2 emissions from US megacities // Science of The Total Environment. 2019a. 695. 133805. (page 18).

Goldberg Daniel L, Lu Zifeng, Streets David G, Foy Benjamin de, Griffin Debora, McLinden Chris A, Lamsal Lok N, Krotkov Nickolay A, Eskes Henk. Enhanced Capabilities of TROPOMI NO2: Estimating NOx from North American Cities and Power Plants // Environmental science & technology. 2019b. 53, 21. 12594–12601. (pages 56, 63, and 108).

Graedel TE, Farrow LA, Weber TA. Kinetic studies of the photochemistry of the urban troposphere // Atmospheric Environment (1967). 1976. 10, 12. 1095–1116. (pages 25, 72, 92, and 114).

Granier Claire, Darras Sabine, Gon Hugo Denier van der, Jana Doubalova, Elguindi Nellie, Bo Galle, Michael Gauss, Marc Guevara, Jalkanen Jukka-Pekka, Kuenen Jeroen, others . The Copernicus atmosphere monitoring service global and regional emissions (April 2019 version). 2019. (pages 21, 66, 90, and 112).

Griffin Debora, McLinden Chris A, Dammers Enrico, Adams Cristen, Stockwell Chelsea, Warneke Carsten, Bourgeois Ilann, Peischl Jeff, Ryerson Thomas B, Zarzana Kyle J, others . Biomass burning nitrogen dioxide emissions derived from space with TROPOMI: methodology and validation // Atmospheric Measurement Techniques Discussions. 2021. 2021. 1–44. (page 56).

Griffin Debora, Zhao Xiaoyi, McLinden Chris A, Boersma Folkert, Bourassa Adam, Dammers Enrico, Degenstein Doug, Eskes Henk, Fehr Lukas, Fioletov Vitali, others . High-resolution mapping of nitrogen dioxide with TROPOMI: First results and validation over the Canadian oil sands // Geophysical Research Letters. 2019. 46, 2. 1049–1060. (pages 104 and 122).

Guenther AB, Jiang Xiaoyan, Heald Colette L, Sakulyanontvittaya T, Duhl Ti any, Emmons LK, Wang X. The Model of Emissions of Gases and Aerosols from Nature version 2.1 (MEGAN2. 1): an extended and updated framework for modeling biogenic emissions // Geoscientific Model Development. 2012. 5, 6. 1471–1492. (page 111).

Guenther Alex, Karl Thomas, Harley Peter, Wiedinmyer Christine, Palmer Paul I, Geron Chris. Estimates of global terrestrial isoprene emissions using MEGAN (Model of Emissions of Gases and Aerosols from Nature) // Atmospheric Chemistry and Physics. 2006. 6, 11. 3181–3210. (page 68).

Gulde ST, Kolm MG, Smith DJ, Maurer R, Courrèges-Lacoste G Bazalgette, Sallusti M, Bagnasco G. Sentinel 4: A geostationary imaging UVN spectrometer for air quality monitoring: Status of design, performance and development // International Conference on Space Optics—ICSO 2014. 10563. 2017. 1158–1166. (page 36).

Gütschow Johannes, Jeffery M Louise, Gieseke Robert, Gebel Ronja, Stevens David, Krapp Mario, Rocha Marcia. The PRIMAP-hist national historical emissions time series // Earth System Science Data. 2016. 8, 2. 571–603. (pages 13, 13, 14, and 139).

Hakkarainen Janne, Ialongo Iolanda, Koene Erik, Szeląg Monika E, Tamminen Johanna, Kuhlmann Gerrit, Brunner Dominik. Analyzing local carbon dioxide and nitrogen oxide emissions from space using the divergence method: an application to the synthetic SMARTCARB dataset // Frontiers in Remote Sensing. 2022. 3. 878731. (page 18).

Hakkarainen Janne, Ialongo Iolanda, Tamminen Johanna. Direct space-based observations of anthropogenic CO2 emission areas from OCO-2 // Geophysical Research Letters. 2016. 43, 21. 11–400. (page 17).

Hakkarainen Janne, Szeląg Monika E, Ialongo Iolanda, Retscher Christian, Oda Tomohiro, Crisp David. Analyzing nitrogen oxides to carbon dioxide emission ratios from space: A case study of Matimba Power Station in South Africa // Atmospheric Environment: X. 2021. 10. 100110. (page 18 and 18).

Hale Thomas, Angrist Noam, Goldszmidt Rafael, Kira Beatriz, Petherick Anna, Phillips Toby, Webster Samuel, Cameron-Blake Emily, Hallas Laura, Majumdar Saptarshi, others . A global panel database of pandemic policies (Oxford COVID-19 Government Response Tracker) // Nature Human Behaviour. 2021. 5, 4. 529–538. (pages 79 and 99).

Hamidi Mehdi, Kavianpour Mohammad Reza, Shao Yaping. Synoptic analysis of dust storms in the Middle East // Asia-Pacific Journal of atmospheric sciences. 2013. 49. 279–286. (page 14).

Hanrahan Patrick L. The plume volume molar ratio method for determining NO2/NOx ratios in modeling—Part II: Evaluation studies // Journal of the Air & Waste Management Association. 1999. 49, 11. 1332–1338. (page 104).

Harker Alan B, Strauss Dennis R. Kinetics of the Heterogeneous Hydrolysis of Dinitrogen Pentoxide Over the Temperature Range 214-263K. 1981. (page 28).

Haynes Peter, Shuckburgh Emily. Effective diffusivity as a diagnostic of atmospheric transport: 2. Troposphere and lower stratosphere // Journal of Geophysical Research: Atmospheres. 2000. 105, D18. 22795–22810. (page 48).

He Mike Z, Kinney Patrick L, Li Tiantian, Chen Chen, Sun Qinghua, Ban Jie, Wang Jiaonan, Liu Siliang, Goldsmith Jeff, Kioumourtzoglou Marianthi-Anna. Short-and intermediate-term exposure to NO2 and mortality: a multi-county analysis in China // Environmental Pollution. 2020. 261. 114165. (page 86).

Hegglin Michaela I, Brunner Dominik, Peter Thomas, Staehelin Johannes, Wirth Volkmar, Hoor Peter, Fischer Horst. Determination of eddy diffusivity in the lowermost stratosphere // Geophysical research letters. 2005. 32, 13. (page 48).

Hersbach Hans, Bell Bill, Berrisford Paul, Hirahara Shoji, Horányi András, Muñoz-Sabater Joaquín, Nicolas Julien, Peubey Carole, Radu Raluca, Schepers Dinand, others . The ERA5 global reanalysis // Quarterly Journal of the Royal Meteorological Society. 2020. 146, 730. 1999–2049. (pages 59, 64, 89, and 111).

Heue K-P, Wagner T, Broccardo SP, Walter D, Piketh SJ, Ross KE, Beirle S, Platt U. Direct observation of two dimensional trace gas distributions with an airborne Imaging DOAS instrument // Atmospheric Chemistry and Physics. 2008. 8, 22. 6707–6717. (page 53).

Hoelzemann Judith J, Schultz Martin G, Brasseur Guy P, Granier Claire, Simon Muriel. Global Wildland Fire Emission Model (GWEM): Evaluating the use of global area burnt satellite data // Journal of Geophysical Research: Atmospheres. 2004. 109, D14. (pages 47, 65, 90, and 113).

Hoerling Martin, Eischeid Jon, Perlwitz Judith, Quan Xiaowei, Zhang Tao, Pegion Philip. On the increased frequency of Mediterranean drought // Journal of climate. 2012. 25, 6. 2146–2161. (page 14).

Hoesly Rachel M, Smith Steven J, Feng Leyang, Klimont Zbigniew, Janssens-Maenhout Greet, Pitkanen Tyler, Seibert Jonathan J, Vu Linh, Andres Robert J, Bolt Ryan M, others . Historical (1750–2014) anthropogenic emissions of reactive gases and aerosols from the Community Emissions Data System (CEDS) // Geoscientific Model Development. 2018. 11, 1. 369–408. (pages 17, 66, 90, and 112).

Höglund-Isaksson L. Global anthropogenic methane emissions 2005–2030: technical mitigation potentials and costs // Atmospheric Chemistry and Physics. 2012. 12, 19. 9079–9096. (page 17).

Hönninger G, Von Friedeburg C, Platt U. Multi axis differential optical absorption spectroscopy (MAX-DOAS) // Atmospheric Chemistry and Physics. 2004. 4, 1. 231–254. (page 32).

Howard Carleton J, Evenson KM. Kinetics of the reaction of HO2 with NO // Geophysical Research Letters. 1977. 4, 10. 437–440. (page 27).

Validation report of the CAMS near-real-time global atmospheric composition service: System evolution and performance statistics. Status up to 1 June 2016; `https://pure.mpg.de/rest/items/item_2441827/component/file_2441834/content`. // . 2016. (pages 64 and 125).

Huijnen Vincent, Pozzer Andrea, Arteta Joaquim, Brasseur Guy, Bouarar Idir, Chabrillat Simon, Christophe Yves, Doumbia Thierno, Flemming Johannes, Guth Jonathan, others . Quantifying uncertainties due to chemistry modelling–evaluation of tropospheric composition simulations in the CAMS model (cycle 43R1) // Geoscientific Model Development. 2019. 12, 4. 1725–1752. (pages 60, 82, 90, 92, 105, 111, and 122).

IEA U. Global energy review 2020 // `https://www.iea.org/countries`. 2020. (page 79).

IPCC . IPCC (Intergovernmental Panel on Climate Change): 2019 Refinement to the 2006 IPCC Guidelines for National Greenhouse Gas Inventories, `https://www.ipcc-nggip.iges.or.jp/public/2019rf/`. 2019. (page 16).

International Monetary Fund . World Economic Outlook database: April 2023, `https://www.imf.org/en/Publications/WEO/weo-database/2023/April/weo-report`. 2023. (page 12).

Irizar J, Melf M, Bartsch P, Koehler J, Weiss S, Greinacher R, Erdmann M, Kirschner V, Albinana A Perez, Martin D. Sentinel-5/UVNS // International Conference on Space Optics—ICSO 2018. 11180. 2019. 41–58. (page 36).

Jacob Daniel J, Turner Alexander J, Maasakkers Joannes D, Sheng Jianxiong, Sun Kang, Liu Xiong, Chance Kelly, Aben Ilse, McKeever Jason, Frankenberg Christian. Satellite observations of atmospheric methane and their value for quantifying methane emissions // Atmospheric Chemistry and Physics. 2016. 16, 22. 14371–14396. (page 57).

Jacobson Mark Z. Fundamentals of atmospheric modeling. 1999. (page 111).

Jaeglé Lyatt, Steinberger Linda, Martin Randall V, Chance Kelly. Global partitioning of NOx sources using satellite observations: Relative roles of fossil fuel combustion, biomass burning and soil emissions // Faraday discussions. 2005. 130. 407–423. (pages 47, 58, 65, and 90).

Jafar Hanan A, Shahrour Isam, Mroueh Hussein. Evaluation of Greenhouse Gas Emissions in Conflict Areas: Application to Palestine // Sustainability. 2023. 15, 13. 10585. (page 16).

Janssens-Maenhout Greet, Crippa Monica, Guizzardi Diego, Muntean Marilena, Schaaf Edwin, Dentener Frank, Bergamaschi Peter, Pagliari Valerio, Olivier Jos GJ, Peters Jeroen AHW, others . EDGAR v4. 3.2 Global Atlas of the three major greenhouse gas emissions for the period 1970–2012 // Earth System Science Data. 2019. 11, 3. 959–1002. (pages 17, 67, 90, and 112).

Jones Matthew D, Abu-Jaber Nizar, AlShdaifat Ahmad, Baird Douglas, Cook Benjamin I, Cuthbert Mark O, Dean Jonathan R, Djamali Morteza, Eastwood Warren, Fleitmann Dominik, others . 20,000 years of societal vulnerability and adaptation to climate change in southwest Asia // Wiley Interdisciplinary Reviews: Water. 2019. 6, 2. e1330. (page 14).

Judd Laura M, Al-Saadi Jassim A, Szykman James J, Valin Lukas C, Janz Scott J, Kowalewski Matthew G, Eskes Henk J, Veefkind J Pepijn, Cede Alexander, Mueller Moritz, others . Evaluating Sentinel-5P TROPOMI tropospheric NO2 column densities with airborne and Pandora spectrometers near New York City and Long Island Soun // Atmospheric measurement techniques. 2020. 13, 11. 6113–6140. (pages 104 and 122).

Kadygrov N, Broquet G, Chevallier F, Rivier L, Gerbig Christoph, Ciais P. On the potential of the ICOS atmospheric CO 2 measurement network for estimating the biogenic CO 2 budget of Europe // Atmospheric Chemistry and Physics. 2015. 15, 22. 12765–12787. (page 17).

Kahramaa . Qatar General Electricity and Water Corporation, `https://www.km.qa/MediaCenter/Pages/Publications.aspx`. 2023. (pages 90 and 103).

Kalabokas PD, Bartzis JG. Photochemical air pollution characteristics at the station of the NCSR-Demokritos, during the MEDCAPHOT-TRACE campaign in Athens, Greece (20 August–20 September 1994) // Atmospheric Environment. 1998. 32, 12. 2123–2139. (pages 25 and 30).

Kasparoglu Sabin, Incecik Selahattin, Topcu Sema. Spatial and temporal variation of O3, NO and NO2 concentrations at rural and urban sites in Marmara Region of Turkey // Atmospheric pollution research. 2018. 9, 6. 1009–1020. (pages 25, 30, and 30).

Kassem Youssef, Çamur Hüseyin, Alhuoti Salman Mohammed Awadh. Solar energy technology for Northern Cyprus: Assessment, statistical analysis, and feasibility study // Energies. 2020. 13, 4. 940. (page 117).

Kenagy Hannah S, Sparks Tamara L, Wooldridge Paul J, Weinheimer Andrew J, Ryerson Thomas B, Blake Donald R, Hornbrook Rebecca S, Apel Eric C, Cohen Ronald C. Evidence of nighttime production of organic nitrates during SEAC4RS, frappé, and KORUS-AQ // Geophysical Research Letters. 2020. 47, 11. e2020GL087860. (page 29).

Khan MAH, Cooke MC, Utembe SR, Morris WC, Archibald AT, Derwent RG, Jenkin ME, Orr-Ewing AJ, Higgins CM, Percival CJ, others . Global modeling of the C1–C3 alkyl nitrates using STOCHEM-CRI // Atmospheric Environment. 2015. 123. 256–267. (page 27).

Khoder MI. Diurnal, seasonal and weekdays–weekends variations of ground level ozone concentrations in an urban area in greater Cairo // Environmental Monitoring and Assessment. 2009. 149, 1. 349–362. (pages 25, 30, 30, and 72).

Kim Hyun Cheol, Bae Changhan, Bae Minah, Kim Okgil, Kim Byeong-Uk, Yoo Chul, Park Jinsoo, Choi Jinsoo, Lee Jae-bum, Lefer Barry, others . Space-Borne Monitoring of NOx Emissions from Cement Kilns in South Korea // Atmosphere. 2020a. 11, 8. 881. (pages 62 and 108).

Kim Jhoon, Jeong Ukkyo, Ahn Myoung-Hwan, Kim Jae H, Park Rokjin J, Lee Hanlim, Song Chul Han, Choi Yong-Sang, Lee Kwon-Ho, Yoo Jung-Moon, others . New era of air quality monitoring from space: Geostationary Environment Monitoring Spectrometer (GEMS) // Bulletin of the American Meteorological Society. 2020b. 101, 1. E1–E22. (page 36).

Koelemeijer RBA, Stammes Piet, Hovenier JW, De Haan JF. A fast method for retrieval of cloud parameters using oxygen A band measurements from the Global Ozone Monitoring Experiment // Journal of Geophysical Research: Atmospheres. 2001. 106, D4. 3475–3490. (page 39 and 39).

Konovalov Igor B, Berezin Evgeny V, Ciais Philippe, Broquet Grégoire, Zhuravlev Ruslan V, Janssens-Maenhout Greet. Estimation of fossil-fuel CO2 emissions using satellite measurements of" proxy" species // Atmospheric Chemistry and Physics. 2016. 16, 21. 13509–13540. (page 18).

Koukouli Maria-Elissavet, Skoulidou Ioanna, Karavias Andreas, Parcharidis Isaak, Balis Dimitris, Manders Astrid, Segers Arjo, Eskes Henk, Geffen Jos van. Sudden changes in nitrogen dioxide emissions over Greece due to lockdown after the outbreak of COVID-19 // Atmospheric Chemistry and Physics. 2021. 21, 3. 1759–1774. (page 19).

Kouyakhi Nima Rajabi. CO2 emissions in the Middle East: Decoupling and decomposition analysis of carbon emissions, and projection of its future trajectory // Science of The Total Environment. 2022. 845. 157182. (page 16).

Kuenen Jeroen, Dellaert Stijn, Visschedijk Antoon, Jalkanen Jukka-Pekka, Super Ingrid, Gon Hugo Denier van der. CAMS-REG-v4: a state-of-the-art high-resolution European emission inventory for air quality modelling // Earth System Science Data. 2022. 14, 2. 491–515. (page 112).

Kuhlmann Gerrit, Broquet Grégoire, Marshall Julia, Clément Valentin, Löscher Armin, Meijer Yasjka, Brunner Dominik. Detectability of CO2 emission plumes of cities and power plants with the Copernicus Anthropogenic CO2 Monitoring (CO2M) mission // Atmospheric Measurement Techniques. 2019. 12, 12. 6695–6719. (page 18).

Kuhlmann Gerrit, Henne Stephan, Meijer Yasjka, Brunner Dominik. Quantifying CO2 emissions of power plants with CO2 and NO2 imaging satellites // Frontiers in Remote Sensing. 2021. 2. 14. (pages 18 and 58).

Kurchaba Solomiia, Vliet Jasper van, Verbeek Fons J, Meulman Jacqueline J, Veenman Cor J. Supervised segmentation of NO2 plumes from individual ships using TROPOMI satellite data // Remote Sensing. 2022. 14, 22. 5809. (page 131).

Labbe Roger. Kalman and bayesian filters in python // Chap. 2014. 7, 246. 4. (page 37).

Lama Srijana, Houweling Sander, Boersma K Folkert, Aben Ilse, Gon Hugo AC Denier van der, Krol Maarten C. Estimation of OH in urban plumes using TROPOMI-inferred NO2/CO // Atmospheric Chemistry and Physics. 2022. 22, 24. 16053–16071. (pages 56 and 125).

Lama Srijana, Houweling Sander, Boersma K Folkert, Eskes Henk, Aben Ilse, Gon Hugo AC Denier van der, Krol Maarten C, Dolman Han, Borsdorff Tobias, Lorente Alba. Quantifying burning efficiency in megacities using the NO2/CO ratio from the Tropospheric Monitoring Instrument (TROPOMI) // Atmospheric Chemistry and Physics. 2020. 20, 17. 10295–10310. (pages 18, 46, 63, 71, 104, and 108).

Lambert Johann Heinrich. Photometria sive de mensura et gradibus luminis, colorum et umbrae. 1760. (page 31).

Lamsal LN, Martin RV, Padmanabhan A, Van Donkelaar A, Zhang Q, Sioris CE, Chance K, Kurosu TP, Newchurch MJ. Application of satellite observations for timely updates to global anthropogenic NOx emission inventories // Geophysical Research Letters. 2011. 38, 5. (page 58 and 58).

Lange Kezia, Richter Andreas, Burrows John Philip. Variability of nitrogen oxide emission fluxes and lifetimes estimated from Sentinel-5P TROPOMI observations // Atmospheric Chemistry and Physics Discussions. 2021. 1–32. (pages 56, 57, 59, 63, and 69).

Latsch Miriam, Richter Andreas, Burrows John P. Improving the detection of global NOx emissions from shipping in S5P/TROPOMI data. 2023. (pages 104, 122, and 133).

Lei Ruixue, Feng Sha, Danjou Alexandre, Broquet Grégoire, Wu Dien, Lin John C, O'Dell Christopher W, Lauvaux Thomas. Fossil fuel CO2 emissions over metropolitan areas from space: A multi-model analysis of OCO-2 data over Lahore, Pakistan // Remote Sensing of Environment. 2021. 264. 112625. (page 17).

Leighton Philip. Photochemistry of Air Pollution. 1961. (page 25).

Lelieveld J, Berresheim H, Borrmann S, Crutzen PJ, Dentener FJ, Fischer H, Feichter J, Flatau PJ, Heland J, Holzinger R, others . Stephanou, 770 EG // Stier, P., Traub, M., Warneke, C., Williams, J. and Ziereis, H.: Global air pollution crossroads over the Mediterranean, Science. 2002. 298. (page 14).

Lelieveld Jos, Beirle Steffen, Hörmann Christoph, Stenchikov Georgiy, Wagner Thomas. Abrupt recent trend changes in atmospheric nitrogen dioxide over the Middle East // Science advances. 2015. 1, 7. e1500498. (pages 19, 86, 103, and 108).

Lelieveld Jos, Gromov Sergey, Pozzer Andrea, Taraborrelli Domenico. Global tropospheric hydroxyl distribution, budget and reactivity // Atmospheric Chemistry and Physics. 2016. 16, 19. 12477–12493. (pages 64 and 92).

Lelieveld Jos, Hadjinicolaou P, Kostopoulou E, Chenoweth J, El Maayar M, Giannakopoulos C, Hannides C, Lange MA, Tanarhte M, Tyrlis E, others . Climate change and impacts in the Eastern Mediterranean and the Middle East // Climatic change. 2012. 114. 667–687. (page 14 and 14).

Leue C, Wenig M, Wagner T, Klimm Oliver, Platt U, Jähne B. Quantitative analysis of NOx emissions from Global Ozone Monitoring Experiment satellite image sequences // Journal of Geophysical Research: Atmospheres. 2001. 106, D6. 5493–5505. (pages 63 and 108).

Levelt Pieternel F, Van Den Oord Gijsbertus HJ, Dobber Marcel R, Malkki Anssi, Visser Huib, De Vries Johan, Stammes Piet, Lundell Jens OV, Saari Heikki. The Ozone Monitoring Instrument // IEEE Transactions on geoscience and remote sensing. 2006. 44, 5. 1093–1101. (pages 33 and 37).

Levy H. Normal atmosphere: Large radical and formaldehyde concentrations predicted // Science. 1971. 173, 3992. 141–143. (pages 64 and 91).

Li Chi, Martin Randall V, Cohen Ronald C, Bindle Liam, Zhang Dandan, Chatterjee Deepangsu, Weng Hongjian, Lin Jintai. Variable effects of spatial resolution on modeling of nitrogen oxides // Atmospheric Chemistry and Physics. 2023a. 23, 5. 3031–3049. (pages 55 and 125).

Li Mengze, Karu Einar, Brenninkmeijer Carl, Fischer Horst, Lelieveld Jos, Williams Jonathan. Tropospheric OH and stratospheric OH and Cl concentrations determined from CH4, CH3Cl, and SF6 measurements // NPJ Climate and Atmospheric Science. 2018. 1, 1. 1–7. (pages 64 and 92).

Li Xiaolu, Cohen Jason Blake, Qin Kai, Geng Hong, Wu Xiaohui, Wu Liling, Yang Chengli, Zhang Rui, Zhang Liqin. Remotely sensed and surface measurement-derived mass-conserving inversion of daily NO x emissions and inferred combustion technologies in energy-rich northern China // Atmospheric Chemistry and Physics. 2023b. 23, 14. 8001–8019. (pages 26 and 131).

Lian Jinghui, Lauvaux Thomas, Utard Hervé, Bréon François-Marie, Broquet Grégoire, Ramonet Michel, Laurent Olivier, Albarus Ivonne, Chariot Mali, Kotthaus Simone, others . Can we use atmospheric CO 2 measurements to verify emission trends reported by cities? Lessons from a 6-year atmospheric inversion over Paris // Atmospheric Chemistry and Physics. 2023. 23, 15. 8823–8835. (page 17).

Lin J-T. Satellite constraint for emissions of nitrogen oxides from anthropogenic, lightning and soil sources over East China on a high-resolution grid // Atmospheric Chemistry and Physics. 2012. 12, 6. 2881–2898. (pages 47, 65, and 91).

Lin Xiaojuan, A Ronald van der, Laat Jos de, Eskes Henk, Chevallier Frédéric, Ciais Philippe, Deng Zhu, Geng Yuanhao, Song Xuanren, Ni Xiliang, others . Monitoring and quantifying CO2 emissions of isolated power plants from space // Atmospheric Chemistry and Physics. 2023. 23, 11. 6599–6611. (page 59).

Lionello Piero, Malanotte-Rizzoli Paola, Boscolo Roberta, Alpert Pinhas, Artale Vincenz, Li L, Luterbacher Jürg, May W, Trigo R, Tsimplis M, others . The Mediterranean climate: an overview of the main characteristics and issues. 2006. 1–26. (page 14).

Liu Fei, Beirle Steffen, Joiner Joanna, Choi Sungyeon, Tao Zhining, Knowland K Emma, Smith Steven J, Tong Daniel Q, Ma Siqi, Fasnacht Zachary T, others . High-resolution Mapping of Nitrogen Oxide Emissions in Large US Cities from TROPOMI Retrievals of Tropospheric Nitrogen Dioxide Columns // EGUsphere. 2023. 2023. 1–18. (pages 46 and 125).

Liu Fei, Tao Zhining, Beirle Steffen, Joiner Joanna, Yoshida Yasuko, Smith Steven J, Knowland K Emma, Wagner Thomas. A new method for inferring city emissions and lifetimes of nitrogen oxides from high-resolution nitrogen dioxide observations: a model study // Atmospheric Chemistry and Physics. 2022. 22, 2. 1333–1349. (page 125).

Logan Jennifer A, Prather Michael J, Wofsy Steven C, McElroy Michael B. Tropospheric chemistry: a global perspective // Journal of Geophysical Research: Oceans. 1981. 86, C8. 7210–7254. (page 64).

Longfellow Cheryl A, Ravishankara AR, Hanson David R. Reactive uptake on hydrocarbon soot: Focus on NO2 // Journal of Geophysical Research: Atmospheres. 1999. 104, D11. 13833–13840. (pages 29 and 68).

Lorente A, Boersma KF, Eskes HJ, Veefkind JP, Van Geffen JHGM, De Zeeuw MB, Denier Van Der Gon HAC, Beirle Steffen, Krol MC. Quantification of nitrogen oxides emissions from build-up of pollution over Paris with TROPOMI // Scientific reports. 2019. 9, 1. 1–10. (pages 56, 63, 71, 88, 104, 104, 108, 110, and 122).

Lorente Alba, Folkert Boersma K, Yu Huan, Dörner Steffen, Hilboll Andreas, Richter Andreas, Liu Mengyao, Lamsal Lok N, Barkley Michael, Smedt Isabelle De, others . Structural uncertainty in air mass factor calculation for NO2 and HCHO satellite retrievals // Atmospheric Measurement Techniques. 2017. 10, 3. 759–782. (pages 40 and 67).

Loughner Christopher P, Lary David J, Sparling Lynn C, Cohen Ronald C, DeCola Phil, Stockwell William R. A method to determine the spatial resolution required to observe air quality from space // IEEE Transactions on Geoscience and Remote Sensing. 2007. 45, 5. 1308–1314. (page 53).

Luterbacher J, Xoplaki E. Palaeoclimatic conditions during the Hellenistic period in the Eastern Mediterranean // Hellenistic Alexandria. 2017. 13. 281. (page 14).

Luterbacher J, Xoplaki E, Fleitmann D, Izdebski A. Palaeoclimatic conditions during the Byzantium (AD 300–1500) in the Central and Eastern Mediterranean. 2021. (page 14).

Maasakkers Joannes D, Varon Daniel J, Elfarsdóttir Aldís, McKeever Jason, Jervis Dylan, Mahapatra Gourav, Pandey Sudhanshu, Lorente Alba, Borsdorff Tobias, Foorthuis Lodewijck R, others . Using satellites to uncover large methane emissions from landfills // Science Advances. 2022. 8, 31. eabn9683. (page 59).

Mahan Alfred Thayer. The Persian Gulf and international relations. 1902. (page 11).

Mansouri Daneshvar Mohammad Reza, Hussein Abadi Nasrin. Spatial and temporal variation of nitrogen dioxide measurement in the Middle East within 2005–2014 // Modeling Earth Systems and Environment. 2017. 3, 1. 1–9. (page 86).

Marais Eloise A, Akker Orianna, Wiedinmyer Christine. Greenhouse gas and air pollutant emissions from power barges (powerships) // Environmental Science: Advances. 2022. 1, 2. 164–169. (page 101).

Mariotti Annarita, Pan Yutong, Zeng Ning, Alessandri Andrea. Long-term climate change in the Mediterranean region in the midst of decadal variability // Climate Dynamics. 2015. 44. 1437–1456. (page 14).

Martin Randall V, Jacob Daniel J, Chance Kelly, Kurosu Thomas P, Palmer Paul I, Evans Mathew J. Global inventory of nitrogen oxide emissions constrained by space-based observations of NO2 columns // Journal of Geophysical Research: Atmospheres. 2003. 108, D17. (pages 63 and 108).

Ipcc, 2021: Summary for policymakers. in: Climate change 2021: The physical science basis. contribution of working group i to the sixth assessment report of the intergovernmental panel on climate change. // . 2021. (pages 12 and 23).

Middleton Nick. Variability and trends in dust storm frequency on decadal timescales: Climatic drivers and human impacts // Geosciences. 2019. 9, 6. 261. (page 14).

Mie Gustav. Beiträge zur Optik trüber Medien, speziell kolloidaler Metallösungen // Annalen der physik. 1908. 330, 3. 377–445. (page 32).

Mijling B, Van Der A RJ. Using daily satellite observations to estimate emissions of short-lived air pollutants on a mesoscopic scale // Journal of Geophysical Research: Atmospheres. 2012. 117, D17. (pages 63 and 108).

Miller Paul Joseph. North American power plant air emissions. 2004. (page 103).

Miyazaki Kazuyuki, Eskes Henk, Sudo Kengo, Boersma K Folkert, Bowman Kevin, Kanaya Yugo. Decadal changes in global surface NOx emissions from multi-constituent satellite data assimilation // Atmospheric Chemistry and Physics. 2017. 17, 2. 807–837. (pages 19 and 108).

Mohammed Safwan A, Fallah Riad Qara. Climate change indicators in AlSheikh-Badr basin (Syria) // Geography, Environment, Sustainability. 2019. 12, 2. 87–96. (page 14).

Mostafa Amira N, Wheida Ali, El Nazer Mostafa, Adel Mona, El Leithy Lamia, Siour Guillaume, Coman Adriana, Borbon Agnes, Magdy Abel Wahab, Omar Mohamed, others . Past (1950–2017) and future (- 2100) temperature and precipitation trends in Egypt // Weather and Climate Extremes. 2019. 26. 100225. (page 14).

Moxim WJ, Levy H, Kasibhatla PS. Simulated global tropospheric PAN: Its transport and impact on NOx // Journal of Geophysical Research: Atmospheres. 1996. 101, D7. 12621–12638. (pages 28, 68, and 113).

Müller J-F, Stavrakou T. Inversion of CO and NOx emissions using the adjoint of the IMAGES model // Atmospheric Chemistry and Physics. 2005. 5, 5. 1157–1186. (pages 47, 65, and 90).

Munro Rosemary, Lang Rüdiger, Klaes Dieter, Poli Gabriele, Retscher Christian, Lindstrot Rasmus, Huckle Roger, Lacan Antoine, Grzegorski Michael, Holdak Andriy, others . The GOME-2 instrument on the Metop series of satellites: instrument design, calibration, and level 1 data processing–an overview // Atmospheric Measurement Techniques. 2016. 9, 3. 1279–1301. (page 37).

Murphy JG, Day DA, Cleary PA, Wooldridge PJ, Millet DB, Goldstein AH, Cohen RC. The weekend effect within and downwind of Sacramento: Part 2. Observational evidence for chemical and dynamical contributions // Atmospheric Chemistry and Physics Discussions. 2006. 6, 6. 11971–12019. (page 53 and 53).

Nassief Mofreh M. Evaluation of electricity consumption of a residential flat in Egypt // American Journal of Electrical Power and Energy Systems. 2014. 3, 2. 7–44. (page 81).

Nastos Panagiotis T, Politi Nadia, Kapsomenakis John. Spatial and temporal variability of the Aridity Index in Greece // Atmospheric Research. 2013. 119. 140–152. (page 14).

Nault Benjamin A, Garland Charity, Wooldridge Paul J, Brune William H, Campuzano-Jost Pedro, Crounse John D, Day Douglas A, Dibb Jack, Hall Samuel R, Huey L Gregory, others . Observational Constraints on the Oxidation of NOx in the Upper Troposphere // The Journal of Physical Chemistry A. 2016. 120, 9. 1468–1478. (pages 46 and 67).

OPEC ASB. OPEC Annual Statistical Bulletin 2019. 2020. (pages 14 and 86).

Oda Tomohiro, Maksyutov Shamil, Andres Robert J. The Open-source Data Inventory for Anthropogenic CO2, version 2016 (ODIAC2016): a global monthly fossil fuel CO2 gridded emissions data product for tracer transport simulations and surface flux inversions // Earth System Science Data. 2018. 10, 1. 87–107. (page 17).

Okonkwo Eric C, Abdullatif Yasser M, Tareq Al-Ansari. A nanomaterial integrated technology approach to enhance the energy-water-food nexus // Renewable and Sustainable Energy Reviews. 2021. 145. 111118. (page 103).

Oner Ecem, Kaynak Burcak. Evaluation of NOx emissions for Turkey using satellite and ground-based observations // Atmospheric Pollution Research. 2016. 7, 3. 419–430. (page 19).

Osipov Sergey, Chowdhury Sourangsu, Crowley John N, Tadic Ivan, Drewnick Frank, Borrmann Stephan, Eger Philipp, Fachinger Friederike, Fischer Horst, Predybaylo Evgeniya, others . Severe atmospheric pollution in the Middle East is attributable to anthropogenic sources // Communications Earth & Environment. 2022. 3, 1. 1–10. (page 86).

PSA . Planning and Statistics Authority, Qatar Monthly Statistics, `https://www.psa.gov.qa/en/statistics1/Pages/default.aspx`. 2023. (page 90).

Palmes ED, Gunnison AF, DiMattio J, Tomczyk C. Personal sampler for nitrogen dioxide // American Industrial Hygiene Association Journal. 1976. 37, 10. 570–577. (page 48).

Park Hayoung, Jeong Sujong, Park Hoonyoung, Labzovskii Lev D, Bowman Kevin W. An assessment of emission characteristics of Northern Hemisphere cities using spaceborne observations of CO2, CO, and NO2 // Remote Sensing of Environment. 2021. 254. 112246. (page 18).

Park Jong Yoon, Lee Yin Nan. Solubility and decomposition kinetics of nitrous acid in aqueous solution // The Journal of Physical Chemistry. 1988. 92, 22. 6294–6302. (page 29).

Pfannerstill Eva Y, Wang Nijing, Edtbauer Achim, Bourtsoukidis Efstratios, Crowley John N, Dienhart Dirk, Eger Philipp G, Ernle Lisa, Fischer Horst, Hottmann Bettina, others . Shipborne measurements of total OH reactivity around the Arabian Peninsula and its role in ozone chemistry // Atmospheric Chemistry and Physics. 2019. 19, 17. 11501–11523. (page 116).

Pisso Ignacio, Real Elsa, Law Kathy S, Legras B, Bousserez N, Attié Jean-Luc, Schlager H. Estimation of mixing in the troposphere from lagrangian trace gas reconstructions during long-range pollution plume transport // Journal of Geophysical Research: Atmospheres. 2009. 114, D19. (page 48).

Platt Ulrich, Stutz Jochen, Platt Ulrich, Stutz Jochen. Differential absorption spectroscopy. 2008. (page 32).

Portmann RW, Daniel JS, Ravishankara AR. Stratospheric ozone depletion due to nitrous oxide: influences of other gases // Philosophical Transactions of the Royal Society B: Biological Sciences. 2012. 367, 1593. 1256–1264. (page 23).

Poulter Benjamin, Bousquet Philippe, Canadell Josep G, Ciais Philippe, Peregon Anna, Saunois Marielle, Arora Vivek K, Beerling David J, Brovkin Victor, Jones Chris D, others . Global wetland contribution to 2000–2012 atmospheric methane growth rate dynamics // Environmental Research Letters. 2017. 12, 9. 094013. (page 17).

Prakash P Jish, Stenchikov G, Kalenderski S, Osipov S, Bangalath HJAC. The impact of dust storms on the Arabian Peninsula and the Red Sea. // Atmospheric Chemistry & Physics Discussions. 2014. 14, 13. (page 14).

Rabiei-Dastjerdi Hamidreza, Mohammadi Shahin, Saber Mohsen, Amini Saeid, McArdle Gavin. Spatiotemporal analysis of NO2 production using TROPOMI time-series images and Google Earth Engine in a middle eastern country // Remote Sensing. 2022. 14, 7. 1725. (page 19).

Rahman AKM Mahbubur, Zaber Moinul, Cheng Qianwei, Nayem Abu Bakar Siddik, Sarker Anis, Paul Ovi, Shibasaki Ryosuke. Applying state-of-the-art deep-learning methods to classify urban cities of the developing world // Sensors. 2021. 21, 22. 7469. (page 134).

Rajab Jasim M, Hassan Ahmed S, Kadhum Jasim H, Al-Salihi Ali M, San Lim Hwee. Analysis of tropospheric NO2 over Iraq using OMI satellite measurements // Scientific Review Engineering and Environmental Sciences. 2020. 2020, 1). 3–16. (page 19).

Ramadan HH, Beighley RE, Ramamurthy AS. Temperature and precipitation trends in Lebanon's largest river: the Litani Basin // Journal of water resources planning and management. 2013. 139, 1. 86–95. (page 14).

Rashki Alireza, Middleton Nick J, Goudie Andrew S. Dust storms in Iran–Distribution, causes, frequencies and impacts // Aeolian Research. 2021. 48. 100655. (page 14).

Reuter Maximilian, Buchwitz Michael, Schneising Oliver, Krautwurst Sven, O'Dell Christopher W, Richter Andreas, Bovensmann Heinrich, Burrows John P. Towards monitoring localized CO2 emissions from space: co-located regional CO2 and NO2 enhancements observed by the OCO-2 and S5P satellites // Atmospheric Chemistry and Physics. 2019. 19, 14. 9371–9383. (page 18).

Rey-Pommier Anthony, Chevallier Frédéric, Ciais Philippe, Broquet Grégoire, Christoudias Theodoros, Kushta Jonilda, Hauglustaine Didier, Sciare Jean. Quantifying NOx emissions in Egypt using TROPOMI observations // Atmospheric Chemistry and Physics. 2022. 22, 17. 11505–11527. (pages 92, 92, 94, 97, 102, 104, 108, and 113).

Rey-Pommier Anthony, Chevallier Frédéric, Ciais Philippe, Kushta Jonilda, Christoudias Theodoros, Bayram I Safak, Sciare Jean. Detecting nitrogen oxide emissions in Qatar and quantifying emission factors of gas-fired power plants–a 4-year study // Atmospheric Chemistry and Physics. 2023. 23, 21. 13565–13583. (pages 119 and 123).

Richter A, Begoin M, Hilboll A, Burrows JP. An improved NO2 retrieval for the GOME-2 satellite instrument // Atmospheric Measurement Techniques. 2011. 4, 6. 1147–1159. (page 116).

Richter A, Burrows JP. Tropospheric NO2 from GOME measurements // Advances in Space Research. 2002. 29, 11. 1673–1683. (page 86).

Rieß T Christoph VW, Vliet Jasper van, Van Roy Ward, Laat Jos de, Dammers Enrico, Boersma Folkert. Aircraft validation reveals a 20% low bias in TROPOMI NO2 over sea caused by TM5 a priori profiles. 2023. (pages 104 and 122).

Rieß TCVW, Boersma K Folkert, vanVliet Jasper, Peters Wouter, Sneep Maarten, Eskes Henk, Geffen Jos van. Improved monitoring of shipping NO2 with TROPOMI: decreasing NOx emissions in European seas during the COVID-19 pandemic // Atmospheric Measurement Techniques Discussions. 2021. 1–35. (pages 131 and 132).

Roberts JM. Reactive odd-nitrogen (NOy) in the atmosphere // Composition, Chemistry, and Climate of the Atmosphere. 1995. 176–215. (pages 26 and 28).

Rohrer Franz, Berresheim Harald. Strong correlation between levels of tropospheric hydroxyl radicals and solar ultraviolet radiation // Nature. 2006. 442, 7099. 184–187. (pages 69 and 92).

Romer Present Paul S, Zare Azimeh, Cohen Ronald C. The changing role of organic nitrates in the removal and transport of NOx // Atmospheric Chemistry and Physics. 2020. 20, 1. 267–279. (pages 28, 68, and 68).

Rosentreter Judith A, Borges Alberto V, Deemer Bridget R, Holgerson Meredith A, Liu Shaoda, Song Chunlin, Melack John, Raymond Peter A, Duarte Carlos M, Allen George H, others . Half of global methane emissions come from highly variable aquatic ecosystem sources // Nature Geoscience. 2021. 14, 4. 225–230. (page 17).

Russell Ashley R, Valin Lukas C, Bucsela Eric J, Wenig Mark O, Cohen Ronald C. Space-based constraints on spatial and temporal patterns of NOx emissions in California, 2005- 2008 // Environmental science & technology. 2010. 44, 9. 3608–3615. (page 53).

Sander SP, Friedl RR, Abbatt JPD, Barker JR, Burkholder JB, Golden DM, Kolb CE, Kurylo MJ, Moortgat GK, Wine PH, others . Chemical kinetics and photochemical data for use in atmospheric studies, JPL Publication 10-6 // Evaluation. 2011. 17. (pages 46 and 67).

Saw Gautam Kumar, Dey Sagnik, Kaushal Hemant, Lal Kanhaiya. Tracking NO2 emission from thermal power plants in North India using TROPOMI data // Atmospheric Environment. 2021. 259. 118514. (pages 88 and 110).

Seinfeld John H. Urban air pollution: state of the science // Science. 1989. 243, 4892. 745–752. (pages 25, 27, 28, 46, 64, 67, 68, 92, 113, and 114).

Atmospheric chemistry and physics from air pollution to climate change. // . 2006. (pages 26, 28, 72, 92, 114, and 130).

Shikwambana Lerato, Mhangara Paidamwoyo, Mbatha Nkanyiso. Trend analysis and first time observations of sulphur dioxide and nitrogen dioxide in South Africa using TROPOMI/Sentinel-5P data // International Journal of Applied Earth Observation and Geoinformation. 2020. 91. 102130. (pages 88 and 110).

Shohami David, Dayan Uri, Morin Efrat. Warming and drying of the eastern Mediterranean: Additional evidence from trend analysis // Journal of Geophysical Research: Atmospheres. 2011. 116, D22. (page 14).

Silva Sam J, Arellano AF. Characterizing regional-scale combustion using satellite retrievals of CO, NO2 and CO2 // Remote Sensing. 2017. 9, 7. 744. (pages 16 and 18).

Singh Anita, Agrawal Madhoolika. Acid rain and its ecological consequences // Journal of Environmental Biology. 2007. 29, 1. 15. (pages 24, 62, and 108).

Sinha Ashish, Kathayat Gayatri, Weiss Harvey, Li Hanying, Cheng Hai, Reuter Justin, Schneider Adam W, Berkelhammer Max, Adalı Selim F, Stott Lowell D, others . Role of climate in the rise and fall of the Neo-Assyrian Empire // Science advances. 2019. 5, 11. eaax6656. (page 14).

Smith Walter HF, Sandwell David T. Global sea floor topography from satellite altimetry and ship depth soundings // Science. 1997. 277, 5334. 1956–1962. (page 129).

Sobanski Nicolas, Thieser Jim, Schuladen Jan, Sauvage Carina, Song Wei, Williams Jonathan, Lelieveld Jos, Crowley John N. Day and night-time formation of organic nitrates at a forested mountain site in south-west Germany // Atmospheric Chemistry and Physics. 2017. 17, 6. 4115–4130. (page 68).

Solyali Davut, Redfern Miles A. Exploiting sun's energy–Comparison of solar technologies for Cyprus // ICCE 2010, Proceedings of ICCE 2010 EMU TRNC. 2010. (page 117).

Spinoni Jonathan, Barbosa Paulo, De Jager Alfred, McCormick Niall, Naumann Gustavo, Vogt Jürgen V, Magni Diego, Masante Dario, Mazzeschi Marco. A new global database of meteorological drought events from 1951 to 2016 // Journal of Hydrology: Regional Studies. 2019. 22. 100593. (page 14, 14, and 14).

Stavrakou T, Müller J-F, Bauwens M, Boersma KF, Geffen J van. Satellite evidence for changes in the NO2 weekly cycle over large cities // Scientific reports. 2020. 10, 1. 1–9. (pages 19, 78, and 97).

Stavrakou T, Müller J-F, Boersma KF, Van Der A RJ, Kurokawa J, Ohara T, Zhang Q. Key chemical NOx sink uncertainties and how they influence top-down emissions of nitrogen oxides // Atmospheric Chemistry and Physics. 2013. 13, 17. 9057–9082. (pages 46, 68, and 120).

Stevenson David S, Derwent Richard G, Wild Oliver, Collins William J. COVID-19 lockdown emission reductions have the potential to explain over half of the coincident increase in global atmospheric methane // Atmospheric Chemistry and Physics. 2022. 22, 21. 14243–14252. (page 18).

Stocker Thomas. Climate change 2013: the physical science basis: Working Group I contribution to the Fifth assessment report of the Intergovernmental Panel on Climate Change. 2014. (page 19).

Strutt John William. LVIII. On the scattering of light by small particles // The London, Edinburgh, and Dublin Philosophical Magazine and Journal of Science. 1871. 41, 275. 447–454. (page 32).

Sun Kang. Derivation of Emissions From Satellite-Observed Column Amounts and Its Application to TROPOMI NO2 and CO Observations // Geophysical Research Letters. 2022. 49, 23. e2022GL101102. (pages 53, 53, 101, 104, 123, and 129).

Tanarhte M, Hadjinicolaou P, Lelieveld J. Intercomparison of temperature and precipitation data sets based on observations in the Mediterranean and the Middle East // Journal of Geophysical Research: Atmospheres. 2012. 117, D12. (page 14).

Tang Ling, Xue Xiaoda, Jia Min, Jing Hong, Wang Tong, Zhen Ruiqing, Huang Mantang, Tian Jun, Guo Jing, Li Ling, others . Iron and steel industry emissions and contribution to the air quality in China // Atmospheric Environment. 2020. 237. 117668. (pages 62 and 108).

Tischner R. Nitrate uptake and reduction in higher and lower plants // Plant, Cell & Environment. 2000. 23, 10. 1005–1024. (page 29).

Tomtom . TomTom, Doha traffic, Qatar, `https://www.tomtom.com/en_gb/traffic-index/doha-traffic/`. 2023. (page 98).

Tubiello Francesco N, Salvatore Mirella, Rossi Simone, Ferrara Alessandro, Fitton Nuala, Smith Pete. The FAOSTAT database of greenhouse gas emissions from agriculture // Environmental Research Letters. 2013. 8, 1. 015009. (page 17).

UNEP . Air quality policies in Egypt // `https://www.unep.org/resources/policy-and-strategy/air-quality-policies-egypt`. 2015. (page 63).

UNFCCC . UNFCCC Nationally Determined Contributions Registry, `https://unfccc.int/resource/docs/natc/qatnc1.pdf`. 2011. (page 87).

United Nations . Accord de Paris, Nations Unies, 2015, `https://unfccc.int/files/cooperation_and_support/cooperation_with_international_organizations/application/pdf/convfr.pdf`. 1992. (page 15).

United Nations . Accord de Paris, Nations Unies, 2015, `https://unfccc.int/sites/default/files/french_paris_agreement.pdf`. 2015. (page 15).

Valin LC, Russell AR, Cohen RC. Variations of OH radical in an urban plume inferred from NO2 column measurements // Geophysical Research Letters. 2013. 40, 9. 1856–1860. (pages 56, 69, 70, and 70).

Valin LC, Russell AR, Hudman RC, Cohen RC. Effects of model resolution on the interpretation of satellite NO2 observations // Atmospheric Chemistry and Physics. 2011. 11, 22. 11647–11655. (pages 53, 54, 54, 54, 55, 64, 71, 92, 99, 113, 125, 140, 140, 142, 171, and 171).

Van Der Werf Guido R, Randerson James T, Giglio Louis, Van Leeuwen Thijs T, Chen Yang, Rogers Brendan M, Mu Mingquan, Van Marle Margreet JE, Morton Douglas C, Collatz G James, others . Global fire emissions estimates during 1997–2016 // Earth System Science Data. 2017. 9, 2. 697–720. (page 17).

Van Geffen Jos, Eskes Henk, Compernolle Steven, Pinardi Gaia, Verhoelst Tijl, Lambert Jean-Christopher, Sneep Maarten, Ter Linden Mark, Ludewig Antje, Boersma K Folkert, others . Sentinel-5P TROPOMI NO2 retrieval: impact of version v2.2 improvements and comparisons with OMI and ground-based data // Atmospheric Measurement Techniques. 2022. 15, 7. 2037–2060. (pages 34, 104, and 122).

Vandaele Ann Carine, Hermans Christian, Simon Paul C, Carleer Michel, Colin Réginald, Fally Sophie, Merienne Marie-France, Jenouvrier Alain, Coquart Bernard. Measurements of the NO2 absorption cross-section from 42 000 cm-1 to 10 000 cm-1 (238–1000 nm) at 220 K and 294 K // Journal of Quantitative Spectroscopy and Radiative Transfer. 1998. 59, 3-5. 171–184. (pages 88 and 110).

Varon Daniel J, Jacob Daniel J, McKeever Jason, Jervis Dylan, Durak Berke OA, Xia Yan, Huang Yi. Quantifying methane point sources from fine-scale satellite observations of atmospheric methane plumes // Atmospheric Measurement Techniques. 2018. 11, 10. 5673–5686. (pages 17, 57, and 58).

Veefkind J Pepijn, Aben I, McMullan K, Förster H, De Vries J, Otter G, Claas Jacques, Eskes HJ, De Haan JF, Kleipool Q, others . TROPOMI on the ESA Sentinel-5 Precursor: A GMES mission for global observations of the atmospheric composition for climate, air quality and ozone layer applications // Remote sensing of environment. 2012. 120. 70–83. (pages 37, 63, and 108).

Venter Zander S, Aunan Kristin, Chowdhury Sourangsu, Lelieveld Jos. COVID-19 lockdowns cause global air pollution declines // Proceedings of the National Academy of Sciences. 2020. 117, 32. 18984–18990. (page 79).

Verhoelst Tijl, Compernolle Steven, Pinardi Gaia, Lambert Jean-Christopher, Eskes Henk J, Eichmann Kai-Uwe, Fjæraa Ann Mari, Granville José, Niemeijer Sander, Cede Alexander, others . Ground-based validation of the Copernicus Sentinel-5P TROPOMI NO2 measurements with the NDACC ZSL-DOAS, MAX-DOAS and Pandonia global networks // Atmospheric Measurement Techniques. 2021. 14, 1. 481–510. (pages 38, 40, and 82).

Vrekoussis M, Pikridas M, Rousogenous C, Christodoulou A, Desservettaz M, Sciare J, Richter A, Bougoudis I, Savvides C, Papadopoulos C. Local and regional air pollution characteristics in Cyprus: A long-term trace gases observations analysis // Science of The Total Environment. 2022. 845. 157315. (pages 25, 30, and 30).

Vrekoussis M, Richter A, Hilboll Al, Burrows JP, Gerasopoulos E, Lelieveld J, Barrie L, Zerefos C, Mihalopoulos N. Economic crisis detected from space: Air quality observations over Athens/Greece // Geophysical Research Letters. 2013. 40, 2. 458–463. (page 19).

Vuuren LF; Smith SJ; Dentener F. DP; Bouwman. Global Projections for Anthropogenic Reactive Nitrogen Emissions to the Atmosphere: An Assessment of Scenarios in the Scientific Literature // Current Opinion in Environmental Sustainability. 2011. 3. 359–369. (page 86).

WHO . WHO global air quality guidelines: particulate matter (PM2.5 and PM10), ozone, nitrogen dioxide, sulfur dioxide and carbon monoxide. 2021. (page 24).

Waha Katharina, Krummenauer Linda, Adams Sophie, Aich Valentin, Baarsch Florent, Coumou Dim, Fader Marianela, Hoff Holger, Jobbins Guy, Marcus Rachel, others . Climate change impacts in the Middle East and Northern Africa (MENA) region and their implications for vulnerable population groups // Regional Environmental Change. 2017. 17. 1623–1638. (page 15).

Wahba Sherine M, Kamel Basil A, Nassar Khaled M, Abdelsalam Ahmed S. Effectiveness of green roofs and green walls on energy consumption and indoor comfort in arid climates // Civil Engineering Journal. 2018. 4, 10. 2284–2295. (page 81).

Walker TW, Martin RV, Van Donkelaar A, Leaitch WR, MacDonald AM, Anlauf KG, Cohen RC, Bertram TH, Huey LG, Avery MA, others . Trans-Pacific transport of reactive nitrogen and ozone to Canada during spring // Atmospheric Chemistry and Physics. 2010. 10, 17. 8353–8372. (pages 58 and 59).

Wang P, Stammes P. FRESCO-GOME2 project. 2007. (pages 40, 41, and 133).

Wang Yang, Beirle Steffen, Lampel Johannes, Koukouli Mariliza, De Smedt Isabelle, Theys Nicolas, Li Ang, Wu Dexia, Xie Pinhua, Liu Cheng, others . Validation of OMI, GOME-2A and GOME-2B tropospheric NO2, SO2 and HCHO products using MAX-DOAS observations from 2011 to 2014 in Wuxi, China: investigation of the effects of priori profiles and aerosols on the satellite products // Atmospheric Chemistry and Physics. 2017. 17, 8. 5007–5033. (page 38).

Wang Yuan, Yuan Qiangqiang, Li Tongwen, Zhu Liye, Zhang Liangpei. Estimating daily full-coverage near surface O3, CO, and NO2 concentrations at a high spatial resolution over China based on S5P-TROPOMI and GEOS-FP // ISPRS Journal of Photogrammetry and Remote Sensing. 2021a. 175. 311–325. (page 104).

Wang Zewei, Yang Pengfei, Liang Haotian, Zheng Change, Yin Jiyan, Tian Ye, Cui Wenbin. Semantic segmentation and analysis on sensitive parameters of forest fire smoke using smoke-unet and landsat-8 imagery // Remote Sensing. 2021b. 14, 1. 45. (pages 122 and 134).

Warhaft Zellman. Passive scalars in turbulent flows // Annual Review of Fluid Mechanics. 2000. 32, 1. 203–240. (page 48).

Wiedinmyer Christine, Tie Xuexi, Guenther Alex, Neilson Ron, Granier Claire. Future changes in biogenic isoprene emissions: how might they affect regional and global atmospheric chemistry? // Earth Interactions. 2006. 10, 3. 1–19. (page 68).

Williams Jason E, Boersma K Folkert, Le Sager Phillipe, Verstraeten Willem W. The high-resolution version of TM5-MP for optimized satellite retrievals: description and validation // Geoscientific Model Development. 2017. 10, 2. 721–750. (page 37).

Wolfe Glenn M, Nicely Julie M, Clair Jason M St, Hanisco Thomas F, Liao Jin, Oman Luke D, Brune William B, Miller David, Thames Alexander, Abad Gonzalo González, others . Mapping hydroxyl variability throughout the global remote troposphere via synthesis of airborne and satellite formaldehyde observations // Proceedings of the National Academy of Sciences. 2019. 116, 23. 11171–11180. (pages 64 and 92).

World Bank . World Bank Indicators: April 2023, https://data.worldbank.org/indicator/SI.POV.GINI. 2022. (pages 12 and 87).

Xie Hai Wei, Zhang Yan. The research status of acid rain // Advanced Materials Research. 2013. 726. 4033–4036. (page 29).

Xoplaki Elena, Fleitmann Dominik, Luterbacher Juerg, Wagner Sebastian, Haldon John F, Zorita Eduardo, Telelis Ioannis, Toreti Andrea, Izdebski Adam. The Medieval Climate Anomaly and Byzantium: A review of the evidence on climatic fluctuations, economic performance and societal change // Quaternary Science Reviews. 2016. 136. 229–252. (page 14).

Xue Bing, Ren Wanxia. China's uncertain CO2 emissions // Nature Climate Change. 2012. 2, 11. 762–762. (page 63).

Yathreb S. Analysis of a residential building energy consumption as "base model" in Tripoli, Lebanon // International Journal of Energy Production and Management. 2016. 1, 4. 359–370. (page 117).

Ye Chunxiang, Gao Honglian, Zhang Ning, Zhou Xianliang. Photolysis of nitric acid and nitrate on natural and artificial surfaces // Environmental science & technology. 2016. 50, 7. 3530–3536. (page 27).

Ye Xinxin, Lauvaux Thomas, Kort Eric A, Oda Tomohiro, Feng Sha, Lin John C, Yang Emily G, Wu Dien. Constraining fossil fuel CO2 emissions from urban area using OCO-2 observations of total column CO2 // Journal of Geophysical Research: Atmospheres. 2020. 125, 8. e2019JD030528. (page 17).

Yew AC. Numerical differentiation: finite differences // Brown University: Providence, RI, USA. 2011. (page 128).

Yienger JJ, Levy H. Empirical model of global soil-biogenic NOx emissions // Journal of Geophysical Research: Atmospheres. 1995. 100, D6. 11447–11464. (pages 47, 65, 90, and 113).

Yogamangalam R, Karthikeyan B, others . Segmentation techniques comparison in image processing // International Journal of Engineering and Technology (IJET). 2013. 5, 1. 307–313. (page 133).

Zeldovich Yakov. The oxidation of nitrogen in combustion and explosions // J. Acta Physicochimica. 1946. 21. 577. (page 24).

Zhang Qianqian, Boersma K Folkert, Zhao Bin, Eskes Henk, Chen Cuihong, Zheng Haotian, Zhang Xingying. Quantifying daily NOx and CO2 emissions from Wuhan using satellite observations from TROPOMI and OCO-2 // Atmospheric Chemistry and Physics. 2023. 23, 1. 551–563. (page 18).

Zhao Bin, Wang SX, Liu Huan, Xu JY, Fu K, Klimont Z, Hao JM, He KB, Cofala J, Amann MJAC. NOx emissions in China: historical trends and future perspectives // Atmospheric Chemistry and Physics. 2013. 13, 19. 9869–9897. (page 18).

Zheng Bo, Chevallier Frédéric, Ciais Philippe, Broquet Grégoire, Wang Yilong, Lian Jinghui, Zhao Yuanhong. Observing carbon dioxide emissions over China's cities and industrial areas with the Orbiting Carbon Observatory-2 // Atmospheric Chemistry and Physics. 2020. 20, 14. 8501–8510. (pages 17 and 59).

Zheng Haotian, Zhao Bin, Wang Shuxiao, Wang Tong, Ding Dian, Chang Xing, Liu Kaiyun, Xing Jia, Dong Zhaoxin, Aunan Kristin, others . Transition in source contributions of PM2.5 exposure and associated premature mortality in China during 2005–2015 // Environment international. 2019. 132. 105111. (page 18).

Zhu Yizhi, Hu Qihou, Gao Meng, Zhao Chun, Zhang Chengxin, Liu Ting, Tian Yuan, Yan Liu, Su Wenjing, Hong Xinhua, others . Quantifying contributions of local emissions and regional transport to NOX in Beijing using TROPOMI constrained WRF-Chem simulation // Remote Sensing. 2021. 13, 9. 1798. (page 58).

Zittis G, Almazroui M, Alpert P, Ciais P, Cramer W, Dahdal Y, Fnais M, Francis D, Hadjinicolaou P, Howari F, others . Climate change and weather extremes in the Eastern Mediterranean and Middle East // Reviews of Geophysics. 2022. 60, 3. e2021RG000762. (pages 12, 13, 13, 13, 14, and 139).

Zittis George, Hadjinicolaou Panos, Lelieveld Jos, others . Comparison of WRF model physics parameterizations over the MENA-CORDEX domain // American Journal of Climate Change. 2014. 3, 05. 490. (page 111).

Zoogman P, Liu X, Suleiman RM, Pennington WF, Flittner DE, Al-Saadi JA, Hilton BB, Nicks DK, Newchurch MJ, Carr JL, others . Tropospheric emissions: Monitoring of pollution (TEMPO) // Journal of Quantitative Spectroscopy and Radiative Transfer. 2017. 186. 17–39. (page 36).

de Foy Benjamin, Lu Zifeng, Streets David G. Satellite NO2 retrievals suggest China has exceeded its NOx reduction goals from the twelfth Five-Year Plan // Scientific reports. 2016. 6, 1. 35912. (pages 19 and 108).

de Foy Benjamin, Lu Zifeng, Streets David G, Lamsal Lok N, Duncan Bryan N. Estimates of power plant NOx emissions and lifetimes from OMI NO2 satellite retrievals // Atmospheric Environment. 2015. 116. 1–11. (pages 63 and 108).

de Foy Benjamin, Schauer James J. An improved understanding of NOx emissions in South Asian megacities using TROPOMI NO2 retrievals // Environmental Research Letters. 2022. 17, 2. 024006. (pages 46, 101, 108, 123, and 130).

de Haan Johan F, Bosma PB, Hovenier JW. The adding method for multiple scattering calculations of polarized light // Astronomy and astrophysics. 1987. 183. 371–391. (page 38).

CIESIN. Global Rural-Urban Mapping Project, Version 1 (GRUMPv1). Center for International Earth Science Information Network - CIESIN - Columbia University, International Food Policy Research Institute - IFPRI, The World Bank, and Centro Internacional de Agricultura Tropical - CIAT. 2011, Palisades, NY: NASA Socioeconomic Data and Applications Center (SEDAC). // . 2019. (page 65).

EEHC . Egyptian Electricity Holding Company annual report 2019/2020 // `http://www.moee.gov.eg/english_new/report.aspx`. 2021. (page 69).

Annexes

Notations

The notation of quantities are given with their dimensions between brackets, the principal dimensions being length L, mass M, time T, electric intensity I, temperature Θ and particle numbers N. For some quantities, the particle number dimension can be replaced with mass (for instance, emissions can be expressed in particle terms or in mass terms). Such quantities are identified here with a star (*).

- t [T] is the time coordinate.
- λ [1] is the zonal coordinate (along the west-east direction). When it is locally substitutable to a Cartesian coordinate, it is noted x [L] and is along the zonal coordinate y and will be expressed in distance units rather than angles. When an integer is used as a subscript (0, 1 or 2), it refers to a source.
- φ [1] is the meridional coordinate (along the south-north direction). When it is locally substitutable to a Cartesian coordinate, it is noted y [L] and is along the zonal coordinate x and will be expressed in distance units rather than angles. When an integer is used as a subscript (0, 1 or 2), it refers to a source.
- z [L] is the vertical coordinate and corresponds to the altitude (above sea level).
- z_0 [L] is the terrain height.
- h [L] is the planetary boundary layer height.
- ξ [L] is a general Cartesian coordinate, notated differently from x and y that are used to refer to Cartesian coordinates in an east-west/south-north plane.
- ν [T^{-1}] is the light frequency.
- Σ [L^2] is the absorption cross-section of molecules.
- θ_0 [1] is the solar zenith angle.
- θ [1] is the viewing zenith angle.
- ζ_0 [1] is the solar azimuth angle.
- ζ [1] is the viewing azimuth angle.
- I_0 [$\mathrm{ML}^2\mathrm{T}^{-2}$] is the initial radiation intensity.
- I [$\mathrm{ML}^2\mathrm{T}^{-2}$] is the measured radiation intensity.
- s [L] is the curviligne coordinate.
- Σ_R [L^2] is the Rayleigh cross-section.

- $\hat{\Omega}_R$ [*NL^{-2}] is the column for Rayleigh scattering.
- Σ_M [L^2] is the Mie cross-section.
- $\hat{\Omega}_M$ [*NL^{-2}] is the column for Mie scattering.
- D [NL^{-2}T^{-1}] is the transport term.
- S [NL^{-2}T^{-1}] is the sink term.
- E [*NL^{-2}T^{-1}] is the emissions by surface unit. The species can be precised as a subscript (e.g. $E_{\mathrm{NO_2}}$ or $E_{\mathrm{NO_x}}$). When an integer is used as a subscript (0, 1 or 2), it refers to a source.
- $\epsilon_{\mathrm{correction}}$ [NL^{-2}T^{-1}] is the topographic corrective term.
- N [*N] number of particles within a tropospheric column.
- C [*NL^{-3}] is the concentration in nitrogen dioxide, also noted [NO_2].
- $\bar{C}$ [*NL^{-3}] is the average NO_2 concentration in a tropospheric column.
- $\hat{\Omega}$ [*NL^{-2}] is the atmospheric vertical column.
- $\hat{\Omega}_s$ [*NL^{-2}] is the atmospheric slant column.
- Ω [*NL^{-2}] is the tropospheric vertical column.
- Ω_s [*NL^{-2}] is the tropospheric slant column.
- $\hat{m}$ [1] is the atmospheric air mass factor.
- m [1] is the tropospheric air mass factor.
- τ [T] is the lifetime.
- ξ_0 [L] is the the distance over which the observed column density within a plum is decreased by a factor of e.
- T [Θ] is the absolute temperature.
- [NO] [*NL^{-3}] is the concentration in nitric oxide.
- [NO_2] [*NL^{-3}] is the concentration in nitrogen dioxide, also noted C.
- $[\mathrm{NO_x}] = [\mathrm{NO}] + [\mathrm{NO_2}]$ [*NL^{-3}] is the concentration in NO_x.
- [OH] [*NL^{-3}] is the concentration in hydroxyl radical.
- [O_3] [*NL^{-3}] is the concentration in ozone.
- [M] [*NL^{-3}] is the total air concentration, used to refer to pressure.
- k_{mean} [*N^{-1}L^{3}T^{-1}] is the kinetic constant for the reaction involving NO_2 and OH.
- $\mathcal{L}$ [1] is the ratio between NO_x concentration and NO_2 concentration.
- k_L [*N^{-1}L^{3}T^{-1}] is the kinetic constant for the reaction between NO and O_3.
- J [T^{-1}] is the photolysis rate constant of NO_2.
- τ_L [T] is the time scale for establishing the photostationary state between NO, NO_2 and O_3.

- $\vec{w} = (w_x, w_y)$ [LT^{-1}] is the horizontal wind.
- w_0 [LT^{-1}] is the horizontal wind module : $w_0 = \sqrt{w_x^2 + w_y^2}$.
- α [1] is the angle of the horizontal wind (the origin of the angles being the east-west direction).
- $\vec{w}_g = (w_{x,g}, w_{y,g})$ [LT^{-1}] is the horizontal wind at ground level : $\vec{w}_g(x, y, t) = \vec{w}(x, y, z = z_0, t)$.
- w_g [LT^{-1}] is the horizontal ground wind module : $w_g = \sqrt{w_{x,g}^2 + w_{y,g}^2}$.
- K_m [L^{2}T^{-1}] is the molecular diffusion coefficient.
- K_e [L^{2}T^{-1}] is the eddy turbulent viscosity.
- n [1] is a generic index counting pixels a plume (n_p), a mask (n_m) or a background area (n_b).
- q_a [1] is the quality flag for NO_2 TROPOMI.
- L [L] is the lenght of a plume.
- Ω_{air} [*ML^{-2}] is the column of dry air (in mass terms).
- g [LT^{-2}] is the acceleration of gravity.
- ℓ [L] is the side of a pixel, assumed to be squared.
- γ [1] is the proportionality coefficient between changes in surface NO_x emissions and changes in tropospheric NO_2 columns.
- p [ML^{-1}T^{-2}] is the pressure.
- p_0 [ML^{-1}T^{-2}] is the standard pressure: $p_0 = 1013.25$ hPa.
- ω [*NL^{-1}] is the line density of NO_2 emissions.
- ω_e [*NL^{-1}] is the exponential decay profile used to calculate the line density of NO_2 emissions.
- ω_g [*NL^{-1}] is the Gaussian spreading profile used to calculate the line density of NO_2 emissions.
- μ [L] is the position of the source relatively to the centre of a line density.
- $\mathcal{N}$ [*N] is the integrated number of particles in a plume.
- β [NL^{-1}] is the NO_2 observed background as column line density.
- e_0 [MT^{-1}] is the residual observed NO_x emissions in a zonal cross-section per longitude unit.
- $\mathcal{E}$ [*NT^{-1}] is the NO_x emissions (flow rate) of an asset.
- σ [L] is the horizontal spreading of emissions due to diffusion. When the Gaussian behaviour is fitted along the meridional and zonal axis, it is noted σ_x and σ_y respectively. When an integer is used as a subscript (0, 1 or 2), it refers to a source.
- R [1] is exclusively used for correlation coefficients within fits.
- X_e [L^{-1}] is the scaling factor.
- χ [1] is the empirical proportional factor to account for minor sinks when they are expected to behave like the OH sink.
- τ_{add} [T] is the empirical additional lifetime to account for minor sinks when they are proportional to the NO_2 tropospheric column.

Acronyms

Acronym	Meaning
ACP	Atmospheric Chemistry and Physics
AMF	Air Mass Factor
CAMS	Copernicus Atmosphere Monitoring Service
CAMS-GLOB-ANT	CAMS Global Anthropogenic emissions
CAMS-REG	CAMS Regional inventory
COVID-19	2019 Novel Coronavirus
CTM	Chemistry-Transport Model
DOAS	Differential Optical Absorption Spectroscopy
ECMWF	European Centre for Medium-Range Weather Forecasts
EDGAR	Emissions Database for Global Atmospheric Research
EGU	European Geosciences Union
EMG	Exponentially-Modified Gaussian
EMME	Eastern Mediterranean and Middle East
ERA5	Fifth generation ECMWF atmospheric reanalysis
ESA	European Space Agency
FAO	Food and Agriculture Organization
GOME	Global Ozone Monitoring Experiment
IEA	International Energy Agency
IPCC	Intergovernmental Panel on Climate Change
Kahramaa	Qatar General Electricity & Water Corporation (in arabic)
LSCE	Laboratoire des Sciences du Climat et de l'Environnement
LT	Local Time
NRT or NRTI	Near Real Time
OCO-2	Orbiting Carbon Observatory-2
OFFL	Offline
OMI	Ozone Monitoring Instrument
PAL	Product Algorithm Laboratory
PAN	Peroxy-Acetyl-Nitrate
PBL	Planetary Boundary Layer
PSA	Planning and Statistics Authority
RGB	Red-Green-Blue
S-5P	Sentinel-5P
SAC	Surface Albedo Climatology
SCD	Slant Column Density
SCIAMACHY	Scanning Imaging Absorption Spectrometer for Atmosphere Chartography
SWIR	Short-Wave Infrared
SZA	Solar Zenith Angle
TM5	Tracer Model 5
TROPOMI	Tropospheric Monitoring Instrument
UNFCCC	United Nations Framework Convention on Climate Change
UTC	Coordinated Universal Time
UV	Ultraviolet
VCD	Vertical Column Density
VIS	Visible
VOC	Volatile Organic Compounds
WRF-Chem	Weather Research and Forecasting model coupled to Chemistry

Table A.0: Acronyms and abbreviations used multiple times in the thesis.

Supplementary Materials

This section gathers all the supplementary materials of all the thesis, which include supplementary materials from different articles.

The NO_x-OH non-linear relationship: comparison between TROPOMI columns and CAMS OH concentrations

We compare seasonal values of TROPOMI VCDs and mean OH concentrations estimated by the CAMS NRT product for the EMME region. The objective is to identify qualitatively how the CAMS NRT data represent the OH concentration during the TROPOMI overpass. Two effects need to be taken into account. The first is the sunlight-induced seasonal cycle of OH, i.e. the increase of mean OH concentration with photochemical activity, giving higher budgets in winter than in summer in the northern hemisphere. The second is the non-linear relationship between NO_x and OH, which results in an increase in OH with the average tropospheric NO_2 content up to a limit concentration beyond which the quantity of OH decreases as the NO_2 concentration increases. To identify this effect, Figure A.1 shows the TROPOMI mean NO_2 columns for the four seasons of 2022 (winter: DJF; spring: MAM; summer: JJA; autumn: SON). The color scale from Valin et al. (2011) for NO_2 VCDs is used, with background levels below $\sim 1\times10^{15}$ molecules.cm^{-2}, intermediate pollution levels between $\sim$ 1 and $\sim 5\times10^{15}$ molecules.cm^{-2}, and high pollution levels above $\sim 5\times10^{15}$ molecules.cm^{-2}. In comparison, the PBL-averaged OH concentration for the same seasons is displayed for the CAMS product on Figure A.2.

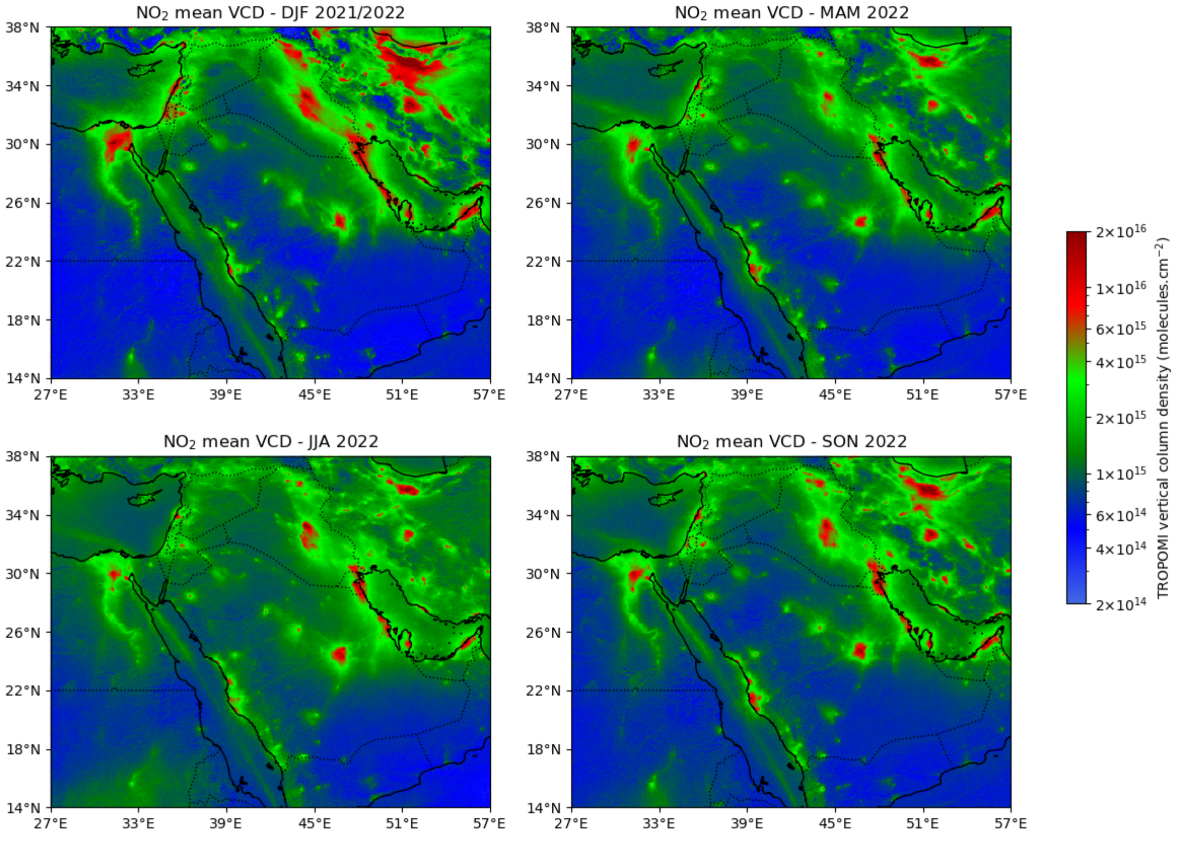

Figure A.1: Seasonal maps of tropospheric vertical NO_2 column densities from TROPOMI above the EMME region on a 0.0625°×0.0625° grid. The logarithmic scale and the choice of colors (blue: low pollution; green: intermediate pollution; red: high pollution) refer to Figures 2.8 and 2.9 from Valin et al. (2011) to illustrate the three different regimes in the NO_x-OH non-linear relationship.

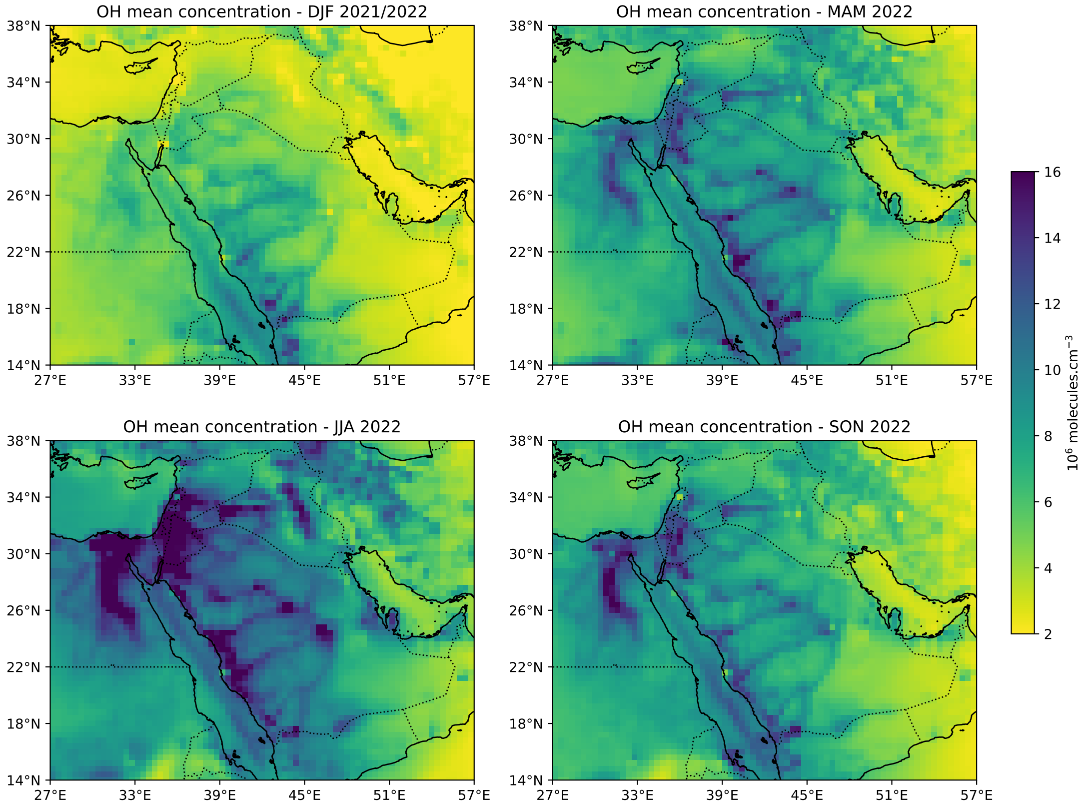

Figure A.2: Seasonal maps of PBL-averaged OH concentrations from CAMS NRT data estimated at 12:00 UTC above the EMME region with a 0.4°×0.4° horizontal resolution.

The seasonal effect is clearly identified on the maps in both figures. Figure A.1 shows higher NO_2 levels in winter, due to lower oxidation of NO_2 by the OH radical. This is concomitant with the lower concentrations of OH during this season on Figure A.2. Conversely, OH concentrations are higher in summer. The effect of the non-linear relationship between NO_x and OH can also be identified: large emitters such as megacities, clearly identified on Figure A.1, display relatively low OH concentrations on Figure A.2 compared to intermediate-pollution areas. Regardless of the mean seasonal OH background value, areas that exhibit the highest OH levels are these areas with intermediate pollution levels, such as smaller cities, highways and shipping routes.

It should be noted that this analysis is qualitative and only seeks to illustrate trends. It does not question the high uncertainties of the OH product, which may lead to errors in the representation of the seasonal cycle of OH and its non-linear relationship with NO_x. Furthermore, since seasonal averages are displayed, the representation of this relationship is not addressed for smaller spatial scales, particularly for NO_2 plumes, where the coarse resolution of CAMS can prevent the observation of a downwind OH pattern.

Estimation NO_x emissions of oil-fired power plants (PP9 and PP10) in Riyadh

In Section 2.1.5, we have displayed the average emissions for the city of Riyadh and its outskirts. Figure 2.7 shows high emissions from two oil-fired power stations located in the north-east and south-east of the country. In Figure A.3, we display the meridional cross-section of obtained emissions in a 28-km band centered around the mean longitude of the plants, for each month of the 2019-2022 period. Mean emissions for the four constitutive years are also displayed. Finally, because the observed emissions display a Gaussian distribution around the power plants, we estimate the mean NO_x emissions of the power plants by fitting a double Gaussian curve $\mathcal{G}(\varphi) = e_0 + \frac{\mathcal{E}_1}{\sigma_1\sqrt{2\pi}}\exp(-\frac{(\varphi-\varphi_1)^2}{2\sigma_1^2}) + \frac{\mathcal{E}_2}{\sigma_2\sqrt{2\pi}}\exp(-\frac{(\varphi-\varphi_2)^2}{2\sigma_2^2})$ on the mean profile for the 4-year period, with e_0 being the residual observed emissions, φ_1 and φ_2 the latitude of the power plants, σ_1 and σ_2 their standard deviations (measured as an angle) and $\mathcal{E}_1$ and $\mathcal{E}_2$ their total emissions. Indices 1 and 2 refer to the north-east (PP9) and south-east (PP10) power plants respectively. φ is the meridional angle.

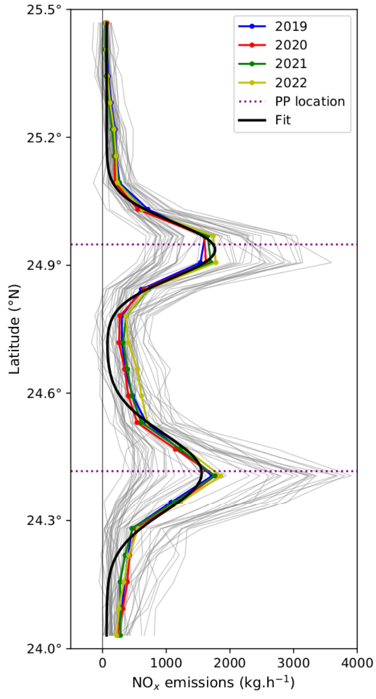

Figure A.3: Estimation of the NO_x emissions of the two fuel-fired power plants in the east of Riyadh using averaged meridional cross-section profiles from 2019 to 2022. The latitude of the two power plants is given with dotted lines and the Gaussian fit is provided with a solid black line.

The best approximation for the average profile is calculated. The inferred Gaussian spreading is slightly larger for the south-east power plant, with $\sigma_1 = 0.057°$ and $\sigma_1 = 0.075°$ (i.e. 6.3 and 8.3 km respectively). The inferred flow rates are $\mathcal{E}_1 = 3.80$ t.h^{-1} and $\mathcal{E}_1 = 4.40$ t.h^{-1}. These emissions corresponds approximately to the values reported by Beirle et al. (2023), who estimated outputs of 3.72 t.h^{-1} and 4.22 t.h^{-1} respectively, despite various differences in the parametrisation of the method. Note that these values correspond approximately to the emissions per unit area already inferred in Section 3.1.6-B, but with an anterior version of the method.

Annual differences in horizontal distribution of NO_x emissions in Qatar

The TROPOMI data used for NO_x emissions estimates were not all taken from the same version. Up to October 2021 included, we use the reprocessed S5P-PAL data (Eskes et al., 2021). This reprocessing provides a single consistent Sentinel-5P (S5P) TROPOMI NO_2 product (processed with same processor – version 2.3.1). The dataset has been generated to allow consistent data analysis (e.g. trends in COVID-19 impact on air pollution) over the period 01/05/2018-14/11/2021. For the remaining period (from November 2021 to December 2022), we use the offline stream (OFFL), with processor versions 2.3.1 from November 2021 to October 2022 included, and 2.4.0 from November 2022. As a result, the emissions displayed in Figure 3.15 use heterogeneous TROPOMI data. To observe the impact of these version changes on the spatial distribution of emissions, the emissions of the four years concerned are displayed in Figure A.4. The main difference that is observed is in the transport term, which is lower in absolute value in 2022 in the main emitting areas. The "dipole" shape that is obtained around the main emitters, i.e. Dammam (Saudi Arabia), Manama (Bahrain), Doha (Qatar), Ras Laffan (Qatar) and the south-east of Qatar is less pronounced in 2022, without being compensated by a lower sink term. As a result, maps for 2019 to 2021 show small areas with slightly negative emissions. The study of the influence of the quality limit factor q_a aims to provide an explanation for these differences.

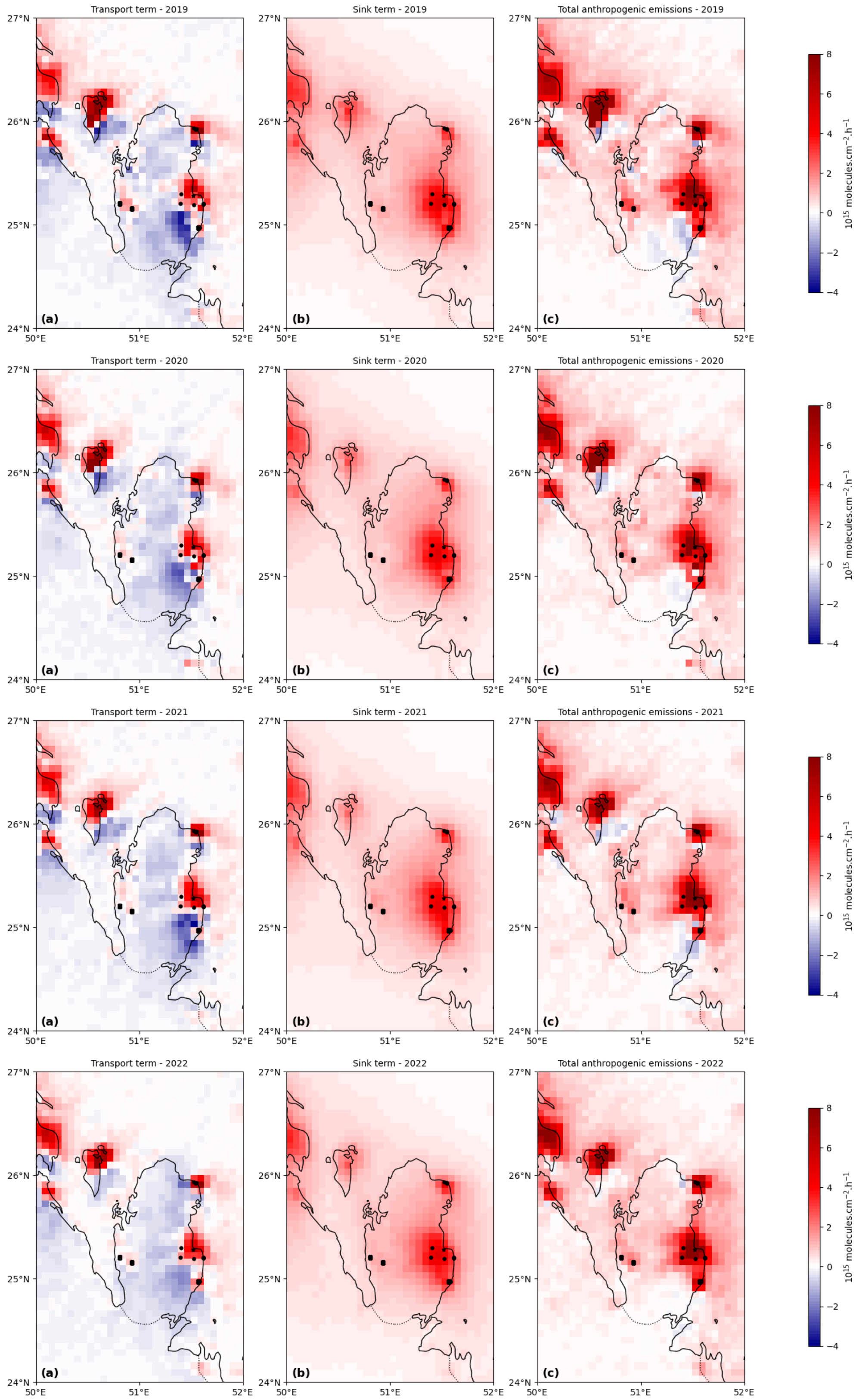

Figure A.4: Mean NO_x emissions above Qatar (13:30 LT): transport term (a), sink term (b), and resulting emissions (c) for years 2019 to 2022 (top to bottom). Power plants are denoted with dots, cement plants with squares, and Doha with a star.

Wind threshold for image filtering in Qatar

Pollution from Bahrain, which is usually transported to Qatar, can reach Doha during strong wind events. In such situations, the errors in ERA5 can alter the estimation of the transport term and thus the NO_x estimates. In our monthly and annual estimates of NO_x emissions, we remove days with high wind speeds in the Bahrain/Qatar direction, i.e. days for which the average wind over Bahrain and the marine area between the two countries has a speed higher than 30 km.h^{-1} and an angle between -15° (E$\frac{1}{4}$SE) and -75° (S$\frac{1}{4}$SE). These thresholds have been chosen as a threshold because it corresponds to the minimal value for the wind module to reach the closest high emitters of Qatar. Manama and the cement plants in the east (angle $\sim$ -75°) are separated by $\sim$ 110 km. Manama and the Ras Laffan power plants (angle $\sim$ -15°) are separated by $\sim$ 105 km. With an mean annual lifetime of 3.5 hours (calculated according to Equation 2), the value of 30 km.h^{-1} corresponds to the minimal wind speed that would allow NO_2 pollution from Bahrain to overlap emissions in Qatar. This threshold value would be increased if mean lifetimes values for spring, summer and fall seasons (3.1 h, 2.1 h and 3.2 h respectively for years 2019-2022) were used. However, higher lifetime values during winter (5.2 h, DJF value for 2019-2022), would lower the threshold the $\sim$ 21 km.h^{-1}.

Using lower values for the wind speed threshold at 25 and 20 km.h^{-1}, we observed that discarded days are increased from 169 to 240 and 309 respectively. About half of the additional discarded days correspond to days between December and March included, for which 4.25 additional days are discarded on average. Lowering the threshold generally leads to a decrease in emissions. On average, this does not impact the value of main emissions: with a threshold of 20 km.h^{-1}, emissions are lowered by about -2.6% for 2019-2022. The decrease is about -6.0% on average for months between December and March included. Months for which the absolute change is higher than 10% are January 2019 (-10.7%, 3 additional discarded days), December 2019 (-20.1%, 7 additional discarded days), February 2021 (-14.2%, 7 additional discarded days) and December 2022 (-10.7%, 3 additional discarded days). These large diminutions are mostly due to the fact that the additional discarded days included moments for which pixels above the cement plants and Doha were visible, increasing thus the number of pixels which are never observed during a month.

Influence of quality assurance value threshold in Qatar

The quality assurance value q_a is related to the presence of clouds and aerosols. Within each pixel, it ranges from 0 (no data) to 1 (high-quality data), and it is recommended to use data with $q_a > 0.75$ for remote sensing analysis. Within the study area, seven areas, including four in Qatar, have particularly low values for this flag. As these areas include several hotspots in the region, the correct estimation of the corresponding daily emissions is prevented, which lowers the robustness of monthly and yearly averages. Table A.5 which is analogous to Figure 3.16, displays, for different periods, the frequency with which each pixel has its insurance quality value exceeding the threshold of $q_{a,\text{lim}} = 0.75$, compared to a threshold of $q_{a,\text{lim}} = 0.70$. For this lower threshold, columns are kept for all the domain most of the time (with a fraction of observed days higher than 80% for all pixels). Here, if the S5P-PAL reprocessed data (version 2.3.1) from January 2019 to November 2021 displays pixels for which the value of q_a frequently falls below 0.75, the use of the OFFL stream (version 2.3.1) from November 2021 to November 2022 is characterised by pixels for which the value of q_a falls below 0.75 less frequently. Furthemore, the last two months of 2022, calculated with the version 2.4.0 of the TROPOMI product (operational since July 2022), do not show any areas with particularly low quality flag values. The latest version of the user manual indicates that in this version, OMI and GOME-2 derived surface albedo climatologies in the NO_2 fitting window were replaced by a surface albedo climatology derived from TROPOMI observations. This new TROPOMI surface is consistently applied in the cloud fraction, the cloud pressure retrievals, and in the air-mass factor calculation. This seems to indicate that the low values for q_a for the older versions originated from the previous algorithms used to calculated parameters involved in the calculation of q_a.

Period	**Data version**	**$q_{a,lim}$ = 0.75**	**$q_{a,lim}$ = 0.70**
2019	2.3.1 with S5P-PAL reprocessing	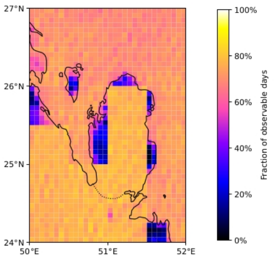	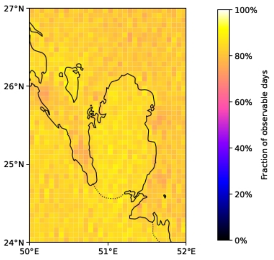
2020	2.3.1 with S5P-PAL reprocessing	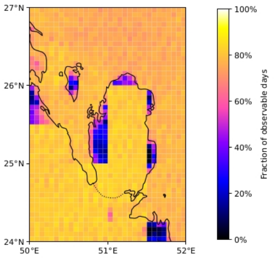	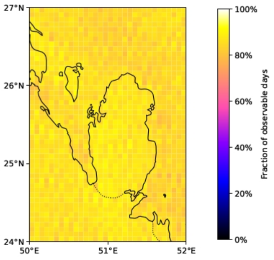
2021	2.3.1 with S5P-PAL reprocessing from Jan. 2021 to Oct. 2021 included	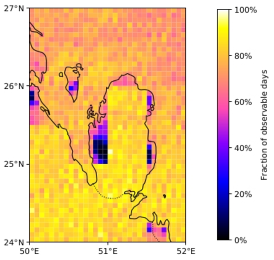	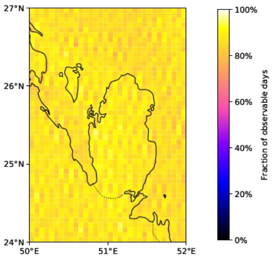
2021/11-2021/12	2.3.1	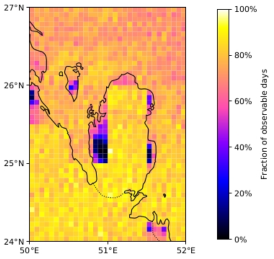	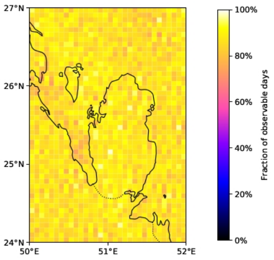
2022	2.3.1 from Jan. 2022 to Oct. 2022 included and 2.4.0 from Nov. 2021 to Dec. 2022 included.	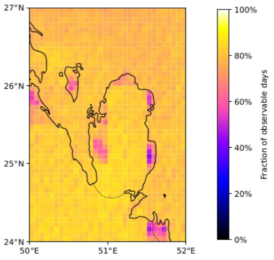	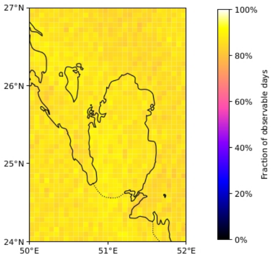
2022/11-2022/12	2.4.0	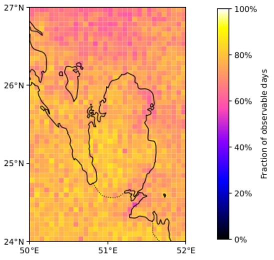	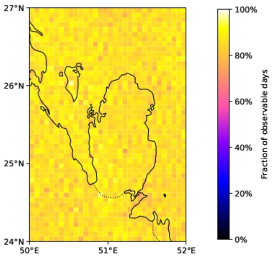

Figure A.5: Comparison between TROPOMI observation densities for different periods between 2019 and 2022 with a quality threshold of $q_{a,\mathrm{lim}} = 0.75$ (left) and $q_{a,\mathrm{lim}} = 0.70$ (right). The corresponding TROPOMI version is indicated for each period.

Figure A.6 shows the annual NO_x emissions at 13:30 LT over Qatar using a quality insurance threshold of $q_{a,\mathrm{lim}} = 0.75$ for years 2019, 2020, 2021 and 2022, while Figure A.7 shows the corresponding emissions with a threshold of $q_{a,\mathrm{lim}} = 0.70$. The comparison between the two figures highlights differences in emissions where high frequencies of pixels with $q_{a,\mathrm{lim}} < 0.75$ were encounted. Because this phenomenon is less marked for 2022, the corresponding maps are very similar, while maps for years 2019, 2020 and 2021 show pixels with lower emissions above several hotspots when the threshold is set to 0.75. In particular, the pixels between the urban area of Doha and the south-eastern part of the country show negative or zero emissions on Figure A.6 but not on Figure A.7.

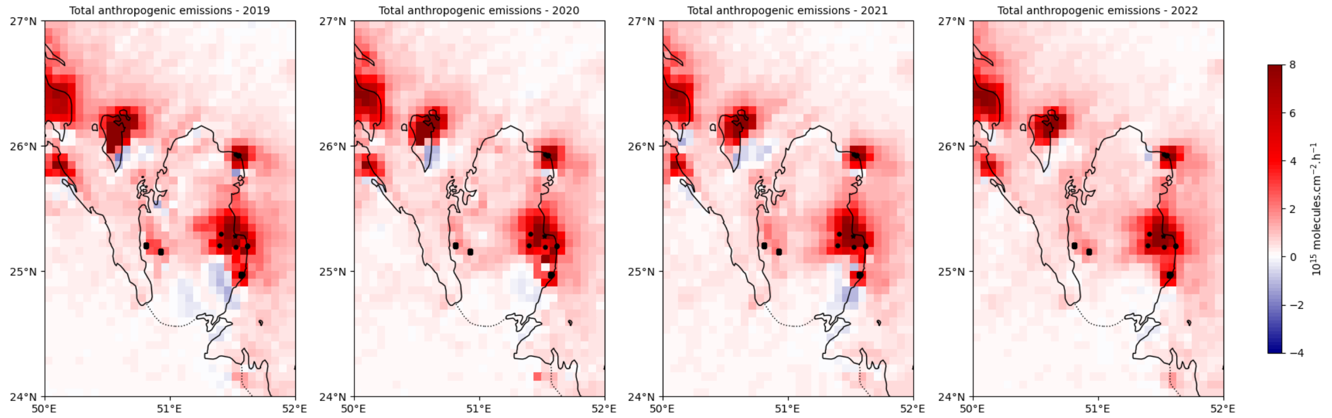

Figure A.6: Annual mean emissions at 13:30 for years 2019 to 2022 (left to right) with quality flag threshold equal to $q_{a,\mathrm{lim}} = 0.75$.

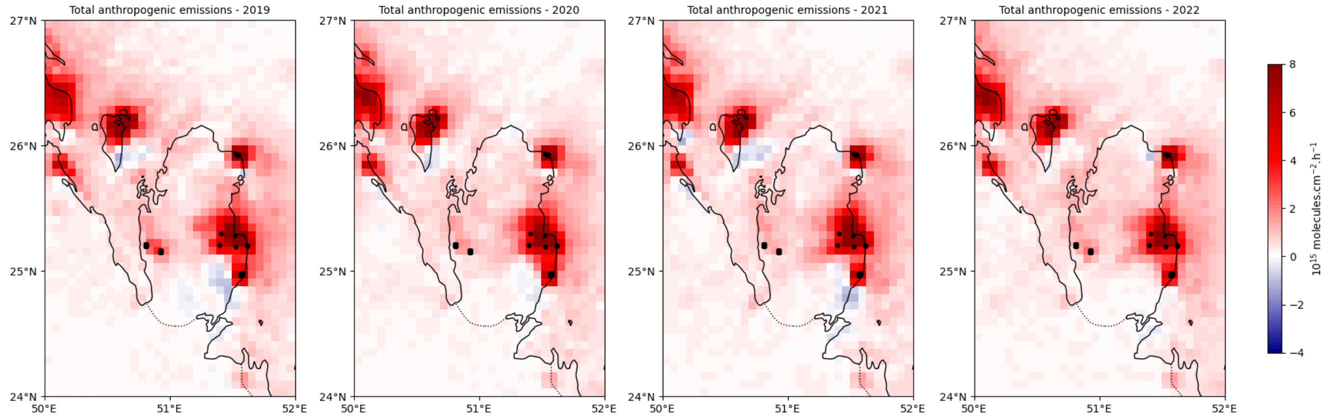

Figure A.7: Annual mean emissions at 13:30 for years 2019 to 2022 (left to right) with quality flag threshold equal to $q_{a,\mathrm{lim}} = 0.70$.

The proper use of quality flags and uncertainty information is critical for an accurate use of the S5P data. Taking all NO_2 retrievals with a q_a value larger than 0.7 add the good quality retrievals over clouds or aerosol layers, which are not sensitive to the NO_2 concentrations near the ground. They still contain useful information, but this should be carefully interpreted. Standard analyses that do not take this into account will provide flawed results. Results shown on Figure S2 and S3 are not intended to replace the results calculated with a threshold of 0.75, as these mix data of different nature.

Weekly cycle for NO_x emissions, NO_2 tropospheric column densities and OH concentration above urban and industrial areas in Qatar

The weekly cycle for NO_x emissions displayed on Figure 8 can be analysed with respect to the different parameters involved in the calculation of emissions. Figure A.8 displays the weekly cycle of

NO_2 VCDs, OH concentrations and NO_x emissions over the whole country (internal mask), the Ras Laffan power plants (using the six pixels that are the closest to the power plants) and the urban area of Doha (urban pixels of the metropolitan area according to the SEDAC-GRUMP dataset) for the 2019-2022 period (at around 13:30 LT). The 4-year average is calculated without accounting for values lower than the 5th percentile or higher than the 95th percentile of the ensemble (as explained in Section 3.2.7-D), and the re-scaling of the emissions using the load curve is not performed.

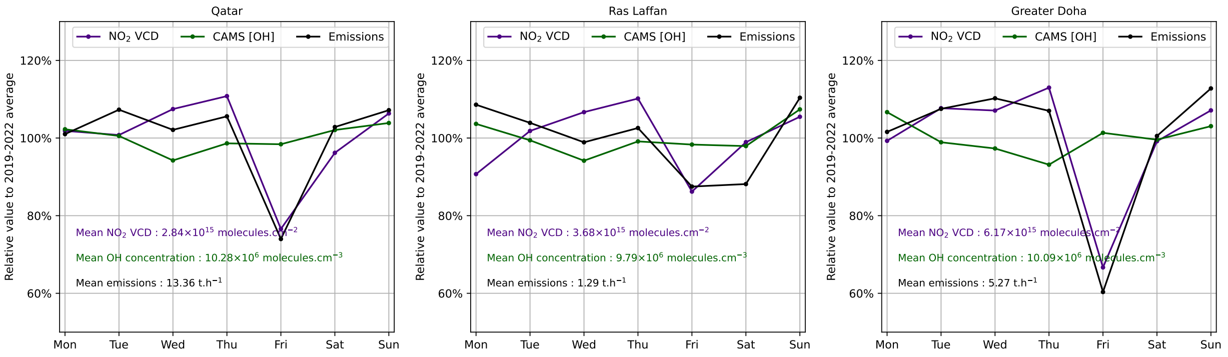

Figure A.8: Mean weekly profiles for NO_2 tropospheric vertical columns, OH concentration and NO_x emissions for the entire country (left), the Ras Laffan power plants in the north (middle), and the Greater Doha area (right). The 2019-2022 average is given and represented by the 100% line.

OH concentrations do not vary much within the week: the observed trend in NO_x emissions is thus mainly driven by changes in tropospheric columns. Moreover, the observed "week-end effect" observed for the country is stronger over Greater Doha, and weaker over the Ras Laffan power plants. It can therefore be assumed that this effect is mainly due to a reduction of transport emissions on Fridays.

Power demand ratio and rescaling of emissions in Qatar

We use power demand time series in Qatar to re-sacle the emissions inferred by our method at 13:30 to obtain mean monthly emissions in Qatar. The power demand dataset has been obtain by Bayram et al. (2018) using C-Sharp by visiting the webpage of the Gulf Cooperation Council Interconnection Authority (GCCIA) and searching for keywords related to demand data. The website publishes data for five Gulf states. The dataset covers the twelve-month period from February 2016 to January 2017 with a one-minute resolution. Data published on the GCCIA website is expected to be accurate. Here, although electricity consumption has increased in Qatar between 2016 and 2019-2022, we assume that this growth has been uniform across days and months. Under these conditions, the ratio between the electricity demand at 13:30 local time and the average electricity demand remains unchanged. The corresponding values for each month are given on Table A.1.

Month	**Ratio** $P_{\mathbf{13:30}}/\langle P\rangle$
January	0.967
February	0.976
March	0.965
April	0.932
May	0.914
June	0.911
July	0.918
August	0.922
September	0.921
October	0.924
November	0.944
December	0.960

Table A.1: Ratio between mean daily power demand and power demand at 13:30 LT, averaged for each month between February 2016 and January 2017 and expected to be valid from 2019 to 2022.

Sectoral comparison with inventories in Qatar

The two inventories that are studied here (EDGARv6.1 for year 2018 and CAMS-GLOB-ANT_v5.3 for years 2019 to 2022) provide gridded maps with a 0.1°×0.1° resolution. In Qatar, most NO_x emissions are concentrated winthin three sectors:

- energy (power industry, IPCC 1A1a)
- transport (shipping, aviation, and road transportation, IPCC 1A3a_CDS + 1A3a_LTO + 1A3d + 1C2 + 1A3a_CRS + 1A3b_noRES)
- industry (oil refineries and transformation industry, combustion for manufacturing, chemical processes, IPCC 2B + 1A2 + 1A1b + 1A1c + 1A5b1 + 1B1b + 1B2a5 + 1B2a6 + 1B2b5 + 2C1b)

Other sectors (agricultural soils, manure management, energy for buildings, fuel exploitation, solid waste incineration, agricultural waste burning, IPCC 4C + 4D + 4B + 1B1a + 1B2a1 + 1B2a2 + 1B2a3 + 1B2a4 + 1B2c + 4F + 1A4 + 6C) only represent a small part of the total NO_x budget. The output for each sector is represented on Figure A.9 for EDGARv6.1 and on Figure A.10 for CAMS-GLOB-ANT_v5.3. Because the resolution is different than what is used in our TROPOMI-inferred estimates of NO_x emissions (0.0625°×0.0625°), we use a 0.1°×0.1° mask which has a similar shape as the internal mask displayed on Figure 3.12. Although the seasonality and amplitude of emissions from the inventories differ from the emissions estimated by our model, their spatial distribution is similar.

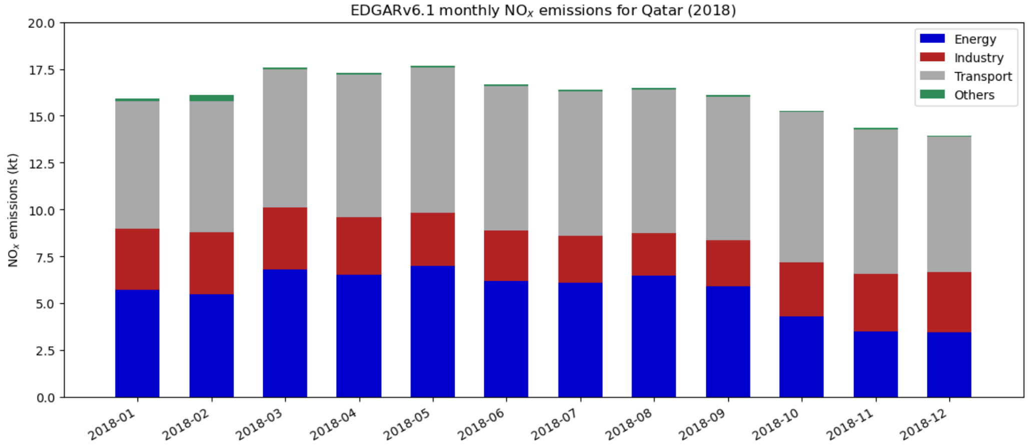

Figure A.9: Monthly terrestrial NO_x emissions in Qatar for year 2018 in EDGARv6.1 by sector

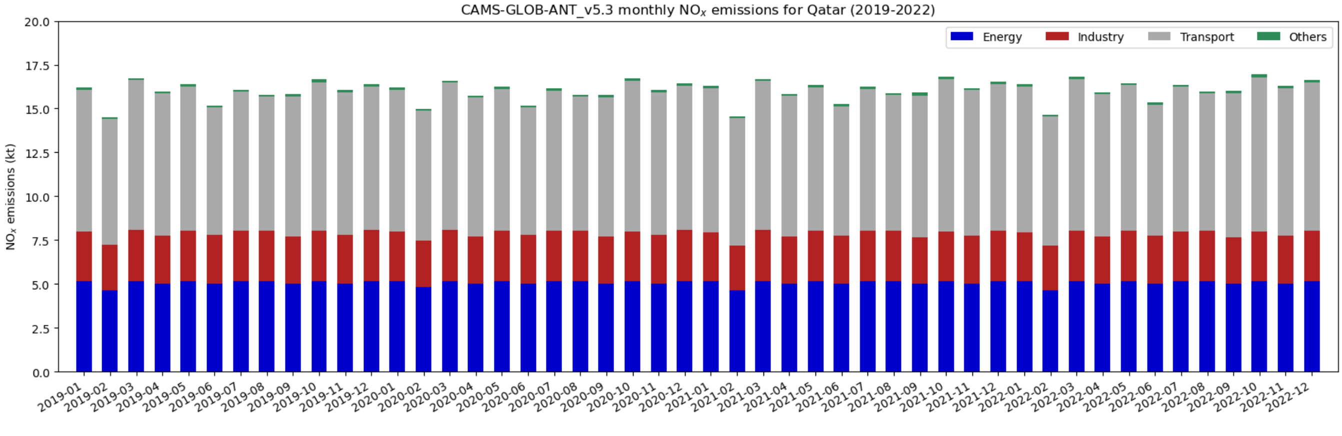

Figure A.10: Monthly terrestrial NO_x emissions in Qatar for years 2019 to 2022 in CAMS-GLOB-ANT_v5.3 by sector.

Power emissions are located in Doha, the south-east of Doha and in the Ras Laffan area. The industrial sites are mainly located in Doha, and we note the presence of an emissive pixel in the west of the country which could correspond to the cement plants previously identified. The transport emissions spreads from Doha to the peripheral areas (north, west and south-west). Figure A.11 displays the map of NO_x emissions for those three sectors for EDGARv6.1. The corresponding map for CAMS-GLOBANT_v5.3 is very similar.

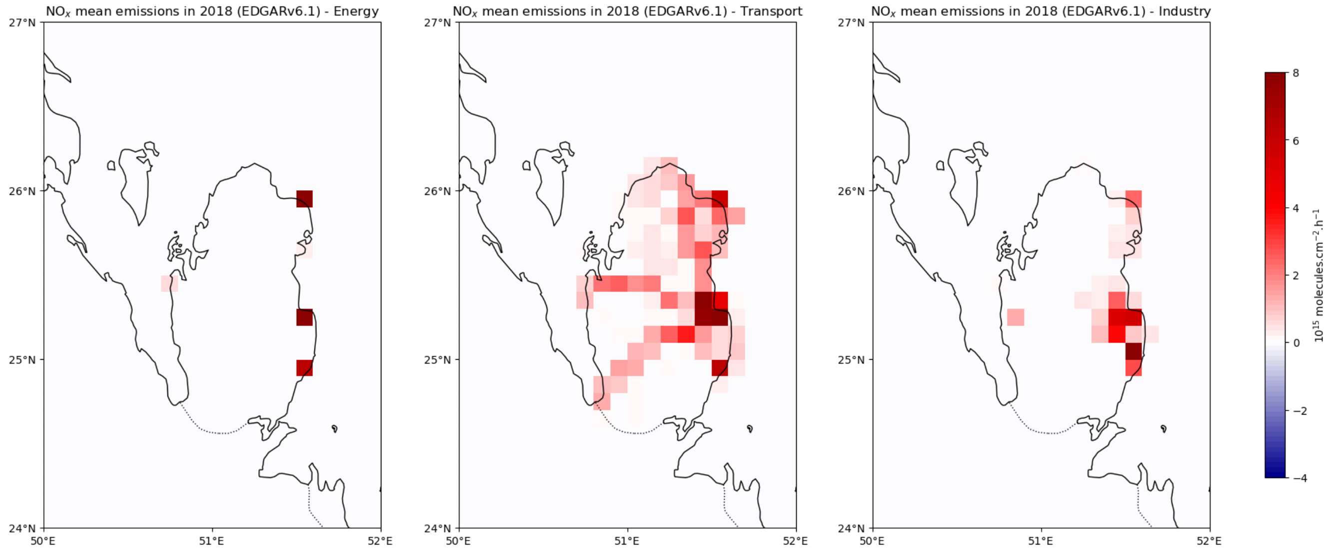

Figure A.11: Map of annual NO_x emissions in Qatar for years for EDGARv6.1 within the internal mask for the power (left), transport (middle) and industry (right) sectors.

Impact of differences between derivative schemes on the calculation of the transport term

The impact of using different derivative calculation schemes is illustrated by the case of two cement plants in Sinai in Figure A.13. In the immediate vicinity of the emitter, pixels close to the emitter have slightly higher absolute values when the fourth-order scheme is used. The mean relative difference for the closest pixels to the emitter is approximately 20%, with an absolute value larger for the fourth-order scheme, as illustrated by the right panel. This relative value is also calculated for other emitters, and when averaging the transport term over longer periods of time.

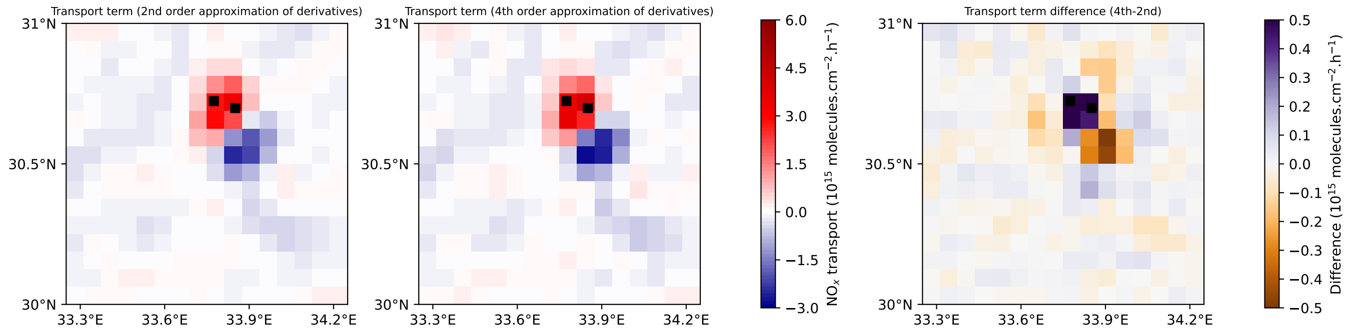

Figure A.13: Transport term for the NO_x emissions estimated for two cement plants in the Sinai region on September 10th 2019 with derivatives calculated with a second-order central-finite difference order approximation (left), a fourth-order central-finite difference order approximation (middle), and the corresponding difference (right). The location of the cement plants are denoted with squares.

Study of the overlapping of emissions on a streamline

Using a construction similar to that of the theoretical graphs in Figure 2.4, two identical emitters are placed along a streamline, and the 1D flux-divergence method is applied to visualise the superposition of emissions. Two parameters are modified: the observed spreading of the emissions for each source and the distance between them. The results are shown in Figure A.12.

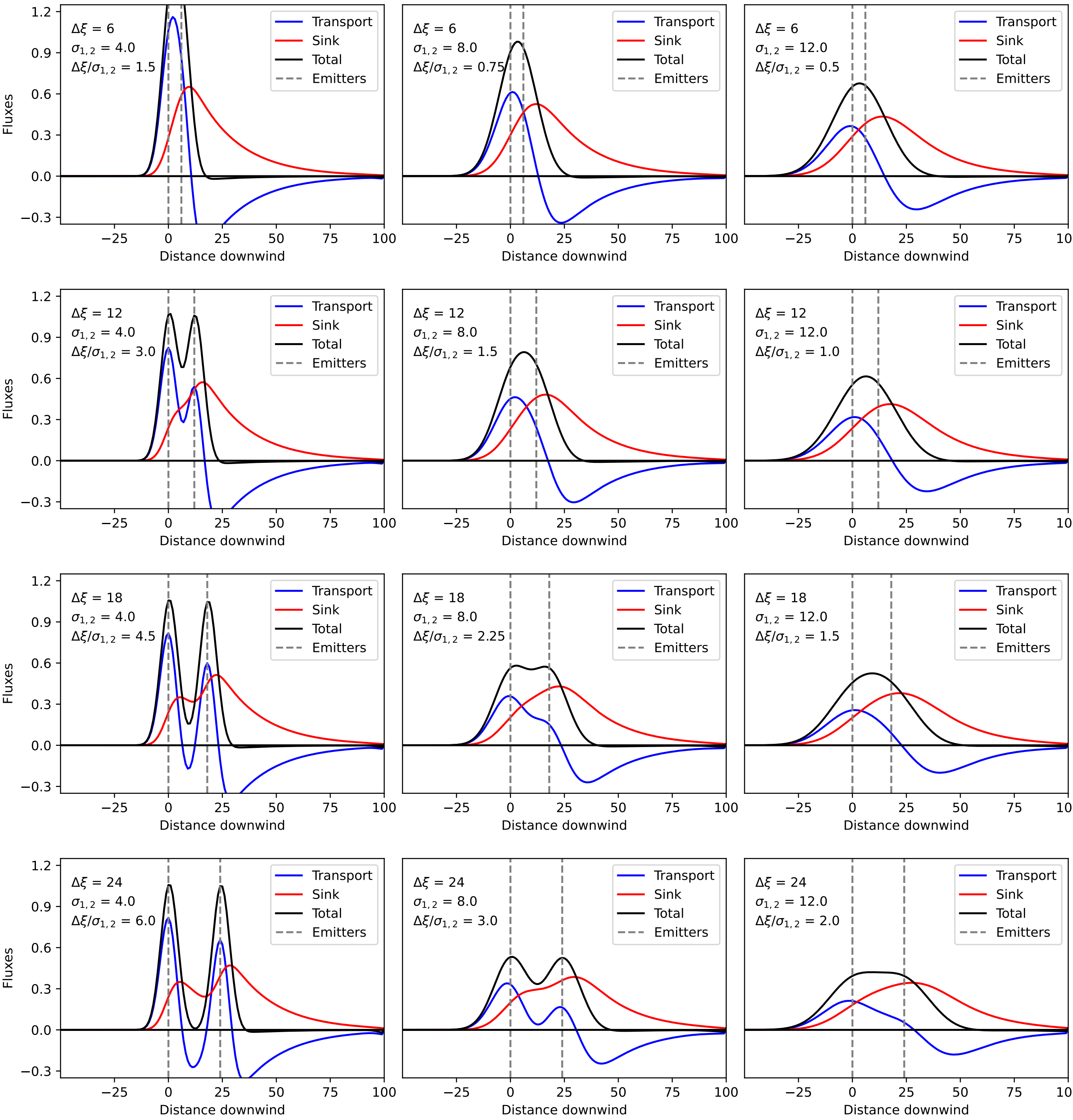

Figure A.12: Dimensionless theoretical illustration of the estimation of emissions from two overlapping sources. The transport and sink terms, as well as total emissions, are calculated along a streamline. With unchanged emissions, both emitters emit over a restricted area (left, characterisation of industrial facilities), an area of intermediate extent (centre), and a large area (right, characterisation of megacities). Lifetime and wind module are unchanged in all three cases. From top to bottom, the distance between emitters increases. All cases are denoted with corresponding distance between emitters $\Delta\xi$, emissions extent $\sigma_{1,2}$ and ratio $\Delta\xi/\sigma_{1,2}$.

In theory, the distance $\Delta\xi$ between the two sources (assuming they have identical emissions) must be greater than twice the Gaussian standard deviation $\sigma_{1,2}$ to be able to distinguish two emission peaks (existence of two local maxima). In practice, for the difference between the local maxima and a local minimum between the two emitters to be visible, it is necessary to go beyond the criterion $\Delta\xi > 2\sigma_{1,2}$. Note here that $\sigma_{1,2}$ represents the observed spread of the emissions. In a 2D frame, the gridded emissions show a visible spread greater than the real spread due to the resolution used. This spread generally corresponds to a radius of 2 pixels in the gridded maps used (0.0625°×0.0625°), i.e. between 12 and 14 km in the EMME region. Therefore, it can be anticipated that when two sources are located on the same streamline, calculating their emissions using the flux-divergence method will not distinguish between the two emission centres if the sources are more than 30 km apart. As a consequence, the flux-divergence method will treat the two sources as a single emitter, with a higher Gaussian standard deviation.

Low levels of inferred NO_x emissions in the Read Sea and the Jeddah-Riyadh highway

Emissions calculated using the flux-divergence method for traffic and shipping sectors are, in terms of emissions per unit area, at very low levels compared with those in urban centres and industrial areas. Using the example of the highway between Jeddah and Riyadh and the Red Sea road in Section 3.5.1, we calculate the emissions per unit length for the months of March and April for the years 2019, 2020 and 2021. We also calculate the emissions that would be obtained by replacing, for each point on the road, the estimated emissions by the residual emissions. These are defined as the 10th and 90th percentiles of the pixels obtained within an 80 km radius of the point under consideration. The results are presented in Figure A.14 using a logarithmic scale.

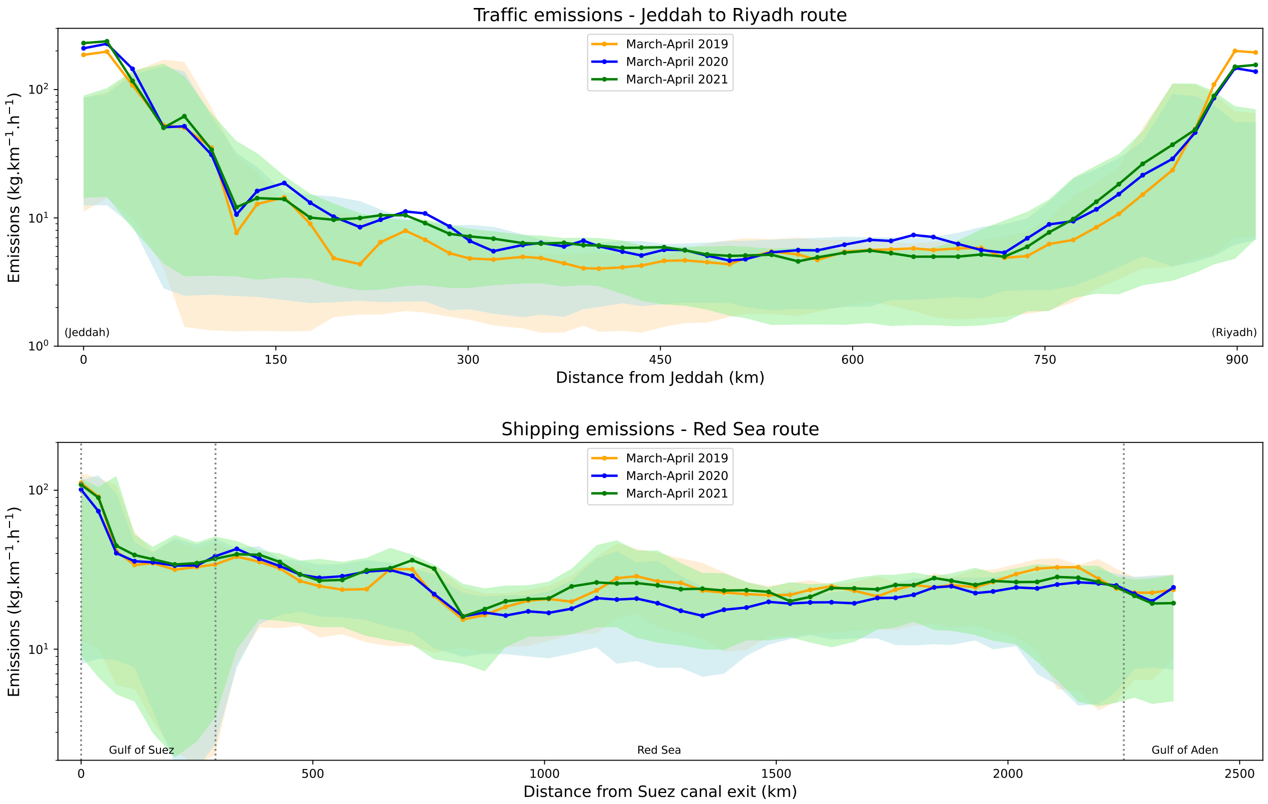

Figure A.14: NO_x emissions for traffic along the terrestrial route from Jeddah to Riyadh (top) and for shipping along the maritime route from the Suez Canal to the Gulf of Aden (bottom) for the March-April period in 2019, 2020 and 2021. To represent the level of residual emissions, the 10th and 90th percentiles of the emissions within a 80 km radius are represented with a shaded area for each point of the route (these points are represented on Figure 3.32).

The quantification of these residual emissions shows the low level of the signal from the traffic and shipping sectors. Thus, although the corresponding emissions are clearly identifiable, it is difficult to interpret the differences observed between the three periods shown. In particular, the lower value of emissions on the Jeddah-Riyadh highway in 2019 (compared with 2020 and 2021), or on the Red Sea shipping route in 2020 (compared with 2019 and 2021), may simply be a noise effect due to the inclusion of residual emissions. This observation questions the calculation of the upper tropospheric background, arbitrarily estimated as a percentile of NO_2 VCDs within a given domain, as explained in Section . The level of residual emissions relies heavily on the calculation of this background.

Demonstations

Expression of the EMG function

In Section 2.1.5, the exponentially modified Gaussian function is introduced. Indeed, the function expressing the Gaussian spreading of the emissions in absence of wind is the following:

$$\omega_g(\xi) = \frac{1}{\sqrt{2\pi}\sigma} \exp{(-\frac{(\xi-\mu)^2}{2\sigma^2})}$$

Here μ is the Gaussian centre and σ is the standard deviation of the distribution. Conversely, the function expressing the concentration decay along the wind is the following:

$$\omega_e(\xi) = \begin{cases} \exp{(-\frac{\xi}{\xi_0})}, & \text{if } \xi > 0 \text{ (downwind).} \\ 0, & \text{if } \xi < 0 \text{ (upwind).} \end{cases}$$

Here ξ is the e-folding distance of the decay. We define $\Lambda = 1/\xi_0$ and $\omega_d = \Lambda\omega_e$. In this case:

$$\omega_d(\xi) = \begin{cases} \Lambda \exp{(-\Lambda\xi)}, & \text{if } \xi > 0 \text{ (downwind).} \\ 0, & \text{if } \xi < 0 \text{ (upwind).} \end{cases}$$

Let one calculate the convolution $h = \omega_g * \omega_d$ between functions ω_g and ω_d:

$$\begin{aligned} h(\xi) &= \int_{-\infty}^{+\infty} \omega_g(\xi')\omega_d(\xi-\xi')\mathrm{d}\xi' \\ &= \frac{\Lambda}{\sqrt{2\pi}\sigma} \int_{-\infty}^{\xi} \exp{(-\frac{(\xi'-\mu)^2}{2\sigma^2} - \Lambda(\xi-\xi')\mathrm{d}\xi'} \\ &= \frac{\Lambda}{\sqrt{2\pi}\sigma} \int_{-\infty}^{\xi} \exp{(-\frac{\xi'^2 - 2\mu\xi' + \mu^2 + 2\sigma^2\Lambda\xi - 2\sigma^2\Lambda\xi'}{2\sigma^2})}\mathrm{d}\xi' \\ &= \frac{\Lambda}{\sqrt{2\pi}\sigma} \int_{-\infty}^{\xi} \exp{(-\frac{\xi'^2 - 2(\mu+\sigma^2\Lambda)\xi' + (\mu^2 + 2\mu\sigma^2\Lambda + \sigma^4\Lambda^2) - 2\mu\sigma^2\Lambda - \sigma^4\Lambda^2 + 2\sigma^2\Lambda\xi}{2\sigma^2})}\mathrm{d}\xi' \\ &= \Lambda e^{\frac{\Lambda}{2}(-2\xi+2\mu+\sigma^2\Lambda)} \int_{-\infty}^{\xi} \frac{1}{\sqrt{2\pi}\sigma} \exp{(-\frac{(\xi'-(\mu+\sigma^2\Lambda))^2}{2\sigma^2})}\mathrm{d}\xi' \end{aligned}$$

By changing the variable $\xi'' \leftarrow \frac{\xi'-(\mu+\sigma^2\Lambda)}{\sqrt{2}\sigma}$, the remaining integral is equal to:

$$\int_{-\infty}^{\xi} \frac{1}{\sqrt{2\pi}\sigma} \exp{(-\frac{(\xi'-(\mu+\sigma^2\Lambda))^2}{2\sigma^2})}\mathrm{d}\xi' = \frac{1}{\sqrt{\pi}} \int_{-\infty}^{\frac{\xi-\mu-\sigma^2\Lambda}{\sqrt{2}\sigma}} \exp{(-\xi''^2)}\mathrm{d}\xi''$$

The function $\xi'' \rightarrow \exp{(-\xi''^2)}$ is even so the boundaries of its integral can be changed to their opposites. One thus has:

$$h(\xi) = \frac{\Lambda}{2}\, e^{\frac{\Lambda}{2}(-2\xi+2\mu+\sigma^2\Lambda)}\, \frac{2}{\sqrt{\pi}} \int_{\frac{-\xi+\mu+\sigma^2\Lambda}{\sqrt{2}\sigma}}^{+\infty} \exp{(-\xi''^2)}\mathrm{d}\xi''$$

The erfc function appears:

$$h(\xi) = \frac{\Lambda}{2}\, e^{\frac{\Lambda}{2}(-2\xi+2\mu+\sigma^2\Lambda)}\mathrm{erfc}(\frac{\mu+\lambda\sigma^2-\xi}{\sqrt{2}\sigma})$$

Using back the notation with ξ_0 instead of Λ, the special case $\mu = 0$ is written as:

$$h(\xi) = \frac{1}{2\xi_0}\ \exp\left(-\frac{\xi}{\xi_0} + \frac{\sigma^2}{2\xi_0^2}\right)\mathrm{erfc}\left(-\frac{1}{\sqrt{2}}\left(\frac{\xi}{\sigma} - \frac{\sigma}{\xi_0}\right)\right)$$

This function is normalised. The profile must be multiplied by the total quantity $\mathcal{N}$ of NO_2 and the observed background β, leading to the line density ω:

$$\omega(\xi) = \beta + \mathcal{N}h(\xi)$$

By noting $f_0 = \frac{\mathcal{N}}{\xi_0}$, one thus has:

$$\omega(\xi) = \beta + \frac{f_0}{2}\ \exp\left(-\frac{\xi}{\xi_0} + \frac{\sigma^2}{2\xi_0^2}\right)\mathrm{erfc}\left(-\frac{1}{\sqrt{2}}\left(\frac{\xi}{\sigma} - \frac{\sigma}{\xi_0}\right)\right)$$

Condition for overlapping of emissions

In the Supplementary Materials, the conditions of the overlapping of emissions from two different sources are highlighted. Let one consider a 1D profile on which emissions of two identical emitters can possibly overlap. Each emitter behaves like a Gaussian function centered on positions ξ_1 and ξ_2 with identical standard deviations σ. We note the centre of the profile $\xi_m = \frac{\xi_1+\xi_2}{2}$. The profile is written as:

$$E(\xi) = \frac{\mathcal{E}}{\sqrt{2\pi}\sigma}\exp\left(-\frac{(\xi-\xi_1)^2}{2\sigma^2}\right) + \frac{\mathcal{E}}{\sqrt{2\pi}\sigma}\exp\left(-\frac{(\xi-\xi_2)^2}{2\sigma^2}\right)$$

We change the frame of reference using ξ_m as the origin and a-dimension the problem by scaling distances by $\sqrt{2}\sigma$ (i.e. we note $\xi' = \frac{\xi}{\sqrt{2}\sigma}$). We also note $\delta = \frac{\xi_2-\xi_1}{2\sqrt{2}\sigma}$. The profile becomes:

$$E(\xi') = \frac{\mathcal{E}}{\sqrt{2\pi}\sigma}(e^{-(\xi'+\delta)^2} + e^{-(\xi'-\delta)^2})$$

The purpose is to find a condition on δ, i.e. a relationship between the distance between both emitters $|\xi_2 - \xi_1|$ and σ for which the two emitters can be distinguished. When it is the case, we observe two maxima of emissions, and a local minimum at the centre of the profile $\xi' = 0$. To find the two maxima, when they exist, we calculate the derivative of E:

$$\frac{\mathrm{d}E}{\mathrm{d}\xi'}(\xi') = \frac{\mathcal{E}}{\sqrt{2\pi}\sigma}((-2\xi' - 2\delta)e^{-(\xi'+\delta)^2} + (-2\xi' + 2\delta)e^{-(\xi'-\delta)^2})$$

The extrema corresponds to the derivative being null. One solves the equation $\frac{\mathrm{d}E}{\mathrm{d}\xi'}(\xi'_{\text{extr}}) = 0$:

$$\begin{aligned}\frac{\mathrm{d}E}{\mathrm{d}\xi'}(\xi'_{\text{extr}}) = 0 &\iff (\xi' + \delta)e^{-(\xi'+\delta)^2} = (-\xi' + \delta)e^{-(\xi'-\delta)^2}\\ &\iff \xi'(e^{-\xi'^2-2\xi'\delta-\delta^2} - e^{-\xi'^2+2\xi'\delta-\delta^2}) = \delta(e^{-\xi'^2+2\xi'\delta-\delta^2} - e^{-\xi'^2-2\xi'\delta-\delta^2})\\ &\iff \xi'(e^{-2\xi'\delta} + e^{2\xi'\delta}) = \delta(e^{2\xi'\delta} - e^{-2\xi'\delta})\\ &\iff \xi' = \delta\tanh(2\xi'\delta)\end{aligned}$$

The obvious solution is $\xi' = 0$ (centre of the profile). The existence of other solutions depends on the slope of the function on the right-hand side of the equation. The development in power series of the tanh function shows a slope of 1 in zero. In zero, the slope of the right-hand side is therefore $2\delta^2$. There are three solutions when $2\delta^2 > 1$, which means that the distinction of two sources is possible if:

$$|\xi_2 - \xi_1| > 2\sigma$$

The EMG function as a solution of the flux-divergence equation

In Section 2.1.5, a 1D version of the flux-divergence model has been introduced. Using the complementary error function $\mathrm{erfc}(\varsigma') = 1 - \frac{2}{\sqrt{\pi}} \int_0^{\varsigma'} e^{-\varsigma^2} \mathrm{d}\varsigma$, the profile of a plume within a streamline is modelled by:

$$\omega(\xi) = \beta + \frac{\mathcal{N}}{2\xi_0} \exp\left(-\frac{\xi}{\xi_0} + \frac{\sigma^2}{2\xi_0^2}\right) \mathrm{erfc}\left(-\frac{1}{\sqrt{2}}\left(\frac{\xi}{\sigma} - \frac{\sigma}{\xi_0}\right)\right)$$

This profile is a solution of the flux-divergence scheme. Indeed, let $\mathcal{C}_1 = \exp \circ \psi_1$ with $\psi_1(\xi) = -\frac{\xi}{\xi_0} + \frac{\sigma^2}{2\xi_0^2}$ and let $\mathcal{C}_2 = \mathrm{erfc} \circ \psi_2$ with $\psi_2(\xi) = -\frac{1}{\sqrt{2}}\left(\frac{\xi}{\sigma} - \frac{\sigma}{\xi_0}\right)$. The profile is thus given by $\omega(\xi) = \beta + \frac{\mathcal{N}}{2\xi_0}\mathcal{C}_1(\xi)\mathcal{C}_2(\xi)$. Discarding the background β in the expression of ω, the derivative of the plume profile with respect to distance is:

$$\begin{aligned}
\frac{\mathrm{d}\omega}{\mathrm{d}\xi}(\xi) &= \frac{\mathcal{N}}{2\xi_0}\left(\frac{\mathrm{d}\mathcal{C}_1}{\mathrm{d}\xi}(\xi)\mathcal{C}_2(\xi) + \mathcal{C}_1(\xi)\frac{\mathrm{d}\mathcal{C}_2}{\mathrm{d}\xi}(\xi)\right) \\
&= \frac{\mathcal{N}}{2\xi_0}\left(\frac{\mathrm{d}\psi_1}{\mathrm{d}\xi}(\xi)e^{\psi_1(\xi)}\mathcal{C}_2(\xi) - \mathcal{C}_1(\xi)\frac{\mathrm{d}\psi_2}{\mathrm{d}\xi}(\xi)\frac{2}{\sqrt{\pi}}\exp\left(-\psi_2(\xi)^2\right)\right) \\
&= \frac{\mathcal{N}}{2\xi_0}\left(-\frac{1}{\xi_0}e^{\psi_1(\xi)}\mathrm{erfc}(\psi_2(\xi)) + e^{\psi_1(\xi)}\frac{1}{\sqrt{2}\sigma}\frac{2}{\sqrt{\pi}}\exp\left(-\psi_2(\xi)^2\right)\right)
\end{aligned}$$

The flux-divergence equation in the plume is written $E = w_0\frac{\mathrm{d}\omega}{\mathrm{d}\xi} + \frac{\omega}{\tau}$ with the lifetime τ and wind module w_0 being linked by $\xi_0 = w_0\tau$. The emissions are thus calculated:

$$\begin{aligned}
E(\xi) = \frac{\mathcal{N}w_0}{2\xi_0}&\left(-\frac{1}{\xi_0}e^{\psi_1(\xi)}\mathrm{erfc}(\psi_2(\xi)) + e^{\psi_1(\xi)}\frac{1}{\sqrt{2}\sigma}\frac{2}{\sqrt{\pi}}\exp\left(-\psi_2(\xi)^2\right)\right) + \frac{w_0}{\xi_0}\frac{\mathcal{N}}{2\xi_0}e^{\psi_1(\xi)}\mathrm{erfc}(\psi_2(\xi)) \\
= \frac{\mathcal{N}/\tau}{\sqrt{2\pi}\sigma}&\exp(\psi_1(\xi) - \psi_2(\xi)^2)
\end{aligned}$$

With $\psi_1(\xi) - \psi_2(\xi)^2 = -\frac{\xi}{\xi_0} + \frac{\sigma^2}{2\xi_0^2} - \frac{\xi^2}{2\sigma^2} - \frac{\sigma^2}{2\xi_0^2} + \frac{\xi}{\xi_0}$, the final Gaussian shape of the emissions appears:

$$E(\xi) = \frac{\mathcal{E}}{\sqrt{2\pi}\sigma}\exp\left(-\frac{\xi^2}{2\sigma^2}\right) \text{ with } \mathcal{E} = \mathcal{N}/\tau \text{ the flow rate of the source.}$$